Synthesis of Functional Nanoporous Materials for Electrocatalytic Applications

VORGELEGT VON

M.Sc. **Xiaojia Zhao**

ORCID: 0000-0001-8912-0241

Von der Fakultät II – Mathematik und Naturwissenschaften

der Technischen Universität Berlin

zur Erlangung des akademischen Grades

Doktor der Naturwissenschaften

Dr. rer. Nat.

genehmigte Dissertation

Promotionsausschuss

Vorsizender: Prof. Dr. Thomas Friedrich

Gutachter: Prof. Dr. Arne Thomas

Gutachterin: Prof. Dr. Maria-Magdalena Titirici

Tag der wissenschaftlichen Aussprache: 05. September 2019

Berlin 2019

Acknowledgments

On September 16, 2015, I arrived at Berlin for my doctoral research. It has been almost four years since then, and I am very grateful to myself for making that decision. Within this 4-year's study in Berlin, I have gained so much and lots of people I would like to acknowledgment here.

At first, I would like to thank my supervisor Prof. Dr. Arne Thomas for his strong support in my research during these four years. He is a knowledgeable talent and full of enthusiastic in scientific research. He can always come up with interesting ideas to inspire us. He is a patient person that always encourages me on the experiments even though I had hardly made any progress in my first year. I sincerely appreciate his help and guidance on my research projects. He is also a very nice person, and always provide a relaxed working environment in our lab. I am very glad to have the chance to complete my PhD research in his wonderful research group.

I am very grateful to all the members of AK Thomas, I feel so lucky to have such great colleagues and friends as well. They help me a lot in my academic research and daily life. Especially, I would like to thank Dr. Pradip Pachfule and Dr. Shuang Li for their strong support on my experiment design and electrochemical testing. I also want to thank to Dr Johannes Schmidt, Dr. Jérôme Roeser, Dr Hefeng Cheng, Dr. Rafael de Lima Oliveira, Dr. Mattithias Trunk, Nicolas Chaoui, Sophie Kucken, Thomas Langenhahn, Daniel Hagemeyer, Amitava Acharjya, Dr. Daniel Becker, Dr Yaozu Liao, Dr. Changxia Li, Dr. Ha Le Vu, Michaela Konig, Sarah Vogl, Vincent Weigelt, Mengyang Ye, Jin Yang and all the members from our group. Thank to our secretary Anne Svilarov for arranging the daily affairs and ordering chemicals for me, and also thank to our technicians Maria Unterweger and Christina Eichenauer for measuring XRD, XPS, BET and TGA. I also thank to the research facilities in Department of Chemistry and ZELMI in TU-Berlin for the basic analyses. Here I also want to say thanks to Julia Grüneberg for helping me to translate the abstract into German.

I am grateful for the financial support afforded by China Scholarship Council (CSC). I also want to express my thanks to Unifying Concepts in Catalysis (UniCat) and Berlin International Graduate of Natural Sciences and Engineering (BIG-NSE). Thank to the coordinator/managing director of the BIG-NSE, Dr Jean-Philippe Lonjaret, for his help during my PhD study.

At last, I would like to express my special acknowledgement to my parents and my sister. I am very grateful for their support and encourage over the years. Looking back on my way to study, there have too many frustrations on the road. But I very much appreciate my father's teachings, my mother's encourage and my sister's guidance, to let me believe in every choice I made, and stick to it.

Abstract

Recently, the International Energy Agency has reported that the global energy demand is growing at the fastest pace this decade, while fossil fuels are leading the charge. The outcome of this is a higher carbon dioxide emission and environmental pollution, which can only be averted by developing all clean energy solutions and improving their efficiency. The development of electrocatalysis for renewable hydrogen production, fuel cell and metal-air batteries provides a promising route to address the abovementioned problems. Current efforts mainly focus on developing low-cost and high-efficient electrocatalysts to drive the electrochemical reactions, including hydrogen evolution reactions (HER), oxygen evolution reactions (OER) and oxygen reduction reactions (ORR). Up to now, noble metal-based electrocatalysts exhibit the best electrocatalytic activities, but their scarcity and high cost largely hinder sustainable application and remain a bottleneck for the commercialization of the abovementioned devices. Consequently, numerous electrocatalysts have been synthesized based on the earth-abundant elements and advanced techniques have been applied to study the reaction mechanisms, thus guiding the catalyst design. It is of significant importance to develop efficient and stable electrocatalysts for HER, OER and ORR, and further for practical applications in hydrogen production and metal-air battery.

In this thesis, we have designed and developed a range of non-noble metal-based electrocatalysts and further explored their potential in energy conversion and storage. Various metal/carbon precursors and unique strategies have been applied to construct these targeted catalysts, ranging from metal-free electrocatalysts, non-noble metal-based carbon composites to polymer-based electrocatalysts. This thesis contributes to exploring promising precursors and developing unique strategies to synthesize electrocatalysts, which can be further applied to many other areas for catalyst design.

For metal-free electrocatalyst studies, an ionic liquid-assisted soft-templating method was applied to construct ordered mesoporous carbons with nitrogen atoms enriched at the pore surface, demonstrated by X-ray photoelectron spectroscopy (XPS) and temperature-programmed desorption of carbon dioxide (CO_2-TPD). The resulting metal-free nitrogen-doped mesoporous carbons exhibit remarkable electrocatalytic activity in HER. The accessibility and efficient utilization of nitrogen atoms is responsible for the superior HER catalytic activity.

Porous crystalline polymers provide a promising platform to construct non-noble metal-based carbon electrocatalysts. Here we carried out two projects taking MOFs and COFs as precursors to synthesized metal-based carbon composites and metal-nitrogen doped carbon (M-N-C) electrocatalyst, respectively. First, a bimetallic MOF (MIL-88-Fe/Ni) was applied as carbon precursor to produce the corresponding bimetal (Fe/Ni)-based carbon electrocatalyst. The crystallinity of the MOF was studied to show its importance on the formation of these unique structures. The obtained hybrid catalyst (Fe-Ni@NC-CNTs) exhibited high OER and HER activity in alkaline solution, and further showed its practical application in an electrochemical water-splitting unit for H_2 and O_2 production. Inspired by these results, we continued to explore

the potential application of COFs as carbon precursor for the construction of M-N-C electrocatalyst, in which bipyridine moieties were deliberately chosen and incorporated within the COF backbone to complex iron (Fe) ions, which then could form $Fe-N_x$ active sites after a subsequent pyrolysis process. In addition, a silica-assisted mechanochemical method was developed to achieve the formation of mesoporous carbon derived from COFs. The influence of crystallinity of COFs and mesoporous structures on electrocatalytic activities was studied. As expect, the obtained catalyst exhibited a large pore volume and surface area, and abundant $Fe-N_x$ sites, showing a high ORR activity and potential application in zinc-air battery.

Polymer-based porous materials represent an emerging set of electrocatalysts due to their controllable synthesis over structure formation and active sites. In our last project, for the first time we developed a practical approach to prepare a hierarchical COFs with macropores in addition to their inherent microporosity. Cobalt ions were introduced into COFs by complexing with bipyridine moieties to form a Co^{2+}-functionalized COF. The resulting COF-based catalyst exhibited a high OER activity, which is much improved compared to the purely microporous COF. This can be attributed to the improved mass diffusion properties in the hierarchically porous COF structures, together with the easily accessible active Co^{2+}-bipyridine sites.

These four studied works prove that the electrocatalytic activities of electrocatalysts can be promoted by design of precursors and controlled conversion strategies into materials that will also be of benefit to many other catalytic reactions for designing efficient catalysts.

Zusammenfassung

Neuesten Berichten der Internationalen Energieagentur zufolge wächst der globale Energiebedarf in diesem Jahrzehnt am schnellsten, wobei besonders der Bedarf an fossilen Brennstoffen gestiegen ist. Als Resultat daraus folgen erhöhte Kohlenstoffdioxid-Emissionen und Umweltverschmutzungen, welchen nur durch die Entwicklung sauberer und verbesserter Energielösungen entgegengearbeitet werden kann. Die Entwicklung der Elektrokatalyse zur Produktion von Wasserstoff als regenerativem Rohstoff, Brennstoffzellen und Metall-Luft-Batterien liefert vielversprechende Ansätze zur Lösung der genannten Probleme. Dabei liegt der Fokus auf der Entwicklung von kostengünstigen und hocheffizienten Elektrokatalysatoren für elektrochemische Reaktionen wie Wasserstoffentwicklungsreaktionen (HER), Sauerstoffentwicklungsreaktionen (OER) und Sauerstoffreduktionsreaktionen (ORR). Bis heute besitzen Edelmetall-basierte Elektrokatalysatoren die beste elektrokatalytische Aktivität, aber ihre nachhaltige Anwendung und Kommerzialisierung ist maßgeblich durch ihr begrenztes Vorkommen und ihren hohen Preis beeinträchtigt. Deshalb wurden zahlreiche Elektrokatalysatoren auf der Grundlage von auf der Erde reichlich vorkommenden Elementen entwickelt und weiterentwickelte Verfahren angewandt um deren Reaktionsmechanismen zu studieren und so ein gezieltes Katalysatordesign zu ermöglichen. Besonders bedeutend ist hierbei die Entwicklung von effizienten und stabilen Elektrokatalysatoren für die HER, OER und ORR, sowie für die praktische Anwendung in der Wasserstoffproduktion und in Metall-Luft-Batterien.

In der vorliegenden Arbeit wurden verschiedene Elektrokatalysatoren auf der Grundlage von unedlen Metallen entwickelt und deren Potential für die Energieumwandlung und Energiespeicherung untersucht. Unterschiedliche Metall/Kohlenstoff Vorläufer und neuartige Strategien wurden angewandt um die angestrebten Katalysatoren darzustellen. So konnten Metall-freie Katalysatoren, auf unedlen Metallen basierte Kohlenstoffkomposite und Polymer-basierte Elektrokatalysatoren erhalten werden. Diese Arbeit trägt damit zur Entwicklung von vielversprechenden Vorstufen und einzigartigen Strategien zur Darstellung von Elektrokatalysatoren bei, welche ebenso auf anderen Bereichen des Katalysatordesigns angewandt werden können.

Für Studien an Metall-freien Elektrokatalysatoren wurde eine ionische Flüssigkeiten-unterstützte weiche Templatierung angewandt, um geordneten, mesoporösen Kohlenstoff mit in den Poren angereicherten Stickstoffatomen zu erhalten, was durch Röntgenphotoelektronenspektroskopie (XPS) und Temperatur-programmierter Kohlenstoffdioxid Desorption (CO_2-TPD) nachgewiesen wurde. Die resultierenden Metall-freien Stickstoff-dotierten mesoporösen Kohlenstoffe zeigen eine bemerkenswerte elektrokatalytische Aktivität für die HER auf, die durch die Zugänglichkeit und effiziente Nutzung der Stickstoffatome begründet ist.

Poröse kristalline Polymere stellen eine vielversprechende Plattform für die Darstellung auf unedlen Metallen basierten Kohlenstoff Elektrokatalysatoren dar. Ausgehend von Metall-

organischen Netzwerken (MOFs) und Kovalent-organischen Netzwerken (COFs) wurden Metall-basierte Kohlenstoffkomposit und Metall-Stickstoff-dotierte Kohlenstoff (M-C-N) Elektrokatalysatoren entwickelt. Zunächst wurde bimetallisches MOF (MIL-88-Fe/Ni) als Kohlenstoffvorstufe verwendet, um den korrespondierenden bimetallisch (Fe/Ni-)basierten Kohlenstoff Elektrokatalysator zu generieren. Dabei wurde zudem die Kristallinität des MOFs wurde untersucht, um dessen Einfluss auf die Bildung dieser einzigartigen Strukturen zu untersuchen. Der erhaltene hybride Katalysator (Fe-Ni@NC-CNTs) besitzt eine hohe OER und HER Aktivität in alkalischem Medium und findet zudem praktische Anwendung in der elektrochemischen Wasserspaltung zur H_2 und O_2 Produktion. Diese Ergebnisse führten zur Untersuchung des Potentials von COFs als Kohlenstoffvorstufe für die Darstellung von M N C Elektrokatalysatoren. Bipyridin-Einheiten im COF Rückgrat ermöglichen dabei die Komplexierung von Eisen-Ionen, welche wiederum nach Pyrolyse die $Fe-N_x$ aktiven Stellen liefern. Zusätzlich wurde eine Silica-unterstütze mechanochemische Methode zur Darstellung von mesoporösem Kohlenstoff ausgehend von COFs entwickelt und wiederum der Einfluss der Kristallinität von COFs und mesoporösen Strukturen auf die elektrokatalytische Aktivität untersucht. Wie erwartet weist der erhaltene Katalysator ein großes Porenvolumen, eine hohe Oberfläche und zahlreiche $Fe-N_x$ Stellen auf, die zu einer hohen ORR Aktivität führen und die Anwendung in Zink-Luft-Batterien ermöglichen.

Polymer-basierte poröse Materialien stellen aufgrund ihrer Kontrollierbarkeit im Hinblick auf die Strukturbildung und aktiven Stellen während der Synthese eine vielversprechende Klasse an Elektrokatalysatoren dar. Dazu wurde ein neuartiger praktischer Ansatz zur Darstellung hierarchischer COFs mit Makroporen und inhärenter Mikroporosität entwickelt. Ein Co^{2+}-funktionalisierter COF wurde durch Komplexierung von Cobalt-Ionen mit im COF-Rückgrat befindlichen Bipyridin-Einheiten erhalten. Durch die verbesserten Massendiffusionseigenschaften und den einfach zugänglichen aktiven Co^{2+}-Bipyridin Stellen besitzt der resultierende COF-basierte Katalysator im Vergleich zum mikroporösen COF eine deutlich erhöhte OER Aktivität.

Wie anhand dieser vier Projekte aufgezeigt werden konnte, kann die elektrokatalytische Aktivität von Elektrokatalysatoren durch das Katalysatordesign und kontrollierte Synthesestrategien gezielt gefördert werden, so dass Materialien erhalten werden können die ebenso für viele andere katalytische Reaktionen und deren effizientes Katalysatordesign von Vorteil sein können.

List of Publications and Author Contributions

This cumulative thesis is based on results that have been published during my PhD period. This section lists all my publications, which are released under the name Xiaojia Zhao during this time. Publications [XJZ01–XJZ04] build the scientific basis of this thesis and are reprinted in Chapter 8.

Parts of this dissertation have been published:

[XJZ01] **Xiaojia Zhao**, Shuang Li, Hefeng Cheng, Johannes Schmidt, Arne Thomas*, Ionic Liquid-Assisted Synthesis of Mesoporous Carbons with Surface-Enriched Nitrogen for the Hydrogen Evolution Reaction, *ACS Appl. Mater. Interfaces* **2018**, 10, 3912-3920. DOI: 10.1021/acsami.7b14919

✦ All materials synthesis, electrochemical analysis and data analysis, as well as the complete manuscript writing were carried out by Xiaojia Zhao.

[XJZ02] **Xiaojia Zhao**, Pradip Pachfule, Shuang Li, Jan Ron Justin Simke, Johannes Schmidt, Arne Thomas*, Bifunctional Electrocatalysts for Overall Water Splitting from an Iron/Nickel-Based Bimetallic Metal-Organic Framework/Dicyandiamide Composite, *Angew. Chem. Int. Ed.* **2018**, 130, 9059-9064. DOI: 10.1002/anie.201803136

✦ The materials and experiments were designed and synthesized by Xiaojia Zhao. All electrochemical analysis and data analysis, as well as the complete manuscript writing were carried out by Xiaojia Zhao.

[XJZ03] **Xiaojia Zhao**, Pradip Pachfule, Shuang Li, Thomas Langenhahn, Mengyang Ye, Guiying Tian, Johannes Schmidt, Arne Thomas*, Silica-Templated Covalent Organic Framework-derived Fe-N-doped Mesoporous Carbon as Oxygen Reduction Electrocatalyst, *Chem. Mater.* **2019**, DOI: 10.1021/acs.chemmater.9b00204. DOI: 10.1021/acs.chemmater.9b00204

✦ The materials and experiments were designed and synthesized by Xiaojia Zhao. All electrochemical analysis and data analysis, as well as the complete manuscript writing were carried out by Xiaojia Zhao.

[XJZ04] **Xiaojia Zhao**, Pradip Pachfule, Shuang Li, Thomas Langenhahn, Mengyang Ye, Christopher Schlesiger, Sebastian Praetz, Johannes Schmidt, Arne Thomas*, Macro/Microporous Covalent Organic Frameworks for Efficient Electrocatalysis, *J. Am, Chem, Soc.* **2019**, 141, 6623-6630. DOI: 10.1021/jacs.9b01226

❖ The materials and experiments were designed and synthesized by Xiaojia Zhao. All electrochemical analysis and data analysis, as well as the complete manuscript writing were carried out by Xiaojia Zhao.

[XJZ05] Shuang Li, Chong Cheng, **Xiaojia Zhao**, Johannes Schmidt, Arne Thomas[*], Active Salt/Silica-Templated 2D Mesoporous FeCo-N_x-Carbon as Bifunctional Oxygen Electrodes for Zinc–Air Batteries, *Angew. Chem. Int. Ed.* **2018**, 57, 1856-1862. DOI: 10.1002/anie.201710852

❖ The electrochemical and catalytic performances were tested and discussion by Xiaojia Zhao.

Contents

1 Introduction

1.1 Outline and Aims of This Thesis

The development of electrocatalysis provide a promising route to tackle energy crisis and environmental pollution with the outstanding achievement in the field of energy conversion and storage, including renewable hydrogen production, fuel cell and metal-air battery.[1-6] Recently, numerous efforts have been devoted to exploring efficient alternatives to noble metals to drive the key electrochemical reactions (i.e. HER, OER and ORR), including non-noble metal-based electrocatalysts,[7,8] carbon-based composites[2,9] and polymer-based electrocatalysts.[10-12]

Carbon-based electrocatalysts have always been considered as one of the most efficient catalysts because of their high surface area, good electrical conductivity, and chemical stability. Especially, when dopants or metal compounds are introduced into carbon matrixes, the electrocatalytic activities can be significantly increased. For example, dopants (e.g. boron(B), nitrogen(N), sulfur(S), phosphorus(P), fluorine(F)) can be chemically attached or incorporated into the backbones of carbon materials.[13] Due to the difference of atomic size and electronegativity of heteroatoms to the matrix carbon atoms, the introduced heteroatoms can efficiently change the charge distribution and electronic properties of carbon skeletons, which is supposed to be responsible for the activities during electrocatalytic processes.[14,15] On the other hand, non-noble metal-based electrocatalysts has been intensively studied in which the earth-abundant transition metals (e.g. iron(Fe), nickel(Ni), cobalt(Co), molybdenum(Mo), tungsten(W)) and their derivatives (e.g. oxides, sulfides, carbides, phosphides) have been finely dispersed into carbon matrixes to form metal-based carbon composites.[16-19] It is supposed that the accessible surface of metal compounds provides the active sites for electrocatalytic reactions. Particularly, decreasing metal nanoparticle size is supposed to efficiently increase the number of coordinated metal atoms to reach the maximum active sites. Consequently, single atom-doped carbon materials have emerged as an unique system for electrocatalysis, especially the atomic metal-nitrogen moieties immobilized or supported in carbons (M-N-C; M= Fe, Co, Ni etc.), which represent an unique class of electrocatalysts with special electronic structure and maximal atomic utilization for a range of electrochemical applications.[20-25]

Besides, these features of carbon matrix, intrinsic properties such as conductivity, graphitization and porosity play a crucial effect on the electrocatalytic activities. For example, carbon nanotubes (CNTs) and graphene are widely used as solid-state supports due to their good electronic conductivity and chemical stability,[16,26,27] whereas porous carbons with hierarchical porosity represent another promising platform to construct metal-based carbon electrocatalysts. In addition to the intrinsic properties, the mesoporosity is especially proved to be beneficial to the mass transport and the accessibility of active sites from the catalysts, which is generally introduced into carbon matrixes by applying various methodologies such as nanocasting/hard-templating, soft-templating and self-assembly.[28-30] In order to prepare the

highly efficient electrocatalysts, recently, MOFs and COFs have been extensively studied as promising precursors.[31-33] In particular, MOFs are proved to be ideal precursors to synthesize M-N-C electrocatalysts, due to their porous structures and ability to hold metal centres as well as chelating moieties in their backbones.[23,34,35]

Apart from carbon-based electrocatalysts, polymeric materials, such as MOFs and COFs, represent an emerging set of electrocatalysts because of their controllable synthesis over structure formation, tuneable and identified active sites, which are supposed to be useful for catalyst optimization and mechanism understanding.[10,12,36,37] Indeed, numerous polymer-based electrocatalysts have been developed, showing their promising applications in HER, OER and ORR. Even though polymer-based electrocatalysts are still in their infancy, they have shown promising potential to explore electrocatalysis and are highly possible to become a topic with extensive scientific significance.[10]

In this thesis, we aim to design efficient electrocatalysts as alternatives to noble metal-based catalysts by applying various metal/carbon precursors and developing unique strategies to construct non-noble metal-based electrocatalysts, ranging from metal-free electrocatalysts, non-noble metal-based carbon composites to polymer-based electrocatalysts. Their electrocatalytic activities have been evaluated for HER, OER and ORR as well as practical applications in overall water splitting and zinc-air batteries.

Metal-free carbon-based materials are one of the most promising electrocatalysts due to their chemical stability and metal-free feature. To develop efficient metal-free electrocatalysts, heteroatoms are generally incorporated into carbon skeletons to tailor the electronic structure. However, the active sites formed from heteroatoms are generally distributed uniformly over the entire volume of the heteroatom-doped carbons, large fractions are hardly accessible to reactants. Advanced strategies are necessary to develop to achieve the preferential distribution of nitrogen atoms at the carbon surface and promote the accessibility of active sites. This project is published in [XJZ01].

Non-noble metal-based electrocatalysts are the most promising alternatives to noble metals to achieve comparable electrochemical performances. Carbon precursors with different metal species and structures are investigated to study their influence on the electrocatalytic activities. This task is performed by applying two different crystalline polymers, i.e. MOFs and COFs, as carbon precursor to construct non-noble metal-based carbon electrocatalysts. The results are published in [XJZ02] and [XJZ03].

As a next step of project [XJZ03], polymer-based electrocatalysts are investigated by incorporating metal ions into COFs. A hard-templating approach is used for the first time to prepare a hierarchical COFs with macropores in addition to their inherent microporosity. This work is published in [XJZ04].

1.2 Structure of the Thesis

The introduction of this thesis (Chapter 1) gives a brief summary on the development of non-noble metal-based electrocatalysts, including heteroatom-doped carbons, non-noble metal-based carbon composites, metal-nitrogen-carbon (M-N-C) electrocatalysts and polymer-based electrocatalysts. Various materials, metal species and strategies are discussed. In addition, the corresponding chemical reactions, i.e. HER, OER, and ORR are presented, with a discussion on the potential mechanisms and currently most studied catalysts.

Each of the following chapters (2-5) summarize one project that was published in [XJZ01], [XJZ02], [XJZ03], and [XJZ04]. The corresponding abstract is reprinted followed by a project summary. Then the results are summarized and set into context in Chapter 6 in a summary. The complete manuscripts are attached in Chapter 8 as publication reprints.

1.3 Heteroatom-doped Carbon Electrocatalysts

Heteroatom-doped carbon nanomaterials represent one of the most promising electrocatalysts in fuel cells, but are also suitable for a wide range of applications in energy conversion and storage such as supercapacitors, fuel cells and batteries.[2,38-40] The introduction of heteroatoms, e.g. N, S, and P, can cause some structural distortions in the carbon lattice resulting in changes in the charge densities of the carbon materials[14,15,39]. Compared to pure carbon, these heteroatom-doped carbons often exhibit high electric conductivities and good stability under acidic/alkaline condition. In addition, their metal-free nature, endows it as an environment-friendly electrocatalyst by avoiding the possible leaching of metal ions.

Heteroatom doping is generally achieved by chemically attaching or incorporating heteroatoms into the backbone of carbon materials. Figure 1.1 shows an illustration of doping heteroatoms, e.g. N, B, P, S and F, and the possible structure changes induced by doping[38,41]. Due to the difference of atomic size and electronegativity of heteroatoms compared to matrix carbon atoms, the introduced heteroatoms can efficiently change the charge distribution and electronic properties of carbon skeletons, which is supposed to be responsible for the activities during electrocatalytic processes.[2,41] In addition, the heteroatom-doping can induce defects within carbon skeletons, which could further change the chemical activity of carbon materials, thus changing the electrocatalytic activity.
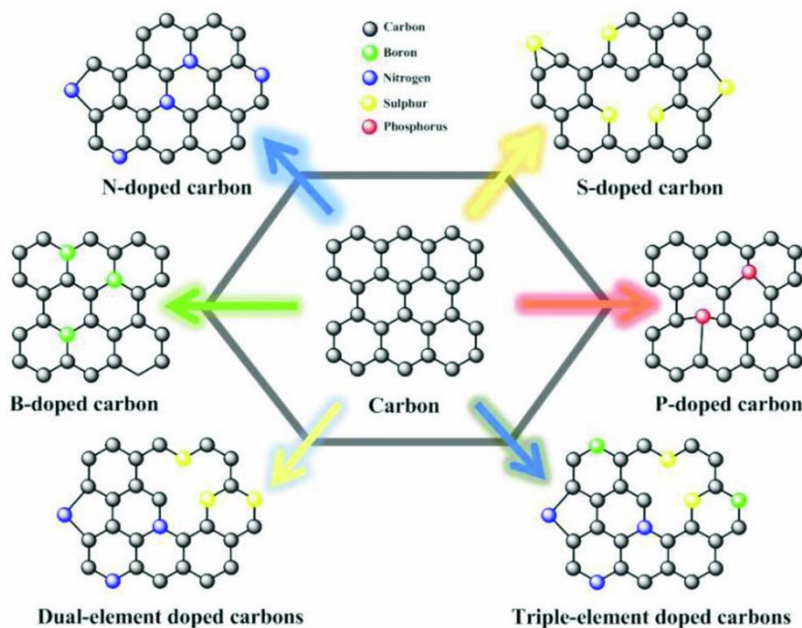
Figure 1.1 Schematic diagram of the structures of various heteroatom-doped carbons.[42] Reproduced with the permission from John Wiley and Sons.

1.3.1 Nitrogen-doped Carbon Electrocatalysts

Nitrogen, as a "neighbor" of carbon in the Periodic Table of Elements, has an atomic size similar to that of carbon atoms, so it is supposed to be relatively easy to combine these two elements with a low lattice mismatch.[2,9,38,40,43-49] Generally, nitrogen atoms are introduced into graphite, i.e. sp^2 hybridized carbon lattices. The conjugated carbons are supposed to dominate the properties of the materials, which are however further tailored by the types of incorporated nitrogen atoms. So it is of importance to define the chemical environment of the doped nitrogen atoms, that can be normally divided into two groups of nitrogen modifications: chemical nitrogen and structural nitrogen.[13] As shown in Figure 1.2, the former refers to the nitrogen-containing functional groups, e.g. amine and nitrosyl groups. The latter appears as nitrogen directly incorporated into the skeleton of carbon materials, e.g. pyrrolic, pyridinic and quaternary-graphitic nitrogen.
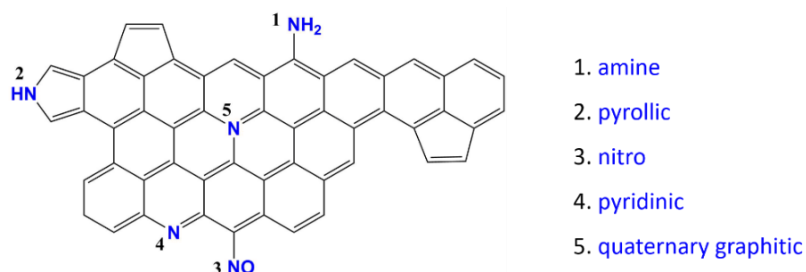

Figure 1.2 Schematic overview of the possible nitrogen species in N-doped carbon materials.[13] Reproduced with the permission from Royal Society of Chemistry.

It is well known that doped nitrogen can lead to the asymmetrical charge distributions of carbon materials, giving rise to wide application in electrocatalysis.[14,50,51] Furthermore, the influence of incorporated nitrogen towards band structure and electric conductivity has been experimentally and theoretically proven.[13,15,39] For example, Qiao and co-workers revealed the activity origin and catalyst design principles of N-doped carbon materials towards HER by density functional theory (DFT) calculations.[14] Besides, the doped nitrogen species were also studied to identify the possible active sites. In that context, well-controlled pyridinic N-doped carbon was synthesized and the carbon atoms with Lewis basicity next to pyridinic N were proven to be the active sites towards ORR.[48]

The synthetic pathways of N-doped carbon materials are commonly derived from the pyrolysis of nitrogen and carbon containing precursors, such as melamine, polydopamine, polyaniline or N-containing ionic liquids.[43,52-54] In the past years, our group has reported several N-doped porous carbon materials by using ionic liquids as precursors.[13,38,43,52,54] The obtained N-doped carbons possess high nitrogen content, good porosity and very favourable electric and electrochemical properties. In addition, mesoporosity structures can be introduced into N-doped carbons to improve the electrocatalytic activities by applying various methodologies such as nanocasting/hard-templating, soft-templating and self-assembly (Figure 1.3).[9,30,45,47,55] The introduced mesoporous structure is proved to be efficiently promoting the mass transfer and the accessibility of active sites during electrocatalytic process, thus improving the electrochemical performances. Besides, carbon nanotubes (CNTs) and graphene provide a good platform to fabricate the corresponding N-doped carbons for energy-related applications, and further mechanism studies.[14,15,39,56-59]
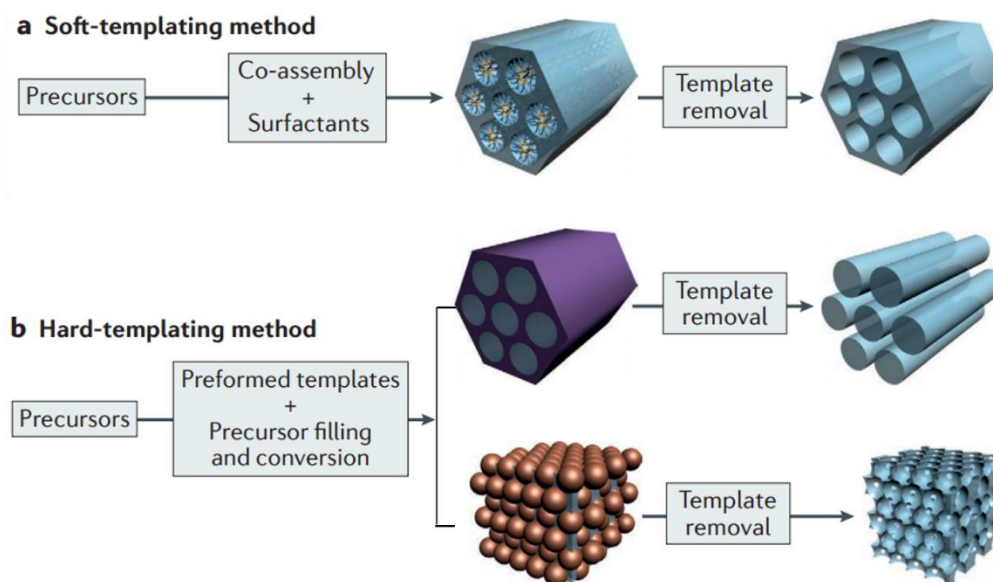

Figure 1.3. Typical methods for constructing mesoporous materials. a) Soft-templating method. b) Hard-templating method.[29] Reproduced with the permission from Springer Nature.

1.4 Non-Noble Metal-based Carbon Electrocatalysts

Recently, non-noble metal-based electrocatalysts have been intensively studied, where various porous carbons act as solid-state supports for dispersion of metal compounds and metal clusters or single atoms.[60]

1.4.1 Non-Noble Metal-based Carbon Composites

In the past few decades, noble metals such as ruthenium (Ru), iridium (Ir) and platinum (Pt), have been used extensively as catalysts in a wide range of electrochemical reactions, such as HER, OER and ORR. However, the limited resources and high cost of these noble metals significantly hinder their practical applications. Recently, non-noble metals such as Fe, Co, Ni, and Mo have received increasing attention as potential alternatives to noble metals. Many non-noble metal-based carbon composites show competitive electrochemical performance in energy-related reactions.[61,62] In addition, a variety of non-noble metal compounds such as metal sulfides (MoS_2, FeS_2),[26,63] metal carbides (MoC_2),[18] metal phosphides (CoP),[64] and metal oxides (Co_3O_4),[17] have been developed to construct the corresponding carbon-based electrocatalysts. Apart from the metals, carbon materials, such as CNTs, graphene and porous carbons, have been intensively studied as supports for metal species due to their electronic conductivity, which promotes the electron transfer during electrocatalytic process. For example, Dai and co-workers synthesized an ultrathin nickel-iron layered double hydroxide (NiFe-LDH) grown on the network of CNTs, where CNTs could form interconnected electrically conducting networks to promote its electrocatalytic performance.[16] On the other hand, porous carbons can be synthesized with macro-, meso-, or hierarchically porous structures via soft-templating, hard-templating or template-free approaches.[29,30] The obtained porous carbons generally possess high surface area and large pore volume, which are promoting the mass transport and the accessibility of active sites during the electrocatalytic process.[28,53,65]
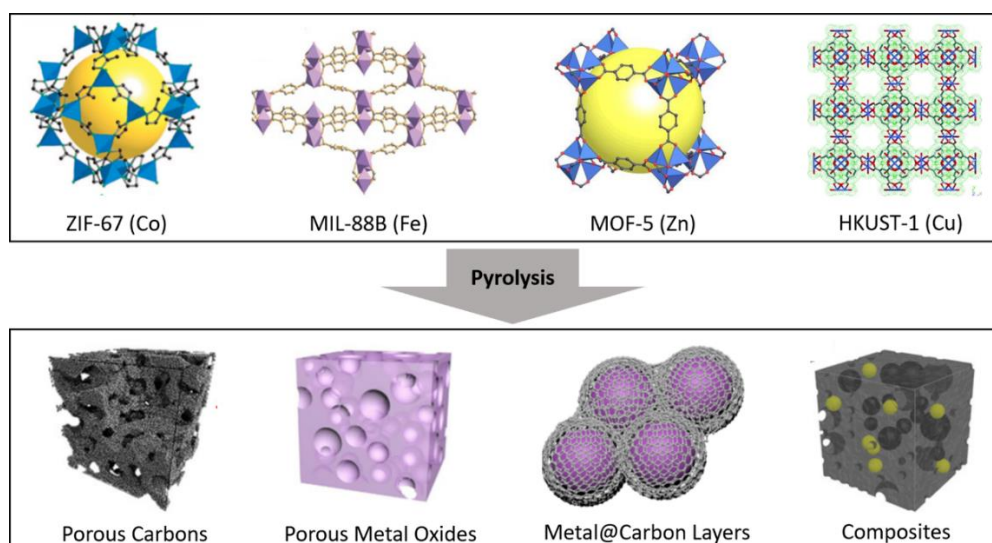

Figure 1.4 Typical transformation of metal-organic frameworks into functional nanostructured materials.[31,66-69] Reproduced with the permission from American Chemical Society.

To synthesize the above non-noble metal-based carbon electrocatalysts, carbon precursors such as polypyrrole (PPy),[70] polyaniline (PANI),[71] and polydopamine (PDA),[53] have been extensively used to generate the carbon supports via pyrolysis/heat treatment. Besides, a new type of carbon precursor, metal organic frameworks (MOFs), have currently drawn much attention as precursors to construct various electrocatalysts, such as heteroatom-doped and metal/metal oxide containing carbons.[31,72-74] It was suggested that the periodically arranged metal ions and organic ligands within MOFs enable their conversion into electrocatalysts with well-defined structures and heteroatom/metal dispersion, which are unattainable by any other synthetic means.[31,75] Figure 1.4 shows some representative MOFs structures, where the organic linkers, e.g. carboxylates and imidazolates, assemble into solid structures with well-defined porosity after linking with metal containing units (Fe, Co, Ni, Cu, Zn, etc.) to form secondary building units (SBUs) and subsequently frameworks in three dimensions. After thermal conversion, the MOF-derived carbon materials show promising electrocatalytic activities for energy conversion and storage, such as HER, OER and ORR.

1.4.2 Non-Noble Metal-Nitrogen Doped Carbon (M-N-C) Electrocatalysts

Shrinking of the metal nanoparticle size down to the sub-nanometer regime can efficiently increase the number of coordinated metal atoms to reach a maximum of active sites.[76] Consequently, single atom-doped carbon materials have emerged as unique system for electrocatalysis, especially the atomic metal-nitrogen moieties supported in carbons (M-N-C). For example, Fe-N-C has been extensively studied as an electrocatalyst for ORR with activity and stability approaching those of Pt/C.[28,71,77] Theoretical studies have proven the role of Fe-N_x sites for oxygen reduction, in which the Fe center is favorable for the adsorption of O_2 and donates electrons to reduce O_2.[78-80] In addition, M-N-C based on other non-noble metals (e.g. Co, Ni, Mo, W) have been prepared as promising candidates for catalyzing a wide range of electrochemical reactions, including HER, OER and CO_2 reduction.[23-25,28,71,81-85]

To synthesize M-N-C electrocatalysts, the selected precursors are generally pyrolyzed at elevated temperatures under an inert atmosphere. For example, a series of non-noble metals (Fe, Co or Ni) embedded in nitrogen doped graphene frameworks have been synthesized (Figure 1.5a).[20] In addition, polymer precursors such as PANI, PDA or PPy have been used to prepare M-N-C catalysts by pyrolyzing a mixture of the polymers and the respective metal salts. Etching process and secondary heat-treatment are usually performed to remove unstable metal species and stabilize the chemical structures, respectively. Our group recently reported an efficient ORR electrocatalyst with FeCo-N_x embedded in mesoporous carbon by using silica as sacrificial template, and dopamine Fe and Co complexes as precursor.[53] After pyrolysis, the templates were removed by NaOH etching leading to a pronounced mesoporous structures with homogenous dispersion of single metal atoms or clusters within the carbon matrixes acting as reversible oxygen electrocatalytic sites.
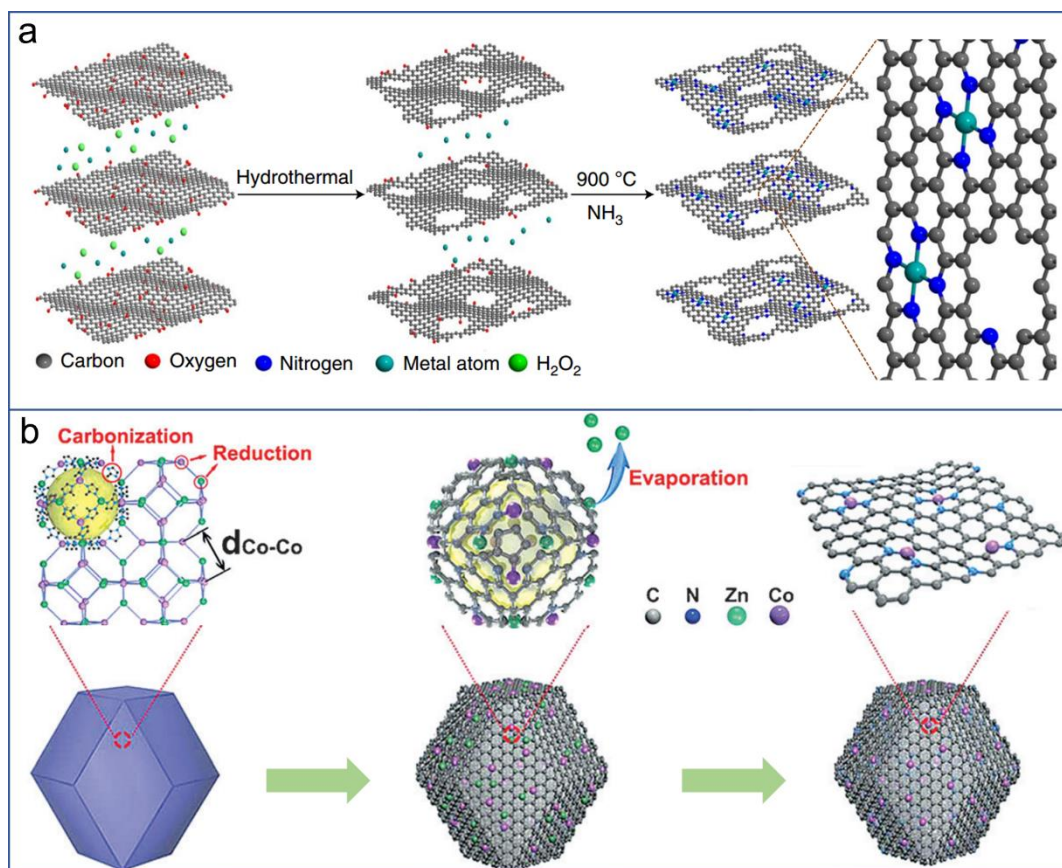
Figure 1.5 a) Preparation of M-N-C (M = Fe, Co, Ni) electrocatalysts by embedding metal ions in graphene lattices.[20] Reproduced with the permission from Springer Nature. b) The formation of Co-N-C derived from bimetallic Zn_1Co_1-BMOF.[23] Reproduced with the permission from John Wiley and Sons.

Very recently, MOFs have been demonstrated to be ideal precursors to construct M-N-C electrocatalysts because of their periodic structures leading to spatial separation of building units and inhibiting the aggregation of metal sites during pyrolysis. Typically, zeolitic imidazolate frameworks (ZIFs) are used as precursors due to their high nitrogen content and structural tailorability. For example, Li and co-workers applied ZIF-67 with half of the Co replaced by Zn, forming the bimetallic counterpart, Zn_1Co_1-BMOF (Figure 1.5b). Subsequently, Co single atom/nitrogen-doped porous carbons have been observed after pyrolysis.[23] The addition of Zn was considered as a "fence" to expend the distance of adjacent Co atoms in space. In fact, the structural adjustability of MOFs endows the possibility to produce other metal single atom sites if the precursors are built up strategically. For instance, Fe and Ni single atoms embedded in carbons were synthesized by confining Fe^{3+} and Ni^{2+} into ZIF-8 pores, respectively.[22,86,87] Moreover, other MOFs have been applied to synthesize various M-N-C electrocatalysts, such as Fe single atoms implanted mesoporous carbons from porphyrinic MOFs based on a novel mixed-ligand strategy[35] and W atoms anchored on N-doped carbons derived from W-hosted UiO-66-NH$_2$.[24]

1.5 Polymer-based Electrocatalysts

As mentioned before, extensive efforts have been devoted toward the preparation and applications of carbon-based electrocatalysts with earth-abundant elements, including doped heteroatoms and non-noble metal compounds. In recent years, also polymeric porous materials, such as MOFs and covalent organic frameworks (COFs), have emerged as electrocatalysts because of their controllable synthesis and structure formation, as well as their tunable and well-defined active sites, which are useful for catalyst optimization and mechanistic studies.[88]

1.5.1 Covalent Organic Framework (COF)-based Electrocatalysts

Recently, well-defined pure organic COF materials have attracted much attention as promising polymer-based electrocatalysts due to their high surface area, tunable pore size, and controllable molecular structures. The first COFs (COF-1 and COF-5) were reported by Yaghi and co-workers in 2005, showing that topological design principles could be applied to their synthesis and structural determinations.[89] By selecting the appropriate building blocks and linker motifs, the constructed COFs provide a novel materials system for electrochemical reactions enabling atomically precise tailoring of the incorporation of heteroatoms and location of active sites. In addition, since COFs are formed through the strong covalent bonds between organic building blocks, the COF-based electrocatalysts exhibit relatively stable chemical structures during electrocatalytic process.
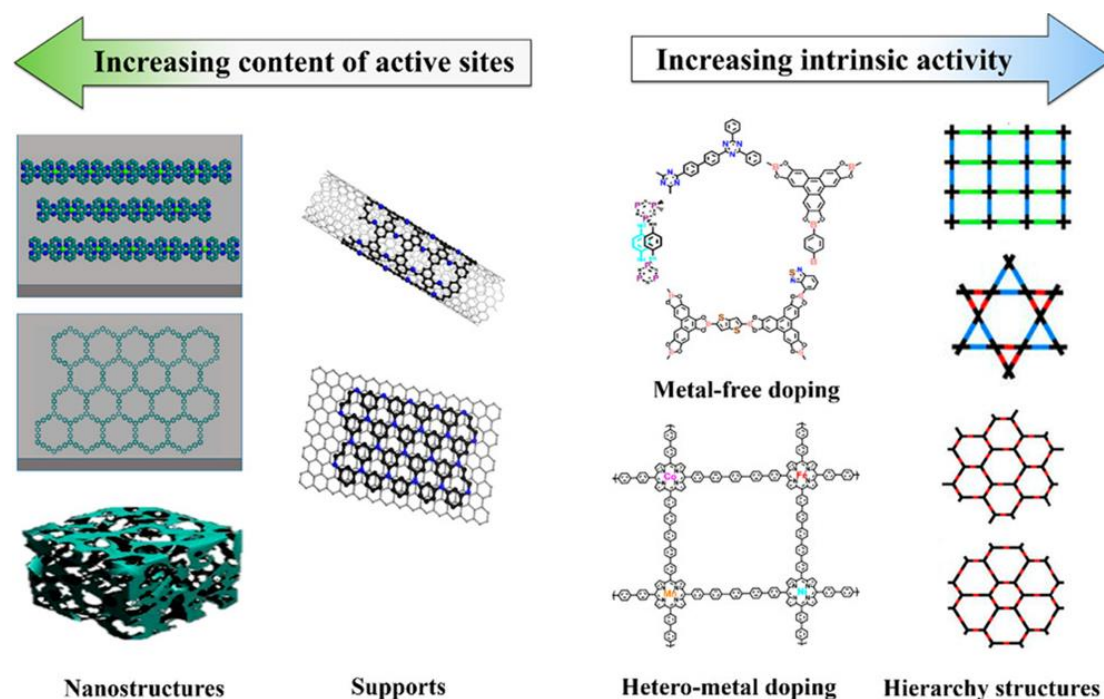

Figure 1.6 Development strategies of well-defined 2D COPs as electrocatalysts by increasing the intrinsic activity of each active site as well as the number of active sites. The intrinsic activity can be promoted by introducing heteroatoms/metal species, and hierarchical porous structures. The content of active sites can be increased by depositing COPs on conductive supporting materials.[10] Reproduced with the permission from American Chemical Society.

The development strategies for COF-based electrocatalysts should aim to increase the intrinsic activity of each active site as well as the number of active sites.[6] As shown in Figure 1.6, the intrinsic activity can be directly related to the incorporated heteroatoms (e.g. B, N, P, S) that are introduced by selecting corresponding dopant-containing linkers.[89-92] In addition, COFs can be incorporated with metal–organic complexes into its skeletons, e.g. metal-porphyrin and metal-bipyridine complexes.[36,93-96] The incorporated metals usually play a major role in catalyzing the electrochemical reactions. For example, Banerjee and co-workers reported a porous, bipyridine functionalized COFs with complexed Co ions. The resulting Co-TpBpy exhibited a high OER activity and good stability in phosphate buffer under neutral pH condition (Figure 1.7a).[36] In addition, theoretical calculations have been used to study the potential application of porphyrin-contained COFs as ORR and OER electrocatalysts with transition metals in the center of porphyrin active sites, and an Fe-COF was identified to be the best ORR/OER catalyst with Fe at the volcano summits (Figure 1.7b).[94] On the downside, COFs are poorly conductive. To circumvent this issue they can be deposited on conductive supporting materials (e.g. graphene and CNTs) to form hybrid systems.[97,98] The electrocatalytic activities are thus enhanced because of the improved electric conductivity as well as the synergetic effect between COFs and the supporting materials.
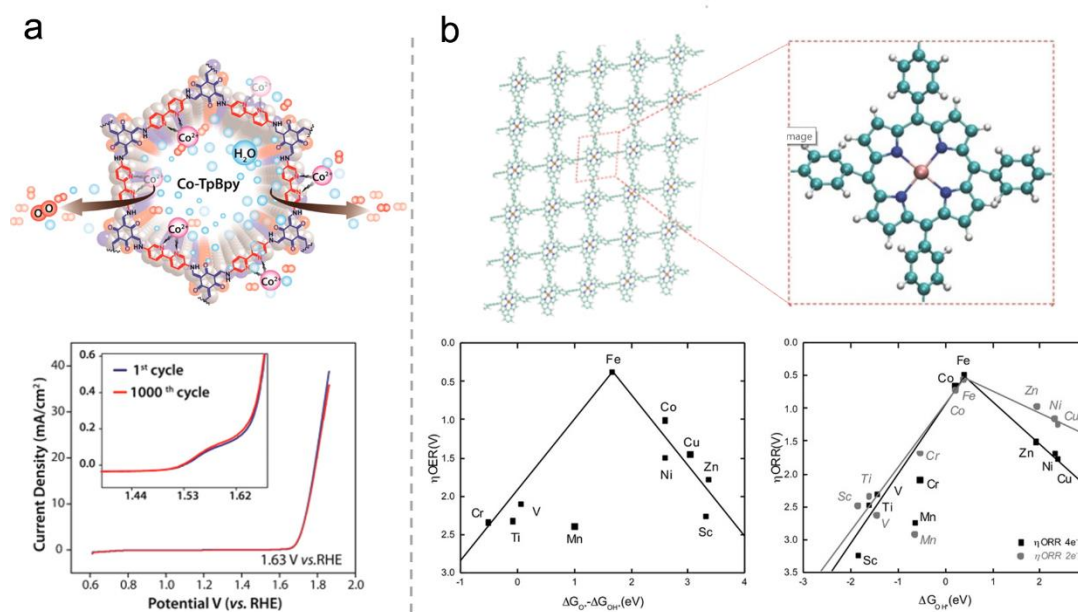

Figure 1.7 a) Schematic representation of the synthesis of Co-TpBpy via Co (II) impregnation and the corresponding linear sweep voltammetry (LSV) stability test profile of Co-TpBpy before and after 1000 cycles (inset shows an enlarged view of the LSV profile).[36] Reproduced with the permission from American Chemical Society. b) Schematic of a TM-COFs (TM = Sc, Ti, V, Cr, Mn, Fe, Co, Ni, Cu, and Zn). The green, blue, deep gold, and silver colors represent C, N, TM, and H, respectively. The figures show OER and ORR overpotentials as a function of adsorption energy for TM-COFs.[94] Reproduced with the permission from John Wiley and Sons.

To increase the number of exposed active sites in COFs, the basic principle is to control porous structures including the pore size and topology. For example, the pore size of COFs can be adjusted by using building units with different length while the different topologies of porous structures can be achieved by applying building units with different shapes, like tetrahedral,[99] trigonal planar,[100] and square planar.[101] Besides, secondary porosities and nanostructures are typically introduced into COFs matrixes, such as hollow tubular porous COFs,[102] hollow spherical COFs with mesoporous wall[103] and imine COFs with hollow microtubular morphology.[104] Such hierarchical porosities are supposed to increase the accessibility of active sites within COFs during the heterogeneous catalysis.

1.5.2 Metal Organic Framework (MOF)-based Electrocatalysts

MOFs, which are generally formed by coordination bonds between organic ligands and metal atoms, possess well-defined chemical structures and accessible active sites. Coordinatively unsaturated metal atoms and functionalized ligands within MOFs endow them promising electrocatalytic activities.[12] However, the poor electronic conductivity of MOFs largely hinder their applications in electrochemical process. To tackle this problem, many strategies have been developed to increase the electronic transport in MOF-based electrocatalysts, including the intrinsic structural modification and combination with conductive substrates. For example, ultrathin MOFs two-dimensional (2D) nanosheets (NiCo-UMOFNs) were synthesized as high-performance electrocatalysts for O_2 production. The nanometer thickness was supposed to promote the electron transfer, and expose more catalytic active surfaces with coordinatively unsaturated metal sites to ensure high catalytic activity.[105] Furthermore, conductive substrates such as nickel/copper foams,[106,107] fluorine-doped tin oxide (FTO)[108,109] and MXenes,[110] have been used as the support matrixes for the growth of selected MOFs. The obtained MOF-based composites usually exhibit higher electrocatalytic performance because of their enhanced electron conductivity.[11,105,107,110]

Recently, Dincă and co-workers reported an intrinsically conductive MOF ($Ni_3(HITP)_2$, HITP = 2, 3, 6, 7, 10, 11-hexaiminotriphenylene), as an ORR electrocatalyst with well-defined $M-N_x$ active sites (Figure 1.8a).[88] Subsequently, 2D MOF-based catalysts with different metal complexation motifs (MS_2N_2, MN_4, MS_4) were designed based on metal dithiolene-diamine coordination by Feng et al (Figure 1.8b).[111] It has been reasoned that the 2D MOFs could serve as promising carbon-rich electrocatalysts and the combination of DFT calculations and experimental studies indicated the superior HER performance for MS_2N_2 motifs, as the coordination of metal, sulfur and nitrogen synergistically facilitated the adsorption/desorption of H_2 leading to accelerated HER kinetics.
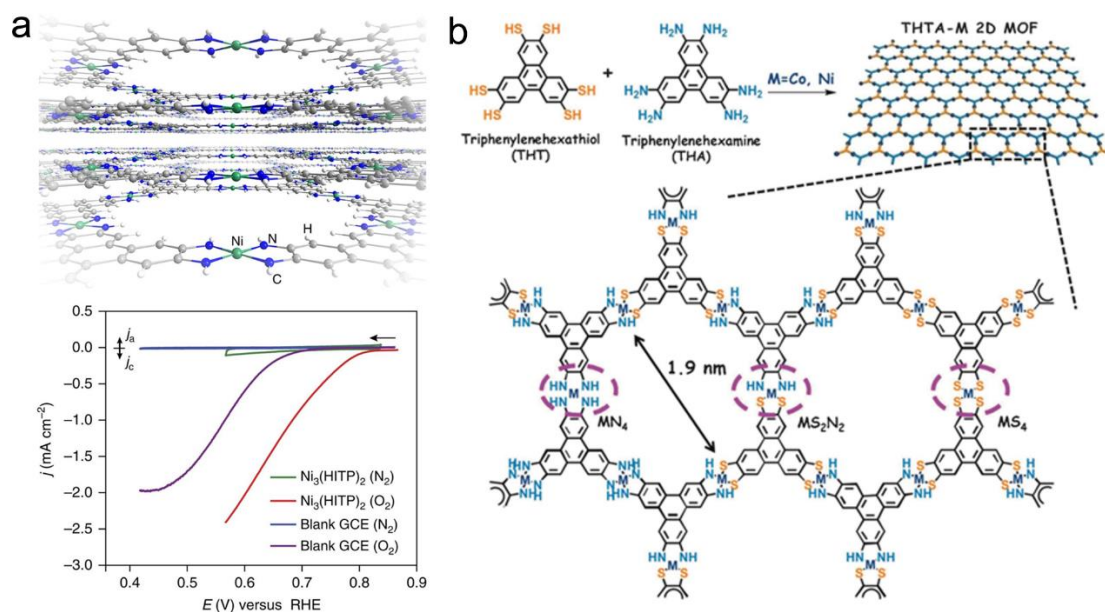
Figure 1.8 a) Perspective view of the two-dimensional layered structure of $Ni_3(HITP)_2$ and the corresponding polarization curves of $Ni_3(HITP)_2$ under N_2 versus O_2 atmosphere.[88] Reproduced with the permission from Springer Nature. b) Synthesis and structure of THTA-M (M = Co/Ni).[111] Reproduced with the permission from John Wiley and Sons.

1.6 Electrochemical Reactions and Applications

After the discussion of the above functional porous materials, a general overview of electrochemical reactions and applications will be given. Electrochemical reactions are considered as an important type of chemical reactions, especially in the field of energy conversion and storage. Depending on the loss and gain of electrons during the electrocatalytic process, the reactions are generally divided into two half reactions at two electrodes, i.e. the reduction reaction at the cathode and oxidation reaction at the anode. These reactions are usually operated in electrochemical devices, such as metal-air batteries, fuel cells and water electrolysers, where the HER, OER and ORR are generally involved as half reactions.

1.6.1 Hydrogen Evolution Reaction (HER)

The HER is one of two half reactions of overall water splitting for hydrogen production. According to the different media (acidic and alkaline) in which water splitting take place, the reaction can be proceeded chemically in different ways (see below). Theoretically, the standard potential of HER is defined as 0 V versus a normal hydrogen electrode at pH=0. However, in fact, a much higher voltage has to be applied to achieve efficient HER performance. The excess potential (known as overpotential) is used to overcome the intrinsic activation barriers on the cathode as well as other resistances, such as solution resistance and contact resistance.[62] The half reactions can be written as:

In acidic electrolyte $2H^+ (aq) + 2e^- \rightarrow H_2 (g)$

$H^+ + e^- + * \rightarrow H^*$ (1)

$2H^* \rightarrow H_2 + 2*$ (2)

$H^+ + e^- + H^* \rightarrow H_2 + *$ (3)

In neutral and alkaline electrolytes $2H_2O + 2e^- \rightarrow H_2(g) + 2OH^- (aq)$

$H_2O + e^- \rightarrow H^* + OH^-$ (4)

$2H^* \rightarrow H_2 + 2*$ (5)

$H_2O + e^- + H^* \rightarrow H_2 + OH^- + *$ (6)

The understanding of the HER mechanism can guide the design of HER electrocatalysts. Recently, the HER in acidic media has been proceeded with two possible reaction steps: the binding of hydrogen to the catalyst in the first step (1), where $*$ denotes a site on the surface able to bind to hydrogen. The second step is the release of molecular hydrogen through one of the two processes (2) or (3).[112] Nevertheless, the HER in alkaline media is comparatively harder to achieve because extra energy is generally needed to produce protons by breaking water molecules (4).[113] The release of molecular hydrogen can in principle also occur via two processes (5) or (6). Considering theoretical predictions and experimental studies, the best-known catalysts for HER are based on Pt. A volcano-plot have been developed to correlate HER exchange current densities for various metals with the chemisorption energy of hydrogen on those metals (Figure 1.9a). Such plots show that there is an optimum hydrogen binding energy at which the maximum catalytic activity is obtained. The locations of various metals in theses plot is supposed to be helpful for the design of efficient hydrogen evolution catalysts, especially for those of non-noble metals-based electrocatalysts (e.g. Fe, Co and Ni).
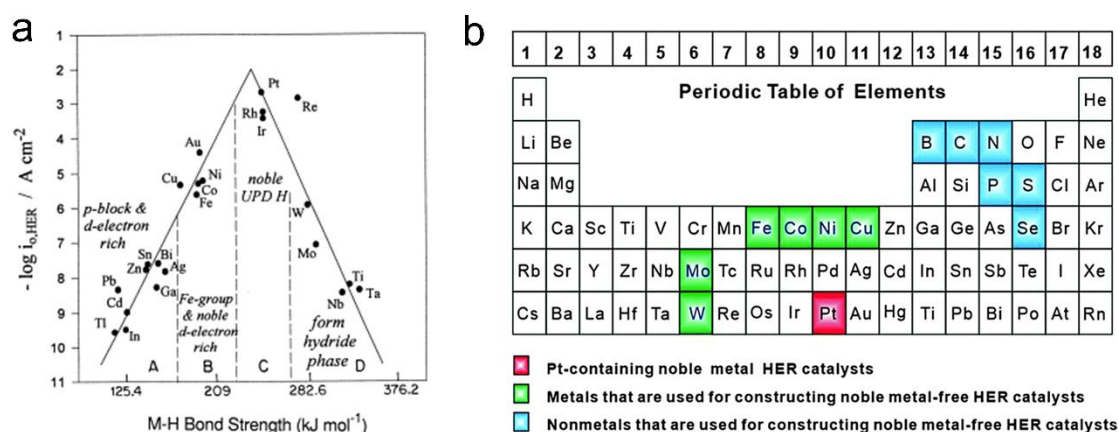

Figure 1.9 a) HER volcano plot of Trasatti for log i_0 values as a function of M-H bond energy.[114] Reproduced with the permission from Elsevier. b) Elements that are used for constructing HER electrocatalysts.[62] Reproduced with the permission from Royal Society of Chemistry.

For example, Figure 1.9b shows a general view of the earth-abundant elements that are used for constructing HER catalysts, including Fe, Ni, Co, Cu, Mo and W. By combining heteroatoms (e.g. S, N, P, Se) with these non-noble metals, numerous metal compounds have

been synthesized as HER catalysts including metal sulfides (MoS_2, FeS_2), metal selenides ($CoSe_2$),[115,116] metal carbides (MoC_x),[18,117,118] metal phosphides (CoP, FeP)[64,119] and their corresponding carbon-based electrocatalysts (MoS_2/rGO,[120] FeP/C,[121] Mo_2C@NC,[117] Co-N-C,[122]).

There are many reviews available on these non-noble metal-based HER electrocatalysts.[5,61,62,113] But, considering the wide range of commercial uses for sustainable hydrogen production with both economic and environmental benefit, there is still a long way to go including the exploration of new catalysts, investigation of the underlying mechanism as well as the exploitation of renewable energy.

1.6.2 Oxygen Evolution Reaction (OER)

OER is the other important half reaction that coupled to various renewable energy systems such as water splitting and metal-air batteries. In particular as an anodic reaction, OER is supposed to be the major bottleneck in water splitting for the sustainable hydrogen economy because of its multi-electron process that generally suffers from sluggish kinetics and high overpotential. Currently, the most efficient OER catalysts are still based on noble metals (e.g. RuO_2 and IrO_2) with the drawback of scarcity and instability. Consequently, extensive efforts have been made to explore alternatives. Non-noble metal (Fe, Co, Ni, Mn etc.) oxides and their derivatives have attracted much attention because of their OER activities and high reaction stabilities, such as spinels (AB_2O_4; A, B= transition metals)[123] and layered structures ($M(OH)_2$, MOOH and $LiMO_2$; M= transition metals).[124-126] To promote the OER performance, the structure and surfaces of these catalysts have to be precisely tuned to optimize the adsorption energies of intermediates for OER catalysis. Moreover, various carbon materials have been introduced into catalytic systems as solid-state supports or active phases to promote the OER performance, such as CNTs,[16] graphene[127,128] and N-doped porous carbons.[129,130]
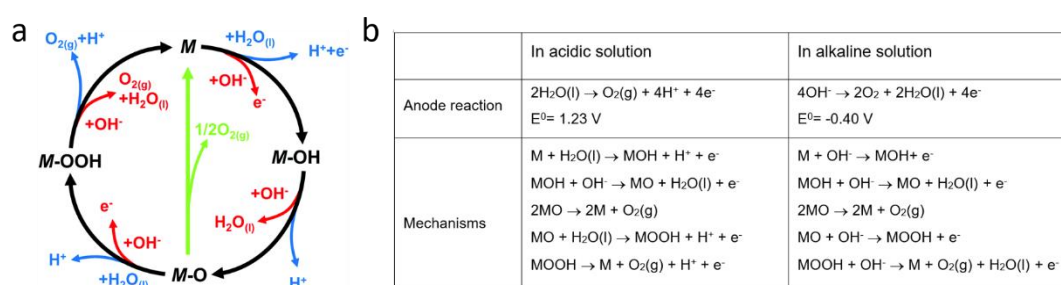

Figure 1.10 a) The proposed mechanism for OER under acidic (blue line) and alkaline (red line) conditions. The blue line indicates one route to form the oxygen through the direct combination of 2M-O; The black line indicates another route through the formation of a peroxide (M–OOH) intermediate.[4] Reproduced with the permission from Royal Society of Chemistry. b) The supposed reaction process of OER under acidic and alkaline conditions.

Due to the multiple-electron process, the mechanism of OER is more complicated than HER either in acidic or alkaline solution. Recently, possible mechanisms have been proposed

with the common consensus that the intermediates such as M-OH and M-O are formed during the OER process which subsequently decomposes to O_2, even though some disparities among these proposed mechanisms are present with respect to the pathway of formed oxygen (Figure 1.10).[4] Nowadays, many measurement techniques and theoretical modeling have been developed in elucidating trends in OER catalysts. For example, metal oxides are generally used as OER catalysts, a volcano plot for reported metal oxides have been constructed in which the experimental overpotentials of these catalysts are observed to be matched well with their theoretical overpotentials (Figure 1.11).[6] However, because of the multiple intermediates (OOH* and OH*) in four-electron OER, the binding energy of which are strongly correlated and there has a scaling relation between OOH* and OH*. As a result, even a catalyst located at the top of volcano, will possess a nonzero theoretical overpotential.[131]
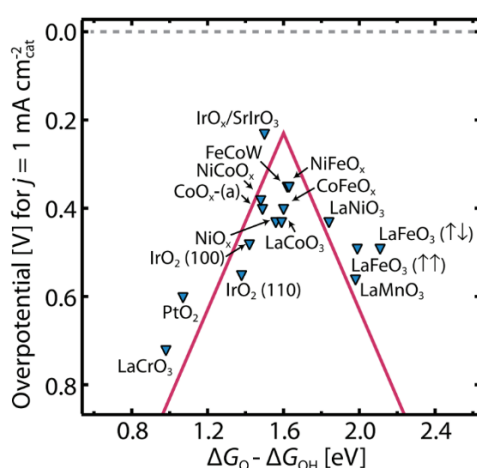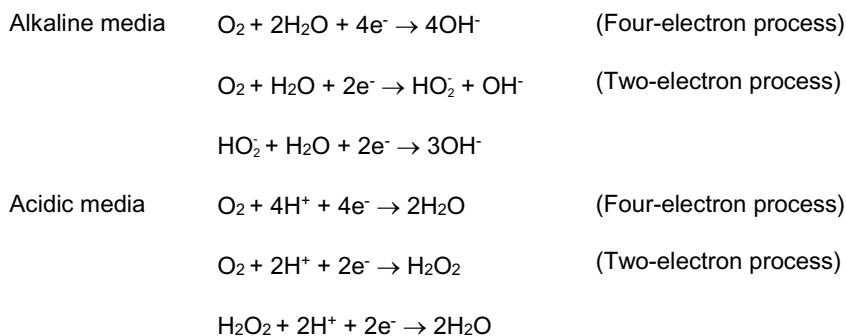

Figure 1.11 OER volcano plot for metal oxides.[6] Reproduced with the permission from The American Association for the Advancement of Science.

Currently, a variety of in situ (operando) techniques have been applied to monitor the actual intermediates and electrochemical behavior on the surface of catalysts for OER.[132-134] These, as well as DFT calculations, could play an important role in understanding the binding energies of reactive intermediates on a surface, and further guide the design for electrocatalysts.

1.6.3 Oxygen Reduction Reaction (ORR)

The ORR is a fundamental reaction in energy-converting systems such as fuel cells and metal-air batteries. In aqueous solution, two pathways are proposed during oxygen reduction process depending on the transferred electron numbers: the direct four-electron transfer pathway from O_2 to H_2O; and the two-electron transfer pathway from O_2 to H_2O_2. The principle ORR processes are listed below, where peroxide species are formed as intermediates in both alkaline and acidic media:

Alkaline media	$O_2 + 2H_2O + 4e^- \rightarrow 4OH^-$	(Four-electron process)
	$O_2 + H_2O + 2e^- \rightarrow HO_2^- + OH^-$	(Two-electron process)
	$HO_2^- + H_2O + 2e^- \rightarrow 3OH^-$	
Acidic media	$O_2 + 4H^+ + 4e^- \rightarrow 2H_2O$	(Four-electron process)
	$O_2 + 2H^+ + 2e^- \rightarrow H_2O_2$	(Two-electron process)
	$H_2O_2 + 2H^+ + 2e^- \rightarrow 2H_2O$	

Typically, the four-electron pathway is expected to achieve a high efficiency fuel cell or metal-air battery. Pt and its alloys are currently considered to be the best electrocatalysts for the four-electron pathway, which is evidenced by the volcano plot that taking experimental ORR activity enhancement as a function of hydroxyl binding energy (Figure 1.12). However, these noble metal-based electrocatalysts usually suffer from the scarcity, instability and CO poisoning. One of the main aims of current research works on ORR is to find an efficient and stable alternative to promote the oxygen reduction process. As expected, many ORR electrocatalysts based on earth-abundant elements, including carbon-based non-noble metal composites (Co_3O_4/RGO,[17,135] Fe_3C/Fe-N-C[19], Co NPs/NC[136]), metal-nitrogen doped carbons (Fe-N-C,[71,77] Co-N-C,[23,28,81,83] Fe,Co-N-C[84]) and heteroatom-doped carbons[2,46,48,49,137] have been reported to achieve efficient ORR for fuel cells and metal-air batteries. The progress of ORR for multiple applications has been summarized in several reviews.[1,2,55,138]
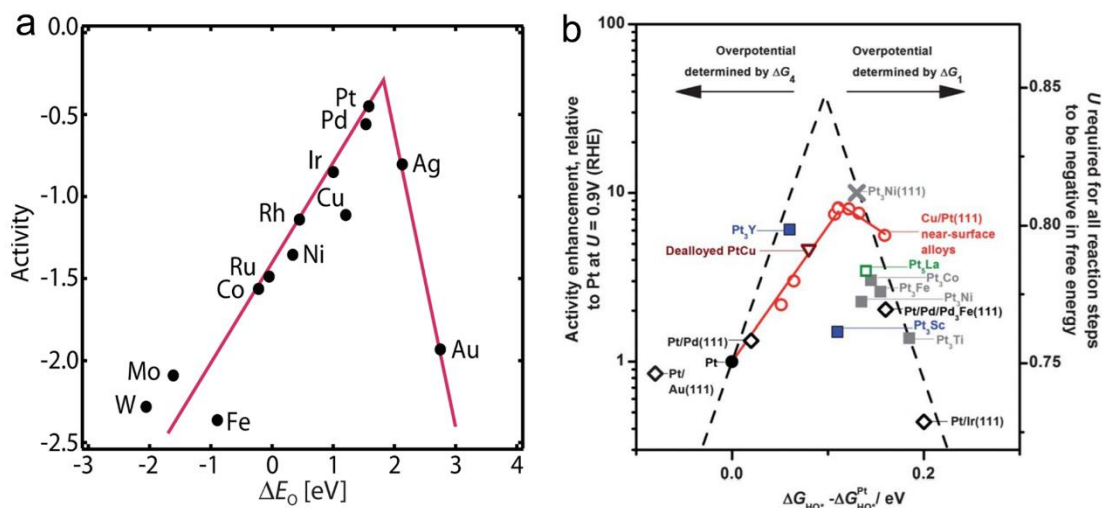

Figure 1.12 a) ORR volcano plot for metals.[139] Reproduced with the permission from American Chemical Society. b) ORR volcano plot for Pt and its alloys: experimental ORR activity enhancement as a function of hydroxyl binding energy.[140] Reproduced with the permission from Royal Society of Chemistry

The electrocatalytic ORR process involves multistep and multiple adsorbed intermediates. It should be noted that H_2O_2 has been detected during ORR through the two-electron pathway, but it remains unclear whether it is a key intermediate of the dominant ORR mechanism or a side-product.[139] Therefore, further studies on the interaction of H_2O_2 with metal surfaces is

essential to understand the ORR mechanism. On the other hand, the emerging of in situ characterizations on the variety of intermediates as well as DFT studies on the electronic structures and energy barriers, can help to rationally design more efficient and stable ORR catalysts. For example, Figure 1.12a shows a volcano plot that constructed relating the theoretical ORR activity and binding energy (ΔE_O), providing insight into the optimum catalyst for a given class of metals. An active catalyst could bind reaction intermediates neither too strongly nor too weakly otherwise the activity could be limited by proton-electron transfer to O* or OH* when the binding is too strong or be limited by proton-electron transfer to O_2* or splitting of the O-O bond in O_2 when the binding is too weak. Figure 1.12b represents the experimental ORR activity of a number of different Pt-alloys, plotted as a function of the theoretical binding energy. According to the volcano plot, Pt binds OH too strongly for optimal activity. It is demonstrated that alloying can decrease the oxygen adsorption energy of the top Pt layer of Pt_3M alloy (M= Ni, Fe, Co, Ti), showing enhancements in activity over pure Pt.[140-142]

2 Synthesis of Mesoporous Carbons with Surface Enriched Nitrogen

The chapter reprints the abstract and conclusion of the publication and gives a summary of the results. Detailed information can be found in the publication reprint in Chapter 8.1

2.1 Abstract

"Heteroatom-doped carbon materials are promising metal-free catalysts for the hydrogen evolution reaction (HER) at low voltage with high durability. However, many of the active sites introduced by heteroatom doping are hardly accessible within the bulk carbon structure and consequently contribute little to the catalytic activity. Here we report a facile ionic liquid-assisted method for synthesizing mesoporous nitrogen-doped carbons, enabling enrichment of nitrogen atoms at the pore surface, demonstrated by X-ray photoelectron spectroscopy (XPS) and temperature-programmed desorption of carbon dioxide (CO_2-TPD). The resulting metal-free nitrogen-doped mesoporous carbons exhibit a remarkable electrocatalytic activity in HER. The accessible and efficient utilization of nitrogen atoms is responsible for the superior HER catalytic activity."

TOC: reprinted from publication [XJZ01]. Reproduced with permission from American Chemical Society

2.2 Project summary

For the successful implementation of electrochemical water splitting technologies the development of active hydrogen evolution reaction (HER) electrocatalysts with low overpotential and high stability is crucial. Nitrogen doped carbon materials are highly promising and sustainable electrocatalysts for the HER but it remains a major challenge to develop facile and efficient protocols for the preparation of such materials with high control on the surface functionalization. In this work, we presented a facile ionic liquid-assisted method for synthesizing nitrogen-doped, ordered mesoporous carbon (NMCs) electrocatalysts with enhanced exposure of nitrogen atoms at the pore surface. The obtained NMCs exhibit a high activity and stability for HER which is attributable to an enrichment of nitrogen atoms at the pore surface of the mesoporous carbon, confirmed by X-ray photoelectron spectroscopy (XPS) and temperature-programmed desorption of carbon dioxide (CO_2-TPD).

Experiments: A combination of two carbon precursors was used, resol for forming the bulk mesoporous carbon structure and 1-ethyl-3-methylimidazolium dicyanamide (EMIM-DCA) for nitrogen doping. Nitrogen doped mesoporous carbons (NMCs) from these precursors are prepared via evaporation induced self-assembly (EISA) using triblock copolymer poly (ethylene oxide)-b-poly(propylene oxide)-b-poly(ethylene oxide) (PEO-PPO-PEO, Pluronic F127) as template. When using EISA for the generation of mesoporous carbons materials, such as FDU-15,[143] resol molecules are used, as their multiple phenolic hydroxyl groups can associate with the F127 template through hydrogen bonding and further co-assemble into the mesostructure. After thermo-polymerization of the F127/EMIM-dca/resol mixture at 100 °C, the obtained mesostructured polymer/EMIM-dca composite was pyrolyzed at 800 °C in argon to enable carbonization (Figure 2.1). The IL was added to this mixture in different resol/IL ratios and the influence on nitrogen doping, mesostructure and catalytic activity was investigated.
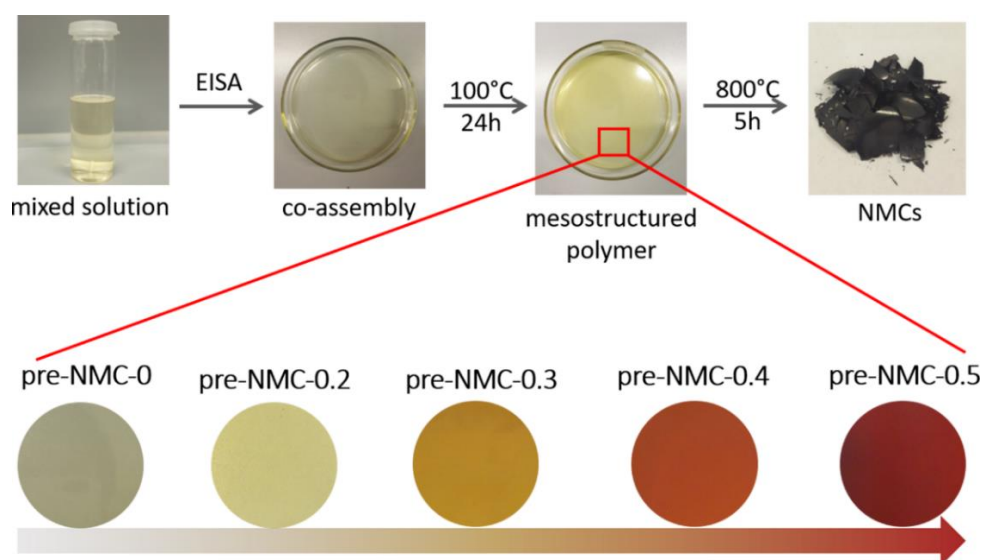

Figure 2.1 The process of evaporation induced self-assembly (EISA). The bottom are pictures of the mesostructured polymer of samples with different mass ratio of EMIM-dca to resol. Reprinted from publication [XJZ01]. Reproduced with permission from American Chemical Society.

Results and discussions: The morphologies of the synthesized NMCs were investigated by transmission electron microscopy (TEM), which provide the information on the change of the mesostructures with increasing EMIM-DCA amount. As shown in Figure 2.2a, b, NMC-0 without addition of EMIM-DCA shows a highly ordered mesoporous structure over large domains with 3D cubic pore symmetry. By adding small amounts of EMIM-DCA, the obtained NMC-0.2 (0.2 stands for the mass ratio of EMIM-DCA to resol) yielded no significant change with partially maintained ordered mesostructure (Figure 2.2c, d). Further EMIM-DCA addition still yielded a mesoporous but rather disordered pore structure, as seen for NMC-0.3 and NMC-0.4 in Figure 2.2e-g. A clear transformation from small and ordered mesopores, to larger, unordered pores is observed. It can be expected that EMIM-DCA, which is preferentially located in the micellar core or corona/resol interphase region during the EISA process will affect micelle formation and aggregation, which is reflected in the change of the pore structure. However, further addition of EMIM-DCA, that is for NMC-0.5 (Figure 2.2h), provoke a major structural transformation, and the porosity is already better described as interparticle voids created by aggregation of small carbon particles.
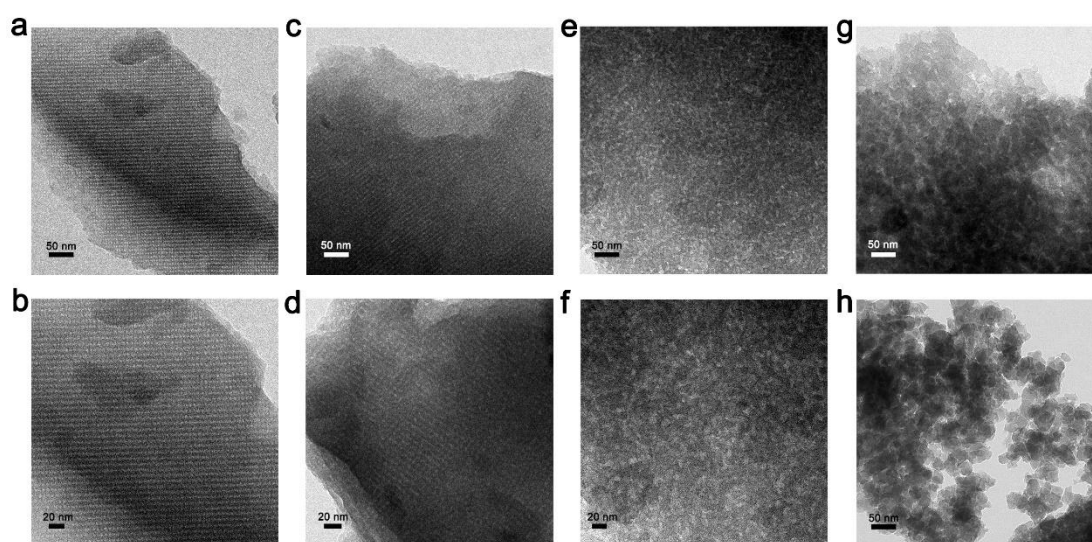

Figure 2.2 TEM images of N-doped mesoporous carbon synthesized with different amounts of EMIM-DCA. (a,b) NMC-0; (c,d) NMC-0.2; (e,f) NMC-0.3; (g) NMC-0.4; (h) NMC-0.5. Reprinted from publication [XJZ01]. Reproduced with permission from American Chemical Society.

The porous characteristics are further investigated by nitrogen adsorption-desorption measurements. The isotherm of NMC-0 show a small capillary condensation step in the relative pressure range of 0.4-0.6, i.e. a type-IV isotherm with a small H2-hysteresis loop indicative for small cage-like mesopores, which is also observed in NMC-0.2. However, with increasing EMIM-dca content i.e. for NMC-0.3, 0.4 and 0.5, respectively, these hysteresis loops show obvious change of shape with the shifts of the capillary condensation step to higher relative pressures indicating that the pore size increases gradually (from 2.90 to 7.12 nm for NMC-0 – NMC-0.5, NLDFT pore size distribution). The BET specific surface areas of all NMCs are in the range of 413-607 m^2/g. The pore volume of NMCs are increasing from 0.249 to 0.464 cm^3/g

and also the mesopore volume increase gradually from NMC-0 to NMC-0.4, reflecting the increased pore size and open mesopore channel structures. The formed open and accessible mesopore structures are supposed to facilitate mass transport and thus promote electrocatalytic activity.

The electrocatalytic activities of the as-synthesized NMCs towards HER were evaluated using a rotating disk electrode (RDE) in an argon-saturated 0.5 M H_2SO_4 solution. Figure 2.3a shows the polarization curves recorded for NMC-0.4 as compared to those measured for NMC-0 and commercial Pt/C. The activity of NMC-0.4 is significantly enhanced by incorporating nitrogen atoms into the carbon framework, as reflected by the large shift of the polarization curve with an overpotential of 384.7 mV at 10 mA/cm^2. Figure 2.3b shows HER activity of all NMC-x samples, which is mainly influenced by the nitrogen content, however also the mesostructure seem to play an important role. NMC-0.2 shows a low electrocatalytic activity for HER. With increasing nitrogen content the activity of the NMCs increases as well, until NMC-0.4 is reached, while, for NMC-0.5 a much lower activity is observed. The normalization process from exchange current density (j_0) to the activity per active sites ($j_{real/site}$) for all samples was achieved by following the method on basis of real surface areas. As shown in Figure 2.3c, a scatter plot containing $j_{real/site}$ versus N/C ratio was established in which a much higher $j_{real/site}$ for NMC-0.4 indicates an improved catalytic activity for active sites on the pore surface of NMC-0.4.
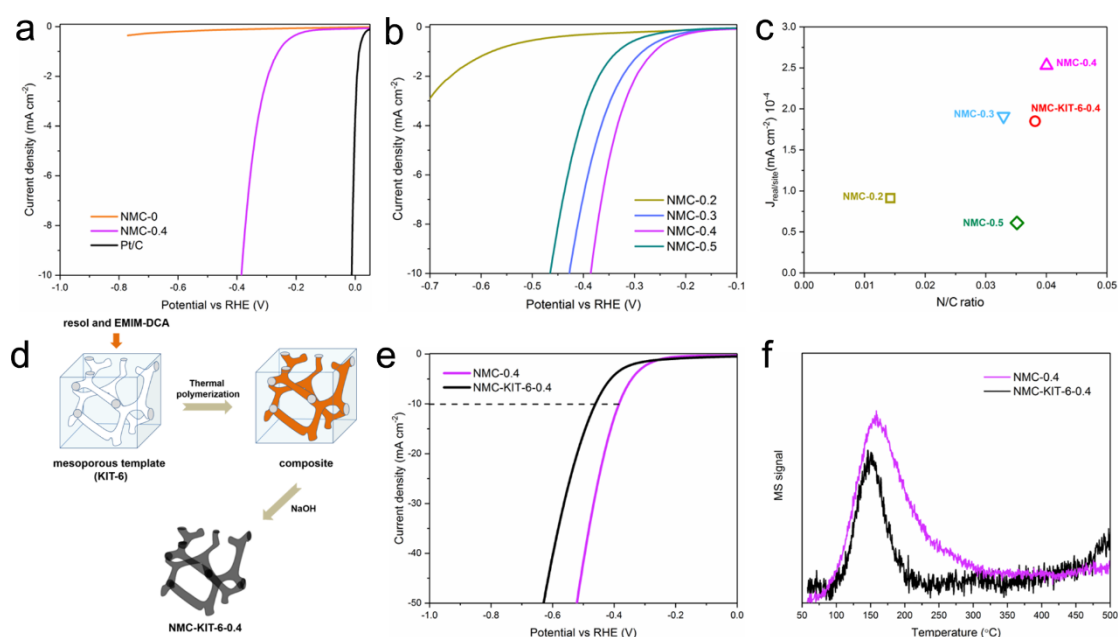

Figure 2.3. a) HER polymerization plots of NMC-0, NMC-0.4, and commercial Pt/C samples in 0.5 M H_2SO_4 solution. b) HER polymerization, c) Scatter plot of $j_{real/site}$ for NMCs with different amount of EMIM-dca. d) Illustration of hard-template (KIT-6) method to prepare NMC-KIT-6-0.4. e) HER polymerization plots, f) CO_2-TPD of NMC-0.4 and contrastive NMC-KIT-6-0.4. Reprinted from publication [XJZ01]. Reproduced with permission from American Chemical Society.

Consequently, to verify the advantageous of enriched nitrogen atoms on the pore surfaces of NMCs, a reference catalyst was prepared by hard templating of KIT-6 using the same EMIM-

DCA/resol ratio as for NMC-0.4 (NMC-KIT-6-0.4, Figure 2.3d). We reasoned that as no surfactant is applied for the hard templating approach, nitrogen atoms should be uniformly dispersed within the carbon matrix. NMC-KIT-6-0.4 possesses comparable nitrogen content and surface area to NMC-0.4 while the HER polarization curves of NMC-KIT-6-0.4 shows a lower HER activity than NMC-0.4 even though having a slightly higher surface area (Figure 2.3e). Furthermore, temperature-programmed desorption of carbon dioxide (CO_2-TPD) was conducted to prove the higher accessibility of nitrogen atoms at the surface of NMC-0.4. Since CO_2 is a weak Lewis acid (electron acceptor) with an electropositive carbon atom, the amount of basic sites on the pore surface can be detected by CO_2-TPD. As shown in Figure 2.3f, NMC-0.4 and NMC-KIT-6-0.4 both show a strong desorption of CO_2 at temperatures higher than 100 °C due to chemically adsorbed CO_2 on the surface of the materials. However, the intensity of CO_2 desorption peak of NMC-0.4 is much stronger than that of NMC-KIT-6-0.4, even though the latter has a higher surface area, which clearly shows that NMC-0.4 provides more Lewis basic sites at the surface.

2.3 Conclusion

"In summary, we report a facile ionic liquid-assisted method for synthesizing NMC electrocatalysts with enhanced exposure of nitrogen atoms at the pore surface. EMIM-DCA co-assembles with the F127 micelles, yielding first an increase of the pore sizes in the final carbons, while after further increase, the pore structure collapses. That EMIM-DCA is mainly located at the micelles and not within the resol matrix can be seen by an enrichment of nitrogen on the surface of the final carbon materials. The obtained NMCs with surface-enriched nitrogen exhibit a high activity and excellent stability as a nonmetal electrocatalyst for HER. The superior HER catalytic activity was attributed to the accessible and efficient utilization of nitrogen atoms on the carbon surface and the open mesoporous channel structures. XPS and CO2-TPD characterization confirmed the enrichment of nitrogen atoms at the pore surface of nitrogen-doped material. This concept is adaptable to design of mesoporous carbon doped with other heteroatoms (S, B, P) or co-doped by choosing appropriate ionic liquids. Moreover, metal-containing ionic liquids can be easily synthesized, and thus, excellent electrocatalysis on mesoporous carbon with surface-enriched transition metals are expected."

Reprinted from publication [XJZ01], Reproduced with permission from American Chemical Society

3 Bimetallic MOF-derived Carbon-based Electrocatalysts

This chapter was published in Angewandte Chemie International Edition with the title "Bifunctional Electrocatalysts for Overall Water Splitting from an Iron/Nickel-Based Bimetallic Metal-Organic Framework/Dicyandiamide Composite"

Xiaojia Zhao, Pradip Pachfule, Shuang Li, Jan Ron Justin Simke, Johannes Schmidt, Arne Thomas*
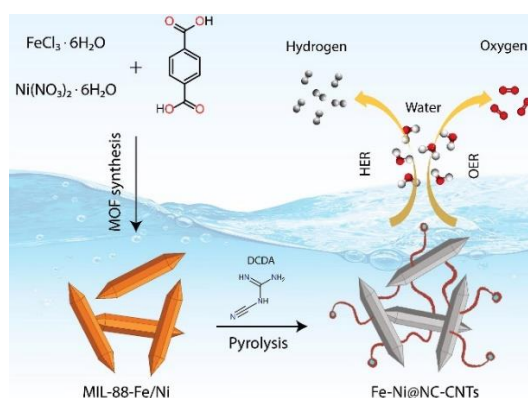
Angew. Chem. Int. Ed. **2018,** 57, 8921–8926

https://onlinelibrary.wiley.com/doi/full/10.1002/anie.201803136

The chapter reprints the abstract and conclusion of the publication and gives a summary of the results. Detailed information can be found in the publication reprint in Chapter 8.2

3.1 Abstract

"Pyrolysis of a bimetallic metal–organic framework (MIL-88-Fe/Ni)-dicyandiamide composite yield a Fe and Ni containing carbonaceous material, which is an efficient bifunctional electrocatalyst for overall water splitting. $FeNi_3$ and $NiFe_2O_4$ are found as metallic and metal oxide compounds closely embedded in an N-doped carbon–carbon nanotube matrix. This hybrid catalyst (Fe-Ni@NC-CNTs) significantly promotes the charge transfer efficiency and restrains the corrosion of the metallic catalysts, which is shown in a high OER and HER activity with an overpotential of 274 and 202 mV, respectively at 10 mA/cm^2 in alkaline solution. When this bifunctional catalyst was further used for H_2 and O_2 production in an electrochemical water-splitting unit, it can operate in ambient conditions with a competitive gas production rate of 1.15 and 0.57 µL/s for hydrogen and oxygen, respectively, showing its potential for practical applications."

TOC: reprinted from publication [XJZ02]. Reproduced with permission from John Wiley and Sons.

3.2 Project summary

Electrochemical water splitting is widely regarded as a sustainable method for large-scale production of hydrogen, which is considered as one of the cleanest fuels, to meet the growing demand for energy and environmental concerns. To efficiently carry out water splitting, the development of highly active and cost-effective catalysts for both half-reactions, i.e. the hydrogen evolution reaction (HER) at the cathode and the oxygen evolution reaction (OER) at the anode, is of paramount importance. However, when two types of catalysts are used for the respective half reactions in an integrated electrolyzer, it can be difficult to operate water splitting efficiently because of the mismatch of optimum electrolyte pH.[72] Consequently, there is a demand for efficiently bifunctional electrocatalysts possessing substantial catalytic performance both for HER and OER at the same electrolyte solutions.

In this work, we report the synthesis of Fe-Ni@nitrogen-doped carbon/CNT composites (Fe-Ni@NC-CNTs) by carbonization of bimetallic MOF (MIL-88-Fe/Ni) - dicyandiamide composites and their application as bifunctional electrocatalyst for overall water splitting. The hybrid catalyst Fe-Ni@NC-CNTs possesses a high conductivity, hierarchical pore structure and stable 3D framework, resulting in high activity, fast mass transport and good stability for electrocatalytic processes. The bifunctional catalyst was further used for H_2 and O_2 production in an electrochemical water-splitting unit, showing its potential for practical applications.

Experiments: The bifunctional catalyst (Fe-Ni@NC-CNTs) was synthesized by the carbonization of a bimetallic MIL-88-Fe/Ni - dicyandiamide composite. Dicyandiamide (DCDA) was added to MIL-88 to enable the formation of nitrogen-doped carbons from the nitrogen-free MOF. At first, the bimetallic MIL-88-Fe/Ni was prepared by solvothermal treatment of terephthalic acid, $FeCl_3 \cdot 6H_2O$, $Ni(NO_3)_2 \cdot 6H_2O$ at 100 °C for 48 h. DCDA was mixed with the crystalline MOF by mechanical grinding, yielding a 1:1 weight ratio followed by pyrolysis at 800 °C for 3h in inert atmosphere (Figure 3.1a). In addition, the pyrolysis temperature (600 °C, 700 °C, 800 °C and 900 °C) and the crystallinity of bimetallic MOF that synthesized by different solvothermal time (3h, 6h, 12h, 48h) have also been varied to study their influence on the electrocatalytic activity of the final products. All materials were synthesized by an otherwise identical procedure. Details can be found in the publication XJZ02.

Results and discussion: First, powder X-ray diffraction (PXRD) was conducted to study the crystalline structures of as-synthesized bimetallic MIL-88-Fe/Ni which confirms the formation of phase-pure materials with high crystallinity (Figure 3.1 b, c). TEM images show that MIL-88-Fe/Ni consist of uniform rod-shaped crystals (60-80 nm wide and 500-700 nm long, aspect ratio = 8-12) (Figure 3.1e). After addition of DCDA and pyrolysis, the PXRD pattern of Fe-Ni@NC-CNTs shows a relatively weak peak around 26.4° that can be assigned to the (002) plane of graphitic carbon, while the more intense peaks appearing at 43.7°, 50.9° and 74.9° can be indexed to (111), (200) and (220) planes of $FeNi_3$, and the peaks at 30.3°, 35.6°, 43.5°, 57.3° and 63.0° can be assigned to (220), (311), (400), (511) and (440) planes of the spinel structure of $NiFe_2O_4$ (Figure 3.1d).
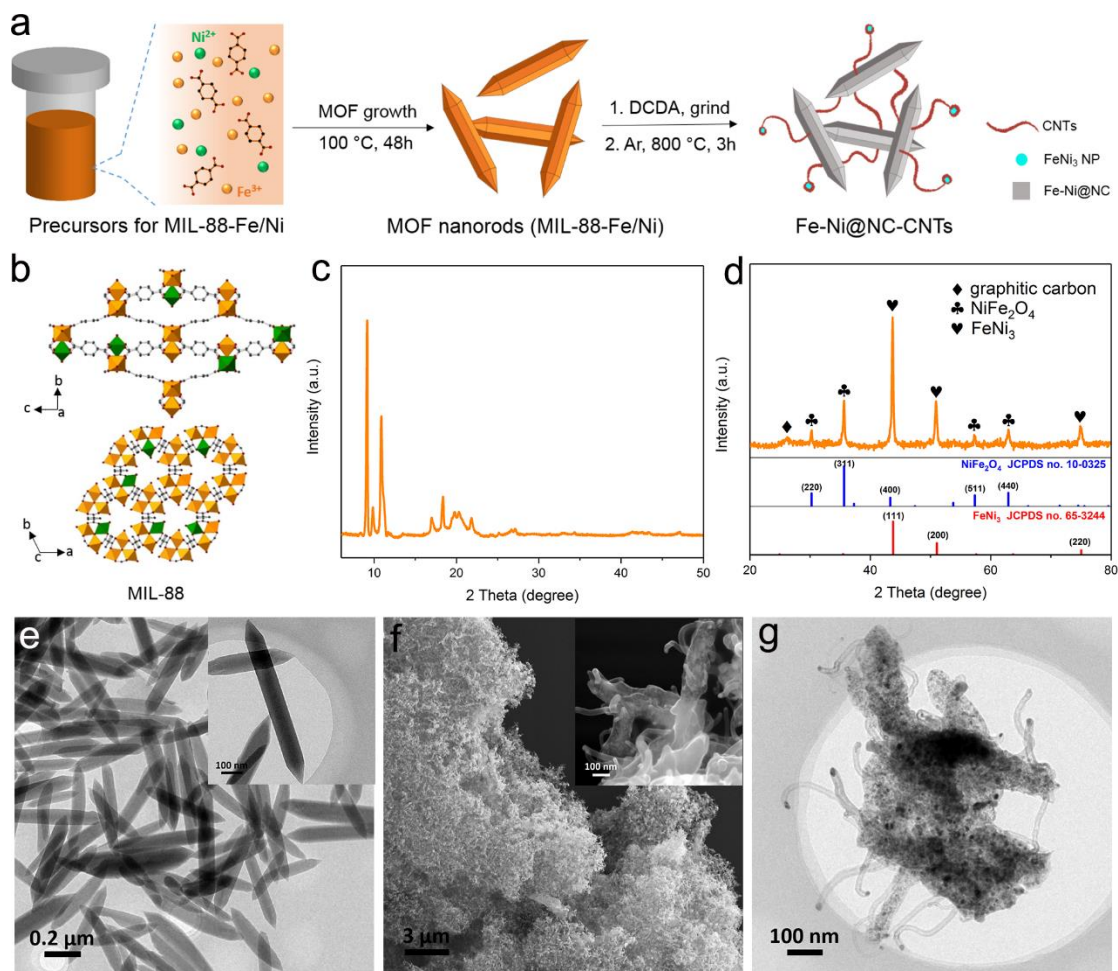
Figure 3.1. a) Scheme of the synthesis of MIL-88-Fe/Ni and Fe-Ni@NC-CNTs. b) The packing diagram of MIL-88-Fe/Ni viewed along the a and c axis. Fe, Ni, O and C atoms are shown in orange, green, red and gray, respectively. H atoms and solvent molecules are omitted for clarity. c) PXRD pattern of MIL-88-Fe/Ni. d) PXRD pattern of the as-synthesized Fe-Ni@NC-CNTs and the comparison with FeNi3 (JCPDS no. 65-3244) and NiFe2O4 (JCPDS no. 10-0325). e) TEM image of MIL-88-Fe/Ni. f) SEM, g) TEM images of Fe-Ni@NC-CNTs. Reprinted from publication [XJZ02]. Reproduced with permission from John Wiley and Sons.

The SEM images of Fe-Ni@NC-CNTs show the formation of a homogeneous and highly porous network and CNT growth from the surface of these nanorods is observed (Figure 3.1f, inset). TEM analyses further confirm the partial preservation of rod-shaped morphologies (Figure 1g). These rods consist of a carbonaceous matrix with embedded metal or metal oxide nanoparticles with diameters between 10-20 nm. By further analyses with HR-TEM as well as selected area electron diffraction (SAED), it is concluded that at the tips of the CNTs $FeNi_3$ nanoparticles are exclusively present and are encapsulated by a few-layered carbon shell. On the other hand, the nanorod structures are embedding both $FeNi_3$ and $NiFe_2O_4$ nanoparticles, coated by graphitic carbon layers

The as-synthesized Fe-Ni@NC-CNTs own a homogeneous interconnected carbon network with high pore volume and surface area which mainly stems from meso- and larger

pores, plus abundant Fe/Ni alloy and oxide nanoparticles. These structural features make this material a promising candidate for electrocatalytic applications. Consequently, the OER and HER activity of Fe-Ni@NC-CNTs in an alkaline aqueous electrolyte (1.0 M KOH) using a three-electrode system was tested, respectively, and their electrocatalytic activities both for OER (274 mV at 10 mA/cm^2) and HER (202 mV at 10 mA/cm^2) are competitive with that of noble metal-based catalysts and some other reported catalysts (Figure 3.2a, b). Furthermore, the stability and durability of Fe-Ni@NC-CNTs was tested at a current density of 10 mA/cm^2. After 40000s, the catalyst shows just negligible difference in the required overpotential for both reactions, OER and HER (Figure 3.2c). To elucidate if the formation of highly crystalline MOF structures is indeed an important factor for the catalytic performance of carbonaceous materials derived therefrom, the electrocatalytic activity of pyrolyzed samples of MIL-88-Fe/Ni prepared via different reaction times was tested. Indeed Fe-Ni@NC-CNT-3h, -6h and -12h exhibit a lower catalytic performance than Fe-Ni@NC-CNT-48h, showing that the formation of extended crystals has a beneficial effect on the final carbon structures. Moreover, etching experiments were carried out to elucidate the role of the metallic compounds on the catalytic performance, showing especially the major contribution of FeNi$_3$ NPs to the HER performance.
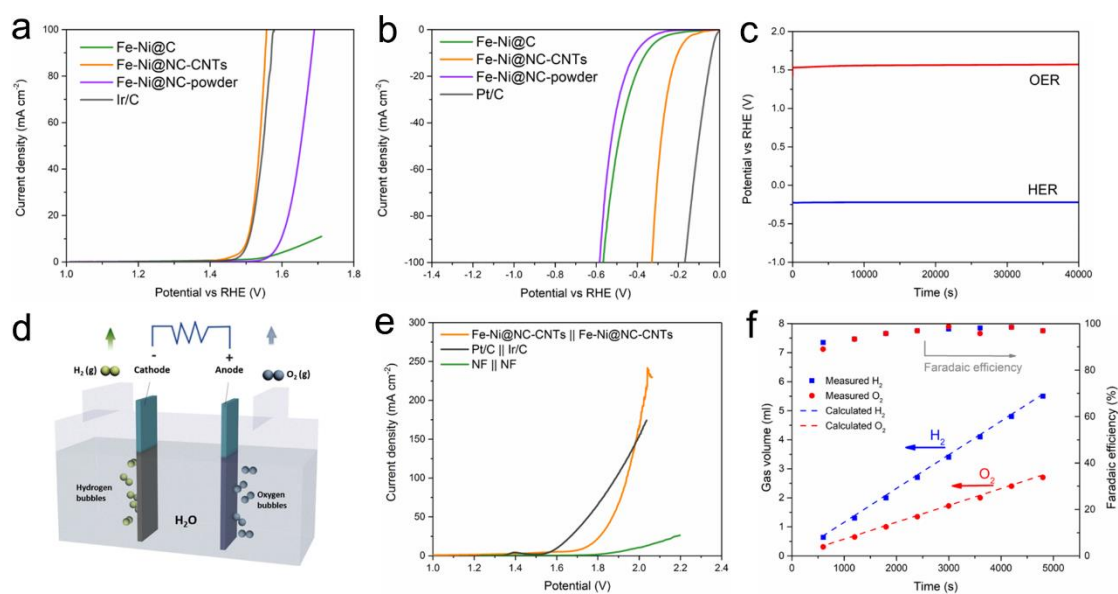

Figure 3.2. a) OER polarization curves for Fe-Ni@C, Fe-Ni@NC-CNT, Fe-Ni@NC-powder and commercial Ir/C catalysts. b) EIS spectra of the catalysts recorded at a constant potential of 1.504 V (vs RHE). c) Long-term stability test for Fe-Ni@NC-CNT for OER and HER at a constant current density of 10 mA/cm^2. d) Schematic diagram of an electrolyzer for water splitting. e) Polarization curve of Fe-Ni@NC-CNTs || Fe-Ni@NC-CNTs, NF || NF and Pt/C || Ir/C. f) O$_2$ and H$_2$ production volumes as a function of water splitting time for Fe-Ni@NC-CNTs. Reprinted from publication [XJZ02]. Reproduced with permission from John Wiley and Sons.

Subsequently, we assembled an electrolyzer using Fe-Ni@NC-CNTs on nickel foam (NF) as both the cathode and anode for overall water splitting (Figure 3.2d). As shown in Figure 3.2e, the Fe-Ni@NC-CNTs exhibits a comparable current density to the noble-metal derived catalysts at a cell voltage of 1.98 V. During overall water splitting, the recorded gas volumes as

a function of water-splitting time under the condition of the chronopotentiometry test shows a linear relationship with a slope of 1.15 and 0.57 µl/s for H_2 and O_2 collection. The good agreement of the experimentally generated and theoretically calculated amount of H_2 and O_2 reveal a Faradaic efficiency of ~100% for both HER and OER, indicating its potential for practical applications. (Figure 3.2f).

3.3 Conclusion

"In summary, we have prepared a hybrid Fe-Ni@NC-CNTs catalyst by simple one-step pyrolysis of a MIL-88-Fe/Ni-DCDA composite. The obtained Fe-Ni@NC-CNTs possesses a high conductivity, hierarchical pore structure and stable 3D framework, resulting in high activity, fast mass transport and good stability for electrocatalytic processes. Consequently, when applied for energy conversion and storage, this unique nanostructure exhibits remarkable OER and HER catalytic activity in alkaline solution and show promising potential for practical applications in overall water splitting. The facile synthesis of inexpensive hybrid nanostructures derived from MOFs with controllable morphologies and functionalities can be certainly expanded to the development of further materials for various electrocatalytic reactions"

4 Silica-Templated COF-derived Carbon-based Electrocatalysts

This chapter was published in Chemistry of Materials with the title "Silica-Templated Covalent Organic Framework-Derived Fe–N-Doped Mesoporous Carbon as Oxygen Reduction Electrocatalyst"

Xiaojia Zhao, Pradip Pachfule, Shuang Li, Thomas Langenhahn, Mengyang Ye, Guiying Tian, Johannes Schmidt, and Arne Thomas*
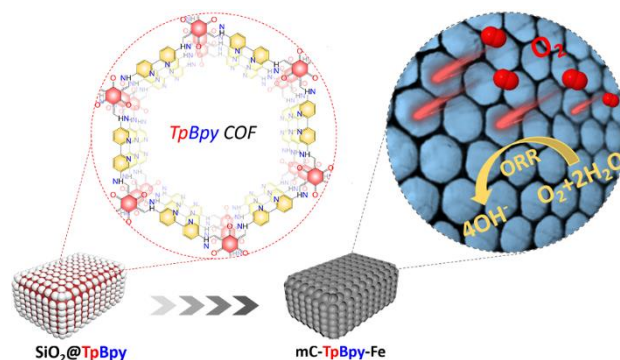
The chapter reprints the abstract and conclusion of the publication and gives a summary of the results. Detailed information can be found in the publication reprint in Chapter 8.3

4.1 Abstract

"The rational design and synthesis of mesoporous functional materials is of great significance to tackle fundamental challenges in materials science and to yield practical solutions for efficient energy utilization. Here, a novel p-toluenesulfonic acid-assisted mechanochemical approach is used to prepare a silica-templated bipyridine-containing covalent organic framework (COF), which can be further converted into an iron–nitrogen-doped mesoporous carbon (mC-TpBpy-Fe) upon carbonization and template removal. The resulting mC-TpBpy-Fe exhibits a large pore volume and surface area, which significantly promote the mass transfer efficiency and increase the accessibility of the active sites, yielding a high ORR activity with a competitive half-wave potential of 0.845 V and limiting current density of 5.92 mA/cm^2 (vs 0.852 V and 5.57 mA/cm^2 for Pt/C). Application of this COF derived mesoporous carbon within a Zn–air battery revealed that it can operate in ambient conditions with a competitive discharge performance, showing its potential for practical applications."

TOC: reprinted from publication [XJZ03]. Reproduced with permission from American Chemical Society.

4.2 Project summary

Porous carbon-based materials have attracted enormous attention for energy conversion and storage, owing to their unique properties such as large specific surface area and high structural stability. Especially transition metal-and nitrogen-doped carbons (M-N-C) have been widely studied as oxygen reduction reaction (ORR) catalysts. Beside the traditional molecular precursors, porous framework materials have recently been increasingly investigated as precursors for carbonaceous electrocatalysts. However, MOFs and COFs derived carbons usually exhibits bulk structures with very low porosity or microporosity only, which can in the first case largely decrease the accessible surface area for the electrolyte and in the second decelerate mass transfer.

In this work, we report a facile strategy to convert COFs into mesoporous carbons using silica nanoparticles as templates. Furthermore, bipyridine moieties within the COF are assisting metal ion coordination, yielding abundant Fe- and N-doping within the resulting carbon material (mC-TpBpy-Fe). mC-TpBpy-Fe exhibits a large pore volume and surface area, and abundant FeN_x sites, yielding a high ORR activity. Application of this COF derived mesoporous carbon within a Zn-air battery showed that it can operate in ambient conditions with a competitive discharge performance, showing its potential for practical applications.

Experiments: The mesoporous Fe-N_x doped carbon (mC-TpBpy-Fe) was synthesized via a PTSA-assisted mechanochemical method (Figure 4.1a).[144] In a typical synthesis, the silica-COF (SiO_2@TpBpy) composite was firstly prepared using the Schiff base reaction between 1,3,5-Triformylphloroglucinol (Tp) and 2,2'-bipyridine-5,5'-diamine (Bpy), in presence of SiO_2 with a diameter of ~24 nm. Iron ions were introduced into SiO_2@TpBpy by soaking a defined amount of the composite in methanolic iron chloride ($FeCl_3 \cdot 6H_2O$) solution and further stirring for 4 h to yield SiO_2@TpBpy-Fe. Pyrolysis at 800 °C for 2 h in Ar atmosphere then yield a carbon-silica composite (C-SiO_2@TpBpy-Fe) which was treated first with HCl and then with NaOH to etch out residual metal salt and finally the silica template, followed by a secondary thermal treatment at 900°C for 2 h to yield the final product named mC-TpBpy-Fe. *p*-Toluenesulfonic acid (PTSA) was used as a molecular organizer for the COF synthesis and SiO_2 were used as hard template to enable the formation of mesoporous structures. Bipyridine moieties were deliberately chosen and incorporated within the COF backbone as they can strongly coordinate to metal ions, here iron (Fe) ions, which then could form Fe-N_x active sites after a subsequent pyrolysis process.
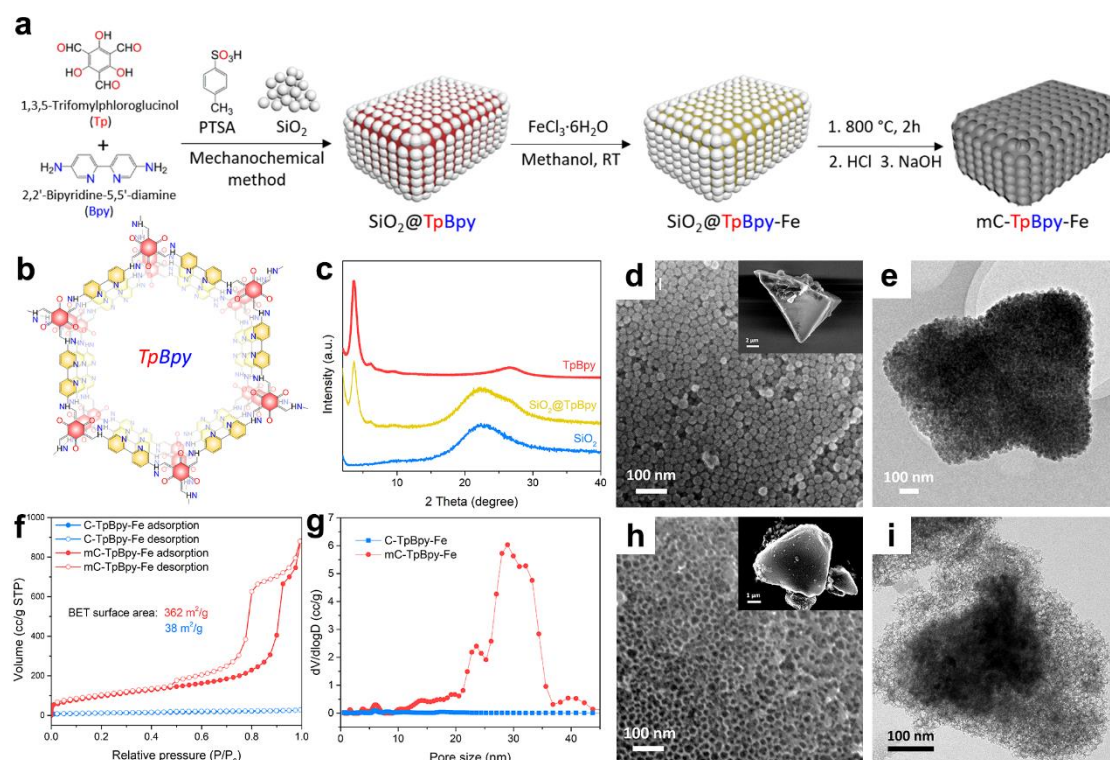
Figure 4.1 a) Synthesis of mC-TpBpy-Fe via PTSA-assisted mechanochemical method, in presence of silica nanoparticles. b) The packing diagram of TpBpy showing the bipyridine coordination sites available in the COF backbone. c) PXRD pattern of TpBpy, SiO$_2$@TpBpy, and SiO$_2$. d) SEM, and e) TEM images of SiO$_2$@TpBpy. f) N$_2$ adsorption-desorption isotherms of C-TpBpy-Fe and mC-TpBpy-Fe. g) Pore size distribution of C-TpBpy-Fe and mC-TpBpy-Fe, calculated from the adsorption branch of isotherms by the QSDFT model. h) SEM and i) TEM images of mC-TpBpy-Fe. Reprinted from publication [XJZ03]. Reproduced with permission from American Chemical Society.

Results and discussion: The PXRD patterns of pristine TpBpy show an intense peak at 3.6° (2θ), corresponding to the reflections from the (100) plane of the COF, which is as well seen in SiO$_2$@TpBpy, confirming that the structure of TpBpy is well preserved even when templated with silica nanoparticles. The extra shoulder of the broad beak at 27° in SiO$_2$@TpBpy is attributable to amorphous silica (Figure 4.1c). SEM and TEM analyses were conducted to study the morphology of SiO$_2$@TpBpy, in which densely packed silica nanoparticles have been observed with a thin coating of TpBpy COF on the surface of each individual nanoparticles (Figure 4.1d, e). Nitrogen sorption isotherms were measured to examine the specific surface area and pore volume of the obtained samples. As shown in Figure 4.1f, mC-TpBpy-Fe reveals a typical type IV isotherm, with an obvious hysteresis loop at higher relative pressures, indicating mesoporosity. The calculated Brunauer-Emmett-Teller (BET) surface area of mC-TpBpy-Fe is 362 m^2/g, almost the entire surface area can be attributed to mesopores. This is also reflected in the pore size distribution calculated by Quenched Solid State Functional Theory (QSDFT) confirming the formation of large mesopores for mC-TpBpy-Fe (Figure 4.1g). This is also confirmed by SEM and TEM images, revealing the uniformly distributed large mesoporous structures (Figure 4.1i), which should be useful to promote the mass transfer

during electrocatalytic reactions. To elucidate the chemical components and the nature of Fe species in mC-TpBpy-Fe, X-ray photoelectron spectroscopy (XPS) and X-ray absorption fine structure (XAFS) measurements were performed, pointing to a coordination of Fe ions to the pyridinic N-doping and the atomically dispersed Fe atoms within the carbon matrix.

As a result, the electrocatalytic activity of mC-TpBpy-Fe was tested as catalyst for ORR under basic conditions (0.1 M KOH). As shown in Figure 4.2a, The linear sweep voltammetry (LSV) curves show a higher half-wave potential (0.845 V) for mC-TpBpy-Fe than for C-TpBpy-Fe (0.804 V), mC-TpBD-Fe (0.808 V) and even a comparable value to commercially available Pt/C (0.852 V). The enhancement of ORR activity for mC-TpBpy-Fe can be attributed to the introduction of the mesoporous structures that efficiently promote the mass transfer and the accessibility of active sites to reactants. On the other hand, the Bpy moieties within COF matrix are supposed to be beneficial to the formation of Fe-N active sites in mC-TpBpy-Fe to promote the ORR performance, which is confirmed by the inferior ORR activity of mC-TpBD-Fe. The transferred number of electrons during ORR are measured by recording the LSV curves of mC-TpBpy-Fe at different rotating rates of the rotating disk electrode (RDE) (Figure 4.2b, inset). Based on the Koutecký–Levich equation, the electron transfer number of mC-TpBpy-Fe is determined to be about 4.0, manifesting an ideal 4e$^-$ transfer ORR mechanism. Notably, the mC-TpBpy-Fe catalyst shows long-term durability, with almost negligible difference in the half-wave potential after 5000 cycles (Figure 4.2c).
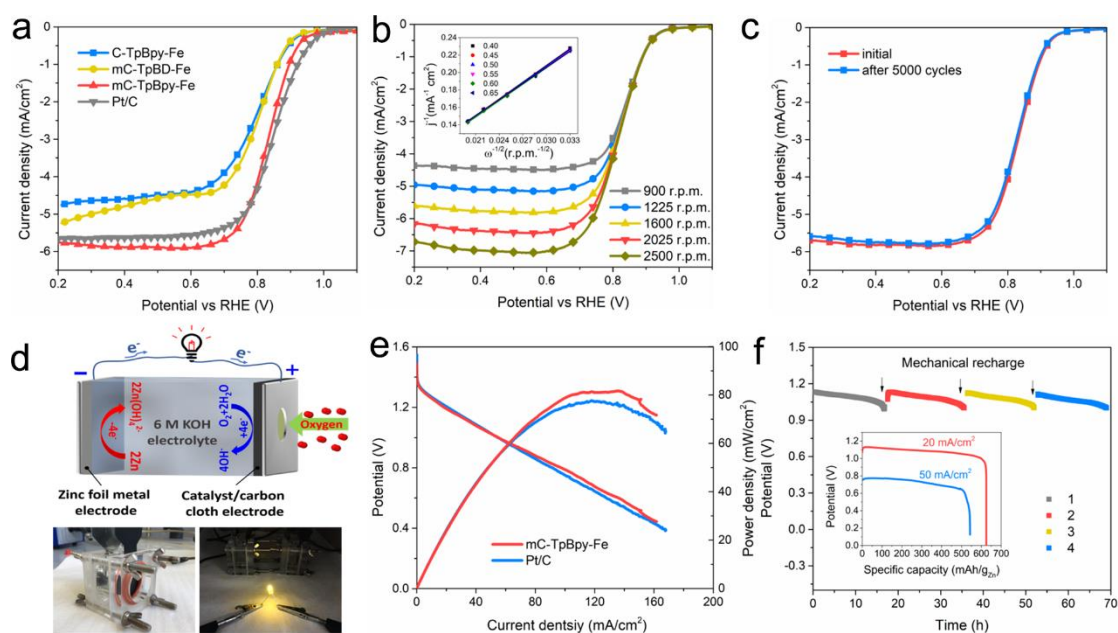

Figure 4.2. a) LSV curves of C-TpBpy-Fe, mC-TpBD-Fe, mC-TpBpy-Fe and Pt/C in oxygen-saturated 0.1 M KOH. b) LSV curves of mC-TpBpy-Fe in oxygen-saturated 0.1 M KOH at various rotating speeds. Inset: K-L plots for mC-TpBpy-Fe at various potentials. c) LSV of mC-TpBpy-Fe before and after 5000 cycles at a voltage range between 0.7 - 1.0 V. d) Schematic diagram of a Zn-air battery and photographs of a lab-made Zn-air battery (left) and a LED connected to two batteries (right). e) Comparison of polarization and power density curves of primary Zn-air batteries using mC-TpBpy-Fe and Pt/C as ORR catalysts. f) Long-time durability of a primary Zn-air battery using mC-TpBpy-Fe at a current density of 20 mA/cm^2. The battery is mechanically rechargeable, i.e. the Zn foil and electrolyte were replaced at the time indicated

by arrows. Inset: Specific capacities of the Zn-air batteries using mC-TpBpy-Fe normalized to the mass of the consumed Zn at various current density (20 and 50 mA/cm^2). Reprinted from publication [XJZ03]. Reproduced with permission from American Chemical Society.

The performance of mC-TpBpy-Fe ORR makes it an interesting cathode material e.g. in Zn-air batteries, devices which have attracted attention due to their high specific energy density and the low cost for next-generation green and sustainable energy technologies (Figure 4.2d). Figure 4.2e compares the polarization and power density curves for Zn-air batteries using mC-TpBpy-Fe and Pt/C air cathodes. The mC-TpBpy-Fe shows a peak power density of ~81 mW/cm^2, comparable to that of the conventional Pt/C catalyst (77 mW/cm^2). Although Zn is gradually consumed during the discharging process, the battery can be mechanically recovered by replacing the Zn foil and KOH electrolyte, featuring no obvious potential decrease after 4 cycles (~70 h) (Figure 4.2f). When normalized to the mass of consumed Zn, the specific capacity of mC-TpBpy-Fe was found as high as ~625 mAh/g$_{Zn}$ at a current density of 20 mA/cm^2 and ~543 mAh/g$_{Zn}$ at 50 mA/cm^2 (Figure 4.2f, inset). These results support the high ORR catalytic activity and excellent stability of the mC-TpBpy-Fe, promoting its promising potential for practical application in Zn-air battery.

4.3 Conclusion

"In summary, we have developed a facile strategy to convert COFs into mesoporous carbons by a PTSA-assisted mechanochemical method for COF growth in presence of silica nanoparticles. Bipyridine moieties within the COF are assisting metal ion coordination, yielding abundant Fe- and N-doping within the resulting carbon material. The mesoporous structure and large pore volume efficiently promote the diffusion of O$_2$ and electrolyte to the homogeneously dispersed Fe-N$_x$ active sites, eventually yielding an excellent ORR performance, making these materials very promising candidates for efficient oxygen electrode in Zn-air batteries. It is further shown that the PTSA-assisted silica-templated synthetic route can be applied to yield various SiO$_2$@COF composites as precursors for tailor-made carbon materials for energy conversion and storage."

Reprinted from publication [XJZ03], Reproduced with permission from American Chemical Society.
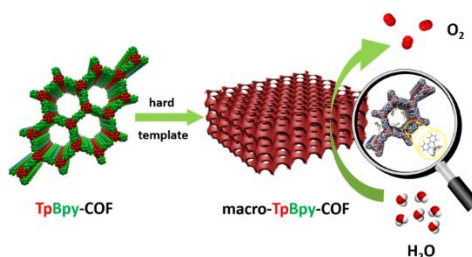
5 Macro/Microporous COFs for Efficient Electrocatalysis

The chapter reprints the abstract and conclusion of the publication and gives a summary of the results. Detailed information can be found in the publication reprint in Chapter 8.4

5.1 Abstract

"Covalent organic frameworks (COFs) are of interest for many applications originating from their mechanically robust architectures, low density, and high accessible surface area. Depending on their linkers and binding patterns, COFs mainly exhibit microporosity, even though COFs with small mesopores have been reported using extended linkers. For some applications, especially when fast mass transport is desired, hierarchical pore structures are an ideal solution, e.g., with small micropores providing large surface areas and larger macropores providing unhindered transport to and from the materials surface. Herein, we have developed a facile strategy for the fabrication of crystalline COFs with inherent microporosity and template-induced, homogeneously distributed, yet tunable, macroporous structures. This method has been successfully applied to obtain various β-ketoenamine-based COFs with interconnected macro–microporous structures. The as-synthesized macroporous COFs preserve high crystallinity with high specific surface area. When bipyridine moieties are introduced into the COF backbone, metals such as Co^{2+} can be coordinated within the hierarchical pore structure (macro-TpBpy-Co). The resulting macro-TpBpy-Co exhibits a high oxygen evolution reaction (OER) activity, which is much improved compared to the purely microporous COF with a competitive overpotential of 380 mV at 10 mA/cm^2. This can be attributed to the improved mass diffusion properties in the hierarchically porous COF structures, together with the easily accessible active Co^{2+}-bipyridine sites."

TOC: reprinted from publication [XJZ04]. Reproduced with permission from American Chemical Society.

5.2 Project summary

Crystalline microporous materials have been intensely studied over the last decades owing to their importance for various applications. One inherent problem of such microporous materials, having pore sizes of molecular dimensions (< 2nm), is diffusion limitation, which is especially problematic for catalytic processes requiring efficient mass transfer to and from the active sites. The construction of hierarchical porous structures, i.e. the introduction of additional larger meso- or macropores into microporous materials is considered to be an effective way to overcome this problem.[103,145] Covalent Organic Frameworks (COFs) are an emerging class of crystalline microporous materials and have been intensely studied for application in gas separation, heterogeneous catalysis, optoelectronics and energy storage. So far, COFs can just be prepared with micro- or small mesopores, which limits their applicability in diffusion-limited processes.

In this work, we report a facile approach for the preparation of crystalline COFs with hierarchical pore structures. Additional macropores were introduced into the COF using monodisperse polystyrene spheres (PSs) as template. The obtained macro/microporous COFs preserve a high crystallinity and high specific surface areas. Enhanced mass transport in hierarchical COF structures is proven by applying cobalt-loaded bipyridine-COFs as OER catalysts. Indeed, the macro/microporous COF exhibits excellent performance as OER catalysts, showing a significantly improved activity compared to the microporous-only COF but also outperforms many other reported cobalt-based electrocatalysts.

Experiment: Macroporous COF (macro-TpBpy) was synthesized by reacting the organic linkers 1,3,5-Triformylphloroglucinol (Tp) and 2,2'-bipyridine-5,5'-diamine (Bpy) in the presence of polystyrene nanoparticles (PSs) via Schiff base reaction, as schematically illustrated in Figure 5.1a. In the first step, the colloidal PSs (~10 wt% in water, 5 ml) were mixed with the Bpy linker (83.8 mg) and PTSA (475.5 mg) to form an organic salt. Then the resulting salt and Tp (63 mg) were thoroughly shaken for 10 min, and then the dispersion was poured into a petri dish to evaporate excess water at room temperature for overnight. Further drying at 80 °C for 24 h yield an orange-colored PS@TpBpy composite. Subsequent, soxhlet extraction of PS@TpBpy was conducted using tetrahydrofuran (THF) as solvent to remove the PS template as well as unreacted monomers, to obtain a COF with macroporous structures (macro-TpBpy). Finally, macro-TpBpy-Co was synthesized by soaking a defined amount of macro-TpBpy in cobalt acetate (Co(OAc)$_2$·4H$_2$O) solutions in methanol and further stirring for 4 h at room temperature. The other materials were synthesized by similar procedure, detailed can be found in the publication [XJZ04]
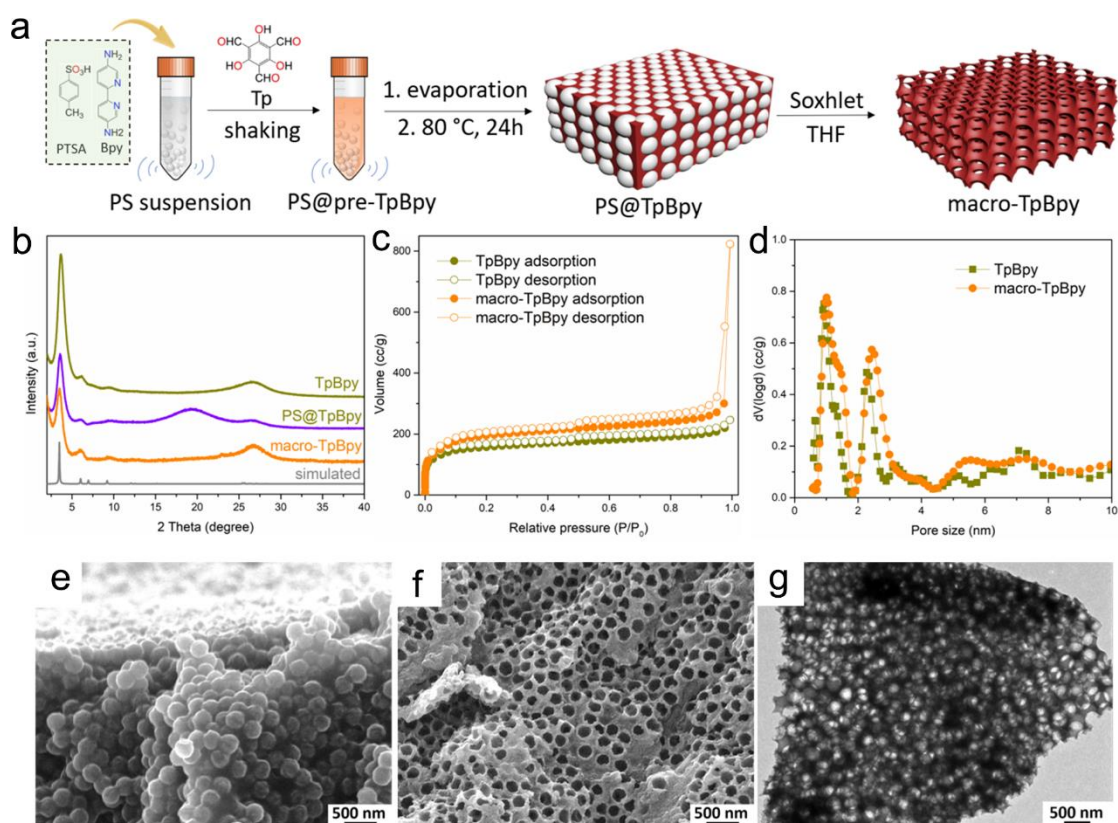
Figure 5.1 a) Schematic representation of macro-TpBpy fabrication in presence of PSs. b) PXRD pattern of TpBpy, PS@TpBpy, and macro-TpBpy showing the preservation of crystallinity in macro-TpBpy with and after removing the PSs. Inset: Space-filling packing diagram of TpBpy COF. c) N_2 adsorption-desorption isotherms of the TpBpy and macro-TpBpy. d) Pore size distribution of the TpBpy and macro-TpBpy, calculated from the adsorption branch of isotherms by the QSDFT model. e) SEM image of PS@TpBpy. f) SEM image of macro-TpBpy. g) TEM image of macro-TpBpy. Reprinted from publication [XJZ04]. Reproduced with permission from American Chemical Society.

Results and discussion: PXRD measurements were conducted to test the crystallinity of the macroporous COFs. As shown in Figure 5.1b, macro-TpBpy displays an intense peak at 3.6° (2θ) corresponding to the reflection from the (100), very similar to the pristine TpBpy, confirming the retention of the crystalline structure of TpBpy even after introducing the macroporous structures. Nitrogen adsorption-desorption isotherms were further performed to examine the specific surface area and microporosity of pristine TpBpy and macro-TpBpy. As shown in Figure 5.1c, the isotherm of macro-TpBpy exhibits a typical type I isotherm with a steep increase at low relative pressures, indicating the microporosity of the COF (Figure 5.1d). On the other hand, the isotherm also shows an additional significant increase in nitrogen uptake at high relative pressure, indicating that an additional macroporosity has been successfully introduced by the PS template. Furthermore, the calculated pore volume confirms the presence of macroporosity in hierarchical macro-TpBpy with a total pore volume of 1.273 cm^3/g, that is much higher than that of pristine TpBpy (0.381 cm^3/g). On the other hand, the calculated Brunauer-Emmett-Teller (BET) surface areas of macro-TpBpy (723 m^2/g) is higher than that of

pristine TpBpy (588 m^2/g), showing that the formation of macropores can efficiently promote the accessibility of micropores.

To verify the formation of macroporous structures, SEM and TEM analyses were conducted to characterize the morphologies of the as-synthesized macroporous COFs. As shown in Figure 5.1e, the PS@TpBpy composites display a pile of densely packed PS nanoparticles with a coating of TpBpy COF on the surface. After removing the PS template using soxhlet extraction with THF, the obtained macro-TpBpy displays a replica of the PS spheres yielding an interconnected uniform macroporous structures (Figure 5.1f), which is also confirmed by TEM measurements with the feature of pronounced interconnected porous structures (Figure 5.1g). In addition, to prove the generality of this method, it was shown that the size of the macropores can be tuned by applying different templates and the microporosity and chemical structure of the COFs can be changed as well by applying different monomers (for details see [XJZ04]).

To verify the advantage of macroporous structures in macro-TpBpy for mass transport during electrocatalysis processes, cobalt ions were used to form macro-TpBpy-Co as OER catalysts by soaking a defined amount of macro-TpBpy in Co(OAc)$_2\cdot$4H$_2$O solutions in methanol. High-angle annular dark-field scanning transmission electron microscopy (HAADF-STEM) was conducted to reveal the morphology and element distribution in the macro-TpBpy-Co. The HAADF STEM images and corresponding elemental mapping for C, N, O and Co prove the uniform distribution of N and Co species within the macro-TpBpy-Co matrix. Moreover, XPS and X-ray absorption spectroscopy (XAS) were conducted to confirm the coordinated environment of Co species. As shown in the normalized Co K-edge spectra (Figure 5.2b), the rising-edge position of macro-TpBpy-Co is located between the Co powder and Co$_3$O$_4$ standard, indicating that the oxidation state of Co within macro-TpBpy-Co is +2 and +3. The Fourier transformed extended X-ray absorption fine structure (EXAFS) data reveals a variation of the neighboring environment for Co^{2+}, confirming the existence of Co-N first coordination shell.
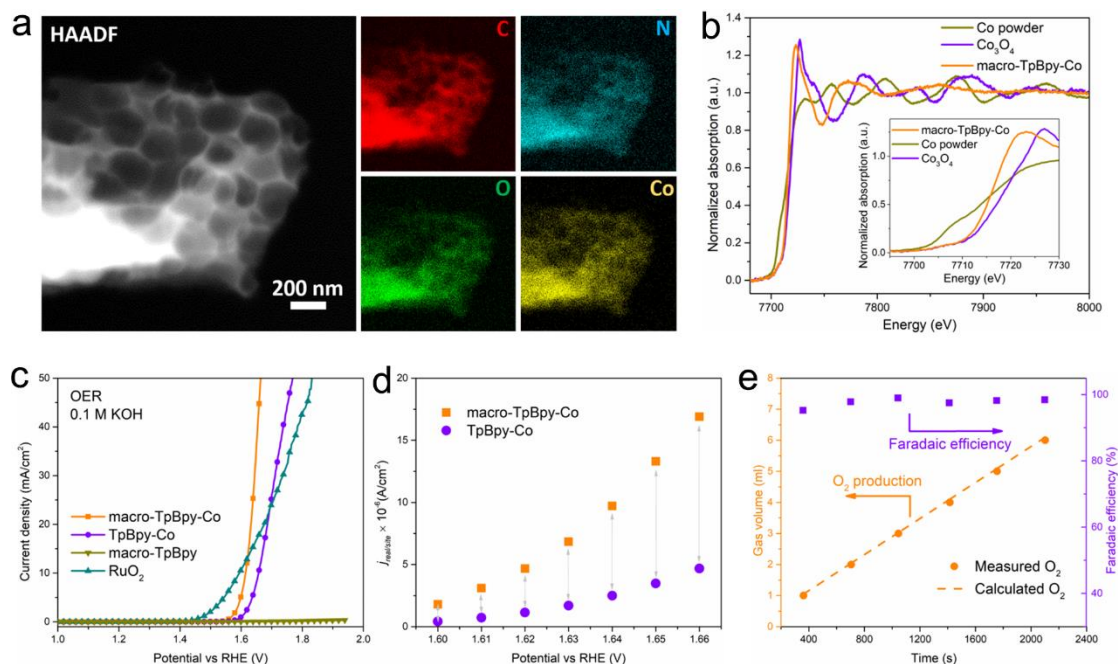
Figure 5.2 a) HAADF-STEM images and the corresponding element mapping of C, N, O, and Co. b) Normalized Co K-edge XAS spectra for macro-TpBpy-Co refer-enced by Co_3O_4 and Co powder; The inset shows the magnified image of the pre-edge XAS spectra. c) OER polarization curves for macro-TpBpy, macro-TpBpy-Co, TpBpy-Co and a commercial RuO_2 catalyst. d) Scatter plot of $j_{real/site}$ for macro-TpBpy-Co and TpBpy-Co, versus applied potential. e) Faradaic efficiency of macro-TpBpy-Co for oxygen production. Reprinted from publication [XJZ04]. Reproduced with permission from American Chemical Society.

The OER activity of macro-TpBpy-Co was evaluated under an alkaline aqueous electrolyte (0.1 M KOH) using a typical three-electrode system. As shown in Figure 5.1c, macro-TpBpy-Co requires an overpotential of 380 mV versus the reversible hydrogen electrode (RHE) to achieve an anodic current density of 10 mA/cm^2, much lower than that of TpBpy-Co (430 mV). The superior OER performance of macro-TpBpy-Co can be attributed to the introduction of homogeneous and interconnected macroporous structures, which was further confirmed by the normalization process from current density (j) to the activity per active sites ($j_{real/site}$) (for details see [XJZ04]). As shown in Figure 5.2d, macro-TpBpy-Co shows a a much higher $j_{real/site}$ compared to TpBpy-Co, indicating an enhanced catalytic activity for active sites. In particular, under a higher potential with larger amount of oxygen production, the prominent enhancement of $j_{real/site}$ for macro-TpBpy-Co gives a strong evidence for the advantage of an additional macroporous structure that efficiently promote the mass transfer and the accessibility of active sites to reactants during electrocatalytic process. Moreover, the Faradaic efficiency of macro-TpBpy-Co was determined by comparing the experimentally produced gas volume with the theoretically calculated one (Figure 5e, for details see SI). The good agreement of the experimentally generated and theoretically calculated amount of O_2 reveal a Faradaic efficiency of ~98% for OER in 0.1 M KOH, confirming the high activity as well as efficiency of macro-TpBpy-Co as an OER catalyst.

5.3 Conclusion

"In summary, we have developed a pathway to fabricate hierarchical and crystalline COFs with interconnected and uniform macroporous structures by employing a facile PS mediated templating method. The obtained macroporous COFs preserve their crystallinity and high specific surface areas. Confirmation of enhanced mass transport in hierarchical COF structures was given by testing Co-coordinated bipyridine-based COFs as OER catalysts. The macro-TpBpy-Co exhibits excellent performance as OER catalysts, with much improved activity compared to the only microporous TpBpy-Co and also compares favorably to other reported cobalt-doped polymer-based electrocatalysts. The enhanced performance of macro-TpBpy-Co can be attributed to the improved mass diffusion properties in the hierarchically porous structure, together with more accessible active sites. The here presented PSs templating method was successfully extended to obtain various macro-microporous imine-based COFs by modulating the corresponding amine-linkers, showing its potential as a convenient route for the preparation of macro-microporous COFs with different functional groups for various applications."

6 Summary

In this thesis, we aim to design and synthesize efficient and low-cost electrocatalysts to face globally increasing concerns like climate change, pollution, and energy security. We have developed novel methodologies and employed various precursors to construct a series of noble metal-free electrocatalysts, including metal-free electrocatalyst, non-noble metal-based carbon electrocatalyst, and polymer-based electrocatalyst. The electrocatalytic activities for these catalysts have been studied as well as their practical application in energy-related areas such as overall water splitting and Zn-air battery.

Chapter 2 describes an ionic liquid (IL)-assisted method for synthesizing nitrogen-doped, ordered mesoporous carbon (NMCs) as metal-free electrocatalysts with enhanced exposure of nitrogen atoms at the pore surface. This self-assembly method is simple and allows the IL to be preferentially located within the forming resol phase, thus achieving an enrichment of nitrogen at the carbon pore surface after carbonization. The obtained NMCs exhibit a high activity and stability for HER. The excellent performance is attributable to an enrichment of nitrogen atoms at the pore surface of the mesoporous carbon. This concept can be easily adapted for the synthesis of a broad range of different mesoporous carbon materials with various heteroatoms or metals enriched at the surface.

Chapter 3 introduces a novel non-noble metal-based carbon electrocatalyst derived from bimetallic MOF (MIL-88-Fe/Ni) - dicyandiamide composites. $FeNi_3$ and $NiFe_2O_4$ are found as metallic and metal oxide compounds, respectively, closely embedded in a N-doped carbon (NC) - carbon nanotube (CNT) matrix. The obtained Fe-Ni@NC-CNTs possesses a high conductivity, hierarchical pore structure and stable 3D framework, resulting in high activity and good stability for both HER and OER. When this bifunctional catalyst was further used for H_2 and O_2 production in an electrochemical water-splitting unit, it can operate in ambient air with a competitive gas production rate of 1.15 and 0.57 μl/s for hydrogen and oxygen, respectively, showing its potential for practical applications. This facile synthesis of inexpensive hybrid nanostructures derived from MOFs can be certainly expanded to the development of further materials for various electrocatalytic reactions.

Chapter 4 delivers an efficient iron-nitrogen doped carbon (Fe-N-C) electrocatalyst by applying covalent organic frameworks (COFs) as carbon precursor. In this project, an additional silica template was used to enable the formation of mesoporous structures and bipyridine moieties were deliberately chosen and incorporated within the COF backbone to coordinate to Fe ions, which then could form $Fe-N_x$ active sites after pyrolysis process. The obtained mC-TpBpy-Fe exhibits a large pore volume and surface area, and abundant $Fe-N_x$ sites, yielding a high ORR activity. Application of this COF derived mesoporous carbon within a Zn-air battery showed that it can operate in ambient conditions with a competitive discharge performance, showing its potential for practical applications. It is further shown that our approach can be applied to yield various SiO_2@COF composites as precursors for tailor-made carbon materials for energy conversion and storage.

Inspired by the research work in Chapter 4, a follow-up project is described in **Chapter 5** to construct a macro/microporous COF and explore its potentially electrocatalytic activity as a polymer-based electrocatalyst. Additional macropores were introduced into the COF using monodisperse polystyrene spheres (PSs) as template. We show that the size of the macropores can be tuned by applying different templates and the microporosity and chemical structure of the COFs can be changed as well applying different monomers. The obtained macro/microporous COFs preserve a high crystallinity and high specific surface areas. Enhanced mass transport in hierarchical COF structures is proven by applying cobalt-loaded bipyridine-COFs as OER catalysts. In this project, we present a versatile method for introducing larger transport pores into a currently intensively investigated material class, the covalent organic frameworks. Our electrocatalytic tests show that this facile method is beneficial to enhance the performance of COFs by far and we are convinced that this will be also true for many other catalytic reactions and all applications in which mass transport in porous systems is of importance.

7 References

[1] Shao, M. H.; Chang, Q. W.; Dodelet, J. P.; Chenitz, R. *Chem. Rev.* **2016**, *116*, 3594-3657.

[2] Dai, L. M.; Xue, Y. H.; Qu, L. T.; Choi, H. J.; Baek, J. B. *Chem. Rev,* **2015**, *115*, 4823-4892.

[3] Jin, H. Y.; Guo, C. X.; Liu, X.; Liu, J. L.; Vasileff, A.; Jiao, Y.; Zheng, Y.; Qiao, S. Z. *Chem. Rev.* **2018**, *118*, 6337-6408.

[4] Suen, N. T.; Hung, S. F.; Quan, Q.; Zhang, N.; Xu, Y. J.; Chen, H. M. *Chem. Soc. Rev.* **2017**, *46*, 337-365.

[5] Roger, I.; Shipman, M. A.; Symes, M. D. *Nat. Rev. Chem.* **2017**, *1*, 0003.

[6] Seh, Z. W.; Kibsgaard, J.; Dickens, C. F.; Chorkendorff, I. B.; Norskov, J. K.; Jaramillo, T. F. *Science* **2017**, *355*, eaad4998.

[7] Xu, X.; Song, F.; Hu, X. L. *Nat. Commun.* **2016**, *7*, 12324.

[8] Huang, Z. F.; Song, J. J.; Li, K.; Tahir, M.; Wang, Y. T.; Pan, L.; Wang, L.; Zhang, X. W.; Zou, J. J. *J. Am. Chem. Soc.* **2016**, *138*, 1359-1365.

[9] Lin, T. Q.; Chen, I. W.; Liu, F. X.; Yang, C. Y.; Bi, H.; Xu, F. F.; Huang, F. Q. *Science* **2015**, *350*, 1508-1513.

[10] Peng, P.; Zhou, Z.; Guo, J.; Xiang, Z. *ACS Energy Lett.* **2017**, *2*, 1308-1314.

[11] Duan, J. J.; Chen, S.; Zhao, C. *Nat. Commun.* **2017**, *8*, 15341.

[12] Liao, P.-Q.; Shen, J.-Q.; Zhang, J.-P. *Coord. Chem. Rev.* **2018**, *373*, 22-48.

[13] Paraknowitsch, J. P.; Thomas, A.; Antonietti, M. *J. Mater. Chem.* **2010**, *20*, 6746-6758.

[14] Jiao, Y.; Zheng, Y.; Davey, K.; Qiao, S. Z. *Nat. Energy* **2016**, *1*, 16130.

[15] Zheng, Y.; Jiao, Y.; Li, L. H.; Xing, T.; Chen, Y.; Jaroniec, M.; Qiao, S. Z. *ACS Nano* **2014**, *8*, 5290-5296.

[16] Gong, M.; Li, Y. G.; Wang, H. L.; Liang, Y. Y.; Wu, J. Z.; Zhou, J. G.; Wang, J.; Regier, T.; Wei, F.; Dai, H. J. *J. Am. Chem. Soc.* **2013**, *135*, 8452-8455.

[17] Liang, Y. Y.; Li, Y. G.; Wang, H. L.; Zhou, J. G.; Wang, J.; Regier, T.; Dai, H. J. *Nat. Mater.* **2011**, *10*, 780-786.

[18] Wu, H. B.; Xia, B. Y.; Yu, L.; Yu, X. Y.; Lou, X. W. *Nat. Commun.* **2015**, *6*, 6512.

[19] Wei, J.; Liang, Y.; Hu, Y. X.; Kong, B. A.; Simon, G. P.; Zhang, J.; Jiang, S. P.; Wang, H. T. *Angew. Chem. Int. Ed.* **2016**, *55*, 1355-1359.

[20] Fei, H. L.; Dong, J. C.; Feng, Y. X.; Allen, C. S.; Wan, C. Z.; Volosskiy, B.; Li, M. F.; Zhao, Z. P.; Wang, Y. L.; Sun, H. T.; An, P. F.; Chen, W. X.; Guo, Z. Y.; Lee, C.; Chen, D. L.; Shakir, I.; Liu, M. J.; Hu, T. D.; Li, Y. D.; Kirkland, A. I.; Duan, X. F.; Huang, Y. *Nat. Catal.* **2018**, *1*, 63-72.

[21] Han, Y. H.; Wang, Y. G.; Chen, W. X.; Xu, R. R.; Zheng, L. R.; Zhang, J.; Luo, J.; Shen, R. A.; Zhu, Y. Q.; Cheong, W. C.; Chen, C.; Peng, Q.; Wang, D. S.; Li, Y. D. *J. Am. Chem. Soc.* **2017**, *139*, 17269-17272.

[22] Chen, Y. J.; Ji, S. F.; Wang, Y. G.; Dong, J. C.; Chen, W. X.; Li, Z.; Shen, R. A.; Zheng, L. R.; Zhuang, Z. B.; Wang, D. S.; Li, Y. D. *Angew. Chem. Int. Ed.* **2017**, *56*, 6937-6941.

[23] Yin, P. Q.; Yao, T.; Wu, Y.; Zheng, L. R.; Lin, Y.; Liu, W.; Ju, H. X.; Zhu, J. F.; Hong, X.; Deng, Z. X.; Zhou, G.; Wei, S. Q.; Li, Y. D. *Angew. Chem. Int. Ed.* **2016**, *55*, 10800-10805.

[24] Chen, W. X.; Pei, J. J.; He, C. T.; Wan, J. W.; Ren, H. L.; Wang, Y.; Dong, J. C.; Wu, K. L.; Cheong, W. C.; Mao, J. J.; Zheng, X. S.; Yan, W. S.; Zhuang, Z. B.; Chen, C.; Peng, Q.; Wang, D. S.; Li, Y. D. *Adv. Mater.* **2018**, *30*, 1800396.

[25] Zhu, C. Z.; Fu, S. F.; Shi, Q. R.; Du, D.; Lin, Y. H. *Angew. Chem. Int. Ed.* **2017**, *56*, 13944-13960.

[26] Li, Y. G.; Wang, H. L.; Xie, L. M.; Liang, Y. Y.; Hong, G. S.; Dai, H. J. *J. Am. Chem. Soc.* **2011**, *133*, 7296-7299.

[27] Yang, J.; Voiry, D.; Ahn, S. J.; Kang, D.; Kim, A. Y.; Chhowalla, M.; Shin, H. S. *Angew. Chem. Int. Ed.* **2013**, *52*, 13751-13754.

[28] Liang, H.-W.; Wei, W.; Wu, Z.-S.; Feng, X.; Müllen, K. *J. Am. Chem. Soc.* **2013**, *135*, 16002-16005.

[29] Li, W.; Liu, J.; Zhao, D. Y. *Nat. Rev. Mater.* **2016**, *1*, 16023.

[30] Zhang, P. F.; Zhang, J. S.; Dai, S. *Chem. Eur. J.* **2017**, *23*, 1986-1998.

[31] Lee, K. J.; Lee, J. H.; Jeoung, S.; Moon, H. R. *Acc. Chem. Res.* **2017**, *50*, 2684-2692.

[32] Chen, L. Y.; Zhang, L.; Chen, Z. J.; Liu, H. J.; Luque, R.; Li, Y. W. *Chem. Sci.* **2016**, *7*, 6015-6020.

[33] Xu, Q.; Tang, Y.; Zhang, X.; Oshima, Y.; Chen, Q.; Jiang, D. *Adv. Mater.* **2018**, 30, 1706330.

[34] Jiao, L.; Jiang, H.-L. *Chem-Us* **2019**, *5*, 786-804.

[35] Jiao, L.; Wan, G.; Zhang, R.; Zhou, H.; Yu, S. H.; Jiang, H. L. *Angew. Chem. Int. Ed.* **2018**, *57*, 8525-8529.

[36] Aiyappa, H. B.; Thote, J.; Shinde, D. B.; Banerjee, R.; Kurungot, S. *Chem. Mater.* **2016**, *28*, 4375-4379.

[37] Lin, C. Y.; Zhang, D. T.; Zhao, Z. H.; Xia, Z. H. *Adv. Mater.* **2018**, *30*, 1703646.

[38] Paraknowitsch, J. P.; Thomas, A. *Energy Environ. Sci.* **2013**, *6*, 2839-2855.

[39] Duan, J. J.; Chen, S.; Jaroniec, M.; Qiao, S. Z. *ACS Catal.* **2015**, *5*, 5207-5234.

[40] Liu, X.; Dai, L. M. *Nat Rev Mater* **2016**, *1*, 16064.

[41] Hu, C. G.; Dai, L. M. *Angew. Chem. Int. Ed.* **2016**, *55*, 11736-11758.

[42] Chen, W.; Wan, M.; Liu, Q.; Xiong, X.; Yu, F.; Huang, Y. *Small Methods* **2018**, *3*, 1800323.

[43] Paraknowitsch, J. P.; Zhang, J.; Su, D. S.; Thomas, A.; Antonietti, M. *Adv. Mater.* **2010**, *22*, 87-92.

[44] Qu, K. G.; Zheng, Y.; Zhang, X. X.; Davey, K.; Dai, S.; Qiao, S. Z. *ACS Nano* **2017**, *11*, 7293-7300.

[45] Song, Y. F.; Chen, W.; Zhao, C. C.; Li, S. G.; Wei, W.; Sun, Y. H. *Angew. Chem. Int. Ed.* **2017**, *56*, 10840-10844.

[46] Zhang, J. T.; Zhao, Z. H.; Xia, Z. H.; Dai, L. M. *Nat. Nanotechnol.* **2015**, *10*, 444-452.

[47] Gong, K. P.; Du, F.; Xia, Z. H.; Durstock, M.; Dai, L. M. *Science* **2009**, *323*, 760-764.

[48] Guo, D. H.; Shibuya, R.; Akiba, C.; Saji, S.; Kondo, T.; Nakamura, J. *Science* **2016**, *351*, 361-365.

[49] Yang, H. B.; Miao, J. W.; Hung, S. F.; Chen, J. Z.; Tao, H. B.; Wang, X. Z.; Zhang, L. P.; Chen, R.; Gao, J. J.; Chen, H. M.; Dai, L. M.; Liu, B. *Sci. Adv.* **2016**, *2*, e1501122.

[50] Kim, D. P.; Lin, C. L.; Mihalisin, T.; Heiney, P.; Labes, M. M. *Chem. Mater.* **1991**, *3*, 686-692.

[51] Czerw, R.; Terrones, M.; Charlier, J. C.; Blase, X.; Foley, B.; Kamalakaran, R.; Grobert, N.; Terrones, H.; Tekleab, D.; Ajayan, P. M.; Blau, W.; Ruhle, M.; Carroll, D. L. *Nano Lett.* **2001**, *1*, 457-460.

[52] Zhao, X. J.; Li, S.; Cheng, H. F.; Schmidt, J.; Thomas, A. *ACS Appl. Mater. Interfaces* **2018**, *10*, 3912-3920.

[53] Li, S.; Cheng, C.; Zhao, X. J.; Schmidt, J.; Thomas, A. *Angew. Chem. Int. Ed.* **2018**, *57*, 1856-1862.

[54] Sahraie, N. R.; Paraknowitsch, J. P.; Gobel, C.; Thomas, A.; Strasser, P. *J. Am. Chem. Soc.* **2014**, *136*, 14486-14497.

[55] Zhang, J. T.; Xia, Z. H.; Dai, L. M. *Sci. Adv.* **2015**, *1*, e1500564.

[56] Zhang, J. T.; Dai, L. M. *ACS Catal.* **2015**, *5*, 7244-7253.

[57] Qu, K. G.; Zheng, Y.; Jiao, Y.; Zhang, X. X.; Dai, S.; Qiao, S. Z. *Adv. Energy Mater.* **2017**, *7*, 1602028.

[58] Chen, S.; Duan, J. J.; Jaroniec, M.; Qiao, S. Z. *Adv. Mater.* **2014**, *26*, 2925-2930.

[59] Lin, D. Q.; Hu, C. G.; Chen, H.; Qu, J.; Dai, L. M. Microporous *Chem. Eur. J.* **2018**, *24*, 18487-18493.

[60] Arico, A. S.; Bruce, P.; Scrosati, B.; Tarascon, J. M.; Van Schalkwijk, W. *Nat. Mater.* **2005**, *4*, 366-377.

[61] Wang, J.; Xu, F.; Jin, H. Y.; Chen, Y. Q.; Wang, Y. *Adv. Mater.* **2017**, *29*, 1605838.

[62] Zou, X. X.; Zhang, Y. *Chem. Soc. Rev.* **2015**, *44*, 5148-5180.

[63] Wang, D. Y.; Gong, M.; Chou, H. L.; Pan, C. J.; Chen, H. A.; Wu, Y. P.; Lin, M. C.; Guan, M. Y.; Yang, J.; Chen, C. W.; Wang, Y. L.; Hwang, B. J.; Chen, C. C.; Dai, H. J. *J. Am. Chem. Soc.* **2015**, *137*, 1587-1592.

[64] Zhang, Z.; Hao, J. H.; Yang, W. S.; Tang, J. L. *ChemCatChem* **2015**, *7*, 1920-1925.

[65] Cheng, C.; Li, S.; Xia, Y.; Ma, L.; Nie, C.; Roth, C.; Thomas, A.; Haag, R. *Adv. Mater.* **2018**, 1802669.

[66] Park, K. S.; Ni, Z.; Cote, A. P.; Choi, J. Y.; Huang, R. D.; Uribe-Romo, F. J.; Chae, H. K.; O'Keeffe, M.; Yaghi, O. M. *Proc. Natl. Acad. Sci.* **2006**, *103*, 10186-10191.

[67] Shi, L.; Wang, T.; Zhang, H. B.; Chang, K.; Meng, X. G.; Liu, H. M.; Ye, J. H. *Adv. Sci.* **2015**, *2*, 1500006.

[68] Li, H.; Eddaoudi, M.; O'Keeffe, M.; Yaghi, O. M. *Nature* **1999**, *402*, 276-279.

[69] Chui, S. S. Y.; Lo, S. M. F.; Charmant, J. P. H.; Orpen, A. G.; Williams, I. D. *Science* **1999**, *283*, 1148-1150.

[70] Zhang, Z. P.; Sun, J. T.; Dou, M. L.; Jo, J.; Wang, F. *ACS Appl. Mater. Interfaces* **2017**, *9*, 16236-16242.

[71] Wu, G.; More, K. L.; Johnston, C. M.; Zelenay, P. *Science* **2011**, *332*, 443-447.

[72] Xu, Y.; Tu, W. G.; Zhang, B. W.; Yin, S. M.; Huang, Y. Z.; Kraft, M.; Xu, R. *Adv. Mater.* **2017**, *29*, 1605957.

[73] Meng, J.; Niu, C.; Xu, L.; Li, J.; Liu, X.; Wang, X.; Wu, Y.; Xu, X.; Chen, W.; Li, Q.; Zhu, Z.; Zhao, D.; Mai, L. *J. Am. Chem. Soc.* **2017**, *139*, 8212-8221.

[74] Pachfule, P.; Shinde, D.; Majumder, M.; Xu, Q. *Nat. Chem.* **2016**, *8*, 718-724.

[75] Xia, W.; Mahmood, A.; Zou, R. Q.; Xu, Q. *Energy Environ. Sci.* **2015**, *8*, 1837-1866.

[76] Roldan Cuenya, B. *Acc. Chem. Res.* **2013**, *46*, 1682-1691.

[77] Li, Q.; Chen, W.; Xiao, H.; Gong, Y.; Li, Z.; Zheng, L.; Zheng, X.; Yan, W.; Cheong, W. C.; Shen, R.; Fu, N.; Gu, L.; Zhuang, Z.; Chen, C.; Wang, D.; Peng, Q.; Li, J.; Li, Y. *Adv. Mater.* **2018**, e1800588.

[78] Wang, Y.; Yuan, H.; Li, Y. F.; Chen, Z. F. *Nanoscale* **2015**, *7*, 11633-11641.

[79] Calle-Vallejo, F.; Martinez, J. I.; Rossmeisl, J. *Phys. Chem. Chem. Phys.* **2011**, *13*, 15639-15643.

[80] Lu, B. Z.; Smart, T. J.; Qin, D. D.; Lu, J. E.; Wang, N.; Chen, L. M.; Peng, Y.; Ping, Y.; Chen, S. W. *Chem. Mater.* **2017**, *29*, 5617-5628.

[81] Wang, X. X.; Cullen, D. A.; Pan, Y. T.; Hwang, S.; Wang, M.; Feng, Z.; Wang, J.; Engelhard, M. H.; Zhang, H.; He, Y.; Shao, Y.; Su, D.; More, K. L.; Spendelow, J. S.; Wu, G. *Adv. Mater.* **2018**, *30*, 1706758.

[82] Palaniselvam, T.; Kashyap, V.; Bhange, S. N.; Baek, J. B.; Kurungot, S. *Adv. Funct. Mater.* **2016**, *26*, 2150-2162.

[83] Han, Y.; Wang, Y. G.; Chen, W.; Xu, R.; Zheng, L.; Zhang, J.; Luo, J.; Shen, R. A.; Zhu, Y.; Cheong, W. C.; Chen, C.; Peng, Q.; Wang, D.; Li, Y. *J. Am. Chem. Soc.* **2017**, *139*, 17269-17272.

[84] Wang, J.; Huang, Z.; Liu, W.; Chang, C.; Tang, H.; Li, Z.; Chen, W.; Jia, C.; Yao, T.; Wei, S.; Wu, Y.; Li, Y. *J. Am. Chem. Soc.* **2017**, *139*, 17281-17284.

[85] Chen, W. X.; Pei, J. J.; He, C. T.; Wan, J. W.; Ren, H. L.; Zhu, Y. Q.; Wang, Y.; Dong, J. C.; Tian, S. B.; Cheong, W. C.; Lu, S. Q.; Zheng, L. R.; Zheng, X. S.; Yan, W. S.; Zhuang, Z. B.; Chen, C.; Peng, Q.; Wang, D. S.; Li, Y. D. *Angew. Chem. Int. Ed.* **2017**, *56*, 16086-16090.

[86] Liu, Q. T.; Liu, X. F.; Zheng, L. R.; Shui, J. L. *Angew. Chem. Int. Ed.* **2018**, *57*, 1204-1208.

[87] Zhao, C. M.; Dai, X. Y.; Yao, T.; Chen, W. X.; Wang, X. Q.; Wang, J.; Yang, J.; Wei, S. Q.; Wu, Y. E.; Li, Y. D. *J. Am. Chem. Soc.* **2017**, *139*, 8078-8081.

[88] Miner, E. M.; Fukushima, T.; Sheberla, D.; Sun, L.; Surendranath, Y.; Dinca, M. *Nat. Commun.* **2016**, *7*, 10942.

[89] Cote, A. P.; Benin, A. I.; Ockwig, N. W.; O'Keeffe, M.; Matzger, A. J.; Yaghi, O. M. *Science* **2005**, *310*, 1166-1170.

[90] Medina, D. D.; Rotter, J. M.; Hu, Y.; Dogru, M.; Werner, V.; Auras, F.; Markiewicz, J. T.; Knochel, P.; Bein, T. *J. Am. Chem. Soc.* **2015**, *137*, 1016-1019.

[91] Huang, N.; Wang, P.; Jiang, D. *Nat. Rev. Mater.* **2016**, *1*, 16068.

[92] Pachfule, P.; Acharjya, A.; Roeser, J.; Langenhahn, T.; Schwarze, M.; Schomacker, R.; Thomas, A.; Schmidt, J. *J. Am. Chem. Soc.* **2018**, *140*, 1423-1427.

[93] Xiang, Z.; Xue, Y.; Cao, D.; Huang, L.; Chen, J. F.; Dai, L. *Angew. Chem. Int. Ed.* **2014**, *53*, 2433-2437.

[94] Lin, C. Y.; Zhang, L.; Zhao, Z.; Xia, Z. *Adv. Mater.* **2017**, *29*, 1606635.

[95] Yi, J. D.; Xu, R.; Wu, Q.; Zhang, T.; Zang, K. T.; Luo, J.; Liang, Y. L.; Huang, Y. B.; Cao, R. *ACS Energy Lett.* **2018**, *3*, 883-889.

[96] Li, B.-Q.; Zhang, S.-Y.; Wang, B.; Xia, Z.-J.; Tang, C.; Zhang, Q. *Energy Environ. Sci.* **2018**, *11*, 1723-1729.

[97] Jia, H. X.; Sun, Z. J.; Jiang, D. C.; Du, P. W. *Chem. Mater.* **2015**, *27*, 4586-4593.

[98] Zheng, Y.; Jiao, Y.; Zhu, Y. H.; Li, L. H.; Han, Y.; Chen, Y.; Du, A. J.; Jaroniec, M.; Qiao, S. Z. *Nat. Commun.* **2014**, *5*, 3783.

[99] El-Kaderi, H. M.; Hunt, J. R.; Mendoza-Cortes, J. L.; Cote, A. P.; Taylor, R. E.; O'Keeffe, M.; Yaghi, O. M. *Science* **2007**, *316*, 268-272.

[100] Dalapati, S.; Addicoat, M.; Jin, S. B.; Sakurai, T.; Gao, J.; Xu, H.; Irle, S.; Seki, S.; Jiang, D. L. *Nat. Commun.* **2015**, *6*, 7786.

[101] Ding, S. Y.; Wang, W. *Chem. Soc. Rev.* **2013**, *42*, 548-568.

[102] Pachfule, P.; Kandmabeth, S.; Mallick, A.; Banerjee, R. *Chem. Commun.* **2015**, *51*, 11717-11720.

[103] Kandambeth, S.; Venkatesh, V.; Shinde, D. B.; Kumari, S.; Halder, A.; Verma, S.; Banerjee, R. *Nat. Commun.* **2015**, *6*, 6786.

[104] Gole, B.; Stepanenko, V.; Rager, S.; Grune, M.; Medina, D. D.; Bein, T.; Wurthner, F.; Beuerle, F. *Angew. Chem. Int. Ed.* **2018**, *57*, 846-850.

[105] Zhao, S. L.; Wang, Y.; Dong, J. C.; He, C. T.; Yin, H. J.; An, P. F.; Zhao, K.; Zhang, X. F.; Gao, C.; Zhang, L. J.; Lv, J. W.; Wang, J. X.; Zhang, J. Q.; Khattak, A. M.; Khan, N. A.; Wei, Z. X.; Zhang, J.; Liu, S. Q.; Zhao, H. J.; Tang, Z. Y. *Nat. Energy* **2016**, *1*, 1-10.

[106] Wang, L.; Wu, Y. Z.; Cao, R.; Ren, L. T.; Chen, M. X.; Feng, X.; Zhou, J. W.; Wang, B. *ACS Appl. Mater. Interfaces* **2016**, *8*, 16736-16743.

[107] Li, F. L.; Shao, Q.; Huang, X. Q.; Lang, J. P. *Angew. Chem. Int. Ed.* **2018**, *57*, 1888-1892.

[108] Johnson, B. A.; Bhunia, A.; Ott, S. *Dalton. T.* **2017**, *46*, 1382-1388.

[109] Hod, I.; Deria, P.; Bury, W.; Mondloch, J. E.; Kung, C. W.; So, M.; Sampson, M. D.; Peters, A. W.; Kubiak, C. P.; Farha, O. K.; Hupp, J. T. *Nat. Commun.* **2015**, *6*, 8304.

[110] Zhao, L.; Dong, B.; Li, S.; Zhou, L.; Lai, L.; Wang, Z.; Zhao, S.; Han, M.; Gao, K.; Lu, M.; Xie, X.; Chen, B.; Liu, Z.; Wang, X.; Zhang, H.; Li, H.; Liu, J.; Zhang, H.; Huang, X.; Huang, W. *ACS Nano* **2017**, *11*, 5800-5807.

[111] Dong, R. H.; Zheng, Z. K.; Tranca, D. C.; Zhang, J.; Chandrasekhar, N.; Liu, S. H.; Zhuang, X. D.; Seifert, G.; Feng, X. L. *Chem. Eur. J.* **2017**, *23*, 2255-2260.

[112] Hinnemann, B.; Moses, P. G.; Bonde, J.; Jorgensen, K. P.; Nielsen, J. H.; Horch, S.; Chorkendorff, I.; Norskov, J. K. *J. Am. Chem. Soc.* **2005**, *127*, 5308-5309.

[113] Mahmood, N.; Yao, Y. D.; Zhang, J. W.; Pan, L.; Zhang, X. W.; Zou, J. J. *Adv. Sci.* **2018**, *5*, 1700464.

[114] Trasatti, S. *J. Electroanal. Chem.* **1972**, *39*, 163-184.

[115] Xia, C.; Liang, H. F.; Zhu, J. J.; Schwingenschlogl, U.; Alshareef, H. N. *Adv. Energy Mater.* **2017**, *7*, 1602089.

[116] Zhou, W. J.; Lu, J.; Zhou, K.; Yang, L. J.; Ke, Y. T.; Tang, Z. H.; Chen, S. W. *Nano Energy* **2016**, *28*, 143-150.

[117] He, C. Y.; Tao, J. Z. *Chem. Commun.* **2015**, *51*, 8323-8325.

[118] Chen, W. F.; Wang, C. H.; Sasaki, K.; Marinkovic, N.; Xu, W.; Muckerman, J. T.; Zhu, Y.; Adzic, R. R. *Energy Environ. Sci.* **2013**, *6*, 943-951.

[119] Zhu, X. H.; Liu, M. J.; Liu, Y.; Chen, R. W.; Nie, Z.; Li, J. H.; Yao, S. Z. *J. Mater. Chem. A* **2016**, *4*, 8974-8977.

[120] Li, F.; Li, J.; Cao, Z.; Lin, X. Q.; Li, X. Z.; Fang, Y. Y.; An, X. C.; Fu, Y.; Jin, J.; Li, R. *J. Mater. Chem. A* **2015**, *3*, 21772-21778.

[121] Chung, D. Y.; Jun, S. W.; Yoon, G.; Kim, H.; Yoo, J. M.; Lee, K. S.; Kim, T.; Shin, H.; Sinha, A. K.; Kwon, S. G.; Kang, K.; Hyeon, T.; Sung, Y. E. *J. Am. Chem. Soc.* **2017**, *139*, 6669-6674.

[122] Liang, H. W.; Bruller, S.; Dong, R. H.; Zhang, J.; Feng, X. L.; Mullen, K. *Nat. Commun.* **2015**, *6*, 7992.

[123] Li, M.; Xiong, Y. P.; Liu, X. T.; Bo, X. J.; Zhang, Y. F.; Han, C.; Guo, L. P. *Nanoscale* **2015**, *7*, 8920-8930.

[124] Subbaraman, R.; Tripkovic, D.; Chang, K. C.; Strmcnik, D.; Paulikas, A. P.; Hirunsit, P.; Chan, M.; Greeley, J.; Stamenkovic, V.; Markovic, N. M. *Nat. Mater.* **2012**, *11*, 550-557.

[125] Lu, Z. Y.; Wang, H. T.; Kong, D. S.; Yan, K.; Hsu, P. C.; Zheng, G. Y.; Yao, H. B.; Liang, Z.; Sun, X. M.; Cui, Y. *Nat. Commun.* **2014**, *5*, 4345.

[126] Song, F.; Hu, X. L. *Nat. Commun.* **2014**, *5*, 4477.

[127] Wang, J.; Ge, X.; Liu, Z.; Thia, L.; Yan, Y.; Xiao, W.; Wang, X. *J. Am. Chem. Soc.* **2017**, *139*, 1878-1884.

[128] Jia, Y.; Zhang, L. Z.; Gao, G. P.; Chen, H.; Wang, B.; Zhou, J. Z.; Soo, M. T.; Hong, M.; Yan, X. C.; Qian, G. R.; Zou, J.; Du, A. J.; Yao, X. D. *Adv. Mater.* **2017**, *29*, 1700017.

[129] Wu, L. H.; Li, Q.; Wu, C. H.; Zhu, H. Y.; Mendoza-Garcia, A.; Shen, B.; Guo, J. H.; Sun, S. H. *J. Am. Chem. Soc.* **2015**, *137*, 7071-7074.

[130] Xia, B. Y.; Yan, Y.; Li, N.; Wu, H. B.; Lou, X. W.; Wang, X. *Nat. Energy* **2016**, *1*, 15006.

[131] Man, I. C.; Su, H. Y.; Calle-Vallejo, F.; Hansen, H. A.; Martinez, J. I.; Inoglu, N. G.; Kitchin, J.; Jaramillo, T. F.; Norskov, J. K.; Rossmeisl, J. *ChemCatChem* **2011**, *3*, 1159-1165.

[132] Saveleva, V. A.; Wang, L.; Teschner, D.; Jones, T.; Gago, A. S.; Friedrich, K. A.; Zafeiratos, S.; Schlogl, R.; Savinova, E. R. *J. Phys. Chem. Lett.* **2018**, *9*, 3154-3160.

[133] Favaro, M.; Yang, J. H.; Nappini, S.; Magnano, E.; Toma, F. M.; Crumlin, E. J.; Yano, J.; Sharp, I. D. *J. Am. Chem. Soc.* **2017**, *139*, 8960-8970.

[134] Zhou, J.; Wang, Y.; Su, X. Z.; Gu, S. Q.; Liu, R. D.; Huang, Y. B.; Yan, S.; Li, J.; Zhang, S. *Energy Environ. Sci.* **2019**, *12*, 739-746.

[135] Mao, S.; Wen, Z. H.; Huang, T. Z.; Hou, Y.; Chen, J. H. *Energy Environ. Sci.* **2014**, *7*, 609-616.

[136] Wei, J.; Liang, Y.; Hu, Y. X.; Kong, B.; Zhang, J.; Gu, Q. F.; Tong, Y. P.; Wang, X. B.; Jiang, S. P.; Wang, H. T. *Angew. Chem. Int. Ed.* **2016**, *55*, 12470-12474.

[137] Zhang, J. T.; Qu, L. T.; Shi, G. Q.; Liu, J. Y.; Chen, J. F.; Dai, L. M. *Angew. Chem. Int. Ed.* **2016**, *55*, 2230-2234.

[138] Wang, D. W.; Su, D. S. *Energy Environ. Sci.* **2014**, *7*, 576-591.

[139] Norskov, J. K.; Rossmeisl, J.; Logadottir, A.; Lindqvist, L.; Kitchin, J. R.; Bligaard, T.; Jonsson, H. *J. Phys. Chem. B* **2004**, *108*, 17886-17892.

[140] Stephens, I. E. L.; Bondarenko, A. S.; Gronbjerg, U.; Rossmeisl, J.; Chorkendorff, I. *Energy Environ. Sci.* **2012**, *5*, 6744-6762.

[141] Stamenkovic, V.; Mun, B. S.; Mayrhofer, K. J. J.; Ross, P. N.; Markovic, N. M.; Rossmeisl, J.; Greeley, J.; Norskov, J. K. *Angew. Chem. Int. Ed.* **2006**, *45*, 2897-2901.

[142] Stamenkovic, V. R.; Mun, B. S.; Arenz, M.; Mayrhofer, K. J. J.; Lucas, C. A.; Wang, G. F.; Ross, P. N.; Markovic, N. M. *Nat. Mater.* **2007**, *6*, 241-247.

[143] Meng, Y.; Gu, D.; Zhang, F. Q.; Shi, Y. F.; Yang, H. F.; Li, Z.; Yu, C. Z.; Tu, B.; Zhao, D. Y. *Angew. Chem. Int. Ed.* **2005**, *44*, 7053-7059.

[144] Karak, S.; Kandambeth, S.; Biswal, B. P.; Sasmal, H. S.; Kumar, S.; Pachfule, P.; Banerjee, R. *J. Am. Chem. Soc.* **2017**, *139*, 1856-1862.

[145] Kui Shen; Lei Zhang; Xiaodong Chen; Lingmei Liu; Daliang Zhang; Yu Han; Junying Chen; Jilan Long; Rafael Luque; Yingwei Li; Chen, B. *Science* **2018**, *359*, 206-210.

8 Publication Reprints

8.1 Ionic Liquid-Assisted Synthesis of Mesoporous Carbons with Surface-Enriched Nitrogen for the Hydrogen Evolution Reaction

Published version

X. J. Zhao, S. Li, H. F. Cheng, J. Schmidt, A. Thomas, Ionic Liquid-Assisted Synthesis of Mesoporous Carbons with Surface-Enriched Nitrogen for the Hydrogen Evolution Reaction, *ACS Appl. Mater. Interfaces* **2018**, 10, 3912-3920.

https://pubs.acs.org/doi/abs/10.1021/acsami.7b14919

Ionic Liquid-Assisted Synthesis of Mesoporous Carbons with Surface-Enriched Nitrogen for the Hydrogen Evolution Reaction

Xiaojia Zhao, Shuang Li,[ORCID] Hefeng Cheng, Johannes Schmidt, and Arne Thomas*[ORCID]

Department of Chemistry, Division of Functional Materials, Technical University Berlin, Hardenbergstraße 40, 10623 Berlin, Germany

S Supporting Information

ABSTRACT: Heteroatom-doped carbon materials are promising metal-free catalysts for the hydrogen evolution reaction (HER) at low voltage with high durability. However, many of the active sites introduced by heteroatom doping are hardly accessible within the bulk carbon structure and consequently contribute little to the catalytic activity. Here we report a facile ionic liquid-assisted method for synthesizing mesoporous nitrogen-doped carbons, enabling enrichment of nitrogen atoms at the pore surface, demonstrated by X-ray photoelectron spectroscopy (XPS) and temperature-programmed desorption of carbon dioxide (CO_2-TPD). The resulting metal-free nitrogen-doped mesoporous carbons exhibit a remarkable electrocatalytic activity in HER. The accessible and efficient utilization of nitrogen atoms is responsible for the superior HER catalytic activity.

KEYWORDS: self-assembly, surface-enriched, nitrogen-doped carbon, nonmetal electrocatalyst, hydrogen evolution reaction
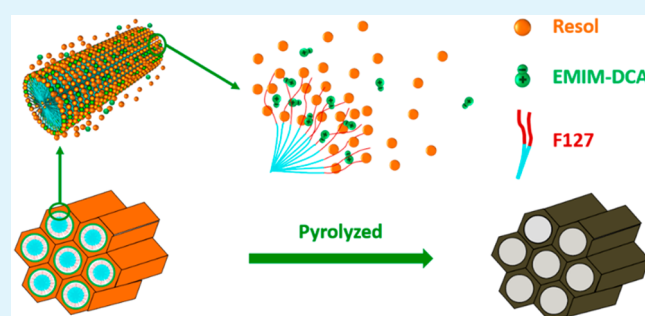
1. INTRODUCTION

Electrochemical water splitting has attracted substantial interest in recent years. In this regard, the development of effective hydrogen evolution reaction (HER) electrocatalysts with low overpotential and high stability is crucial for the successful implementation of water splitting technologies.[1−3] Currently, platinum-based catalysts are the most efficient HER catalysts, while the high price and earth scarcity of platinum hinder its large-scale practical application. Consequently, much effort has been devoted to develop low-cost catalysts by employing a wide variety of transition metals (e.g., Fe, Co, Ni, Mo) as derivatives for platinum catalysts.[4−10] However, due to the inherent corrosion and oxidation susceptibility, these transition-metal-based catalysts often suffer from poor stability in acidic electrolysis. On the other hand, metal-free heteroatom-doped carbon materials, which combine low cost and long durability and are composed of earth-abundant elements, are highly promising for energy-related electrocatalytic reactions.[1,11−18] Generally, the incorporation of heteroatoms (N, P, B, and S) in the carbonaceous skeleton can effectively tailor the electronic structure and electrochemical properties of the surrounding carbon atoms.[12,17,19] In particular, nitrogen-doped mesoporous carbons (NMCs) can efficiently reduce the Gibbs free energy of hydrogen adsorption by inducing the charge delocalization of the carbon atoms and consequently improve HER activity.[11,20,21]

To achieve high efficiency in heterogeneous catalysis, it is of paramount importance to expose the active sites at the surfaces of catalysts. However, the active sites formed from nitrogen atoms are generally distributed uniformly over the entire volume of the NMCs, and thus, large fractions are hardly accessible to reactants and thus contribute scarcely to the corresponding catalytic property. To obtain more accessible active sites, recent research has mainly focused on two strategies: increasing the nitrogen content by using different nitrogen-rich precursors or increasing the surface area of carbon materials to expose more active sites.[18,22−25] NMCs with an ordered pore structure are currently mainly prepared by a nanocasting approach using nitrogen-rich precursors.[25,26] Also, nitrogen-rich molecules or polymers have been added during synthesis of soft-templated carbons to obtain nitrogen-rich materials.[22,27−32] Dicyanamide-based ionic liquids (ILs) are interesting precursors for the synthesis of NMCs, yielding high nitrogen content and carbon yields. Furthermore, the resulting N-doped carbons show high electrical conductivity even at relatively low calcination temperatures. Moreover, as liquids at room temperature with negligible vapor pressure, dicyanamide-based ILs are highly suitable N-doped carbon precursors enabling facile processing, shaping, and the formation of composites.[23,25,33,34] However, the main drawback of this approach is the high price of ILs, especially when compared to other typical carbon precursors. In recent years, our group has therefore developed methods to coat low-priced carbon materials with thin layers of nitrogen-doped carbons prepared

ACS Applied Materials & Interfaces   Research Article

Scheme 1. Schematic Illustration of the Ionic Liquid-Assisted Co-Assembly Process for the Synthesis of Mesoporous Carbon with Surface-Enriched Nitrogen
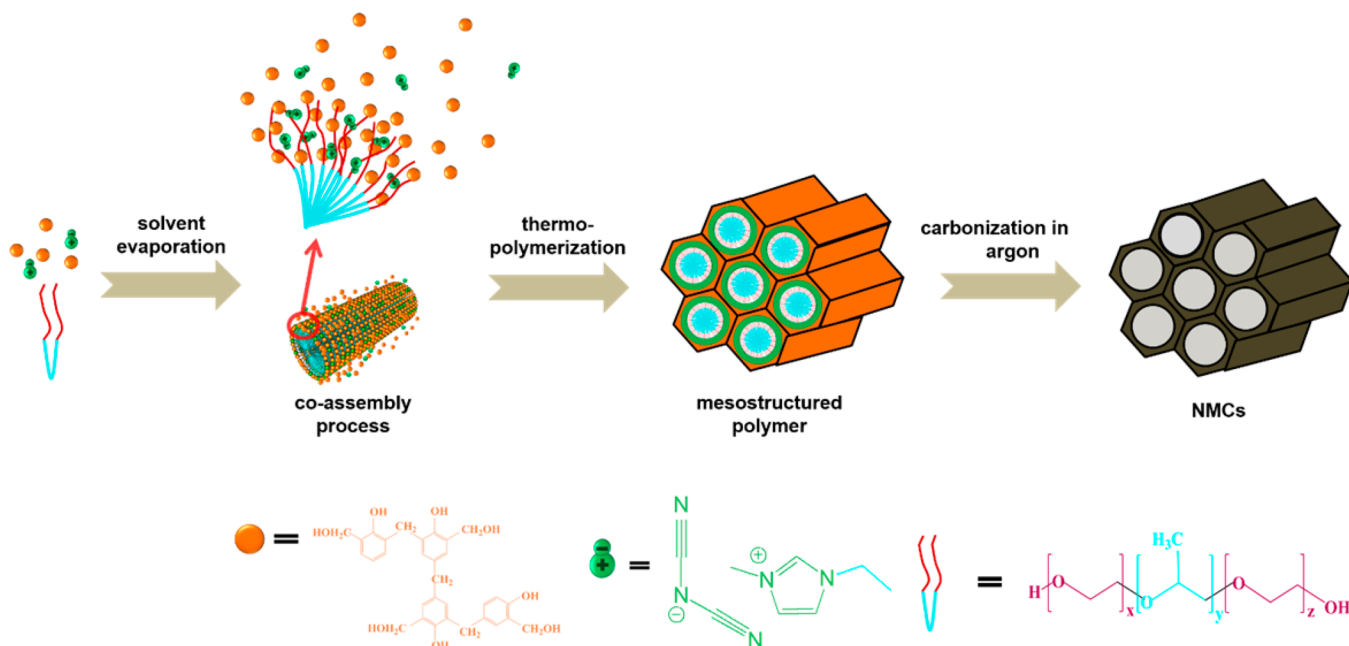
from more valuable dicyanamide-based ILs.[33] For this, preceding nanostructured carbon materials are dipped into the IL and heated again to enable the formation of NMC thin layers.

In this work, we report a facile ionic liquid-assisted method for synthesizing nitrogen-doped mesoporous carbon electro-catalysts, in which the ILs are added directly during nanostructured carbon synthesis. Moreover, it is observed that this method yields enrichment of nitrogen atoms at the pore surface. This is achieved by using a combination of two carbon precursors, resol for forming the bulk mesoporous carbon structure and 1-ethyl-3-methylimidazolium dicyanamide (EMIM-DCA) for nitrogen doping. NMCs from these precursors are prepared via evaporation-induced self-assembly (EISA) using triblock copolymer poly(ethylene oxide)-*b*-poly(propylene oxide)-*b*-poly(ethylene oxide) (PEO-PPO-PEO, Pluronic F127) as template. When using EISA for the generation of mesoporous carbon materials, such as FDU-15,[35] resol molecules are used, as their multiple phenolic hydroxyl groups can associate with the F127 template through hydrogen bonding and further co-assemble into the mesostructure. The IL was added to this mixture in different resol/IL ratios, and the influence on nitrogen doping, mesostructure, and catalytic activity was investigated (Scheme 1). It should be noted that ILs have interesting solubility properties, and the polarity of imidazolium ILs can be, for example, strongly influenced by the R-groups on the imidazolium moiety as well as the choice of the counterions. For example, EMIM-DCA is miscible in water and ethanol but also in less polar solvents like acetone and acetonitrile. During synthesis, the IL might be therefore preferentially located within the forming resol phase or in the micellar core or corona/resol interphase region. After carbon-ization, the two latter possibilities should be visible in an enrichment of nitrogen at the carbon pore surface. After thermopolymerization of the F127/EMIM-DCA/resol mixture at 100 °C, the obtained mesostructured polymer/EMIM-DCA composite was pyrolyzed at 800 °C in argon to enable

carbonization. It is assumed that resol will form a rigid carbon framework, comparable to that of the conventional FDU-15 synthesis, while EMIM-DCA will decompose into nitrogen-doped carbons as recently reported.[25]

2. EXPERIMENTAL SECTION

2.1. Chemicals. All reagents in this work were of analytical grade and were obtained from commercial source. EMIM-DCA was obtained from Ionic Liquid Technologies (>98%) and used without further treatment. Pluronic F127 was acquired from Sigma-Aldrich. The resol precursor was synthesized from phenol (detached crystals, 99+%) and formaldehyde (37% w/w aq. soln., stab. with 7−8% methanol). The monomers were acquired from Alfa Aesar.

2.2. Methods. Synthesis of mesoporous carbons with surface-enriched nitrogen: the resol precursor was synthesized according to the reported procedure.[35] The NMC electrocatalysts were prepared using the EISA process. F127 (1.0 g) was dissolved in ethanol (20.0 g), and then, the resol ethanol solution (20 wt %, 9.0 g) was added and stirred for 10 min at 500 rpm, followed by adding EMIM-DCA (0.36−0.90 g) dropwise and stirring for 10 min at 500 rpm to form a homogeneous solution with a mass ratio of resol to F127 of 1.8:1.0. The solution was poured into a Petri dish to evaporate the ethanol at room temperature for 8 h. The obtained film was transferred to an oven at 100 °C for 24 h for thermopolymerization, and then, the product was scratched off and calcined in an Ar oven at 350 °C for 2 h and then 800 °C for 5 h with a ramp rate of 1 °C min^{-1}. The samples were denoted as NMC-*x*, where *x* is the mass fraction of EMIM-DCA to resol.

For comparison, NMC-KIT-6-0.4 was prepared by using the same amount of EMIM-DCA as in NMC-0.4 while taking KIT-6 as a hard template to produce the mesoporous structure. KIT-6 was synthesized according to reported procedures.[36] KIT-6 (0.9 g) was dispersed in 12.0 g of ethanol, and then, resol (20 wt %, 9.0 g) and EMIM-DCA (0.72 g) were added and stirred at room temperature for 1 h. The obtained solution was transferred to a rotary evaporator to evaporate the ethanol at 40 °C for 40 min. Then, the composite was heated in an Ar oven at 350 °C for 2 h and then 800 °C for 5 h with a ramp rate of 1 °C min^{-1}. The as-made NMC-KIT-6-0.4 was treated with aqueous sodium hydroxide (2.0 M) to remove silica, followed by washing with deionized water and drying in vacuum at 80 °C.
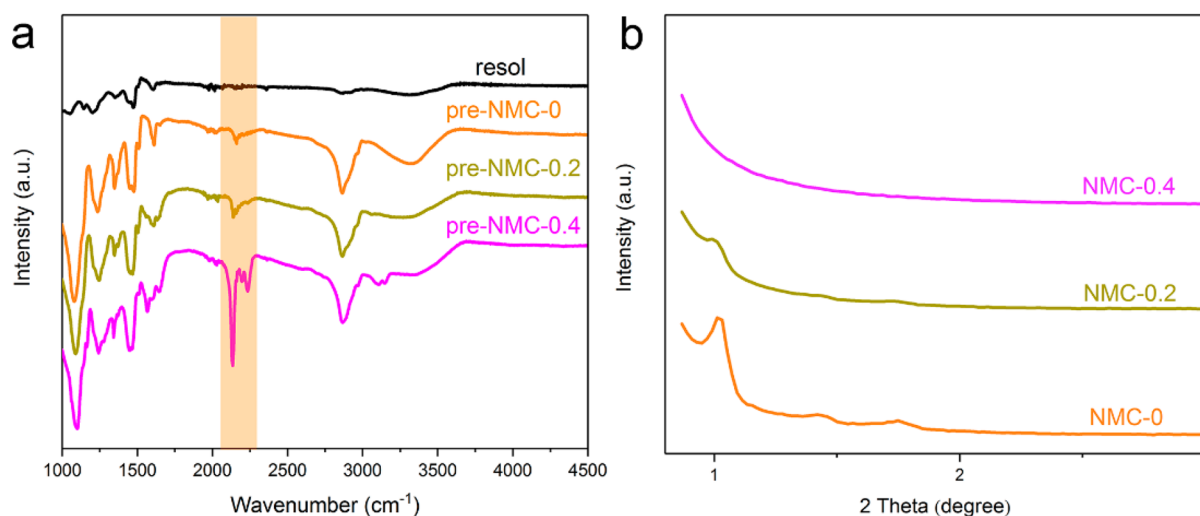
Figure 1. (a) FT-IR spectra of pure resol and mesostructure polymers (pre-NMC-0, 0.2, and 0.4); (b) SAXS spectra of the NMC-0, NMC-0.2, and NMC-0.4.

2.3. Characterization. Fourier transform infrared (FT-IR) spectra were carried out on a Varian 1000 FTIR spectrometer using an ATR technique. Thermogravimetric analysis (TGA) experiments were performed on a Netzsch TG209-F1 apparatus at a heating rate of 10 K min^{-1}. XRD analysis was performed on a Bruker D8 Advance instrument using Cu Kα radiation (k = 1.54 Å). Scanning electron microscope (SEM) images were obtained from a Hitachi S-2700 microscope. Transmission electron microscopy (TEM) images were obtained from a FEI Tecnai G2 20 STWIN microscope at an operating voltage of 200 kV. Nitrogen sorption measurements were carried out on a Quantachrome Quadrasorb SI porosimeter, and all samples were degassed at 150 °C for 12 h before measurement. The surface area was calculated by using Brunauer−Emmett−Teller (BET) calculations, and the pore-sized distribution plot was obtained from the adsorption branch of the isotherms based on the NLDFT method. X-ray photoelectron spectroscopy (XPS) was performed on a Thermo Fisher Scientific ESCALAB 250Xi. The size of the X-ray spot on the sample is 100 μm. Elemental analysis (EA) was measured on a Thermo Flash EA 1112 Organic Elemental Analyzer as dynamic flash combustion analysis.

Temperature-programmed desorption of carbon dioxide (CO_2-TPD) experiments were performed on a Micro-tracBEL BelCat II setup, coupled to a mobile Pfeiffer Vacuum QMG 220 mass spectrometer. Samples were placed in the quartz tube and outgassed at 500 °C for 2 h with a helium flow (30 mL min^{-1}). Then, the sample was cooled down to 50 °C in a flow of helium and treated with a CO_2 flow for 60 min. Subsequently, the sample was treated with a helium flow for 60 min to remove weakly adsorbed CO_2. The desorption of CO_2 was performed by heating the sample from 50 to 600 °C in helium flow at 10 °C min^{-1}. The number of basic sites was calculated from the CO_2 peaks (the molecular ion, m/z = 44).

2.4. Electrochemical Measurements. All electrochemical measurements were carried out in a three-electrode cell Gamry Reference 600 workstation (Gamry, U.S.A.) at room temperature. A rotating disk electrode (RDE) with a glassy carbon dish (5.0 mm diameter) served as the working electrode, and platinum wire and Ag/AgCl were used as counter and reference electrodes, respectively. In a typical preparation of catalyst ink, 10 mg of each catalyst was carefully ground and blended with 1.0 mL of Nafion ethanol solution (0.5 wt %) in an ultrasonic bath. Then, 20 μL of catalyst ink was pipetted onto the glassy carbon surface and dried in ambient environment, leading to a catalyst loading of 1.0 mg cm^{-2}. The measured HER polarization curves were carried out in an Ar-saturated H_2SO_4 electrolyte with a sweep rate of 2 mV s^{-1} at 1600 rpm. For comparison, the commercial 20 wt % Pt on Vulcan carbon black (Pt/C from Alfa) was measured for comparison. Electrochemical impedance spectroscopy (EIS) spectra were carried out in an Ar-saturated H_2SO_4 electrolyte from

10 kHz to 0.01 Hz with a 5 mV AC potential at 1600 rpm. All potentials in this study were referenced to those of the RHE.

3. RESULTS AND DISCUSSION

NMCs were synthesized via the EISA process using resol/F127 mixtures as previously reported, with additional EMIM-DCA (Figure S1).[35] To elucidate the influence of the IL, the mass ratio of resol to F127 was held constant at 1.8:1, and a series of samples was synthesized, changing the mass ratio of EMIM-DCA to resol from 0 to 0.5. The samples are denoted as pre-NMC-x and NMC-x for the samples before and after carbonization, respectively, where x is the mass ratio of EMIM-DCA to resol. After solvent evaporation, thermopolymerization at 100 °C yielded thin, homogeneous, and transparent films of pre-NMC-x, which changed their color from off-white to dark-red with increasing EMIM-DCA content. Homogeneity and transparency of the film prove that no macrophase separation occurs in the F127/resol/IL mixture. FT-IR spectroscopy shows the typical −C≡N stretch vibrations at ~2200 cm^{-1} for all pre-NMCs with EMIM-DCA addition, indicating the successful introduction of the EMIM-DCA precursor in the polymers (Figure 1a).[23] The negligible signal for pre-NMC-0 at ~2200 cm^{-1} is derived from F127 (Figure S2a). With increasing amount of EMIM-DCA, the intensity of this peak is obviously increased (Figures 1a and S2b). Furthermore, TGA shows an additional weight loss for the films with added EMIM-DCA in a temperature range corresponding to the first decomposition of EMIM-DCA. This weight loss is not observed for pre-NMC-0 (Figure S2c). As F127 shows a mass loss starting at a temperature of 350 °C, the polymer/EMIM-DCA composites were first heated to 350 °C for 2 h under inert atmosphere in order to decompose the F127 to create open and accessible mesopores and subsequently carbonized at 700, 800, or 900 °C, respectively, for 5 h to yield NMC-x as black flakes. From the literature and the TGA measurement of NMC-0, it can be assumed that the surfactant molecules are completely removed at this temperature to create open and accessible mesopores. Indeed, small-angle X-ray scattering (SAXS) for NMC-0 prepared without addition of EMIM-DCA reveals three well-resolved scattering peaks, which can be indexed as (110), (200), and (211) of the body-centered cubic space group (Figure 1b), consistent with the structure
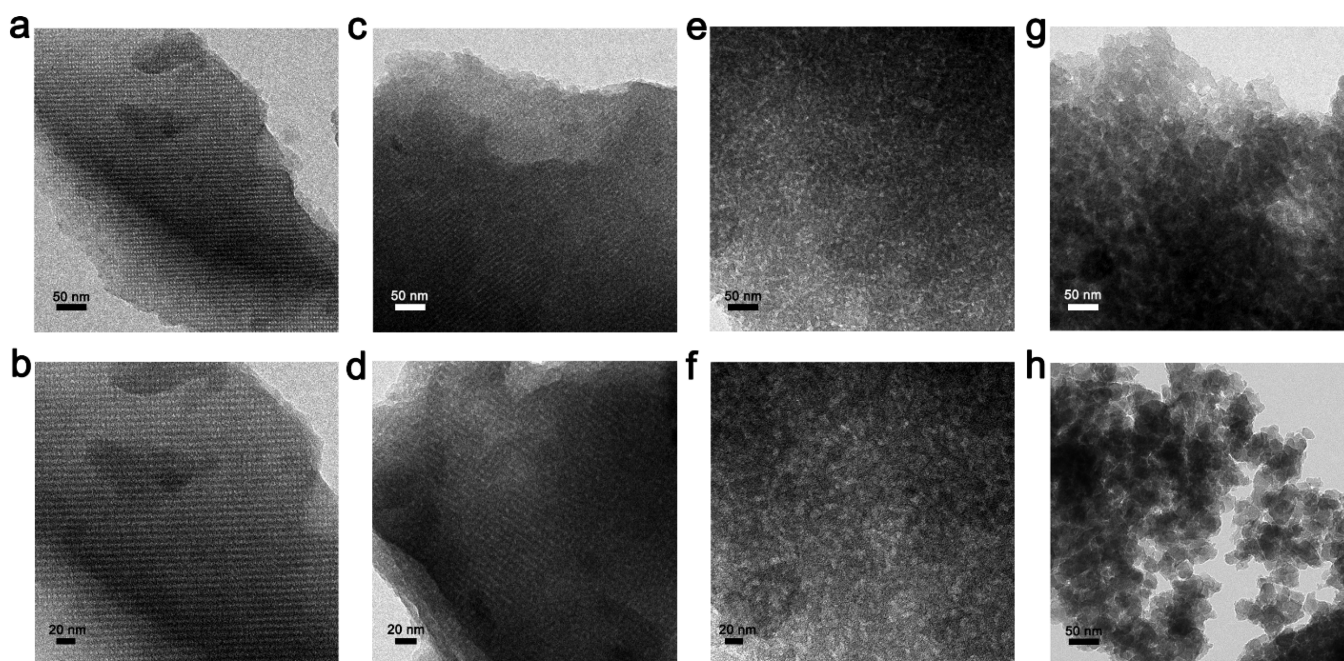
ACS Applied Materials & Interfaces   Research Article

Figure 2. TEM images of N-doped mesoporous carbon synthesized with different amounts of EMIM-DCA. (a,b) NMC-0; (c,d) NMC-0.2; (e,f) NMC-0.3; (g) NMC-0.4; (h) NMC-0.5.

reported for FDU-16 mesoporous carbons.[35,37] Adding smaller amounts of EMIM-DCA to the mixtures, e.g., as in NMC-0.2, clearly influences the mesostructure, as the peak intensity obviously decreased, while the scattering peaks are still observed at the same diffraction angles. Further increase in the EMIM-DCA content then yielded a total collapse of the ordered mesostructure as far as can be observed from XRD (Figures 1b and S2d). This suggests that a higher amount of EMIM-DCA can hamper the co-assembly process and subsequently hinder formation of an ordered mesostructure.

TEM images provide more information on the change of the mesostructures with increasing EMIM-DCA amount. As shown in Figure 2a,b, NMC-0 shows a highly ordered mesoporous structure over large domains with 3D cubic pore symmetry. Adding small amounts of EMIM-DCA yielded no significant change, and NMC-0.2 still shows an ordered mesostructure corresponding to the XRD results. However, also from TEM measurements, it seems that the high amount of order as observed for NMC-0 is partially lost (Figure 2c,d). Further EMIM-DCA addition still yielded a mesoporous but rather disordered pore structure, as seen for NMC-0.3 in Figure 2e,f. A clear transformation from small and ordered mesopores, to larger, unordered pores is observed. It can be expected that EMIM-DCA, which is preferentially located in the micellar core or corona/resol interphase region during the EISA process will affect micelle formation and aggregation, which is reflected in the change of the pore structure. A further increase in pore size is seen for NMC-0.4, i.e., with continued addition of EMIM-DCA, which could be beneficial as the more open and accessible mesopore structure seen could facilitate mass transport and thus promote electrocatalytic activity (Figure 2g). However, further addition of EMIM-DCA, that is for NMC-0.5 (Figure 2h), provoke a major structural transformation, and the porosity is already better described as interparticle voids created by aggregation of small carbon particles. SEM images further show the morphology changes for the NMC materials, starting from an increasing surface

roughness with lower EMIM-DCA addition (NMC-0.2 to NMC-0.4) to a more particulate structure for NMC-0.5 (Figure S3).

The porous characteristics are further investigated by nitrogen adsorption−desorption measurements. The isotherm of NMC-0 shows a small capillary condensation step in the relative pressure range of 0.4−0.6, i.e., a type IV isotherm with a small H2 hysteresis loop indicative for small cage-like mesopores (Figure 3a).[35] Similar to NMC-0, NMC-0.2 shows a typical H2 hysteresis loop for ordered mesostructures, which is however more pronounced as nitrogen uptake shifts slightly to higher relative pressures.

With increasing EMIM-DCA content, i.e., for NMC-0.3, 0.4, and 0.5, respectively, these hysteresis loops show an obvious change of shape that is consistent with the TEM results suggesting that the morphology of the mesostructures change from ordered to disordered. In addition, the shifts of the capillary condensation step to higher relative pressures shows that the pore size increases gradually, which is also seen in the NLDFT pore size distribution with an average pore diameter from 2.90 to 7.12 nm for NMC-0 to NMC-0.5 (Figure 3b and Table 1). The BET specific surface areas of all NMCs are in the range of 413−607 $m^2 g^{-1}$ (Table 1). While NMC-0 and NMC-0.2 show nearly identical surface areas, reflecting the similar mesostructures observed, higher EMIM-DCA content yields decreasing surface areas, which can be mainly attributed to the increased pore sizes and reduced micropore surface area (Table 1). The opposing trend for NMC-0.5 might be associated with the change of morphology from bulk porous to nanoparticulate. The pore volume of NMCs are increasing from 0.249 to 0.464 $cm^3 g^{-1}$, and also, the mesopore volume increases gradually from NMC-0 to NMC-0.4, again reflecting the increased pore size and open mesopore channel structures.

Based on the above observations, it is seen that addition of the EMIM-DCA affects the formation of mesostructures and, especially in higher concentrations, hampers the co-assembly process, yielding nonordered mesostructures. In previous
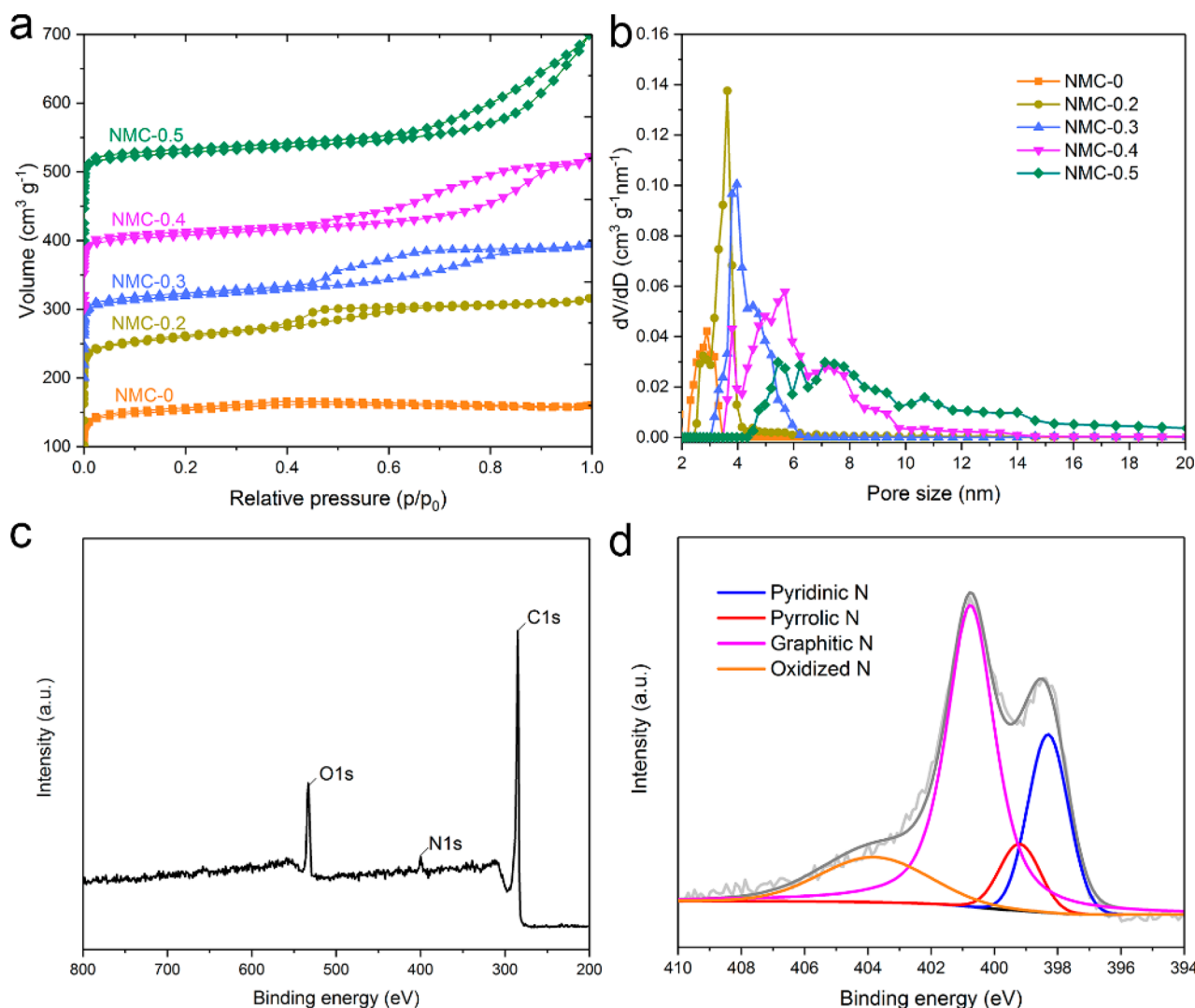
Research Article

Figure 3. (a) N_2 adsorption−desorption isotherms of the mesoporous carbon with surface-enriched nitrogen. The isotherms for NMC-0.2, NMC-0.3, NMC-0.4, and NMC-0.5 are offset vertically by 100 cm^3 g^{-1} STP for clarity; (b) the corresponding NLDFT pore size distributions; (c,d) survey spectra and N 1s core level XPS spectra of NMC-0.4.

Table 1. Structure and Textural Properties of the Mesoporous Carbon with Surface-Enriched Nitrogen Prepared by Ionic Liquid-Assisted EISA Process

sample	S_{BET},[a] m^2 g^{-1}	S_{mic},[b] m^2 g^{-1}	V_t,[c] cm^3 g^{-1}	V_{mic},[d] cm^3 g^{-1}	D_p,[e] nm
NMC-0	603.34	501.58	0.249	0.192	2.90
NMC-0.2	607.28	432.84	0.334	0.170	3.63
NMC-0.3	455.22	336.51	0.300	0.132	3.97
NMC-0.4	413.75	312.33	0.344	0.122	5.69
NMC-0.5	495.06	394.58	0.464	0.154	7.12

[a]BET specific surface areas calculated in p/p_0 from 0.003 to 0.05. [b]Micropore surface areas evaluated through the t-plot method. [c]Total pore volumes calculated based on the volume adsorbed at p/p_0 of ∼0.995. [d]Micropore volumes evaluated through the t-plot method. [e]Average pore size derived from the highest point of adsorption branches of the isotherms by using the NLDFT method.

works, the interaction between ionic liquids and PEO-PPO-PEO block copolymers was investigated, and the results demonstrated that the addition of ILs could alter the critical micellization size,[38−40] which corresponds to the observations about the change of pore size.

Elemental analysis was applied to measure the total bulk nitrogen content in NMCs. The nitrogen content increases significantly from 1.25 to 4.44 wt % for NMC-0.2 to NMC-0.5 (Table S2). The chemical environment of nitrogen in the near-surface region of the catalysts was further determined by using XPS. The entire set of survey spectra show strong signals from carbon, nitrogen, and oxygen in all NMC-x materials (Figures 3c and S4a). All N 1s core level spectra (Figures 3d and S4) exhibit four domain peaks which were assigned to pyridinic N (398.3−398.4 eV), pyrrolic N (399.4−399.6 eV), graphitic N (400.7−400.9 eV), and oxidized N (>403.5 eV).[17,33] As XPS is highly surface-sensitive, we also calculated the atomic N/C ratio of NMCs to compare with that determined by EA (Supplementary Note 1). As shown in Figure S5, the atomic N/C ratio determined by XPS is slightly higher than the one from EA for NMC-0.2 to NMC-0.4. The higher atomic N/C ratio by XPS gave a first indication that the nitrogen atoms are concentrated on the surfaces of the NMC catalysts.[18] Notably, for NMC-0.5, in which a significant change of morphology is observed, a lower atomic N/C ratio from XPS than from EA is observed, indicating that nitrogen atoms have preferentially penetrated into the carbon matrix.
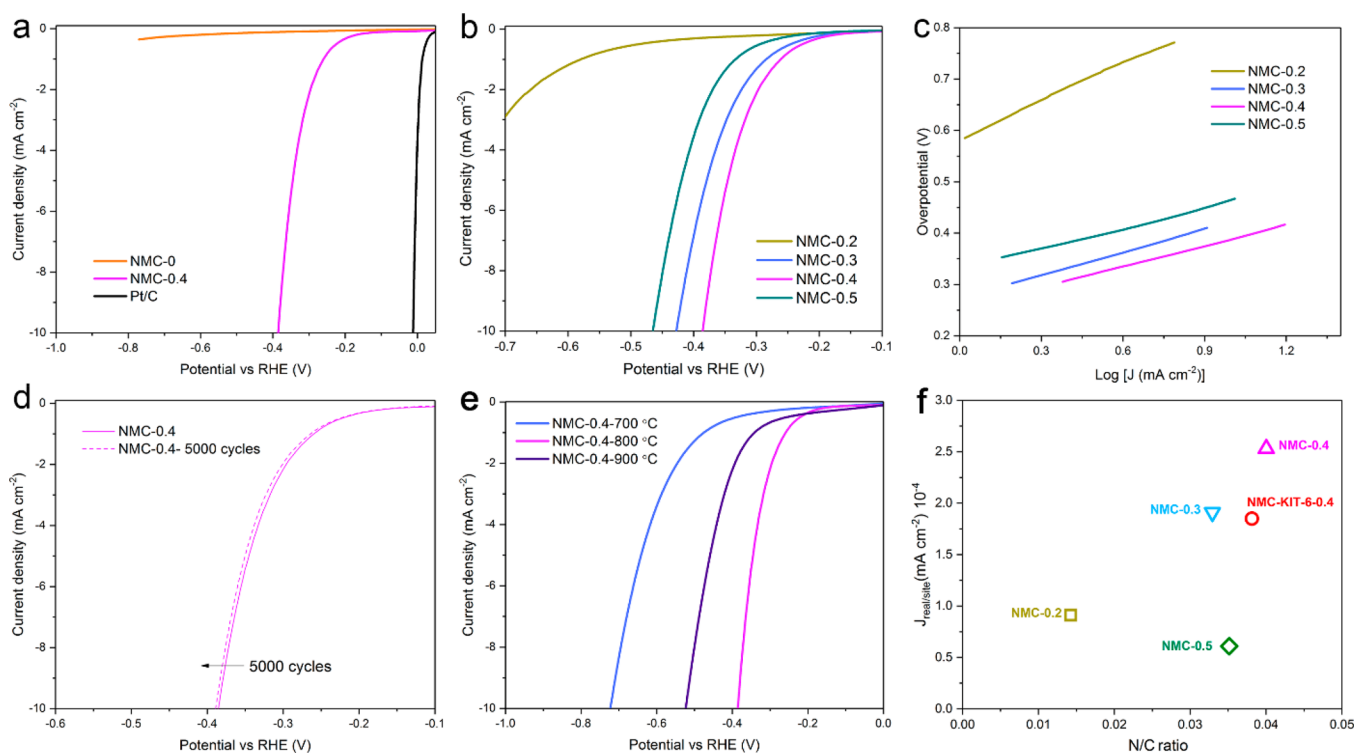
ACS Applied Materials & Interfaces   Research Article

Figure 4. (a) HER polymerization plots of NMC-0, NMC-0.4, and commercial Pt/C samples in 0.5 M H_2SO_4 solution; (b,c) HER polymerization and corresponding Tafel plots for NMCs with different amounts of EMIM-DCA; (d) initial and postpotential cyclic voltammograms of NMC-0.4 (5000 cycles); (e) HER polymerization plots of NMC-0.4 with different pyrolysis temperatures; (f) scatter plot of $j_{real/site}$ for NMC samples.

The electrocatalytic activities of the as-synthesized NMCs toward HER were evaluated using the RDE in an argon-saturated 0.5 M H_2SO_4 solution.[7,10] Figure 4a shows the polarization curves recorded for NMC-0.4 as compared to those measured for NMC-0 and commercial Pt/C. NMC-0 shows a negligible electrocatalytic activity, while the activity of NMC-0.4 is significantly enhanced by incorporating nitrogen atoms into the carbon framework, as reflected by the large shift of the polarization curve to a lower overpotential. To achieve a 10 mA cm^{-2} HER current density, NMC-0.4 only requires an overpotential of 384.7 mV, which is much lower than that for most single N-doped carbons even with a higher nitrogen content (Table S5). Figure 4b shows the HER activity of all NMC-x samples, which is mainly influenced by the nitrogen content; however, the mesostructure also seems to play an important role. NMC-0.2 shows a low electrocatalytic activity for HER. With increasing nitrogen content, the activity of the NMCs increases as well, until NMC-0.4 is reached, while, for NMC-0.5, a much lower activity is observed. This can be attributed to the structural changes observed for NMC-0.5, which is composed of aggregates of spherical carbon particles, which should strongly and unfavorably influence the conductivity of the material.[41,42]

Further insight into the HER pathway of NMCs can be derived from Tafel plots. As shown in Figure 4c, all samples show Tafel slopes in a range of 130 to 150 mV decade^{-1} (Table S3), suggesting that an initial proton adsorption (i.e., Volmer step: $H^+ + e^- \rightarrow H^*$) is the rate-determining step of the HER process.[43] To further estimate the intrinsic activity of the NMCs, the exchange current density (j_0) was calculated by extrapolating the Tafel plots to the x-axis (Table S3). NMC-0.4, possessing superior HER performance, has the higher j_0 due to more accessible nitrogen atoms at the pore surface. To meet

sustainable hydrogen production, the electrocatalyst should have strong tolerance to acidic solution. Therefore, an accelerated degradation study was carried out in 0.5 M H_2SO_4 to evaluate the stability of NMC-0.4.[44] After 5000 cyclic voltammetry (CV) cycles (Figure 4d), the overpotential required to achieve the current density of 10 mA cm^{-2} shows a negligible degradation, suggesting a potential application for these hybrid materials as efficient electrocatalysts for sustainable hydrogen production. The durability of NMC-0.4 is ascribed to the nonmetallic catalytic system and the superior rigid mesostructures of carbon material. The polarization curves of NMC-0.4 at different pyrolysis temperatures (700, 800, and 900 °C) are also evaluated (Figure 4e). NMC-0.4 at 800 °C shows much higher electrocatalytic activity than the ones carbonized at higher or lower temperatures. It should be noted that the as-made NMCs show the best activities after several hundred cycles of CV at an active reaction window (Figure S6a), and a graphite rod was used as the counter electrode instead of Pt nanowire to avoid the deposition of platinum during a long-term operation (Figure S6b).[45]

Based on the observed differences in HER activities of the samples, it can be assumed that the activity of the samples is derived from the nitrogen atoms that affect their H* adsorption abilities. The normalization process from exchange current density (j_0) to the activity per active sites ($j_{real/site}$) for all samples was achieved by following the method on the basis of real surface areas (Supplementary Note 2). Consequently, a scatter plot containing $j_{real/site}$ versus N/C ratio was established (Figure 4f), in which a much higher $j_{real/site}$ for NMC-0.4 indicates a much higher catalytic activity for active sites on the pore surface of NMC-0.4. It was described that heteroatoms can efficiently reduce the Gibbs free energy of hydrogen adsorption while the active sites are generally the carbons next
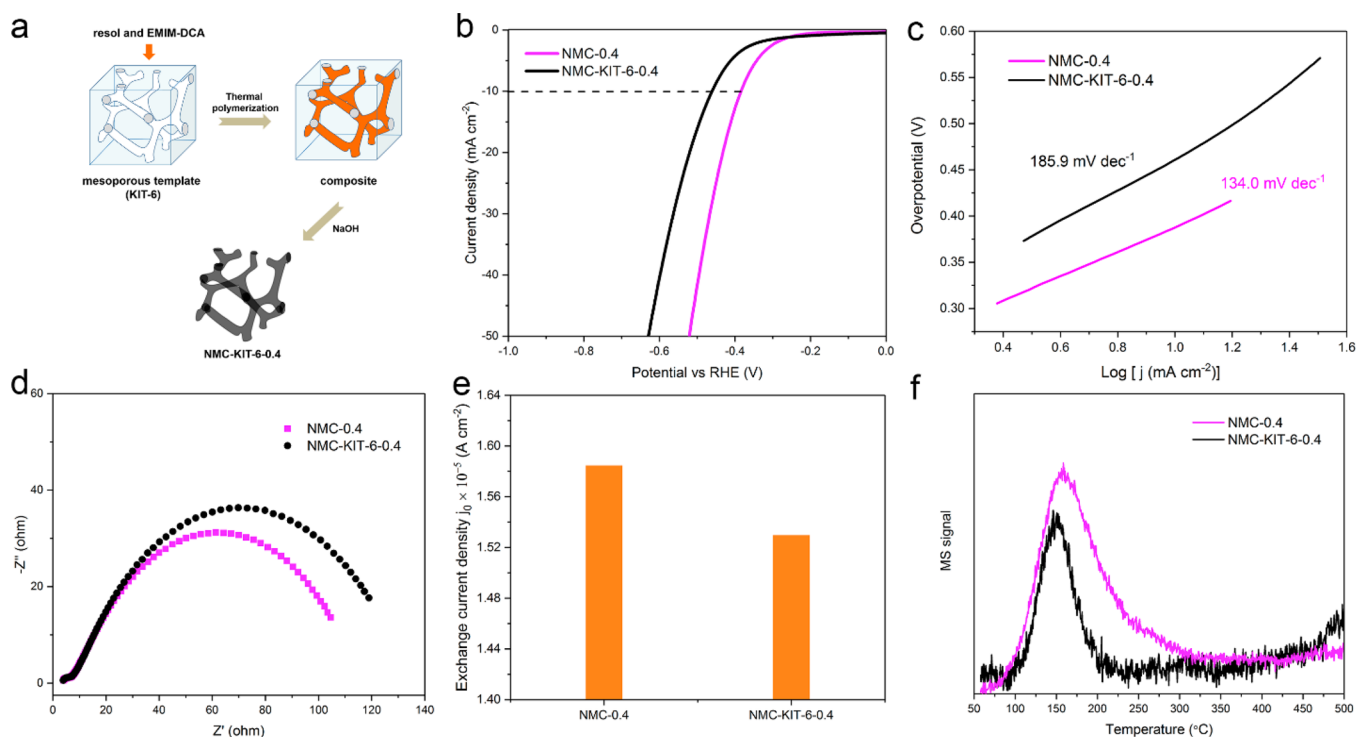
Figure 5. (a) Illustration of the hard-template (KIT-6) method to prepare NMC-KIT-6-0.4; (b,c) HER polymerization plots and corresponding Tafel plots of NMC-0.4 and contrastive NMC-KIT-6-0.4; (d) electrochemical impedance spectroscopy (EIS) analyses of NMC-0.4 and NMC-KIT-6-0.4; (e) exchange current density of NMC-0.4 and NMC-KIT-6-0.4; (f) CO_2-TPD of NMC-0.4 and contrastive NMC-KIT-6-0.4

to each dopant. Increasing the heteroatom, e.g., nitrogen content, in a certain range should therefore further improve the HER performance,[12,46] as it is seen for the surface enrichment of N atoms in NMC-0.4

As the assumed enrichment of nitrogen atoms on the pore surface is hard to prove with the available methods, a reference catalyst was prepared by hard templating of KIT-6 (Figure 5a). The same resol/EMIM-DCA mixture as for NMC-0.4 was applied; however, this time KIT-6 was used as the hard template instead of F127 as the soft template. We reasoned that as no surfactant is applied for the hard templating approach, EMIM-DCA should be uniformly dispersed within the resol matrix, which then is of course also true for the nitrogen atoms in the carbon matrix. NMC-KIT-6-0.4 possesses a comparable nitrogen content and surface area to those of NMC-0.4 (Tables S2 and S4). However, comparing the HER polarization curves (Figure 5b), it is seen that NMC-KIT-6-0.4, even though having a slightly higher surface area, still shows a lower HER activity than NMC-0.4. The $j_{\mathrm{real/site}}$ for the NMC-0.4 is also much higher than that of NMC-KIT-6-0.4 (Figure 4f). Tafel plot (Figure 5c) analysis further demonstrates the superior electrocatalytic activity of NMC-0.4. Figure 5d shows the electrochemical impedance spectra (EIS) of NMC-0.4 and NMC-KIT-6-0.4. The high-frequency semicircles in the Nyquist plots are ascribed to the charge transfer resistance (R_{ct}), where the lower R_{ct} value of NMC-0.4 suggests that the unique nanostructure with the nitrogen-rich surface can promote the electron transfer kinetics under HER operating conditions.[7,47] The enhanced electrochemical performance for NMC-0.4 was also observed by comparing the exchange current density (Figure 5e). This improvement in HER activity could indeed be explained by an enrichment, that is, better availability of nitrogen atoms at the pore surface of NMC-0.4.

This assumption is further verified by the slightly higher surface atomic N/C ratio from XPS than the bulk atomic N/C ratio from EA (Figure S7b),[18] which is exactly opposite to the result found for NMC-KIT-6-0.4. However, the most convincing proof for a higher accessibility of nitrogen atoms at the surface probably can be made by CO_2-TPD. Since CO_2 is a weak Lewis acid (electron acceptor) with an electropositive carbon atom, the amount of basic sites on the pore surface can be detected by CO_2-TPD.[48−50] As shown in Figure 5f, NMC-0.4 and NMC-KIT-6-0.4 both show a strong desorption of CO_2 at temperatures higher than 100 °C due to chemically adsorbed CO_2 on the surface of the materials. However, the intensity of CO_2 desorption of NMC-0.4 is much stronger than that of NMC-KIT-6-0.4, even though the latter has a higher surface area, which clearly shows that NMC-0.4 provides more Lewis basic sites at the surface. This result, combined with XPS as well as with TEM analyses, strongly confirmed that by introducing EMIM-DCA to the EISA process, the nitrogen atoms are distributed preferentially on the pore surface of the mesoporous carbons.

■ CONCLUSIONS

In summary, we report a facile ionic liquid-assisted method for synthesizing NMC electrocatalysts with enhanced exposure of nitrogen atoms at the pore surface. EMIM-DCA co-assembles with the F127 micelles, yielding first an increase of the pore sizes in the final carbons, while after further increase, the pore structure collapses. That EMIM-DCA is mainly located at the micelles and not within the resol matrix can be seen by an enrichment of nitrogen on the surface of the final carbon materials. The obtained NMCs with surface-enriched nitrogen exhibit a high activity and excellent stability as a nonmetal electrocatalyst for HER. The superior HER catalytic activity

ACS Applied Materials & Interfaces

was attributed to the accessible and efficient utilization of nitrogen atoms on the carbon surface and the open mesoporous channel structures. XPS and CO_2-TPD characterization confirmed the enrichment of nitrogen atoms at the pore surface of nitrogen-doped material. This concept is adaptable to design of mesoporous carbon doped with other heteroatoms (S, B, P) or co-doped by choosing appropriate ionic liquids. Moreover, metal-containing ionic liquids can be easily synthesized, and thus, excellent electrocatalysis on mesoporous carbon with surface-enriched transition metals are expected.

■ ASSOCIATED CONTENT

Ⓢ Supporting Information

The Supporting Information is available free of charge on the ACS Publications website at DOI: 10.1021/acsami.7b14919.

Normalization of j_0, atomic N/C ratio, thermogravimetric analysis (TGA), XPS, electrocatalysis data (PDF)

■ AUTHOR INFORMATION

Corresponding Author

*E-mail: arne.thomas@tu-berlin.de.

ORCID Ⓞ

Shuang Li: 0000-0001-7414-630X
Arne Thomas: 0000-0002-2130-4930

Author Contributions

The manuscript was written through contributions of all authors.

Notes

The authors declare no competing financial interest.

■ ACKNOWLEDGMENTS

■ ABBREVIATIONS

NMC, nitrogen-doped mesoporous carbon
XPS, X-ray photoelectron spectroscopy
CO_2-TPD, temperature-programmed desorption of carbon dioxide
HER, hydrogen evolution reaction
ILs, ionic liquids
EMIM-DCA, 1-ethyl-3-methylimidazolium dicyanamide
EISA, evaporation-induced self-assembly
Pluronic F127, poly(ethylene oxide)-*b*-poly(propylene oxide)-*b*-poly(ethylene oxide)
BET, Brunauer−Emmett−Teller
FT-IR, Fourier transform infrared
SAXS, small-angle X-ray scattering
TEM, transmission electron microscopy
RDE, rotating disk electrode
CV, cyclic voltammetry

■ REFERENCES

(1) Liu, J.; Liu, Y.; Liu, N. Y.; Han, Y. Z.; Zhang, X.; Huang, H.; Lifshitz, Y.; Lee, S. T.; Zhong, J.; Kang, Z. H. Metal-free efficient photocatalyst for stable visible water splitting via a two-electron pathway. *Science* **2015**, *347*, 970−974.

(2) Zou, X. X.; Zhang, Y. Noble metal-free hydrogen evolution catalysts for water splitting. *Chem. Soc. Rev.* **2015**, *44*, 5148−5180.

(3) Walter, M. G.; Warren, E. L.; McKone, J. R.; Boettcher, S. W.; Mi, Q. X.; Santori, E. A.; Lewis, N. S. Solar Water Splitting Cells. *Chem. Rev.* **2010**, *110*, 6446−6473.

(4) Li, J. S.; Wang, Y.; Liu, C. H.; Li, S. L.; Wang, Y. G.; Dong, L. Z.; Dai, Z. H.; Li, Y. F.; Lan, Y. Q. Coupled molybdenum carbide and reduced graphene oxide electrocatalysts for efficient hydrogen evolution. *Nat. Commun.* **2016**, *7*, 11204.

(5) Morozan, A.; Goellner, V.; Nedellec, Y.; Hannauer, J.; Jaouen, F. Effect of the Transition Metal on Metal-Nitrogen-Carbon Catalysts for the Hydrogen Evolution Reaction. *J. Electrochem. Soc.* **2015**, *162*, H719−H726.

(6) Wang, D. Y.; Gong, M.; Chou, H. L.; Pan, C. J.; Chen, H. A.; Wu, Y. P.; Lin, M. C.; Guan, M. Y.; Yang, J.; Chen, C. W.; Wang, Y. L.; Hwang, B. J.; Chen, C. C.; Dai, H. J. Highly Active and Stable Hy-brid Catalyst of Cobalt-Doped FeS2 Nanosheets-Carbon Nanotubes for Hydrogen Evolution Reaction. *J. Am. Chem. Soc.* **2015**, *137*, 1587−1592.

(7) Liang, H. W.; Bruller, S.; Dong, R. H.; Zhang, J.; Feng, X. L.; Mullen, K. Molecular metal-Nx centres in porous carbon for electrocatalytic hydrogen evolution. *Nat. Commun.* **2015**, *6*, 7992.

(8) Wang, S. P.; Wang, J.; Zhu, M. L.; Bao, X. B.; Xiao, B. Y.; Su, D. F.; Li, H. R.; Wang, Y. Molybdenum-Carbide-Modified Nitrogen-Doped Carbon Vesicle Encapsulating Nickel Nanoparticles: A Highly Efficient, Low-Cost Catalyst for Hydrogen Evolution Reaction. *J. Am. Chem. Soc.* **2015**, *137*, 15753−15759.

(9) Wu, H. B.; Xia, B. Y.; Yu, L.; Yu, X. Y.; Lou, X. W. Porous molybdenum carbide nano-octahedrons synthesized via confined carburization in metal-organic frameworks for efficient hydrogen production. *Nat. Commun.* **2015**, *6*, 6512.

(10) Bayatsarmadi, B.; Zheng, Y.; Tang, Y. H.; Jaroniec, M.; Qiao, S. Z. Significant Enhancement of Water Splitting Activity of N-Carbon Electrocatalyst by Trace Level Co Doping. *Small* **2016**, *12*, 3703−3711.

(11) Guo, D. H.; Shibuya, R.; Akiba, C.; Saji, S.; Kondo, T.; Nakamura, J. Active sites of nitrogen-doped carbon materials for oxygen reduction reaction clarified using model catalysts. *Science* **2016**, *351*, 361−365.

(12) Jiao, Y.; Zheng, Y.; Davey, K.; Qiao, S. Z. Activity origin and catalyst design principles for electrocatalytic hydrogen evolution on heteroatom-doped graphene. *Nat. Energy* **2016**, *1*, 16130.

(13) Ito, Y.; Cong, W. T.; Fujita, T.; Tang, Z.; Chen, M. W. High Catalytic Activity of Nitrogen and Sulfur Co-Doped Nanoporous Graphene in the Hydrogen Evolution Reaction. *Angew. Chem., Int. Ed.* **2015**, *54*, 2131−2136.

(14) Zheng, Y.; Jiao, Y.; Zhu, Y. H.; Li, L. H.; Han, Y.; Chen, Y.; Du, A. J.; Jaroniec, M.; Qiao, S. Z. Hydrogen evolution by a metal-free electrocatalyst. *Nat. Commun.* **2014**, *5*, 3783.

(15) Zhang, J. T.; Zhao, Z. H.; Xia, Z. H.; Dai, L. M. A metal-free bifunctional electrocatalyst for oxygen reduction and oxygen evolution reactions. *Nat. Nanotechnol.* **2015**, *10*, 444−452.

(16) Zhao, Y.; Nakamura, R.; Kamiya, K.; Nakanishi, S.; Hashimoto, K. Nitrogen-doped carbon nanomaterials as non-metal electrocatalysts for water oxidation. *Nat. Commun.* **2013**, *4*, 2390.

(17) Zheng, Y.; Jiao, Y.; Li, L. H.; Xing, T.; Chen, Y.; Jaroniec, M.; Qiao, S. Z. Toward Design of Synergistically Active Carbon-Based Catalysts for Electrocatalytic Hydrogen Evolution. *ACS Nano* **2014**, *8*, 5290−5296.

(18) Tian, G. L.; Zhang, Q.; Zhang, B. S.; Jin, Y. G.; Huang, J. Q.; Su, D. S.; Wei, F. Toward Full Exposure of "Active Sites": Nanocarbon Electrocatalyst with Surface Enriched Nitrogen for Superior Oxygen Reduction and Evolution Reactivity. *Adv. Funct. Mater.* **2014**, *24*, 5956−5961.

(19) Zhang, J. T.; Dai, L. M. Nitrogen, Phosphorus, and Fluorine Tri-doped Graphene as a Multifunctional Catalyst for Self-Powered

ACS Applied Materials & Interfaces   Research Article

Electrochemical Water Splitting. *Angew. Chem., Int. Ed.* **2016**, *55*, 13296−13300.

(20) Kim, D. P.; Lin, C. L.; Mihalisin, T.; Heiney, P.; Labes, M. M. Electronic-Properties of Nitrogen-Doped Graphite Flakes. *Chem. Mater.* **1991**, *3*, 686−692.

(21) Czerw, R.; Terrones, M.; Charlier, J. C.; Blase, X.; Foley, B.; Kamalakaran, R.; Grobert, N.; Terrones, H.; Tekleab, D.; Ajayan, P. M.; Blau, W.; Ruhle, M.; Carroll, D. L. Identification of electron donor states in N-doped carbon nanotubes. *Nano Lett.* **2001**, *1*, 457−460.

(22) Wei, J.; Zhou, D. D.; Sun, Z. K.; Deng, Y. H.; Xia, Y. Y.; Zhao, D. Y. A Controllable Synthesis of Rich Nitrogen-Doped Ordered Mesoporous Carbon for CO2 Capture and Supercapacitors. *Adv. Funct. Mater.* **2013**, *23*, 2322−2328.

(23) Paraknowitsch, J. P.; Thomas, A.; Antonietti, M. A detailed view on the polycondensation of ionic liquid monomers towards nitrogen doped carbon materials. *J. Mater. Chem.* **2010**, *20*, 6746−6758.

(24) Yang, W.; Fellinger, T. P.; Antonietti, M. Efficient Metal-Free Oxygen Reduction in Alkaline Medium on High-Surface-Area Mesoporous Nitrogen-Doped Carbons Made from Ionic Liquids and Nucleobases. *J. Am. Chem. Soc.* **2011**, *133*, 206−209.

(25) Paraknowitsch, J. P.; Zhang, J.; Su, D. S.; Thomas, A.; Antonietti, M. Ionic Liquids as Precursors for Nitrogen-Doped Graphitic Car-bon. *Adv. Mater.* **2010**, *22*, 87−92.

(26) Mane, G. P.; Talapaneni, S. N.; Anand, C.; Varghese, S.; Iwai, H.; Ji, Q. M.; Ariga, K.; Mori, T.; Vinu, A. Preparation of Highly Ordered Nitrogen-Containing Mesoporous Carbon from a Gelatin Biomolecule and its Excellent Sensing of Acetic Acid. *Adv. Funct. Mater.* **2012**, *22*, 3596−3604.

(27) Song, Y.; Li, L.; Wang, Y.; Wang, C.; Guo, Z.; Xia, Y. Nitrogen-doped ordered mesoporous carbon with a high surface area, synthesized through organic-inorganic coassembly, and its application in supercapacitors. *ChemPhysChem* **2014**, *15*, 2084−2093.

(28) Li, M.; Xue, J. Integrated Synthesis of Nitrogen-Doped Mesoporous Carbon from Melamine Resins with Superior Performance in Supercapacitors. *J. Phys. Chem. C* **2014**, *118*, 2507−2517.

(29) Kailasam, K.; Jun, Y.-S.; Katekomol, P.; Epping, J. D.; Hong, W. H.; Thomas, A. Mesoporous Melamine Resins by Soft Templating of Block-co-Polymer Mesophases. *Chem. Mater.* **2010**, *22*, 428−434.

(30) Zhu, J.; Yang, J.; Miao, R.; Yao, Z.; Zhuang, X.; Feng, X. Nitrogen-enriched, ordered mesoporous carbons for potential electrochemical energy storage. *J. Mater. Chem. A* **2016**, *4*, 2286−2292.

(31) Bayatsarmadi, B.; Zheng, Y.; Jaroniec, M.; Qiao, S. Z. Soft-Templating Synthesis of N-Doped Mesoporous Carbon Nano-spheres for Enhanced Oxygen Reduction Reaction. *Chem. - Asian J.* **2015**, *10*, 1546−1553.

(32) Yang, J.; Zhai, Y.; Deng, Y.; Gu, D.; Li, Q.; Wu, Q.; Huang, Y.; Tu, B.; Zhao, D. Direct triblock-copolymer-templating synthesis of ordered nitrogen-containing mesoporous polymers. *J. Colloid Interface Sci.* **2010**, *342*, 579−585.

(33) Sahraie, N. R.; Paraknowitsch, J. P.; Gobel, C.; Thomas, A.; Strasser, P. Noble-Metal-Free Electrocatalysts with Enhanced ORR Performance by Task-Specific Functionalization of Carbon using Ionic Liquid Precursor Systems. *J. Am. Chem. Soc.* **2014**, *136*, 14486−14497.

(34) Paraknowitsch, J. P.; Thomas, A. Functional Carbon Materials From Ionic Liquid Precursors. *Macromol. Chem. Phys.* **2012**, *213*, 1132−1145.

(35) Meng, Y.; Gu, D.; Zhang, F. Q.; Shi, Y. F.; Yang, H. F.; Li, Z.; Yu, C. Z.; Tu, B.; Zhao, D. Y. Ordered mesoporous polymers and homologous carbon frameworks: Amphiphilic surfactant templating and direct transformation. *Angew. Chem., Int. Ed.* **2005**, *44*, 7053−7059.

(36) Freddy, K.; Choi, S. H.; Ryoo, R. Cubic Ia3d large mesoporous silica: synthesis and replication to platinum nanowires, carbon nanorods and carbon nanotubes. *Chem. Commun.* **2003**, *17*, 2136−2137.

(37) Meng, Y.; Gu, D.; Zhang, F. Q.; Shi, Y. F.; Cheng, L.; Feng, D.; Wu, Z. X.; Chen, Z. X.; Wan, Y.; Stein, A.; Zhao, D. Y. A family of highly ordered mesoporous polymer resin and carbon structures from organic-organic self-assembly. *Chem. Mater.* **2006**, *18*, 4447−4464.

(38) Zheng, L.; Guo, C.; Wang, J.; Liang, X. F.; Chen, S.; Ma, J. H.; Yang, B.; Jiang, Y. Y.; Liu, H. Z. Effect of ionic liquids on the aggregation behavior of PEO-PPO-PEO block copolymers in aque-ous solution. *J. Phys. Chem. B* **2007**, *111*, 1327−1333.

(39) Nambam, J. S.; Philip, J. Effects of Interaction of Ionic and Nonionic Surfactants on Self-Assembly of PEO-PPO-PEO Triblock Copolymer in Aqueous Solution. *J. Phys. Chem. B* **2012**, *116*, 1499−1507.

(40) Parmar, A.; Aswal, V. K.; Bahadur, P. Interaction between the ionic liquids 1-alkyl-3-methylimidazolium tetrafluoroborate and Pluronic (R) P103 in aqueous solution: A DLS, SANS and NMR study. *Spectrochim. Acta, Part A* **2012**, *97*, 137−143.

(41) Liang, J.; Zheng, Y.; Chen, J.; Liu, J.; Hulicova-Jurcakova, D.; Jaroniec, M.; Qiao, S. Z. Facile Oxygen Reduction on a Three-Dimensionally Ordered Macroporous Graphitic C3N4/Carbon Composite Electrocatalyst. *Angew. Chem., Int. Ed.* **2012**, *51*, 3892−3896.

(42) Ma, T. Y.; Dai, S.; Jaroniec, M.; Qiao, S. Z. Graphitic Carbon Nitride Nanosheet-Carbon Nanotube Three-Dimensional Porous Composites as High-Performance Oxygen Evolution Electrocatalysts. *Angew. Chem., Int. Ed.* **2014**, *53*, 7281−7285.

(43) Conway, B. E.; Tilak, B. V. Interfacial processes involving electrocatalytic evolution and oxidation of H-2, and the role of chemisorbed H. *Electrochim. Acta* **2002**, *47*, 3571−3594.

(44) Popczun, E. J.; McKone, J. R.; Read, C. G.; Biacchi, A. J.; Wiltrout, A. M.; Lewis, N. S.; Schaak, R. E. Nanostructured Nickel Phosphide as an Electrocatalyst for the Hydrogen Evolution Reac-tion. *J. Am. Chem. Soc.* **2013**, *135*, 9267−9270.

(45) Dong, G.; Fang, M.; Wang, H.; Yip, S.; Cheung, H.-Y.; Wang, F.; Wong, C.-Y.; Chu, S. T.; Ho, J. C. Insight into the electrochemical activation of carbon-based cathodes for hydrogen evolution reac-tion. *J. Mater. Chem. A* **2015**, *3*, 13080−13086.

(46) Yang, Y.; Lun, Z. N.; Xia, G. L.; Zheng, F. C.; He, M. N.; Chen, Q. W. Non-precious alloy encapsulated in nitrogen-doped graphene layers derived from MOFs as an active and durable hydrogen evolution reaction catalyst. *Energy Environ. Sci.* **2015**, *8*, 3563−3571.

(47) Long, X.; Li, G. X.; Wang, Z. L.; Zhu, H. Y.; Zhang, T.; Xiao, S.; Guo, W. Y.; Yang, S. H. Metallic Iron-Nickel Sulfide Ultrathin Nanosheets As a Highly Active Electrocatalyst for Hydrogen Evolution Reaction in Acidic Media. *J. Am. Chem. Soc.* **2015**, *137*, 11900−11903.

(48) Lavalley, J. C. Infrared spectrometric studies of the surface basicity of metal oxides and zeolites using adsorbed probe mole-cules. *Catal. Today* **1996**, *27*, 377−401.

(49) Auroux, A.; Gervasini, A. Microcalorimetric Study of the Acidity and Basicity of Metal-Oxide Surfaces. *J. Phys. Chem.* **1990**, *94*, 6371−6379.

(50) Han, X. W.; Li, C. Q.; Guo, Y.; Liu, X. H.; Zhang, Y. G.; Wang, Y. Q. N-doped carbon supported Pt catalyst for base-free oxidation of 5-hydroxymethylfurfural to 2,5-furandicarboxylic acid. *Appl. Catal., A* **2016**, *526*, 1−8.

Supporting Information

Ionic Liquid-Assisted Synthesis of Mesoporous Carbons with Surface Enriched Nitrogen for Hydrogen Evolution Reaction

Xiaojia Zhao, Shuang Li, Hefeng Cheng, Johannes Schmidt, Arne Thomas*

Department of Chemistry, Division of Functional Materials, Technical University Berlin, Hardenbergstraße 40, 10623 Berlin, Germany

*Corresponding author:

arne.thomas@tu-berlin.de.

Supplementary note 1

Atomic N/C ratio

Atomic N/C is calculated to evaluate the degree of concentration of nitrogen atoms on the pore surface. As XPS is highly surface-sensitive, it was worth calculating the atomic N/C ratio of NMCs to compare with that determined by EA

For EA, the atomic N/C ratio is calculated as follows:

$$\text{atomic N/C ratio} = \frac{\text{weight percentage of nitrogen}/14}{\text{weight percentage of carbon}/12}$$

For XPS, to get the data as accurate as possible, the spot size of X-Ray was set as 400µm to increase the detectable field for the samples. For N1s scan, the scan number was set as 100 cycles to get relatively smooth curves.

Each sample was tested 3 times both for XPS and EA, the average value was calculated as the final N/C ratio of samples and the standard deviation S was calculated as follows:

$$S = \sqrt{\frac{\sum_{i=1}^{N}(X_i - \bar{X})^2}{n}}$$

Supplementary note 2

Normalization of j_0

The normalization process from exchange current density (j_0) to the activity per active sites ($j_{\text{real/site}}$) was operated by following:

jreal (A/cm^2) = j_0(A/cm^2 geo) × (1/catalyst mass Loading (mg(cat)/cm^2 geo) × (1/ Real active area (cm^2 real / mg(cat)))

Real active surface area (cm^2 real / mg(cat)) = BET (cm^2 real /mg(cat)) × total N at% × N-function at%

Table S1. The corresponding database for the normalization of j_0

	exchange current density j_0(A/cm^2)	catalyst loading (mg/cm^2)	surface area (cm^2/mg)	Total N at%	N-function %	J (A/cm^2 real) ×10^{-7}
NMC-0.2	0.420 x 10^{-5}	1.0	6033.4	1.71	44.7	0.91
NMC-0.3	1.472 x 10^{-5}	1.0	6072.8	2.94	43.2	1.91
NMC-0.4	1.585 x 10^{-5}	1.0	4552.2	3.60	38.2	2.53
NMC-0.5	0.316 x 10^{-5}	1.0	4137.5	3.15	43.1	0.56
NMC-KIT-6-0.4	1.530 x 10^{-5}	1.0	5014.0	3.42	48.1	1.85

N-function% was calculated based on g-N, because the most active sites for each N type is identified by DFT calculation that g-N model shows the lowest value of ΔG_H* which indicates a promotion for hydrogen adsorption step.[1]
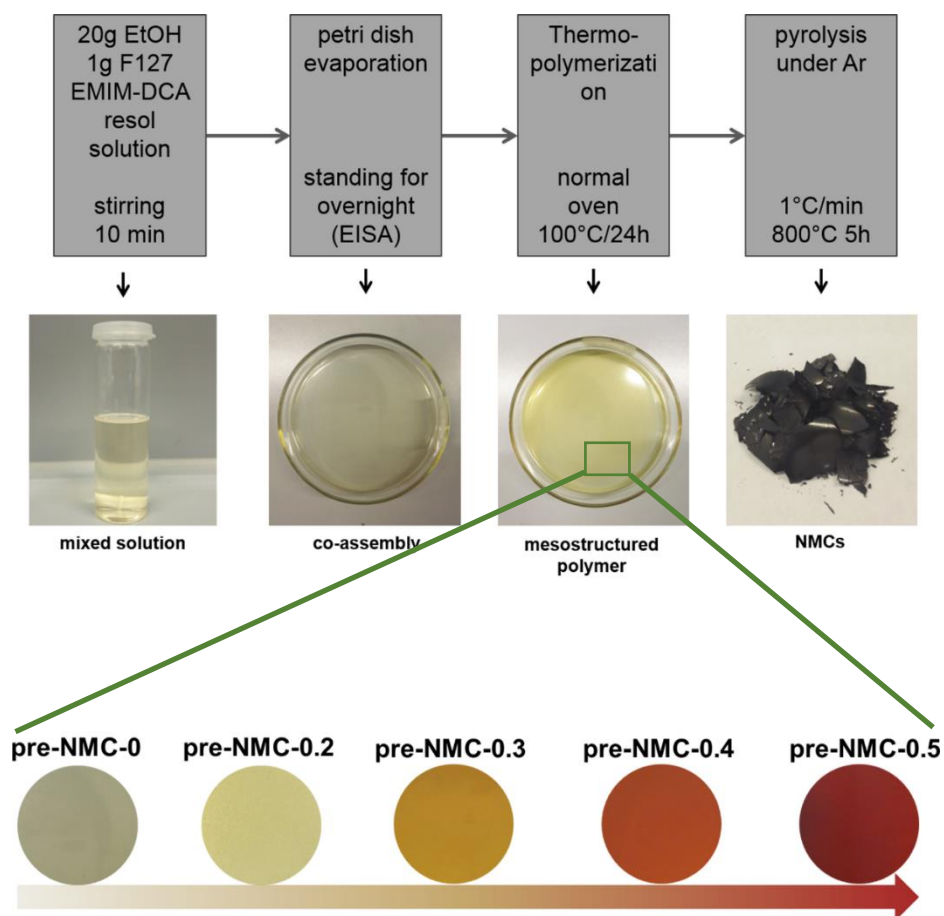
Figure S1. The process of evaporation induced self-assembly (EISA). The bottom are pictures of the mesostructured
polymer of samples with different mass ratio of EMIM-DCA to resol
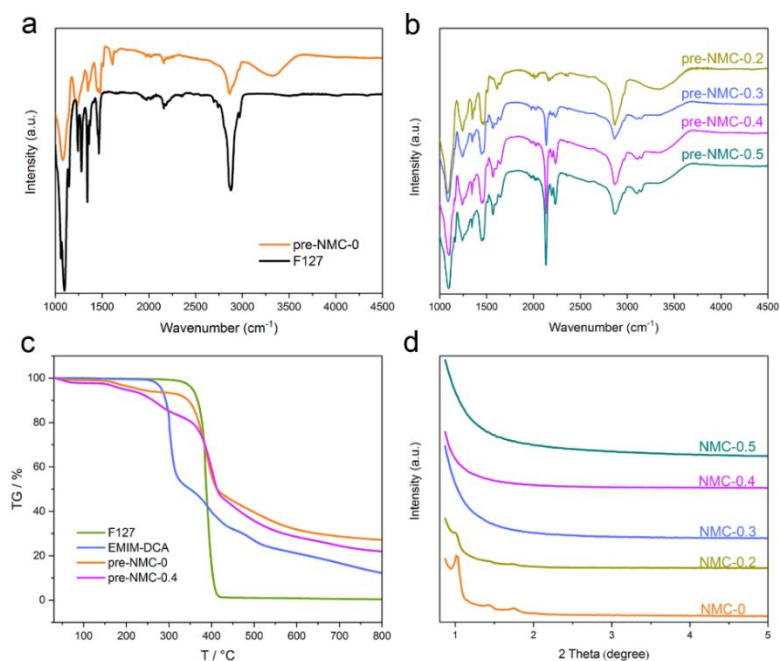
Figure S2. (a) FT-IR of pre-NMC-0 and F127, (b) FT-IR of the mesostructured polymers with different ratio of EMIM-DCA to resol, showing an obvious increase in intensity of -C≡N stretch vibrations at∼2200 cm^{-1}, (c) TGA of NMC-0, NMC-0.4, EMIM-DCA and F127, NMC-0.4 shows a mass loss at the decomposition temperature of EMIM-DCA compared with NMC-0, (d) SAXS of the series of NMC-x samples. No obvious scattering peaks can be observed for NMC-0.3, NMC-0.4 and NMC-0.5, implying the absence of ordered mesostructures
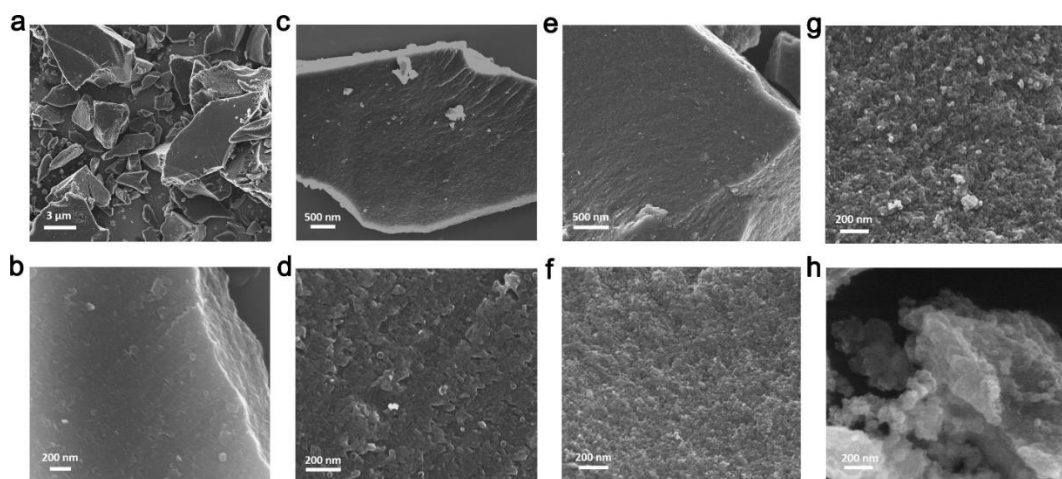
Figure S3. SEM images of N-doped mesoporous carbon synthesized with different amount of EMIM-DCA. (a,b) NMC-0, (c,d) NMC-0.2, (e,f) NMC-0.3, (g) NMC-0.4, (h) NMC-0.5
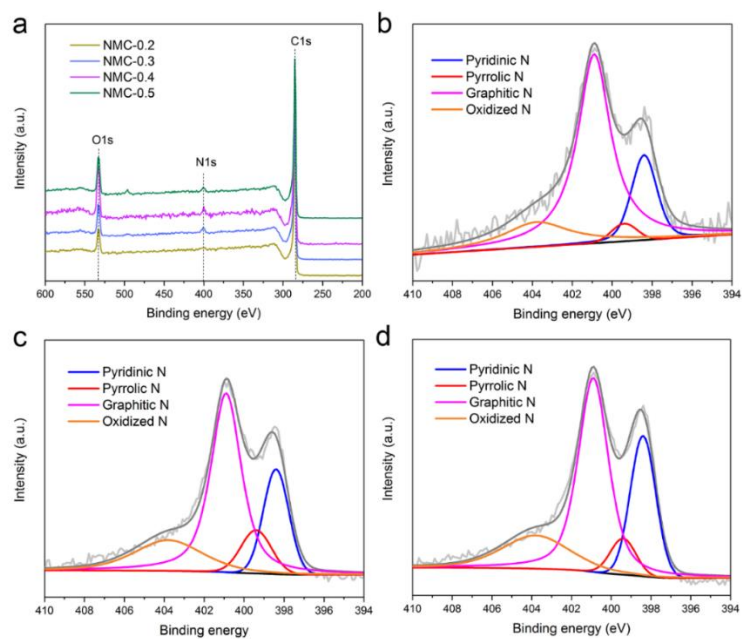
Figure S4. Survey spectra of the series of NMC-x samples(a) and N 1s core level XPS spectra for NMC-0.2(b), NMC-0.3(c), NMC-0.5(d)
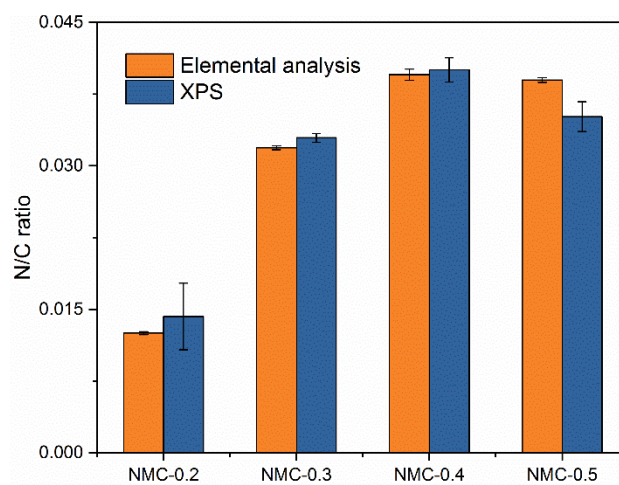
Figure S5. N/C ratio of the series of NMC-x samples determined by XPS and EA
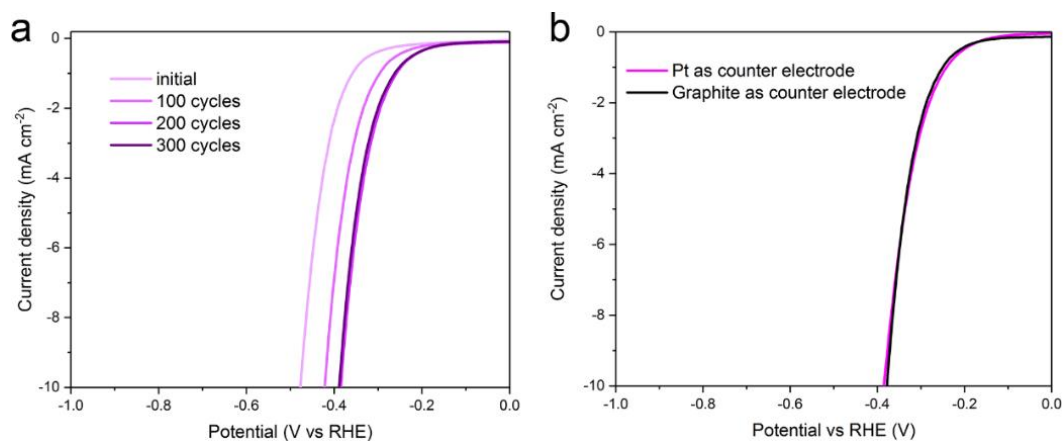
Figure S6. HER polymerization plots of NMC-0.4 in 0.5 M H_2SO_4 with: (a) initial and post-potential cyclic voltammograms, the potential range is between -0.1 V and -0.5 V (vs RHE) with a sweep rate of 20 mV s^{-1}, (b) using different counter electrode
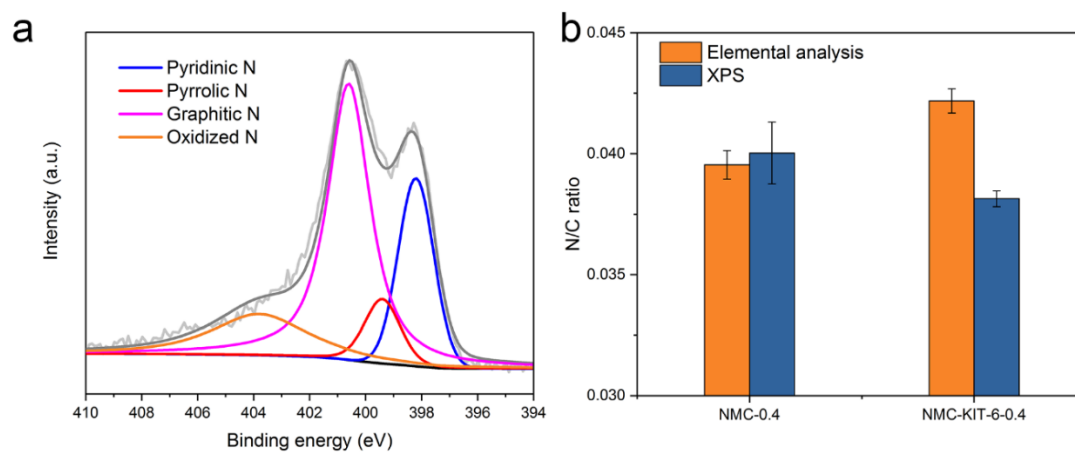
Figure S7. (a) High-resolution N1s spectra of NMC-KIT-6-0.4, (b) N/C ratio of NMC-0.4 and NMC-KIT-6-0.4 determined by XPS and EA

Table S2. Nitrogen concentration of NMCs determined by XPS and EA analysis

Sample	XPS analysis			EA	
	C/at%	N/at%	g-N/ at%	C/wt%	N/wt%
NMC-0.2	90.22	1.71	44.7	85.84	1.25
NMC-0.3	87.56	2.94	43.2	82.63	3.07
NMC-0.4	86.17	3.60	38.2	82.71	3.82
NMC-0.5	86.30	3.15	43.1	84.27	4.44
NMC-KIT-6-0.4	89.24	3.42	48.1	76.01	3.74

Table S3. The electrocatalysis of performance of NMCs

Sample	Overpotentail at 10 mA cm^{-2} (mV)	Tafel slop (mV dec^{-1})	Exchange current density j$_0$ (A cm^{-2})*
NMC-0.2	—	245.8	0.420 x 10-5
NMC-0.3	426.9	149.0	1.472 x 10-5
NMC-0.4	384.7	134.0	1.585 x 10-5
NMC-0.5	464.4	131.7	0.316 x 10-5

*Exchange current density determined by extrapolating the Tafel plots to x-axis. According to ŋ=blogj + a (a and b are calculated from Tafel plot) the j0 can be calculated assuming ŋ=0

Table S4. Characterization and electrocatalysis performance of NMC-0.4 and NMC-KIT-6-0.4

Sample	Surface area (m^2 g^{-1})	Overpotential at 10 mA cm^{-2} (mV)	Tafel slope (mV dec^{-1})	Exchange current density j$_0$ (A cm^{-2})
NMC-0.4	413.75	384.7	134.0	1.585 x 10-5
NMC-KIT-6-0.4	501.40	461.0	185.9	1.530 x 10-5

Table S5. Summary of HER performance of reported N-doped carbon materials in acidic solution

Catalyst	Catalysis condition	Overpotential at 10 mA cm^{-2} (mV)	Reference
NMC-0.4	0.5 M H$_2$SO$_4$	384.7	**This work**
HNDCM	0.5 M H$_2$SO$_4$	832	DOI: 10.1021/acsnano.7b01946
HNDCM-Co		247	
N-doped graphene	0.5 M H$_2$SO$_4$	480	Nat. Energy 2016, 1, 16130
N,S-doped graphene		310	
N-doped graphene	0.5 M H$_2$SO$_4$	490	ACS Nano 2014, 8, 5290
N, P –doped graphene		422	
N-doped graphene-800	0.5 M H$_2$SO$_4$	559	Angew. Chem. Int. Ed. 2015, 54, 2131
N-doped graphene-500		474	
N-graphene	0.5 M H$_2$SO$_4$	570	Nat. Commun. 2014, 5, 3783
C$_3$N$_4$/NG mixture		380	
C$_3$N$_4$@NG		240	
N-doped graphene	0.5 M H$_2$SO$_4$	490	ACS Nano 2014, 8, 5290
N, P –doped graphene		422	

References

1 Jiao, Y.; Zheng, Y.; Davey, K.; Qiao, S. Z. Activity origin and catalyst design principles for electrocatalytic hydrogen evolution on heteroatom-doped graphene. Nat. Energy **2016**, *1*:16130.

8.2 Bifunctional Electrocatalysts for Overall Water Splitting from an Iron/Nickel-Based Bimetallic Metal-Organic Framework/Dicyandiamide Composite

Published version

X. J. Zhao, P. Pachfule, S. Li, J. R. J. Simke, J. Schmidt, A. Thomas, Bifunctional Electrocatalysts for Overall Water Splitting from an Iron/Nickel-Based Bimetallic Metal-Organic Framework/Dicyandiamide Composite *Angew. Chem. Int. Ed*. **2018**, 130, 9059-9064.

https://onlinelibrary.wiley.com/doi/full/10.1002/anie.201803136

Communications

Water Splitting Hot Paper

Bifunctional Electrocatalysts for Overall Water Splitting from an Iron/Nickel-Based Bimetallic Metal–Organic Framework/Dicyandiamide Composite

Xiaojia Zhao, Pradip Pachfule, Shuang Li, Jan Ron Justin Simke, Johannes Schmidt, and Arne Thomas*

Abstract: *Pyrolysis of a bimetallic metal–organic framework (MIL-88-Fe/Ni)-dicyandiamide composite yield a Fe and Ni containing carbonaceous material, which is an efficient bifunctional electrocatalyst for overall water splitting. $FeNi_3$ and $NiFe_2O_4$ are found as metallic and metal oxide compounds closely embedded in an N-doped carbon–carbon nanotube matrix. This hybrid catalyst (Fe-Ni@NC-CNTs) significantly promotes the charge transfer efficiency and restrains the corrosion of the metallic catalysts, which is shown in a high OER and HER activity with an overpotential of 274 and 202 mV, respectively at 10 mA cm^{-2} in alkaline solution. When this bifunctional catalyst was further used for H_2 and O_2 production in an electrochemical water-splitting unit, it can operate in ambient conditions with a competitive gas production rate of 1.15 and 0.57 $\mu L\,s^{-1}$ for hydrogen and oxygen, respectively, showing its potential for practical applications.*

Electrochemical water splitting is widely regarded as a sustainable method for large-scale production of hydrogen as clean fuel.[1] To efficiently carry out water splitting, the development of highly active and cost-effective catalysts for both half-reactions, that is, the hydrogen evolution reaction (HER) at the cathode and the oxygen evolution reaction (OER) at the anode, is of paramount importance.[2] To date, Pt-based precious metal alloys and Ir/Ru-based metal oxides remain the best catalysts for HER and OER in strongly acidic and basic conditions, respectively. However, the cost and scarcity of these noble-metals largely limits their widespread application as catalyst, especially for large scale applications. Furthermore, when two types of catalysts are used for the respective half reactions in an integrated electrolyzer it can be difficult to operate water splitting efficiently because of the mismatch of optimum electrolyte pH. Consequently there is a demand for bifunctional electrocatalysts possessing substantial catalytic performance both for HER and OER at the

same electrolyte solutions.[2b] Indeed, various electrocatalysts based on transition metals and their derivatives, that is, metal chalcogenides,[2c–e] metal phosphides,[2f] as well as metal oxides or hydroxides[2g] have been investigated as bifunctional electrocatalysts for water splitting. Nevertheless, owing to their often unsatisfactory conductivity and durability, the efficiency of water splitting for these electrocatalysts is still not competitive with noble-metal based electrocatalysts.

Recently, metal–organic frameworks (MOFs), have been found to be suitable starting materials for constructing various electrocatalysts such as heteroatom-doped and metal or metal oxide containing carbons by pyrolysis.[2f,h,3] These MOF-derived carbonaceous materials usually exhibit an entirely microporous nature, low graphitization degrees and frequently the undesired aggregation of metal nanoparticles is observed. These observations are generally unfavorable for mass and electron transport during the electrocatalytic process. To achieve a better activity, conductive substrates like nickel foam,[3b] graphene,[2h] carbon aerogel,[3c] and others were applied as supports for MOF growth and subsequent carbonization, indeed promoting the charge-transport ability and reducing the aggregation of MOF-derived catalysts. MOFs have also been reported as a promising precursor for the synthesis of carbon composites containing significant amounts of carbon nanotubes (CNTs).[3d–h] For example, Lou et al. used ZIF-67 particles as the precursor to synthesize a framework constructed from interconnected CNTs with embedded Co nanoparticles.[3g] Such in situ grown MOF-derived CNTs can significantly promote electron transfer and are therefore interesting structures to drive electrochemical reactions. However, while these Co-CNT based carbons usually show improved HER activity, this is paid-off by an inferior OER activity, which significantly restrict their application for overall water splitting.[3d,f] Therefore, there is still a demand to explore novel MOF precursors to construct high-performance bifunctional electrocatalysts for HER and OER, that is, overall water splitting.

Herein, we report the synthesis of such a bifunctional catalyst (Fe-Ni@NC-CNTs) by carbonization of a bimetallic MIL-88-Fe/Ni–dicyandiamide composite and its application for overall water splitting. Dicyandiamide (DCDA) was added to MIL-88 to enable the formation of nitrogen-doped carbons from the nitrogen-free MOF. The preparation of Fe-Ni@NC-CNT is illustrated in Figure 1a (for details see Supporting Information). The bimetallic MIL-88-Fe/Ni was prepared by solvothermal treatment of terephthalic acid,

[*] X. J. Zhao, Dr. P. Pachfule, S. Li, Dr. J. Schmidt, Prof. Dr. A. Thomas
Functional Materials, Department of Chemistry
Technische Universität Berlin
Hardenbergstrasse 40, 10623 Berlin (Germany)
E-mail: arne.thomas@tu-berlin.de

J. R. J. Simke
Zentraleinrichtung Elektronenmikroskopie (ZELMI)
Technische Universität Berlin
Strasse des 17. Juni 135, 10623 Berlin (Germany)

Supporting information and the ORCID identification number(s) for the author(s) of this article can be found under:
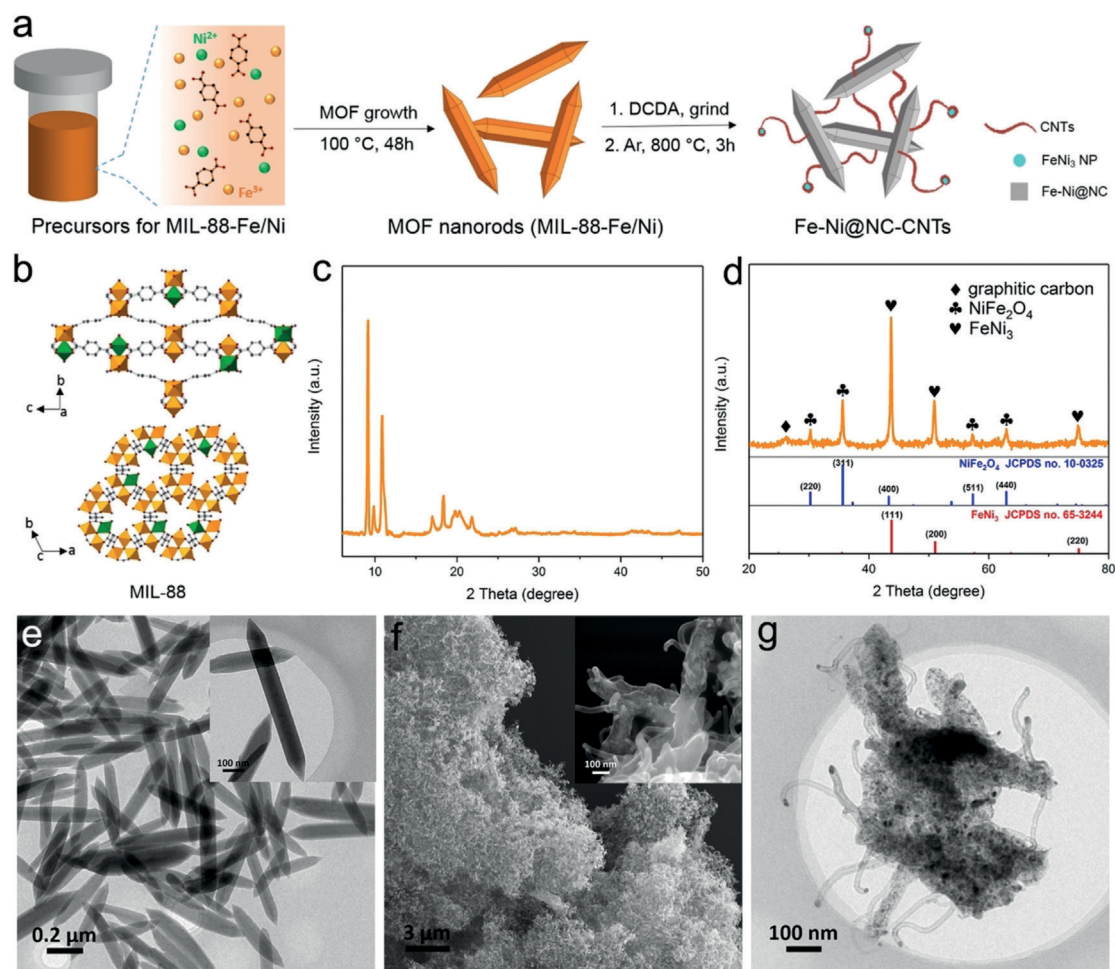https://doi.org/10.1002/anie.201803136.

Communications

Figure 1. a) Synthesis of MIL-88-Fe/Ni and Fe-Ni@NC-CNTs. b) The packing diagram of MIL-88-Fe/Ni viewed along the *a* and *c* axis. Fe orange, Ni green, O red, C gray. H atoms and solvent molecules are omitted for clarity. c) PXRD pattern of MIL-88-Fe/Ni. d) PXRD pattern of the as-synthesized Fe-Ni@NC-CNTs and FeNi$_3$ (JCPDS no. 65-3244) and NiFe$_2$O$_4$ (JCPDS no. 10-0325). e) TEM images of MIL-88-Fe/Ni. f) SEM and g) TEM images of Fe-Ni@NC-CNTs.

FeCl$_3$·6H$_2$O, Ni(NO$_3$)$_2$·6H$_2$O at 100°C for 48 h. DCDA was mixed with the crystalline MOF by mechanical grinding, yielding a 1:1 weight ratio followed by pyrolysis at 800°C for 3 h in inert atmosphere. Figure 1b shows the structure of MIL-88-Fe/Ni viewed along the *a* and *c* axis with possible positions of Fe and Ni metals in the 3D structure. The powder X-ray diffraction (PXRD) pattern of MIL-88-Fe/Ni matches well with literature reported transition-metal-doped MOFs, confirming the formation of phase-pure material with high crystallinity (Figure 1c).[4] Transmission electron microscopy (TEM) showed that MIL-88-Fe/Ni consist of uniform rod-shaped crystals (60–80 nm wide and 500–700 nm long, aspect ratio = 8–12) (Figure 1e), also seen by scanning electron microscopy (SEM; Figure S1). Upon mixing and grinding with DCDA, the XRD pattern shows reflections for both MIL-88-Fe/Ni and DCDA, indicating the preservation of the MOF structure (Figure S2). As DCDA melts slightly above 200°C an intimate mixture of the two compounds can be assumed during the following heat treatment (Figure S3).

The PXRD pattern of Fe-Ni@NC-CNTs shows a relatively weak peak around 26.4° that can be assigned to the (002) plane of graphitic carbon,[5] while the more intense peaks

appearing at 43.7°, 50.9°, and 74.9° can be indexed to the (111), (200), and (220) planes of FeNi$_3$, and the peaks at 30.3°, 35.6°, 43.5°, 57.3°, and 63.0° can be assigned to the (220), (311), (400), (511), and (440) planes of the spinel structure of NiFe$_2$O$_4$ (Figure 1d).[6] The SEM images of Fe-Ni@NC-CNTs show the formation of a homogeneous and highly porous network (Figure 1f). Notably, the initial nanorod-structure is partially preserved seen in the formation of rod-like structures with dimensions in the range of the former MOF morphologies. Additionally, CNT growth from the surface of these nanorods is observed (Figure 1f, inset). TEM analyses further confirm the partial preservation of rod-shaped morphologies (Figure 1g). These rods consist of a carbonaceous matrix with embedded metal or metal oxide nanoparticles with diameters between 10–20 nm. These larger nanorods are furthermore threaded with CNTs having lengths mainly between 100–250 nm and width of 12–24 nm (Figure S4), with FeNi$_3$ nanoparticles at their tips (Figure 2a). It can be assumed that such an open porous and interlaced carbon nanorod/CNT structure could be beneficial for ion and electron transport during an electrocatalytic processes.[3e,g,7]

Communications
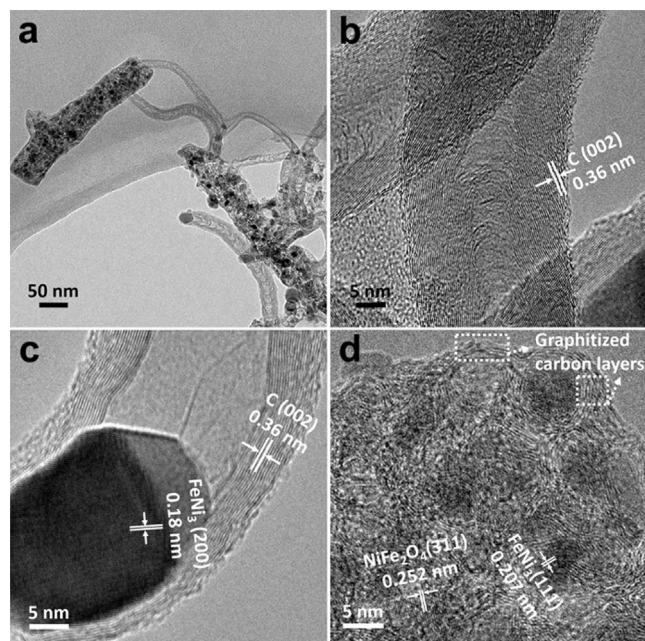
Figure 2. a) TEM and b)–d) HRTEM images of Fe-Ni@NC-CNTs.

High-resolution TEM (HR-TEM) images reveal graphitic layers in the CNT walls (Figure 2b), as reported for other MOF derived CNTs.[3g] The small graphitic layers (interlayer spacing of ca. 0.36 nm) are not oriented parallel to the axis direction of the CNTs and show considerable defects and edges on the surface of the CNTs. The HR-TEM images also show that $FeNi_3$ nanoparticles are present at the tips of the CNTs (Figure 2c) and are encapsulated by a few-layered carbon shell (with an interlayer distance of again 0.36 nm). The crystal planes in these nanoparticles with a d-spacing of approximately 0.18 nm correspond to the (200) lattice of the $FeNi_3$ alloy, which can also be confirmed by selected area electron diffraction (SAED) patterns with bright rings corresponding to the (111), (200), and (220) planes of $FeNi_3$ cubic crystal structure (Figure S5). On the other hand, the nanorod structures are embedding both $FeNi_3$ and $NiFe_2O_4$ nanoparticles, coated by graphitic carbon layers (Figure 2d). The SAED pattern from this region confirm the coexistence of the $FeNi_3$ alloy with bright rings corresponding to (111) and (200) planes and the $NiFe_2O_4$ crystal spinel structure with (220), (311), (511), and (440) planes, respectively (Figure S5).

In a control experiment, MIL-88-Fe/Ni was directly pyrolyzed without addition of DCDA to obtain a sample without nitrogen doping (denoted Fe-Ni@C). Furthermore, to analyze the influence of the crystal structure and morphology of the MOF crystallites on the final material, in a subsequent control experiment, direct pyrolysis of a plain mixture of the precursors of MIL-88-Fe/Ni (i.e. terephthalic acid, $FeCl_3·6H_2O$, $Ni(NO_3)_2·6H_2O$) and DCDA was carried out (denoted Fe-Ni@NC-powder, for details see SI). As shown in Figure 3a, all three pyrolyzed

materials show similar diffraction patterns indicating the formation $FeNi_3$ alloy and $NiFe_2O_4$ spinel, while the broad diffraction peak at 26.4° for graphitic carbon is not observed for Fe-Ni@C. The analyses of Fe-Ni@C by electron microscopy indeed confirm the absence of CNTs and also the rod-shaped morphology of the MOF is not preserved. Furthermore, much larger nanoparticles of $FeNi_3$ and $NiFe_2O_4$ are formed in comparison to the samples with addition of DCDA (Figure S6). It is supposed that the DCDA favors the formation of CNTs owing to the NH_3 evolved during its decomposition, which facilitate the reduction of metal ions to metal nanocatalysts finally promoting the formation of CNTs.[3e,h] On the other hand, the SEM and TEM images of Fe-Ni@NC-powder show the formation of bulk structures without any specific morphologies, promoting the role of MOF crystallites and uniform distribution of metals within the MOF for the preparation of highly dispersed and uniformly distributed metal nanoparticles-doped carbons (Figure S7).

Nitrogen adsorption-desorption isotherms were measured to examine the specific surface area and pore structures of Fe-Ni@NC-CNTs, Fe-Ni@C, and Fe-Ni@NC-powder. As shown in Figure 3b, all isotherms show a steep increase at low relative pressures, a continuous further uptake of nitrogen with increasing relative pressures for Fe-Ni@NC-CNTs, Fe-Ni@C and a small hysteresis loop in the P/P_0 range between 0.4–0.6, indicating the existence of micro- and mesopores, respectively. A further significant increase in nitrogen uptake at high relative pressures (0.95–1.0) further indicate the presence of large mesopores or macropores. Fe-Ni@NC-powder shows the highest total surface area (401 $m^2 g^{-1}$),
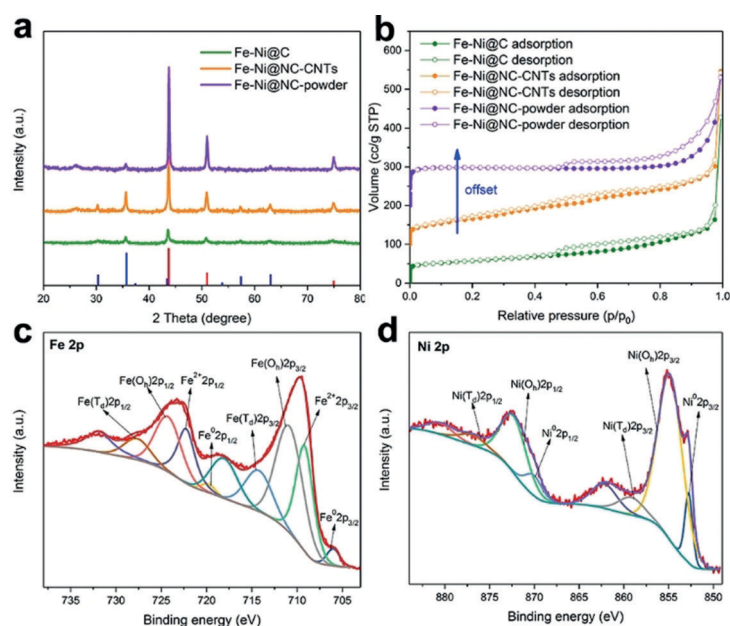
Figure 3. a) PXRD analyses of Fe-Ni@C, Fe-Ni@NC-CNTs and Fe-Ni@NC-powder and the simulated patterns for $FeNi_3$ (red) and $NiFe_2O_4$ (blue). b) N_2 adsorption-desorption isotherms of the catalysts. For clarity, the isotherms have a vertical offset by 100 $cm^3 g^{-1}$ STP for Fe-Ni@NC-CNTs and 200 $cm^3 g^{-1}$ STP for Fe-Ni@NC-powder. High-resolution c) Fe 2p, d) Ni 2p XPS spectra of Fe-Ni@NC-CNTs.

Communications

mainly dominated by micropores ($255 \, \text{m}^2 \text{g}^{-1}$). In strong contrast, for Fe-Ni@NC-CNTs, almost the entire surface area ($246 \, \text{m}^2 \text{g}^{-1}$) can be attribute to *meso*-/macropores while the micropore surface area ($12 \, \text{m}^2 \text{g}^{-1}$) is negligible. Finally, Fe-Ni@C shows the lowest surface area ($206 \, \text{m}^2 \text{g}^{-1}$), also with just a very small contribution of microporosity ($20 \, \text{m}^2 \text{g}^{-1}$). This is also reflected in the pore size distribution calculated by QSDFT confirming the formation of mainly larger ($>2 \, \text{nm}$) pores for Fe-Ni@NC-CNTs (Figure S8), yielding also the highest pore volume ($0.690 \, \text{cm}^3 \text{g}^{-1}$) of all samples (Table S1).

X-ray photoelectron spectroscopy (XPS) survey scans were conducted (Figure S9a) showing the presence of Fe, Ni, C, and O, in all samples, plus the presence of nitrogen in Fe-Ni@NC-CNTs and Fe-Ni@NC-powder (with 2.6 at% and 6.8 at% nitrogen, respectively), proving the successful utilization of DCDA as nitrogen source. The deconvolution of the magnified N 1s XPS spectra for both samples show four peaks, which can be assigned to pyridinic N, pyrrolic N, graphitic N, and oxidized N, with a higher ratio of surface bound pyridinic/pyrolic nitrogen to graphitic nitrogen for Fe-Ni@NC-CNTs in comparison to Fe-Ni@NC-powder (Figure S9b,c). The Fe 2p and Ni 2p spectra of Fe-Ni@NC-CNTs were fitted by a Gaussian-Lorentzian function with spin-orbit doublets (Figure 3c,d).[6a,8] The lowest binding energy peaks in both Fe and Ni spectra correspond to metallic Fe ($706.0 \, \text{eV}$) and Ni ($852.6 \, \text{eV}$) from the FeNi$_3$ alloy.[6a] The appearance of Fe(O$_\text{h}$), Fe(T$_\text{d}$), Ni(O$_\text{h}$) and Ni(T$_\text{d}$) peaks in the spectra are derived from the octahedral (O$_\text{h}$) and tetrahedral (T$_\text{d}$) binding environment of Fe^{3+} and Ni^{2+} in the spinel structure of NiFe$_2$O$_4$ (Figure S10).[9] Similar spectra confirm the formation of Fe-Ni doped carbons for Fe-Ni@C and Fe-Ni@NC-powder (Figure S11). For the O 1s spectrum, the peak located at $530.7 \, \text{eV}$(O2) correspond to low oxygen coordinated defects sites in the spinel structure, which were reported to increase the affinity to oxygen-containing groups thus enhancing the electrocatalytic activity.[3b,9b] As seen in Figure S12 and Table S2 Fe-Ni@NC-CNTs possess the most of these defect sites.

The combined analytical measurements show that Fe-Ni@NC-CNTs own a homogeneous interconnected carbon network with high pore volume and surface area which mainly stems from *meso*- and larger pores, plus abundant Fe/Ni alloy and oxide nanoparticles. These structural features make this material a promising candidate for electrocatalytic applications. At first the OER activity of Fe-Ni@NC-CNTs in an alkaline aqueous electrolyte ($1.0 \, \text{M} \, \text{KOH}$) using a three-electrode system was tested. For comparison, the electrocatalytic activity of Fe-Ni@C, Fe-Ni@NC-powder and Ir/C with the same mass loadings of $0.5 \, \text{mg cm}^{-2}$ (geometrical area) were studied. As shown in Figure 4a, Fe-Ni@NC-CNTs shows the lowest overpotential of $274 \, \text{mV}$ versus the reversible hydrogen electrode (RHE) at $10 \, \text{mA cm}^{-2}$ (Table S3), compared to those of Fe-Ni@C ($470 \, \text{mV}$), Fe-Ni@NC-powder ($370 \, \text{mV}$). This value is even superior to Ir/C ($278 \, \text{mV}$) and
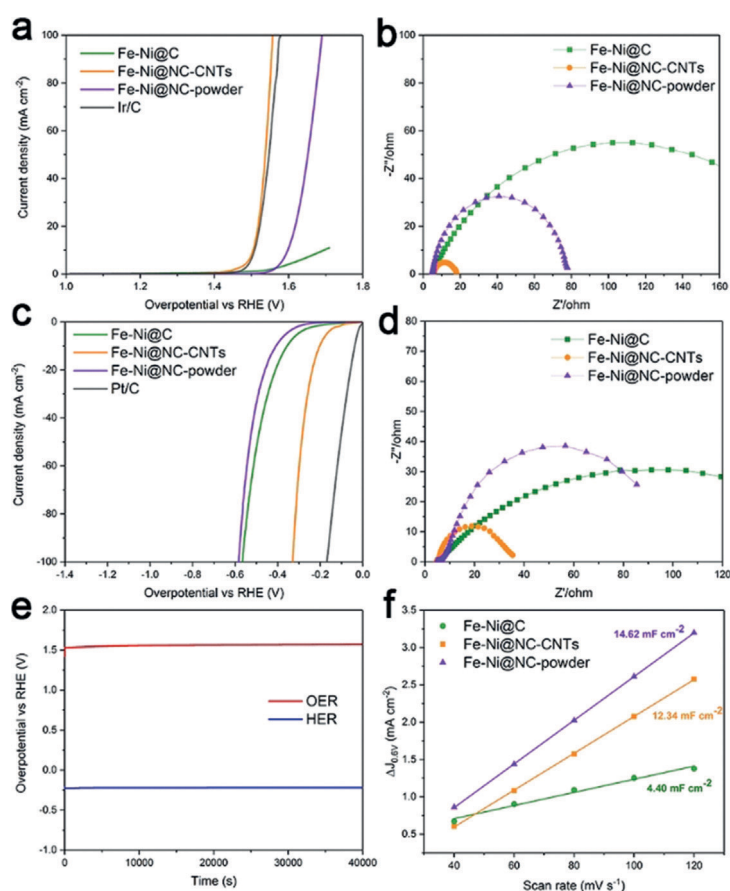
Figure 4. a) OER polarization curves for Fe-Ni@C, Fe-Ni@NC-CNT, Fe-Ni@NC-powder and commercial Ir/C catalyst. b) EIS spectra of the catalysts recorded at a constant potential of $1.504 \, \text{V}$ (vs. RHE). c) HER polarization curves, and d) corresponding EIS spectra recorded at a constant potential of $0.202 \, \text{V}$ (vs. RHE). e) Long-term stability test for Fe-Ni@NC-CNT for OER and HER at a constant current density of $10 \, \text{mA cm}^{-2}$. f) Current density differences (ΔJ) plotted against scan rates of various Fe-Ni@NC samples.

some other reported OER catalysts (Table S4). Furthermore, Fe-Ni@NC-CNTs shows a similar Tafel slope ($45.47 \, \text{mV dec}^{-1}$) to Ir/C ($43.72 \, \text{mV dec}^{-1}$), which is smaller than that of Fe-Ni@C ($178.6 \, \text{mV dec}^{-1}$) and Fe-Ni@NC-powder ($56.44 \, \text{mV dec}^{-1}$), indicating favorable reaction kinetics in the OER process (Figure S13a). The importance of the interlaced CNTs for conductivity enhancement is demonstrated by electrochemical impedance spectroscopy (EIS). As shown in Figure 4b, the high-frequency semicircles in the Nyquist plots, ascribed to the charge transfer resistance (R_ct), give the lowest R_ct value for Fe-Ni@NC-CNTs suggesting that its unique network structure can significantly promote the electron transfer kinetic under OER operating conditions.

Motivated by the promising OER performance of Fe-Ni@NC-CNTs, the electrocatalytic hydrogen evolution reaction (HER) was also investigated in the same alkaline environment ($1.0 \, \text{M} \, \text{KOH}$). For comparison, a commercial 20 wt% Pt/C catalyst was tested with same mass loadings of $0.5 \, \text{mg cm}^{-2}$ (geometrical area). As shown in Figure 4c, the Pt/C catalyst exhibits the best HER activity, whereas Fe-Ni@NC-CNTs shows competitive performance with an overpotential of $202 \, \text{mV}$ at a current density of $10 \, \text{mA cm}^{-2}$ (Table S5),

GDCh

Communications

Angewandte
International Edition *Chemie*

which is much lower than that of Fe-Ni@C (356 mV), Fe-Ni@NC-powder (409 mV) and most literature reported HER catalysts (Table S6). The corresponding Tafel slopes and Nyquist plots further prove the higher reaction kinetics and lower electron transfer resistance of Fe-Ni@NC-CNTs under HER reaction conditions (Figure 4d and Figure S13b). Furthermore, the stability and durability of Fe-Ni@NC-CNTs was tested at a current density of 10 mA cm^{-2}. After 40000 s, the catalyst show just negligible difference in the required overpotential for both reactions, OER and HER (Figure 4e). Notably, no leaching of Fe and Ni species was detected as confirmed by inductively coupled plasma-optical emission spectrometry (ICP-OES) analyses of the electrolyte solution after 40000 s. Moreover, no obvious changes in morphology and nanoparticle distribution of the Fe-Ni@NC-CNTs sample obtained after 40000 s electrocatalysis reaction further confirmed the sufficient stability and durability of the catalyst (Figure S14).

To elucidate if the formation of highly crystalline MOF structures is indeed an important factor for the catalytic performance of carbonaceous materials derived therefrom, the electrocatalytic activity of pyrolyzed samples of MIL-88-Fe/Ni prepared via different reaction times was tested (Figure S15, S16). MIL-88-Fe/Ni obtained after 3 h, 6 h, 12 h, and 48 h were mixed with DCDA, pyrolyzed and their catalytic activity in OER and HER compared (Figure S17). Indeed, Fe-Ni@NC-CNT-3h, -6h and -12h exhibit a lower catalytic performance than Fe-Ni@NC-CNT-48h, showing that the formation of extended crystals has a beneficial effect on the final carbon structures. Furthermore, the pyrolysis temperature can be a critical factor affecting for example, the degree of graphitization of carbonaceous materials and the particle size of catalytic metal or metal oxides and thus the electrochemical performance.[10] Indeed, electrocatalytic activity tests for Fe-Ni@NC-CNTs prepared at different pyrolysis temperatures from 600 to 900°C revealed that 800°C is the optimum temperature as these materials exhibit superior performance for both OER and HER (Figure S18). PXRD analyses confirm the enhancing crystallinity of the metallic compounds and graphitization of the carbon matrix with increasing temperature (Figure S19). However, at a pyrolysis temperature of 900°C pronounced aggregation of metal particles and the collapse of the interconnected framework structure is observed yielding again a deterioration of catalytic performance (Figure S20). To better understand the intrinsic electrocatalytic activity of Fe-Ni@NC-CNTs, the electrochemical surface areas (ECSAs) was investigated by measuring the double-layer capacitance (C_{dl}; Figure S21).[3b,11] The C_{dl} of Fe-Ni@NC-CNTs (12.34 mF cm^{-2}) is much higher than for Fe-Ni@C (4.40 mF cm^{-2}; Figure 4f). It should be noted that Fe-Ni@NC-powder with slightly higher C_{dl} (14.62 mF cm^{-2}) still exhibits a lower electrocatalytic activity probably due to the absence of CNTs and negligible crystallinity of the NiFe$_2$O$_4$ spinel structures. Etching experiments were carried to elucidate the role of the metallic compounds on the catalytic

performance, showing especially the major contribution of FeNi$_3$ NPs to the HER performance (for details see Supporting Information, Figure S22).

Based on the above studies, it can be concluded that Fe-Ni@NC-CNTs is highly efficient bifunctional electrocatalysts for both HER and OER. Accordingly, we assembled an electrolyzer using Fe-Ni@NC-CNTs on nickel foam (NF) as both the cathode and anode for overall water splitting (Figure 5a). Figure 5b shows the linear sweep voltammetry (LSV) of water electrolysis on the Fe-Ni@NC-CNTs || Fe-Ni@NC-CNTs electrodes in 1.0 M aqueous KOH electrolyte solution. Pure nickel foam (NF || NF) and Pt/C || Ir/C were also tested for comparison with the same geometric reactive area and mass loading (1.0 × 1.0 cm^2, 1.0 mg cm^{-2}; Figure S23). During overall water splitting, the Fe-Ni@NC-CNTs exhibits a comparable current density of 145 mA cm^{-2} to the noble-metal derived catalysts Pt/C || Ir/C at a cell voltage of 1.98 V. In addition, the chronopotentiometry curve at an applied current density of 10 mA cm^{-2} reveals that the Fe-Ni@NC-CNTs has a good durability after 40000 s operation (Figure 5c). The recorded gas volumes as a function of water-splitting time under the condition of the chronopotentiometry test shows a linear relationship with a slope of 1.15 and 0.57 μL s^{-1} for H$_2$ and O$_2$ collection. The good agreement of the experimentally generated and theoretically calculated amount of H$_2$ and O$_2$ reveal a Faradaic efficiency of approximately 100 % for both HER and OER in 1.0 M KOH, with a ratio of H$_2$ to O$_2$ of nearly 2 (Figure 5d, Figure S24 and Table S7).

In summary, we have prepared a hybrid Fe-Ni@NC-CNTs catalyst by simple one-step pyrolysis of a MIL-88-Fe/Ni-DCDA composite. The obtained Fe-Ni@NC-CNTs possesses
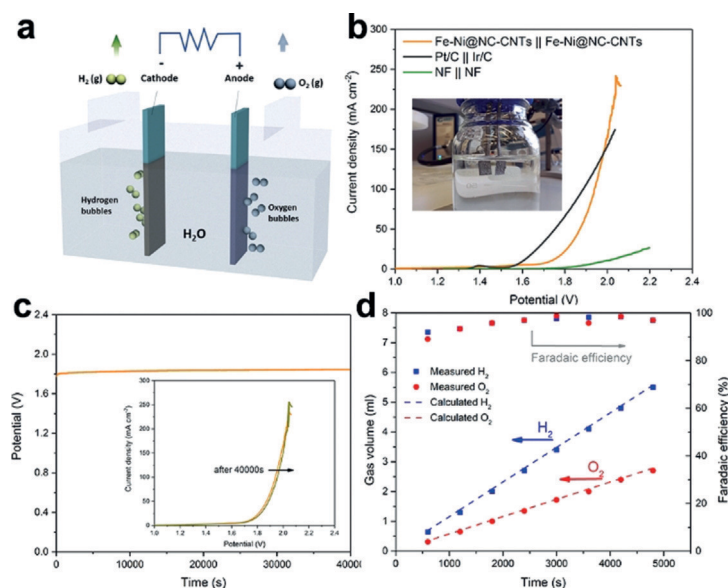

Figure 5. a) Schematic diagram of an electrolyzer for water splitting. b) Polarization curve of Fe-Ni@NC-CNTs || Fe-Ni@NC-CNTs, NF || NF and Pt/C || Ir/C. Inset: photograph of two-electrode configuration. c) Stability test for Fe-Ni@NC-CNT at a constant current density of 10 mA cm^{-2} with a catalyst loading 1.0 mg cm^{-2} (geo). Inset: LSV curves before and after 40000 s durability test at 10 mA cm^{-2}. d) O$_2$ and H$_2$ production volumes as a function of water splitting time for Fe-Ni@NC-CNTs.

Communications

a high conductivity, hierarchical pore structure and stable 3D framework, resulting in high activity, fast mass transport and good stability for electrocatalytic processes. Consequently, when applied for energy conversion and storage, this unique nanostructure exhibits remarkable OER and HER catalytic activity in alkaline solution and show promising potential for practical applications in overall water splitting. The facile synthesis of inexpensive hybrid nanostructures derived from MOFs with controllable morphologies and functionalities can be certainly expanded to the development of further materials for various electrocatalytic reactions.

Acknowledgements

Conflict of interest

The authors declare no conflict of interest.

[1] a) X. X. Zou, Y. Zhang, *Chem. Soc. Rev.* **2015**, *44*, 5148–5180; b) J. Wang, F. Xu, H. Y. Jin, Y. Q. Chen, Y. Wang, *Adv. Mater.* **2017**, *29*, 1605838; c) M. R. Gao, Y. R. Zheng, J. Jiang, S. H. Yu, *Acc. Chem. Res.* **2017**, *50*, 2194–2204; d) M. R. Gao, J. X. Liang, Y. R. Zheng, Y. F. Xu, J. Jiang, Q. Gao, J. Li, S. H. Yu, *Nat. Commun.* **2015**, *6*, 5982.

[2] a) H. Wang, S. X. Min, C. Ma, Z. X. Liu, W. Y. Zhang, Q. Wang, D. B. Li, Y. Y. Li, S. Turner, Y. Han, H. B. Zhu, E. Abou-hamad, M. N. Hedhili, J. Pan, W. L. Yu, K. W. Huang, L. J. Li, J. Y. Yuan, M. Antonietti, T. Wu, *Nat. Commun.* **2017**, *8*, 13592; b) Y. Xu, W. G. Tu, B. W. Zhang, S. M. Yin, Y. Y. Huang, M. Kraft, R. Xu, *Adv. Mater.* **2017**, *29*, 1605957; c) J. Zhang, T. Wang, D. Pohl, B. Rellinghaus, R. H. Dong, S. H. Liu, X. D. Zhuang, X. L. Feng, *Angew. Chem. Int. Ed.* **2016**, *55*, 6702–6707; *Angew. Chem.* **2016**, *128*, 6814–6819; d) C. Gu, S. J. Hu, X. S. Zheng, M. R. Gao, Y. R. Zheng, L. Shi, Q. Gao, X. Zheng, W. S. Chu, H. B. Yao, J. F. Zhu, S. H. Yu, *Angew. Chem. Int. Ed.* **2018**, *57*, 4020–4024; *Angew. Chem.* **2018**, *130*, 4084–4088; e) M. R. Gao, Y. F. Xu, J. Jiang, Y. R. Zheng, S. H. Yu, *J. Am. Chem. Soc.* **2012**, *134*, 2930–2933; f) J. H. Song, C. Z. Zhu, B. Z. Xu, S. F. Fu, M. Engelhard, R. F. Ye, D. Du, S. Beckman, Y. H. Lin, *Adv. Energy Mater.* **2017**, *7*, 1601555; g) Y. Jia, L. Z. Zhang, G. P. Gao, H. Chen, B. Wang, J. Z. Zhou, M. T. Soo, M. Hong, X. C. Yan, G. R. Qian, J. Zou, A. J. Du, X. D. Yao, *Adv. Mater.* **2017**, *29*, 1700017; h) K. Jayaramulu, J. Masa, O. Tomanec, D. Peeters, V. Ranc, A. Schneemann, R. Zboril, W. Schuhmann, R. A. Fischer, *Adv. Funct. Mater.* **2017**, *27*, 1700451; i) X. J. Zhao, S. Li, H. F. Cheng, J. Schmidt, A. Thomas, *ACS Appl. Mater. Interfaces* **2017**, *10*, 3912–3920.

[3] a) P. Pachfule, D. Shinde, M. Majumder, Q. Xu, *Nat. Chem.* **2016**, *8*, 718–724; b) X. F. Lu, L. F. Gu, J. W. Wang, J. X. Wu, P. Q. Liao, G. R. Li, *Adv. Mater.* **2017**, *29*, 1604437; c) X. L. Xu, W. H. Shi, P. Li, S. F. Ye, C. Z. Ye, H. J. Ye, T. M. Lu, A. A. Zheng, J. X. Zhu, L. X. Xu, M. Q. Zhong, X. H. Cao, *Chem. Mater.* **2017**, *29*, 6058–6065; d) S. G. Wang, J. W. Qin, T. Meng, M. H. Cao, *Nano Energy* **2017**, *39*, 626–638; e) J. S. Meng, C. J. Niu, L. H. Xu, J. T. Li, X. Liu, X. P. Wang, Y. Z. Wu, X. M. Xu, W. Y. Chen, Q. Li, Z. Z. Zhu, D. Y. Zhao, L. Q. Mai, *J. Am. Chem. Soc.* **2017**, *139*, 8212–8221; f) W. J. Zhou, J. Lu, K. Zhou, L. J. Yang, Y. T. Ke, Z. H. Tang, S. W. Chen, *Nano Energy* **2016**, *28*, 143–150; g) B. Y. Xia, Y. Yan, N. Li, H. B. Wu, X. W. Lou, X. Wang, *Nat. Energy* **2016**, *1*, 15006; h) P. P. Su, H. Xiao, J. Zhao, Y. Yao, Z. G. Shao, C. Li, Q. H. Yang, *Chem. Sci.* **2013**, *4*, 2941–2946; i) R. Das, P. Pachfule, R. Banerjee, P. Poddar, *Nanoscale* **2012**, *4*, 591.

[4] a) G. Huang, F. F. Zhang, L. L. Zhang, X. C. Du, J. W. Wang, L. M. Wang, *J. Mater. Chem. A* **2014**, *2*, 8048–8053; b) C. Scherb, R. Koehn, T. Bein, *J. Mater. Chem.* **2010**, *20*, 3046–3051.

[5] L. Shuang, C. Cheng, H. W. Liang, X. L. Feng, A. Thomas, *Adv. Mater.* **2017**, *29*, 1700707.

[6] a) Y. D. Ma, X. P. Dai, M. Z. Liu, J. X. Yong, H. Y. Qiao, A. X. Jin, Z. Z. Li, X. L. Huang, H. Wang, X. Zhang, *ACS Appl. Mater. Interfaces* **2016**, *8*, 34396–34404; b) T. Ma, M. W. Yuan, S. M. Islam, H. F. Li, S. L. Ma, G. B. Sun, X. J. Yang, *J. Alloys Compd.* **2016**, *678*, 468–477.

[7] T. Chen, Z. W. Zhang, B. R. Cheng, R. P. Chen, Y. Hu, L. B. Ma, G. Y. Zhu, J. Liu, Z. Jin, *J. Am. Chem. Soc.* **2017**, *139*, 12710–12715.

[8] T. Yamashita, P. Hayes, *Appl. Surf. Sci.* **2008**, *254*, 2441–2449.

[9] a) Q. Zhao, Z. H. Yan, C. C. Chen, J. Chen, *Chem. Rev.* **2017**, *117*, 10121–10211; b) H. Perron, T. Mellier, C. Domain, J. Roques, E. Simoni, R. Drot, H. Catalette, *J. Phys. Condens. Matter* **2007**, *19*, 346219.

[10] G. Jia, W. Zhang, G. Z. Fan, Z. S. Li, D. G. Fu, W. C. Hao, C. W. Yuan, Z. G. Zou, *Angew. Chem. Int. Ed.* **2017**, *56*, 13781–13785; *Angew. Chem.* **2017**, *129*, 13969–13973.

[11] D. S. Kong, H. T. Wang, Z. Y. Lu, Y. Cui, *J. Am. Chem. Soc.* **2014**, *136*, 4897–4900.

Angewandte Chemie

Eine Zeitschrift der Gesellschaft Deutscher Chemiker

Supporting Information

Bifunctional Electrocatalysts for Overall Water Splitting from an Iron/Nickel-Based Bimetallic Metal–Organic Framework/Dicyandiamide Composite

Xiaojia Zhao, Pradip Pachfule, Shuang Li, Jan Ron Justin Simke, Johannes Schmidt, and Arne Thomas*

anie_201803136_sm_miscellaneous_information.pdf
anie_201803136_sm_Movie.mp4

Chemical regents and materials

$FeCl_3 \cdot 6H_2O$ (97+%) and dicyandiamide (DCDA; 99.5%) were obtained from Acros Organics. $Ni(NO_3)_2 \cdot 6H_2O$ (98%) was acquired from Alfa Aesar. 1,4-benzenedicarboxylic acid (BDC; 98%) was obtained from abcr GmbH. Dimethylformamide (DMF; ≥99.5%, for synthesis) was obtained from Carl Roth. Unless otherwise stated, all the reagents were of analytical grade and were used as received. All aqueous solutions were prepared with DI water.

Experiment

Synthesis of MIL-88-Fe/Ni nanorods

MIL-88-Fe/Ni was synthesized according to the reported procedure.[1] In a typical synthesis, $FeCl_3 \cdot 6H_2O$ (0.1811g, 0.66 mmol), $Ni(NO_3)_2 \cdot 6H_2O$ (0.096g, 0.33 mmol), and 1,4-benzenedicarboxylic acid (BDC; 0.1661g, 0.99mmol) were mixed with DMF (10 mL) in a 25 mL Teflon-lined autoclave under stirring until the solution became clear. Then 2 mL NaOH (0.4 M) was added dropwise under stirring. After stirring for 15 min, the autoclave was transferred to normal oven and heated at 100 °C for different time (3h, 6h, 12h and 48h) to obtain MIL-88-Fe/Ni, which were donated as MIL-88-Fe/Ni-3h, MIL-88-Fe/Ni-6h, MIL-88-Fe/Ni-12h and MIL-88-Fe/Ni-48h. The products were filtered and washed with DMF and water for three times and finally dried at 60 °C for overnight. If no specific declaration has been made, MIL-88-Fe/Ni discussed in the paper refers to the MIL-88-Fe/Ni-48h.

Synthesis of Fe-Ni@NC catalysts

The as-synthesized MIL-88-Fe/Ni (50 mg) mixed with dicyandiamide (DCDA; 50 mg) were grinded slowly in a quartz mortar. Then the mixed solid powder was placed in the crucible and transferred to an argon oven at different temperatures (600 °C, 700 °C, 800 °C and 900 °C) for 3h with a ramp rate of 2 °C min^{-1} to obtain Fe-Ni@NC-CNTs electrocatalysts, which were donated as Fe-Ni@NC-CNTs-600, Fe-Ni@NC-CNTs-700, Fe-Ni@NC-CNTs-800 and Fe-Ni@NC-CNTs-900, respectively. If no specific declaration has been made, Fe-Ni@NC-CNTs discussed in the paper refers to the Fe-Ni@NC-CNTs-800.

Fe-Ni@NC-CNTs-3h, Fe-Ni@NC-CNTs-6h and Fe-Ni@NC-CNTs-12h were synthesized based on the same process as Fe-Ni@NC-CNTs-48h, by pyrolizing the

corresponding MIL-88-Fe/Ni (3h, 6h, 12h) precursors mixed with DCDA. If no specific declaration has been made, Fe-Ni@NC-CNTs discussed in the paper refers to the Fe-Ni@NC-CNTs-48h.

Fe-Ni@NC-CNTs-3h-acid, Fe-Ni@NC-CNTs-6h-acid and Fe-Ni@NC-CNTs-12h-acid were prepared by using 1.0 M HCl to etch the Fe-Ni@NC-CNTs with different time at room temperature. The products were filtered and washed with water and acetone for three times and finally dried at 60 °C for overnight.

The control samples, Fe-Ni@C was prepared by the same process as Fe-Ni@NC-CNTs, but without DCDA addition. Fe-Ni@NC-powder was synthesized by mixing $FeCl_3 \cdot 6H_2O$ (0.1811 g, 0.66 mmol), $Ni(NO_3)_2 \cdot 6H_2O$ (0.096 g, 0.33 mmol), 1,4-benzenedicarboxylic acid (BDC; 0.1661 g, 0.99 mmol) and DCDA (0.185 g, equal mass with obtained MIL-88-Fe/Ni), and then gridded to form a homogeneous viscous solid. The obtained solid powder was transferred to an argon oven at the same pyrolysis condition as Fe-Ni@NC-CNTs-800.

Electrochemical measurements

All electrochemical measurements were carried out in a three-electrode cell using a Gamry Reference 600 Potentiostat at room temperature. A RDE with a glassy carbon dish (5.0 mm diameter) severed as the working electrode. The graphite rod and Ag/AgCl (4.0 M KCl) were used as counter and reference electrodes, respectively. All measured potentials were converted to the reversible hydrogen electrode (RHE). The potential *vs* RHE was calibrated as $E_{RHE} = E_{Ag/AgCl} + 1.010$.

In a typical preparation of catalyst ink, 10 mg of each catalyst was blended with 1.0 ml Nafion ethanol solution (0.5 wt%) in an ultrasonic bath for 30 min. Then 10 µl of catalyst ink (10 mg mL^{-1}) was pipetted onto the glassy carbon surface and dried in ambient environment to form a catalyst film with a mass loading to 0.5 mg cm^{-2}. The measured hydrogen evolution reaction (HER) polarization curves were carried out in an N_2-saturated 1.0 M KOH electrolyte between 0.0 and -1.0 (*vs* RHE) with a sweep rate of 5 mV s^{-1} at 1600 r.p.m. For comparison, the commercial 20 wt% Pt on Vulcan carbon catalyst was measured under identical conditions. The measured oxygen evolution reaction (OER) polarization curves were carried out in an N_2-saturated 1.0 M KOH electrolyte between 1.0 and 2.0 (*vs* RHE) with a sweep rate of 5 mV s^{-1} at 1600

r.p.m. For comparison, the commercial 20 wt% Ir on Vulcan carbon black catalyst was measured under identical conditions. All polarization curves were corrected with IR-compensation.

Electrochemical active surface area (ECSA) was estimated by measuring the capacitance of the double layer at the solid-liquid interface with cyclic voltammetry (CV). The measurement was performed among a potential window of 0.51-0.61 V *vs* RHE, where the Faradic current on working electrode is negligible. The series of scan rates ranging from 40 to 120 mV s^{-1} were applied to build a plot of the charging current density differences against the scan rate at a fixed potential 0.56 V. The slope of the obtained linear is twice of the double-layer capacitance C_{dl}, which is used to estimate ECSA.

Electrochemical impedance spectroscopy (EIS) for HER and OER were carried out in an N_2-saturated 1.0 M KOH electrolyte from 10 kHz to 0.01 Hz with a 5 mV AC potential at 1600 r.p.m. The stability tests for the Fe-Ni@NC-CNTs were conducted using chronoamperometry at a constant applied overpotential.

Overall water splitting was performed in a two electrode cell using nickel foam as electrodes with dimensions of 1.0×1.0 cm^2 modified with catalysts with a loading of 1.0 mg cm^{-2}. To prepare the electrodes, nickel foam was first immersed in 0.6 M HCl for 30 min, then rinsed with acetone and ethanol in an ultrasonic bath for 10 min, respectively. Afterwards, the electrode was dried first in vacuum oven at 60 °C for 30 min and then drop coated with 100 µl of already prepared catalysts ink that prepared before with a concentration of 10.0 mg mL^{-1}. The modified nickel foam was then again dried in a vacuum oven at 60 °C for 30 min. Before measuring, the electrodes were first moistened by dipping in a mixture of ethanol and water (50:50 v/v), then multiple times in electrolyte.

The Faradaic efficiency was calculated by comparing the experimentally produced gas volume with the theoretically calculated one:

$$\eta_{Faraday} = V_{experimental} / V_{theoretical}$$

The experiment volume of H_2 or O_2 can be obtained from experiment data. The theoretical volume can be calculated using the formula:

$$V_{theoretical} = I \cdot t \cdot V_m / n \cdot F$$

Where I is the current measured in the experiment, t is the measured time, V_m is the molar volume of H_2 or O_2 in 1/mol, n is the number of electrons required for one molecule of H_2 or O_2 and F is the Faraday's constant (96485 C/mol).

Characterization:

PXRD patterns for the MOF and carbon samples were measured on a Bruker D8 Advance instrument with Cu Kα radiation (λ=1.54 Å) at a generator voltage of 40 kV and a generator current of 50 mA with a scanning speed of 5 °/min from 10° to 90° for carbon catalysts and 1 °/min from 5° to 50° for MIL-88-Fe/Ni samples. ICP-OES analyses were performed using ULTIMA-2. TEM and HR-TEM images were obtained from a Jeol-2100 and FEI Tecnai G^2 20 S-TWIN electron microscope at an operating voltage of 200 kV, respectively. The samples for TEM and HR-TEM analyses were prepared dispersing the electrocatalysts in ethanol, followed by dropping it onto a copper grid covered with carbon film. Nitrogen sorption measurements were carried out on a Quantachrome Quadrasorb SI instrument. All samples were degassed at 150 °C for 12 h before actual measurement. The surface area was calculated by using Brunauer-Emmett-Teller (BET) calculations and the pore sized distribution plot was obtained from the adsorption branch of isotherms based on "cylindr. pores, QSDFT adsorption branch" method. XPS spectra were performed on a Thermo Fisher Scientific ESCALAB 250Xi. The size of the X-ray spot on the sample is 100 µm.
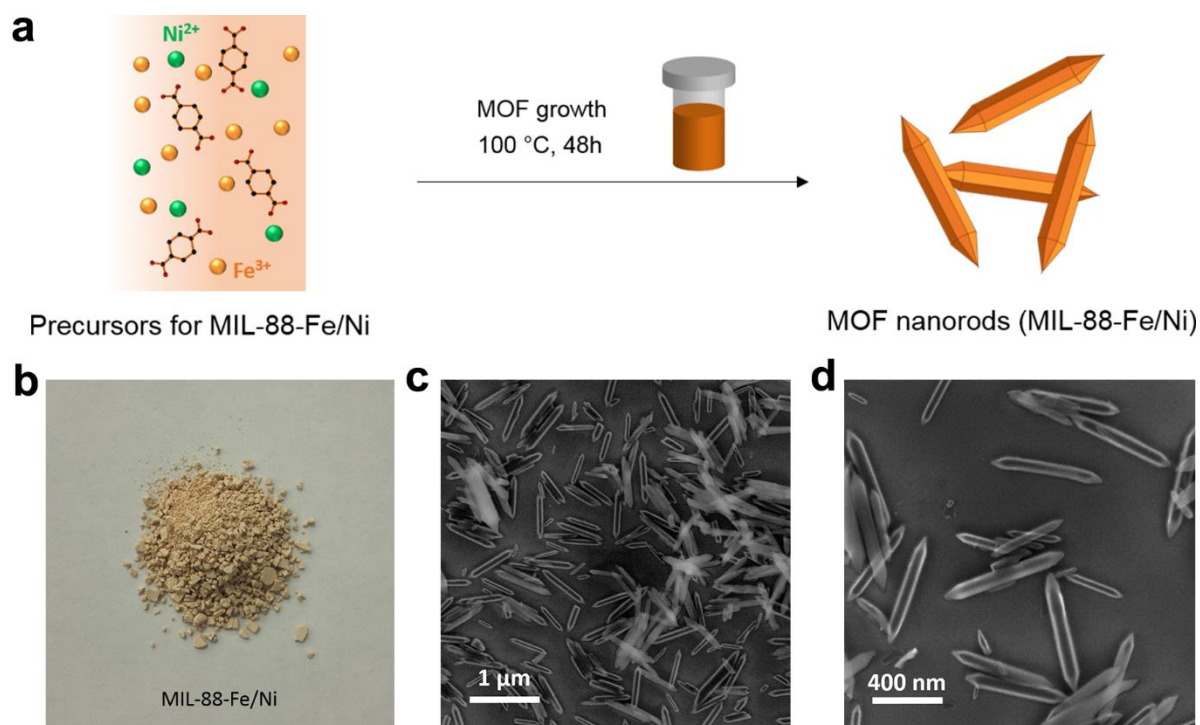
Figure S1. a) The process of the synthesis of MIL-88-Fe/Ni. b) Optical image, and c,d) SEM images of the as-synthesized MIL-88-Fe/Ni.
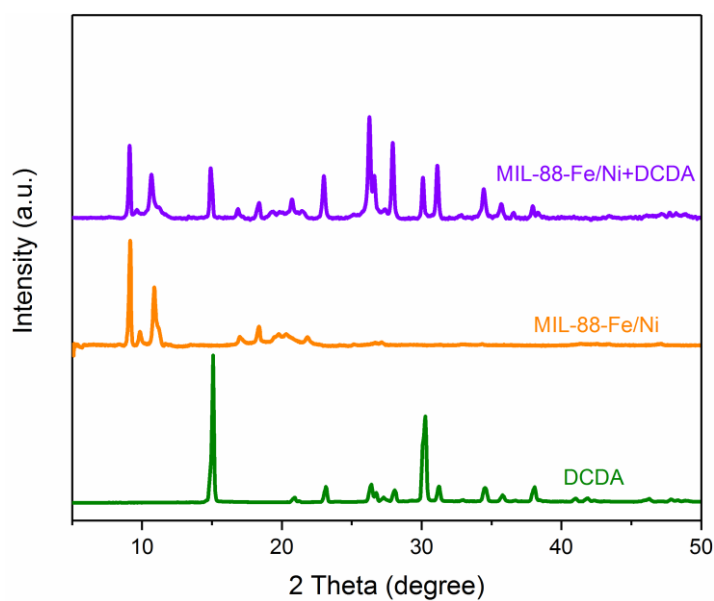
Figure S2. PXRD analyses of DCDA, MIL-88-Fe/Ni and MIL-88-Fe/Ni mixed with DCDA.
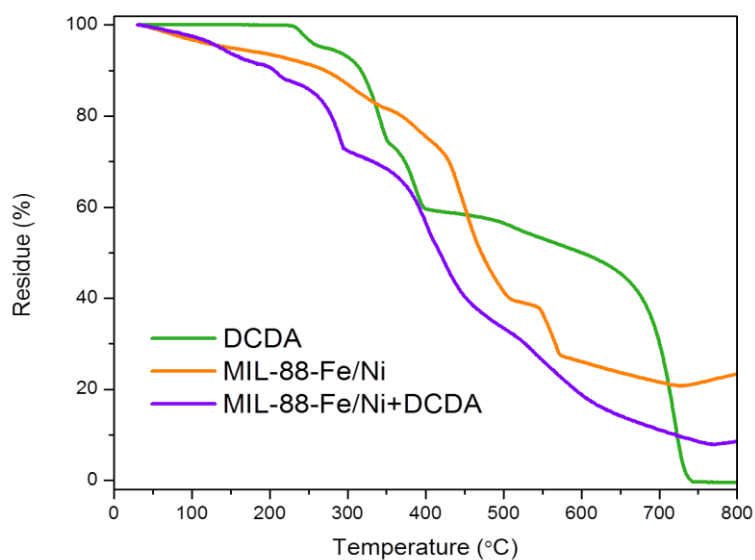
Figure S3. TGA analyses of DCDA, MIL-88-Fe/Ni and MIL-88-Fe/Ni mixed with DCDA.
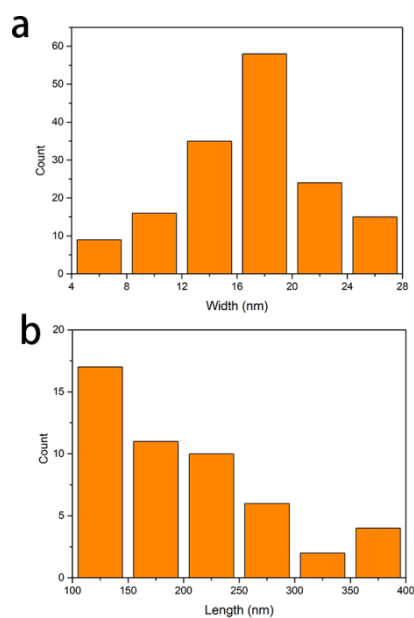
Figure S4. Distribution of the a) length and b) width of CNTs in Fe-Ni@NC-CNTs.
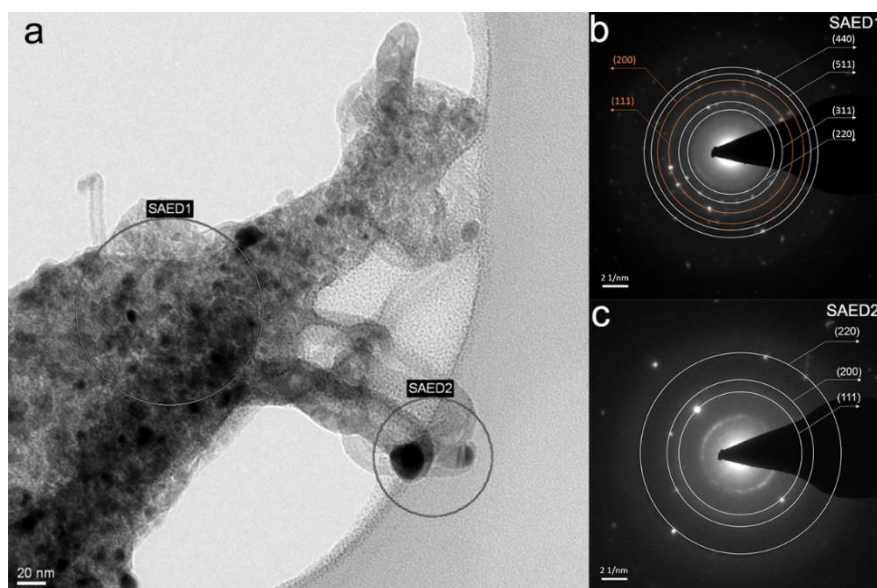
Figure S5. a) TEM image of the Fe-Ni@NC-CNTs sample. The corresponding SAED patterns b) SAED1, c) SAED2.
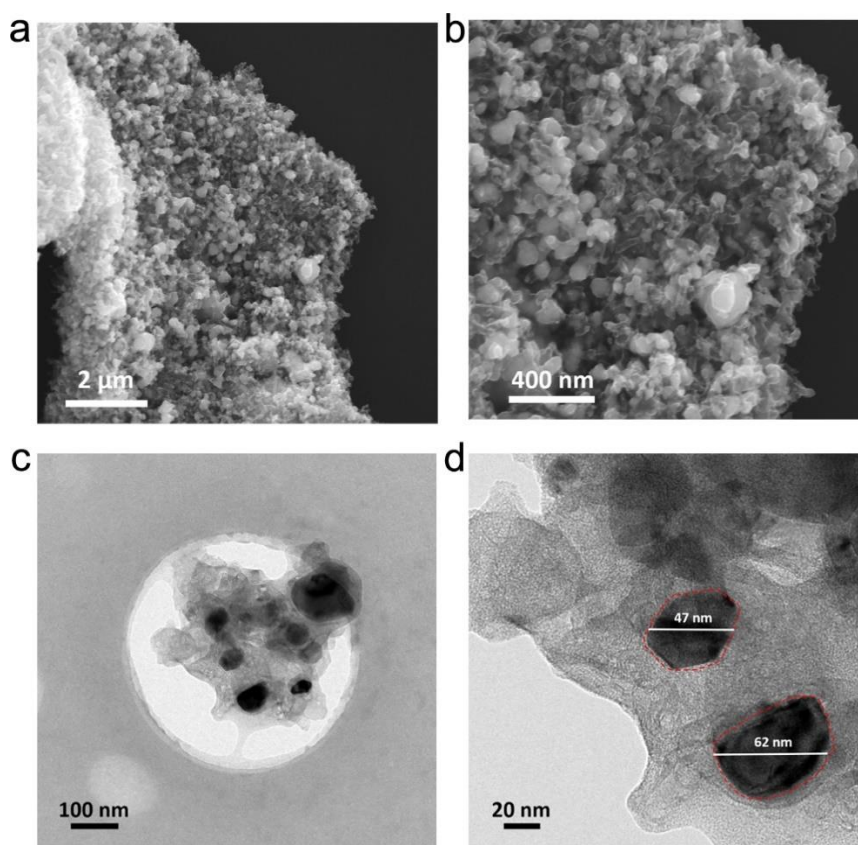
Figure S6. a, b) SEM, and c, d) TEM images of the Fe-Ni@C showing the complete destruction of morphologies of MOF-crystallites.
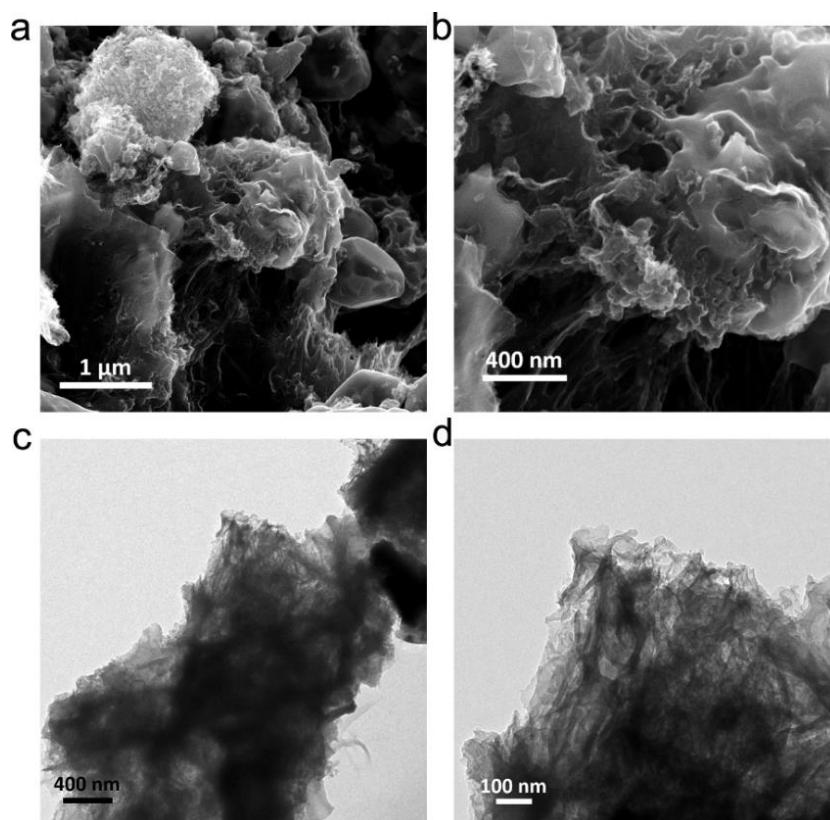
Figure S7. a, b) SEM, and c, d) TEM images of the Fe-Ni@NC-powder showing formation of agglomerated metal nanoparticles and carbon materials.
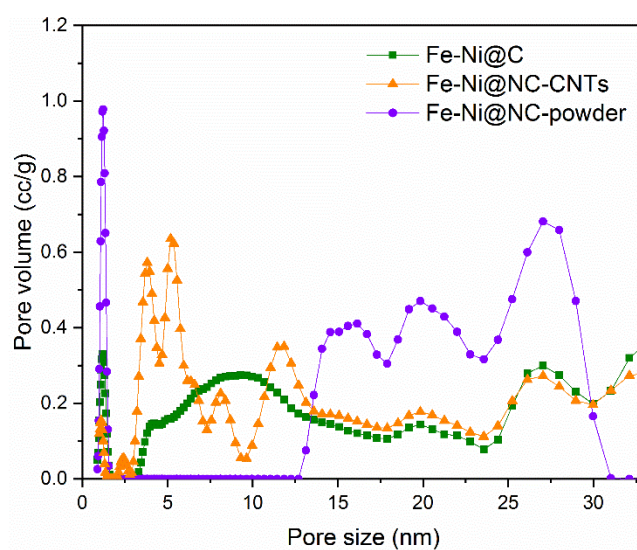
Figure S8. Pore size distribution of Fe-Ni@C, Fe-Ni@NC-CNTs and Fe-Ni@NC-powder, calculated by QSDFT.

Table S1. Structure and textural properties of the obtained Fe-Ni@NC electrocatalysts.

Samples	[a]Total surface area $(m^2\,g^{-1})$	[b] Total pore volume $(cm^3\,g^{-1})$	[c]Micropore area $(m^2\,g^{-1})$
Fe-Ni@C	206	0.662	20
Fe-Ni@NC-CNTs	246	0.690	12
Fe-Ni@NC-powder	401	0.512	255

[a]BET specific surface areas calculated in P/P_0 from 0.003 to 0.05. [b]Total pore volumes calculated based on the volume adsorbed at P/P_0 of ~ 0.995. [c]Micropores surface areas evaluated through the t-plot method.
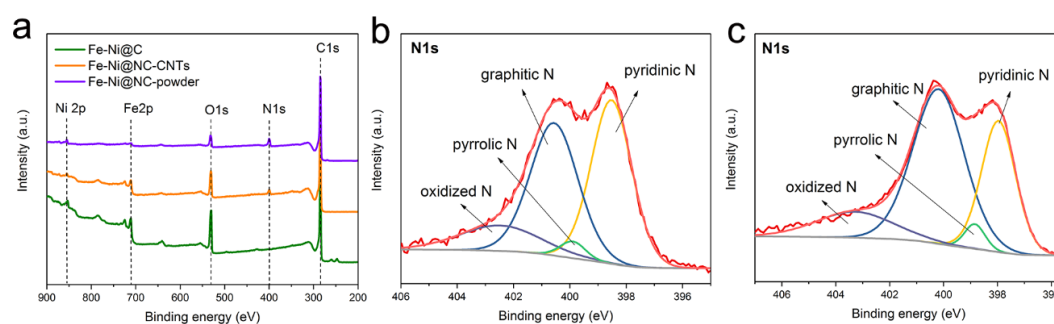
Figure S9. a) Survey scan of the Fe-Ni@C, Fe-Ni@NC-CNTs and Fe-Ni@NC-powder. b) The deconvolution of magnified N1s XPS spectra of Fe-Ni@NC-CNTs. c) The deconvolution of magnified N1s XPS spectra of Fe-Ni@NC-powder.
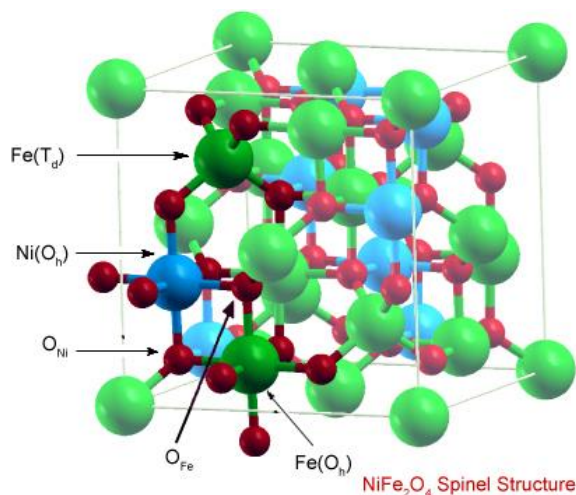
Figure S10. The inverse spinel structure of $NiFe_2O_4$ showing the coordination of Ni, Fe and O in 3-dimenstions.[2] Ni atoms are shown in blue, Fe atoms in green and O atoms in red.
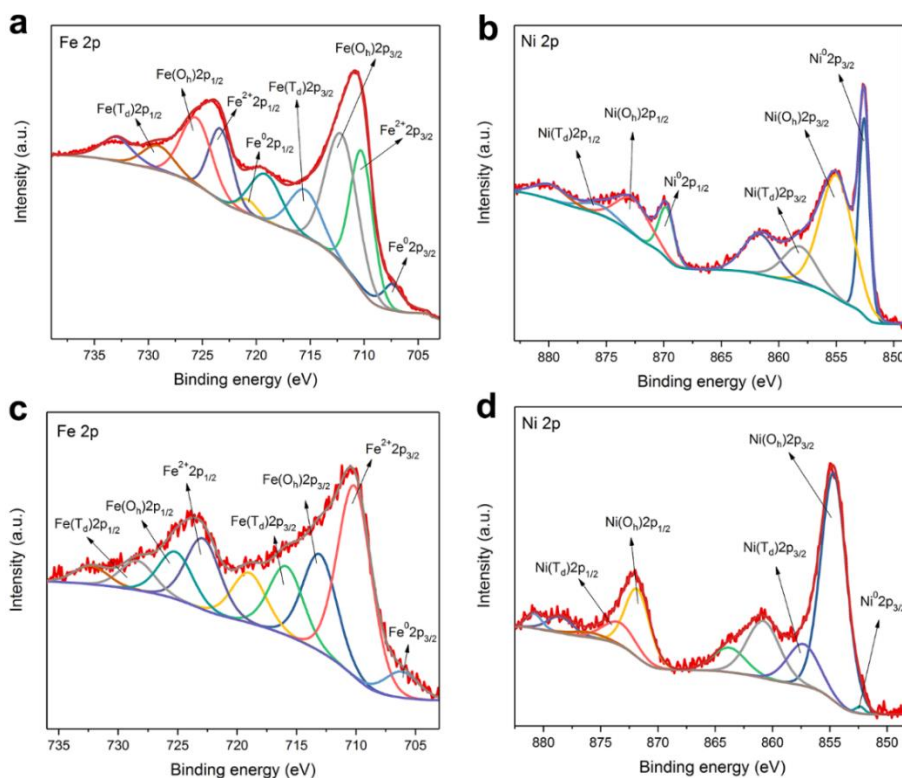
Figure S11. a) Fe2p and b) Ni2p spectra for Fe-Ni@C. c) Fe2p and d) Ni2p spectra for Fe-Ni@NC-powder.
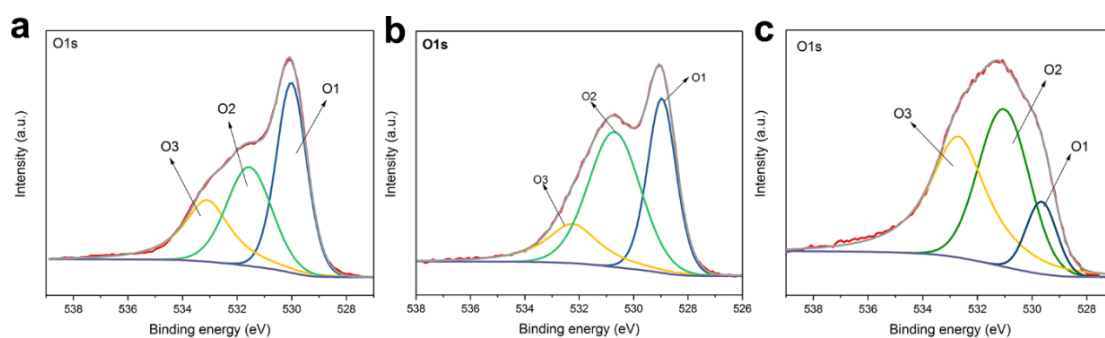
Figure S12. O1s spectra for a) Fe-Ni@C, b) Fe-Ni@NC-CNTs and c) Fe-Ni@NC-powder.

The appearance of peak corresponding to Fe^{2+} $2p_{3/2}$ indicates the oxygen vacancy due to charge neutrality.[3] The oxygen vacancy concentration (O2) was calculated from the integrated intensity (**Table S2**).

Table S2. The O concentration of the obtained Fe-Ni@NC electrocatalysts.

Sample Name	O / at. %	O2 / %
Fe-Ni@C	16.79	36.0
Fe-Ni@NC-CNTs	10.30	51.6
Fe-Ni@NC-powder	6.26	45.5
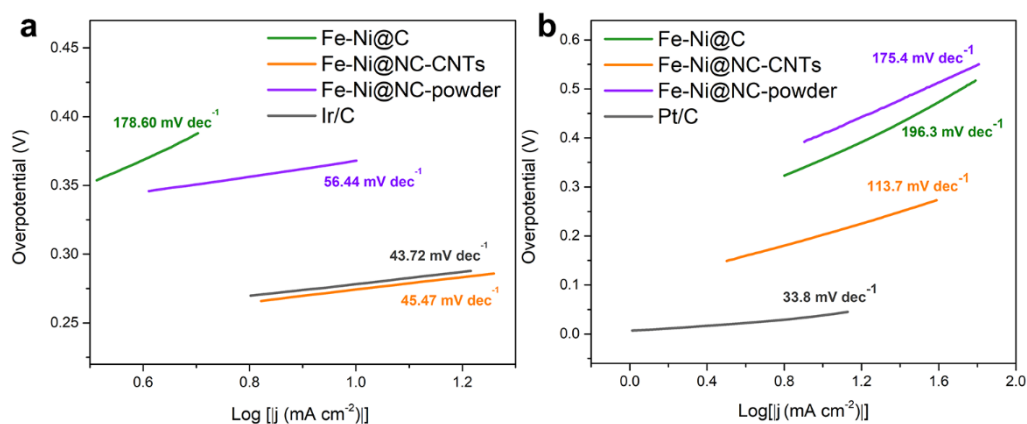
Figure S13. The corresponding Tafel plots for Fe-Ni@C, Fe-Ni@NC-CNTs, Fe-Ni@NC-powder and commercial noble metal-based catalyst under alkaline condition: a) OER and b) HER.

Table S3. The OER performance of the as-synthesized Fe-Ni@NC samples

Sample Name	Onset potential (mV)	Overpotential at 10 mA cm^{-2} (mV)	Tafel slope (mV dec^{-1})
Fe-Ni@C	320	470	178.6
Fe-Ni@NC-CNTs	220	274	45.47
Fe-Ni@NC-powder	330	370	56.44
Ir/C	240	278	43.72

Table S4. The Comparison of the OER performance of Fe-Ni@NC-CNTs with that of reported non-precious metal electrocatalysts tested under similar conditions.

Electrocatalysts	$E_j=10$ mA cm^{-2} (mV)	Tafel slope (mV dec^{-1})	electrolyte	substrate	references
Fe-Ni@NC-CNTs	**274**	**45.47**	**1 M KOH**	**GCE**	**This work**
Co$_1$Mn$_1$CH/NF	294 ($E_j=30$)		1 M KOH	Nickel foam	*J. Am. Chen. Soc.* **2017**, *139, 8320-8328*
Co$_2$B-500	380	45.0	1 M KOH	GCE	*Adv. Energy. Mater.* **2016**, *6, 1502313*
Cu$_{0.3}$Co$_{2.7}$P/NC	190	44	1 M KOH	GCE	*Adv. Energy. Mater.* **2017**, *7, 1601555*
W$_{0.5}$Co$_{0.4}$Fe$_{0.1}$/NF	310	32	1 M KOH	Nickel foam	*Angew. Chem. Int. Ed.* **2017**, *56, 4502-4506*
Polyoxometalate/NF	360	126	0.1 M KOH	Nickel foam	*Angew. Chem. Int. Ed.* **2017**, *56, 4941-4944*
N-doped carbon	158	93.4	1 M KOH	Copper tape	*Nat. Commun.* **2017**, *8, 13592*
Ni$_{0.9}$Fe$_{0.1}$/NC	330	45	1 M KOH	GCE	*ACS Catal.* **2016**, *6, 580-588*
Co-P	345	47	1 M KOH	Copper foils	*Angew. Chem. Int. Ed.* **2015**,*54,6251*
Ni$_3$Se$_2$-GC	310	79.5	0.3 M KOH	Au-coated glass	*Energy Environ. Sci.* **2016**, *9, 1771*
NiFeOx/CFP	280	31.5	1 M KOH	Carbon nanofibe	*Nat. Commun.* **2015**, *6, 7261*
FeB$_2$	296	52.4	1 M KOH	GCE	*Adv. Energy. Mater.* **2017,** *7, 1700513*
CoMn LDH	320	43	1M KOH	GCE	*J. Am. Chem. Soc.* **2014**,*136,16481*
NiFe LDH	250	–	1.0 M NaOH	GCE	*Science* **2014**, *345, 1593*
NiFe LDH/NF	240	–		Nickel foam	
NiFe-NS	302	40	1 M KOH	GCE	*Nat. Commun.* **2014**, *5, 4477*
Ni-Fe film	280	~40	0.1 M KOH		*J. Am. Chem. Soc.* **2013**,*135,12329*

Table S5. The HER performance of the as-synthesized Fe-Ni@NC samples

Sample Name	Onset potential (mV)	Overpotential at 10 mA cm^{-2} (mV)	Tafel slope (mV dec^{-1})
Fe-Ni@C	311	356	196.3
Fe-Ni@NC-CNTs	123	202	113.7
Fe-Ni@NC-powder	237	409	175.4
Ir/C	14	39	33.8

Table S6. The comparison of the HER performance of Fe-Ni@NC-CNTs with that of reported non-precious metal electrocatalysts tested under similar conditions.

Electrocatalysts	E$_j$=10 mA cm^{-2} (mV)	Tafel slope (mV dec^{-1})	Electrolyte	Substrate	References
Fe-Ni@NC-CNTs	202	113.7	1 M KOH	GCE	This work
Co$_1$Mn$_1$CH/NF	180	–	1 M KOH	Nickel foam	*J. Am. Chen. Soc.* **2017**, *139, 8320-8328*
Co$_2$B-500	328	177	1 M KOH	GCE	*Adv. Energy. Mater.* **2016**, *6, 1502313*
Cu$_{0.3}$Co$_{2.7}$P/NC	220	122	1 M KOH	GCE	*Adv. Energy. Mater.* **2017**, *7, 1601555*
Co-MoS$_2$	203	158	1 M KOH	GCE	*Energy. Environ. Sci.* **2016**, *9, 2789*
CoSe$_2$/carbon cloth	190	85	1 M KOH	Carbon cloth	*Adv. Mater.* **2016**, *28, 7527*
NiCo$_2$O$_4$	110	49.7	1 M NaOH	GCE	*Angew. Chem. Int. Ed.* **2016**, *55, 6290*
(Co-NMC)$_1$/NC	220	81	0.1 M KOH	GCE	*Small* **2016**, *12, 3703-3711*
EG/Co$_{0.85}$Se/NiFe-LDH	260	160	1 M KOH	GCE	*Energy. Environ. Sci.,* **2016**, *9, 478*
Ni$_5$P$_4$ nanosheets on Ni foil	150	53	1 M KOH	Nickel foam	*Angew. Chem. Int. Ed.* **2015**, *54, 12361*
Ni$_3$S$_2$/NF	223	–	–	Nickel foam	*J.Am.Chem.Soc.***2015**,*137,14023*
Porous Co-P film	380	–	1 M KOH	–	*Adv. Mater.* **2015**, *27, 3175*

CoP nanowire array	209	129	1 M KOH	Carbon cloth	*J. Am. Chem. Soc.* **2014**, *136, 7587*
Co-NRCNTs	370	–	1 M KOH	GCE	*Angew. Chem. Int. Ed.* **2014**, *53, 4372*
FeP	218	146	1 M KOH	Carbon cloth	*ACS Catal.* **2014**, *4, 4065*
Ni$_2$P nanoparticles	170	–	1 M KOH	Titanium foil	*J. Am. Chem. Soc.* **2013**, *135, 9267*
N-Ni$_3$S$_2$/ NF	110	–	1 M KOH	Nickel foam	*Adv. Mater.* **2017**, *29, 1701584*
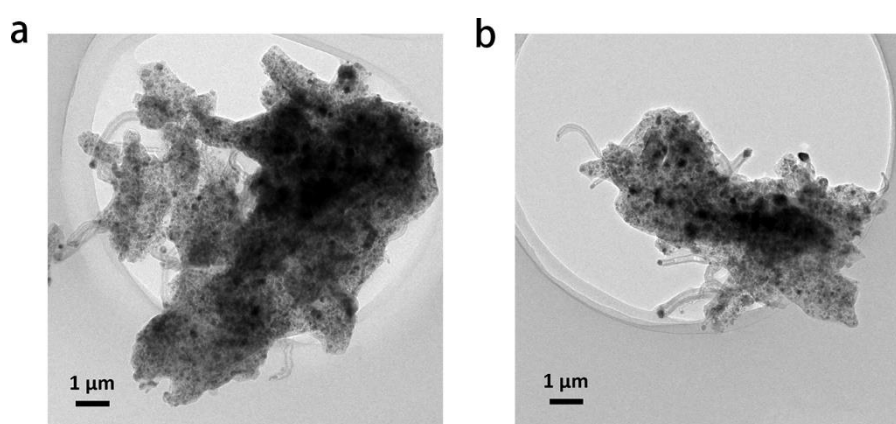
Figure S14. TEM images of Fe-Ni@NC-CNTs a) OER, b) HER after 40.000s electrocatalysis reaction.
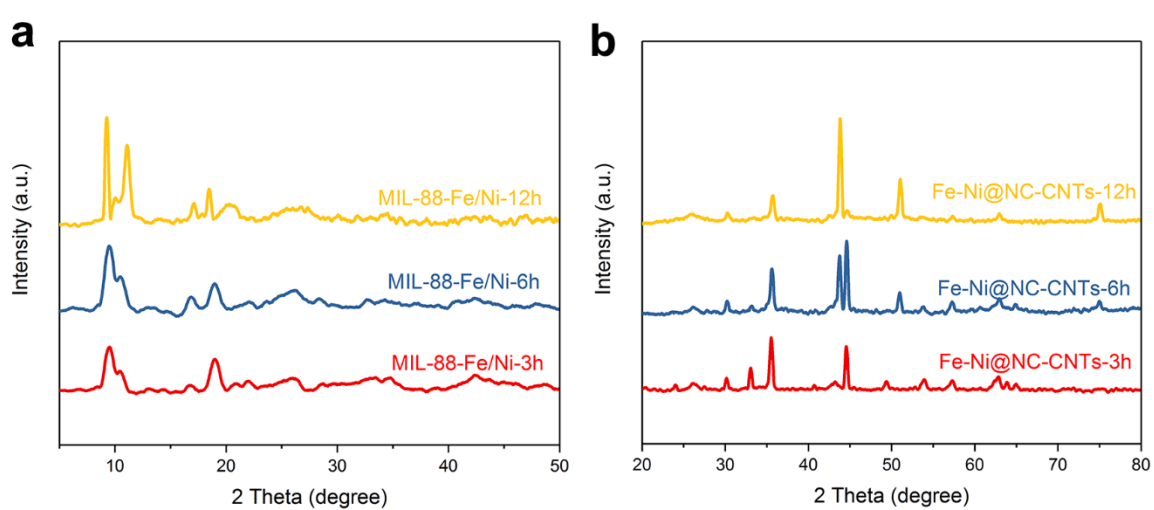
Figure S15. PXRD pattern of a) MIL-88-Fe/Ni with different solvothermal time, b) corresponding MOF-derived carbon samples.
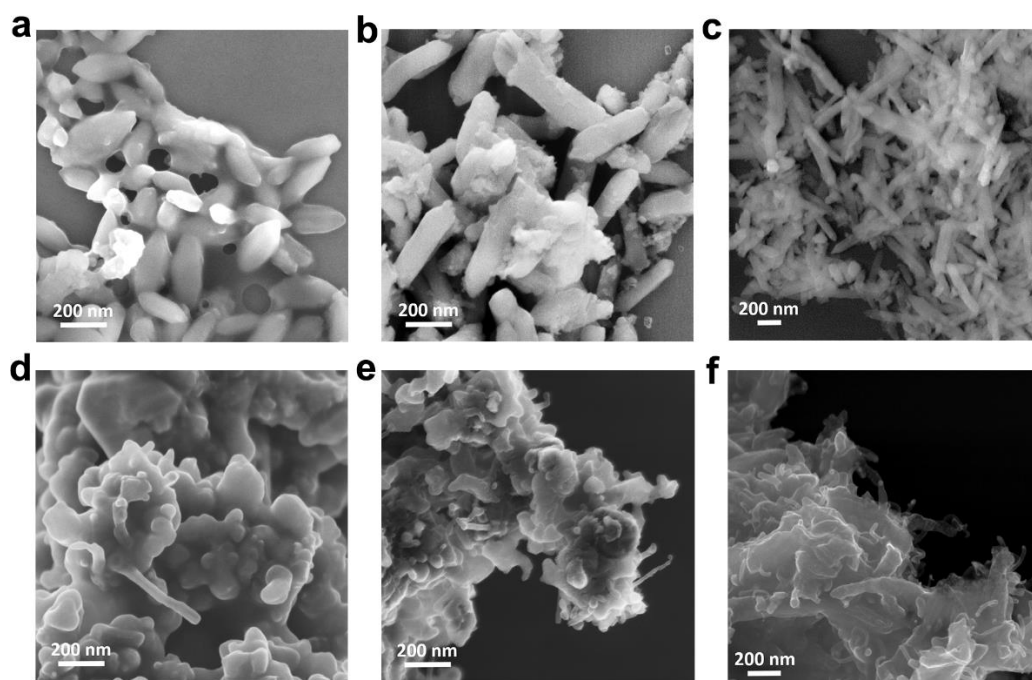
Figure S16. SEM images of a) MIL-88-Fe/Ni-3h, b) -6h, c) -12h and d) Fe-Ni@NC-CNTs-3h, e) -6h, f) 12h.
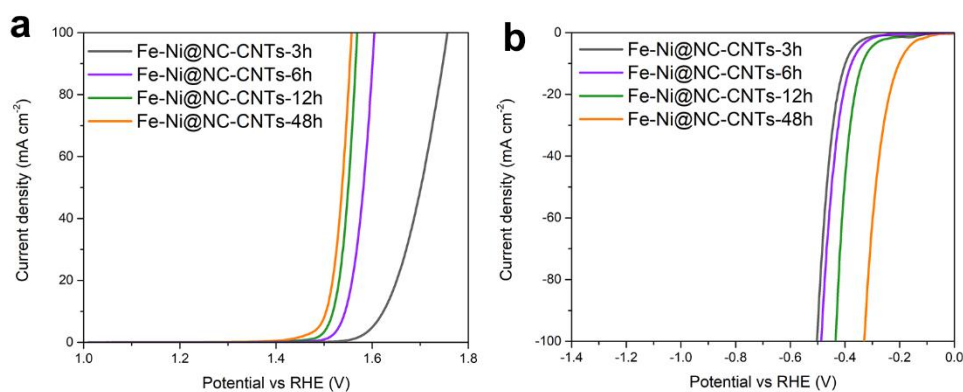
Figure S17. a) The OER polarization curves, and b) HER polarization curves of the Fe-Ni@NC-CNTs-3h, Fe-Ni@NC-CNTs-6h, Fe-Ni@NC-CNTs-12h and Fe-Ni@NC-CNTs-48h.
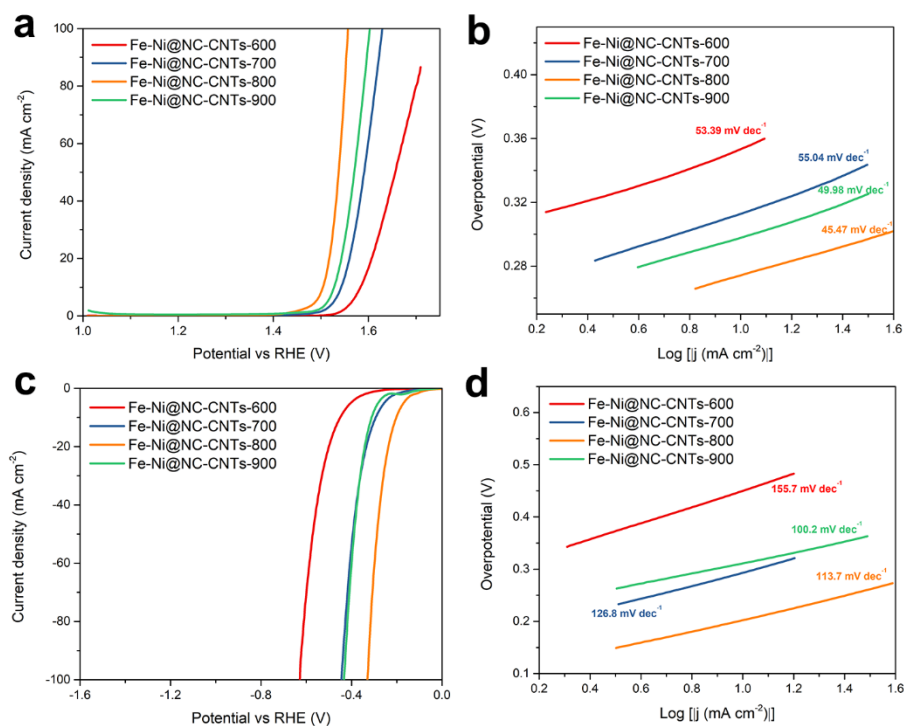
Figure S18. a) The OER polarization curves, and b) the corresponding Tafel plots of the Fe-Ni@NC-CNTs at different pyrolysis temperatures. c) The HER polarization curves, and d) the corresponding Tafel plots of the Fe-Ni@NC-CNTs at different pyrolysis temperature.
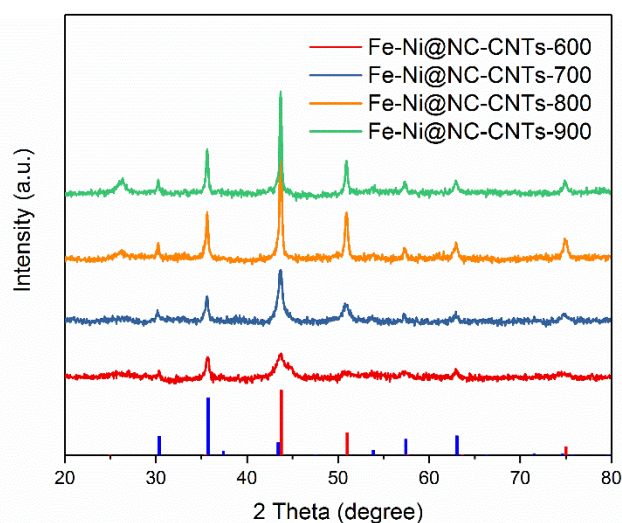
Figure S19. XRD patterns of the Fe-Ni@NC-CNTs at different pyrolysis temperature.
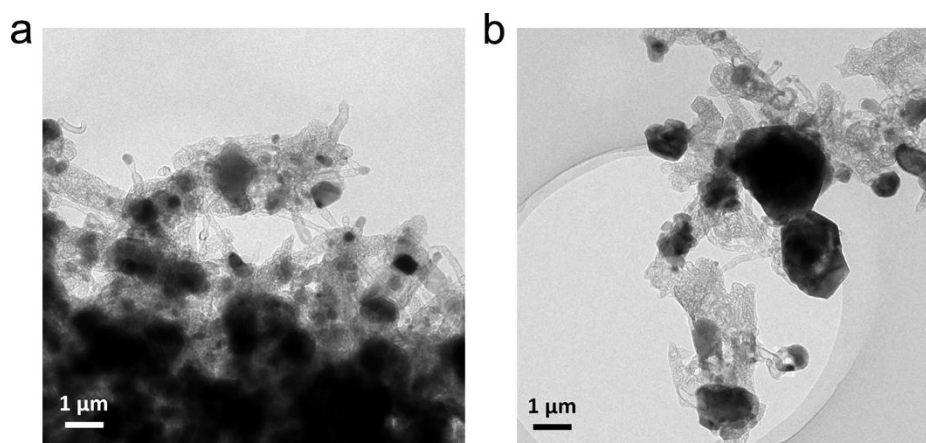
Figure S20. TEM images of the Fe-Ni@NC-CNTs synthesized at 900 °C.
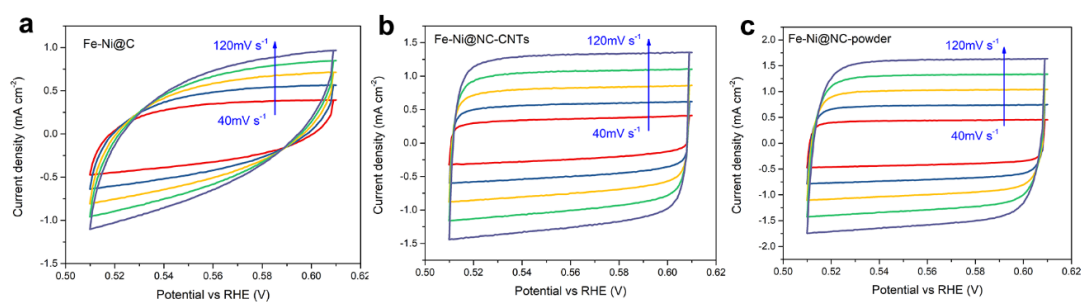
Figure S21. CVs of a) Fe-Ni@C, b) Fe-Ni@NC-CNTs, c) Fe-Ni@NC-powder in 1.0 M KOH at different scan rates from 40, 60, 80, 100 and 120 mV s^{-1}. The measurement was performed among a potential window of 0.51-0.61 V *vs* RHE, where the Faradic current on working electrode is negligible.
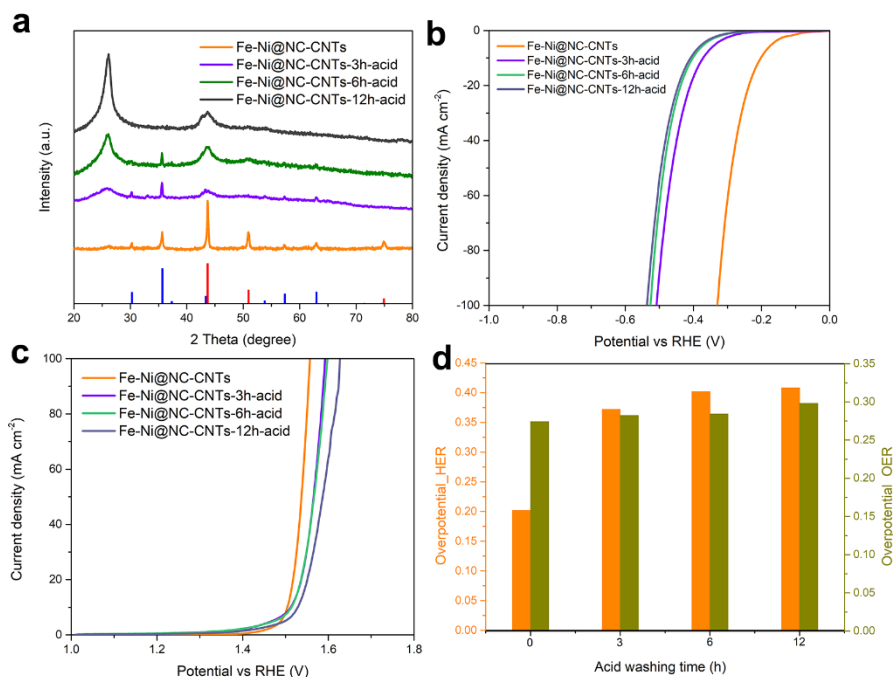
Figure S22. a) PXRD analyses of Fe-Ni@NC-CNTs after different etching time in 1.0 M HCl. (the simulated patterns of $FeNi_3$ and $NiFe_2O_4$ are shown in red and blue colors, respectively). Note that after 3h the peaks for $FeNi_3$ have nearly disappeared which strongly influences the HER (b) but less the OER (c) performance of Fe-Ni@NC-CNTs. d) Overpotential difference of Fe-Ni@NC-CNTs with different etching time at 10 mA cm^{-2}.
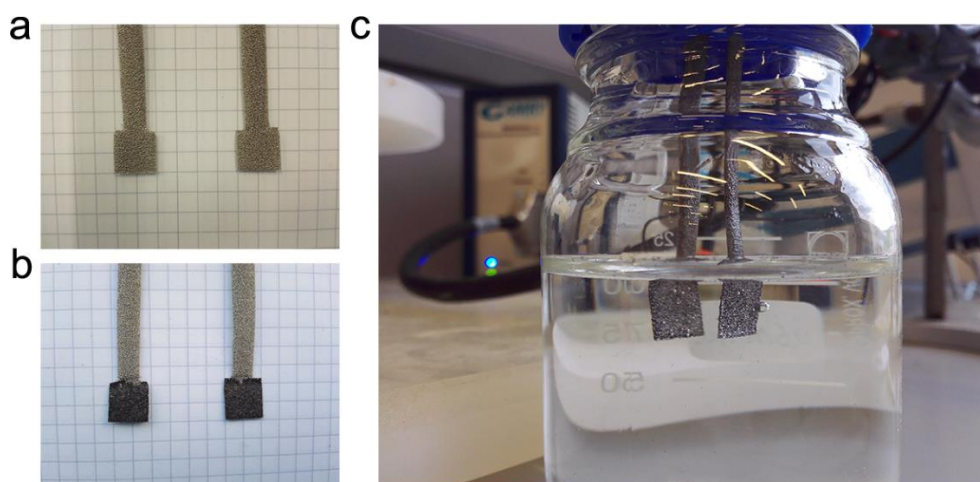
Figure S23. The photographs of lab-made nickel foam electrode and the corresponding assembled electrolyzer. a) Pure nickel foam electrodes (1.0×1.0 cm^2). b) Nickel foam electrodes coated with electrocatalysts (1.0×1.0 cm^2, mass loading: 1.0 mg cm^{-2}). c) The working electrolyzer in 1.0 M KOH solution.
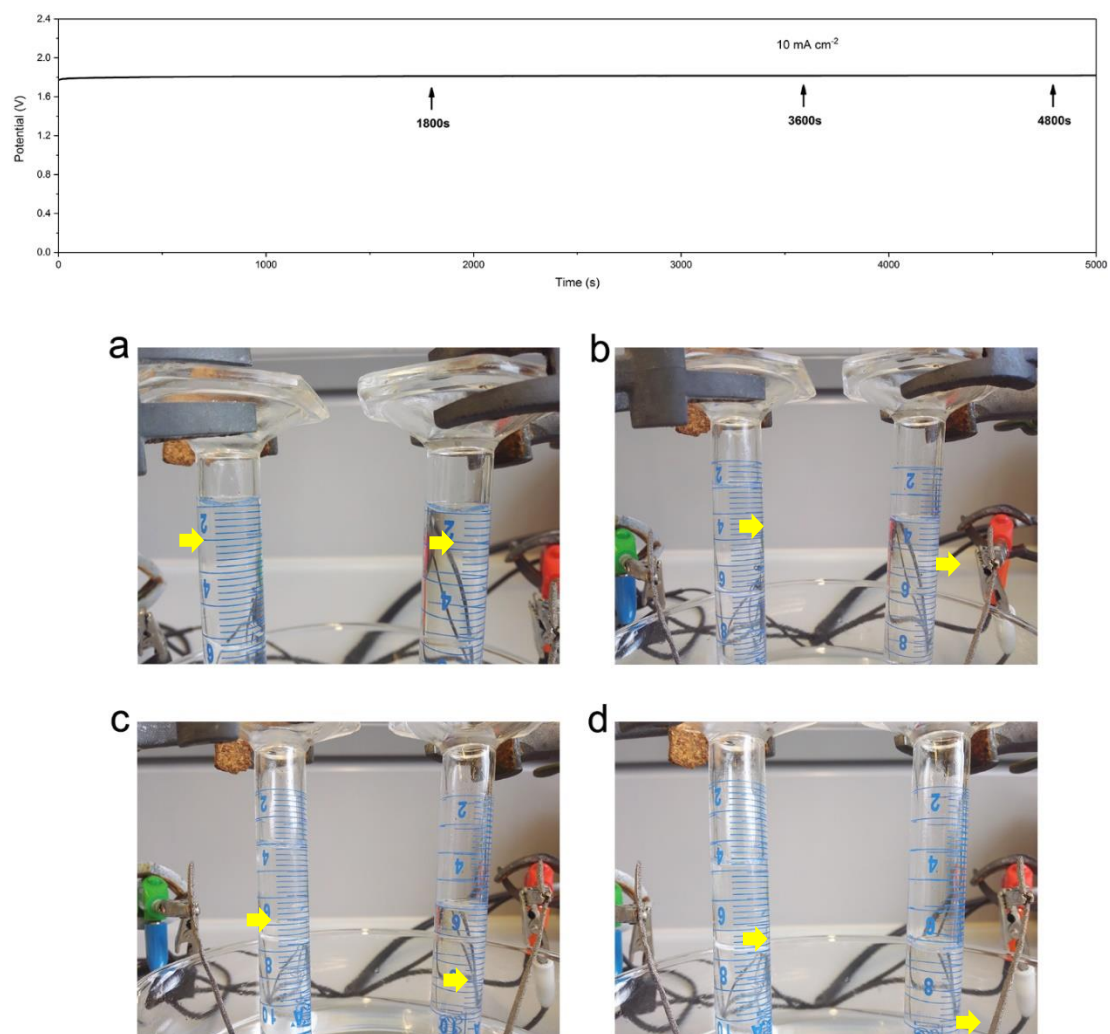
Figure S24. Chronopotentiometry of the Fe-Ni@NC-CNTs electrocatalyst (top), and photographs of lab-made gas collectors at the time of: a) 0s, b) 1800, c) 3600s, and d) 4800s.

Table S7. Faradaic efficiency of the produced hydrogen and oxygen amount during the water-splitting process.

Time/s	H$_2$			O$_2$		
	V$_{experimental}$/ml	V$_{theoritical}$/ ml	ηFaraday/%	V$_{experimental}$/ml	V$_{theoritical}$/ ml	ηFaraday/%
0	0	0	0	0	0	0
600	0.64	0.6964	91.89	0.31	0.3482	89.01
1200	1.3	1.3929	93.32	0.65	0.6964	93.32
1800	2	2.0894	95.71	1	1.0447	95.71
2400	2.7	2.7859	96.91	1.35	1.3929	96.91
3000	3.4	3.4824	97.63	1.72	1.7412	98.78
3600	4.1	4.1788	98.11	2	2.0894	95.71
4200	4.8	4.8753	98.45	2.4	2.4376	98.45
4800	5.4	5.5718	96.92	2.7	2.7859	96.91

Reference

[1] G. Huang, F. F. Zhang, L. L. Zhang, X. C. Du, J. W. Wang, L. M. Wang, *J. Mater. Chem. A* **2014**, 2, 8048-8053.

[2] H. Perron, T. Mellier, C. Domain, J. Roques, E. Simoni, R. Drot, H. Catalette, *J. Phys.: Condens. Matter* **2007**, 19, 346219.

[3] B,Sarkar, B. Dalal, V. D. Ashok, K. Chakrabarti, A. Mitra, S. K. De, *J. Appl. Phys.* **2014,** 115, 123908

8.3 Silica-Templated Covalent Organic Framework-derived Fe-N-doped Mesoporous Carbon as Oxygen Reduction Electrocatalyst

Published version

X. J. Zhao, P. Pachfule, S. Li, T. Langenhahn, M. Y. Ye, G. Y. Tian, J. Schmidt, A. Thomas, Silica-Templated Covalent Organic Framework-derived Fe-N-doped Mesoporous Carbon as Oxygen Reduction Electrocatalyst, *Chem. Mater.* **2019**, 31, 3274-3280

Silica-Templated Covalent Organic Framework-Derived Fe−N-Doped Mesoporous Carbon as Oxygen Reduction Electrocatalyst

Xiaojia Zhao,[†] Pradip Pachfule,[†] Shuang Li,[†] Thomas Langenhahn,[†] Mengyang Ye,[†] Guiying Tian,[‡] Johannes Schmidt,[†] and Arne Thomas*[,†]

[†]Functional Materials, Department of Chemistry, Technische Universität Berlin, Hardenbergstr. 40, 10623 Berlin, Germany

[‡]Institute for Applied Materials (IAM-ESS), Karlsruhe Institute of Technology (KIT), Hermann-von-Helmholtz-Platz 1, 76344 Karlsruhe, Germany

S *Supporting Information*

ABSTRACT: The rational design and synthesis of mesoporous functional materials is of great significance to tackle fundamental challenges in materials science and to yield practical solutions for efficient energy utilization. Here, a novel *p*-toluenesulfonic acid-assisted mechanochemical approach is used to prepare a silica-templated bipyridine-containing covalent organic framework (COF), which can be further converted into an iron−nitrogen-doped mesoporous carbon (mC-TpBpy-Fe) upon carbonization and template removal. The resulting mC-TpBpy-Fe exhibits a large pore volume and surface area, which significantly promote the mass transfer efficiency and increase the accessibility of the active sites, yielding a high ORR activity with a competitive half-wave potential of 0.845 V and limiting current density of 5.92 mA/cm^2 (vs 0.852 V and 5.57 mA/cm^2 for Pt/C). Application of this COF derived mesoporous carbon within a Zn−air battery revealed that it can operate in ambient conditions with a competitive discharge performance, showing its potential for practical applications.

INTRODUCTION

To meet the growing energy demands in a low-carbon economy, the development of new materials that improve the efficiency of energy conversion and storage systems is essential.[1] Recently, porous carbon-based materials have attracted attention in energy conversion and storage owing to their unique properties, such as large specific surface area and pore volume, good electronic conductivity, and high structural stability.[2−5] One of the most widely employed applications of such porous carbonaceous materials is catalysis of the oxygen reduction reaction (ORR), which is the core electrochemical process in metal−air batteries and fuel cells. In particular, transition-metal-coordinated nitrogen-doped carbon catalysts (MNCs, M = Fe, Co, Ni, Mo, etc.) were suggested to be one of the most suitable non-noble metal based catalysts for ORR due to their high efficiency and considerable stability.[6−11] Recently, it has been shown that carbonaceous materials with mesoporous structures promote electrolyte infiltration and mass transfer during the electrocatalytic process, which further improves the ORR activity.[1,11] To achieve the synthesis of such mesoporous carbons, traditional carbon precursors such as polypyrrole (PPy),[12] polyaniline (PANI),[10] polydopamine (PDA),[11] and graphene[13] were widely studied, and hard and soft templating approaches were used for generating mesopores in the materials.[1,3] For example, Feng et al. developed a family of mesoporous Fe−N−C catalysts, which exhibit remarkable ORR activities, using silica NPs, ordered

mesoporous silica, and montmorillonite as templates.[14] Considering the promising properties of mesoporous carbon structures, there is an increasing interest to explore new carbon precursors for the facile generation of efficient mesoporous ORR catalysts.

Porous framework structures such as metal organic frameworks (MOFs), porous polymers, and covalent triazine frameworks (CTFs) have been frequently studied as materials for energy storage and conversion.[15−21] For example, MOFs, constructed by bridging metal atoms and ligands into three-dimensional (3D) ordered frameworks, have recently been used to fabricate a variety of M−N−C electrocatalysts by pyrolysis.[6,7,22−25] Similarly, covalent organic frameworks (COFs), the fully organic counterparts of MOFs, have been applied as prescursors for porous carbon materials.[26−33] For example, Jiang et al. used phytic acid to guide pyrolysis and convert the 2D COF into high-performance carbon sheets for ORR applications.[26] However, MOF and COF derived carbons usually exhibit bulk structures with very low porosity, which largely decrease the accessible surface area for the electrolyte and decelerate mass transfer.[26,32] Although several COF derived heteroatom-doped carbons have been reported and applied as electrocatalysts, a facile method to convert COFs
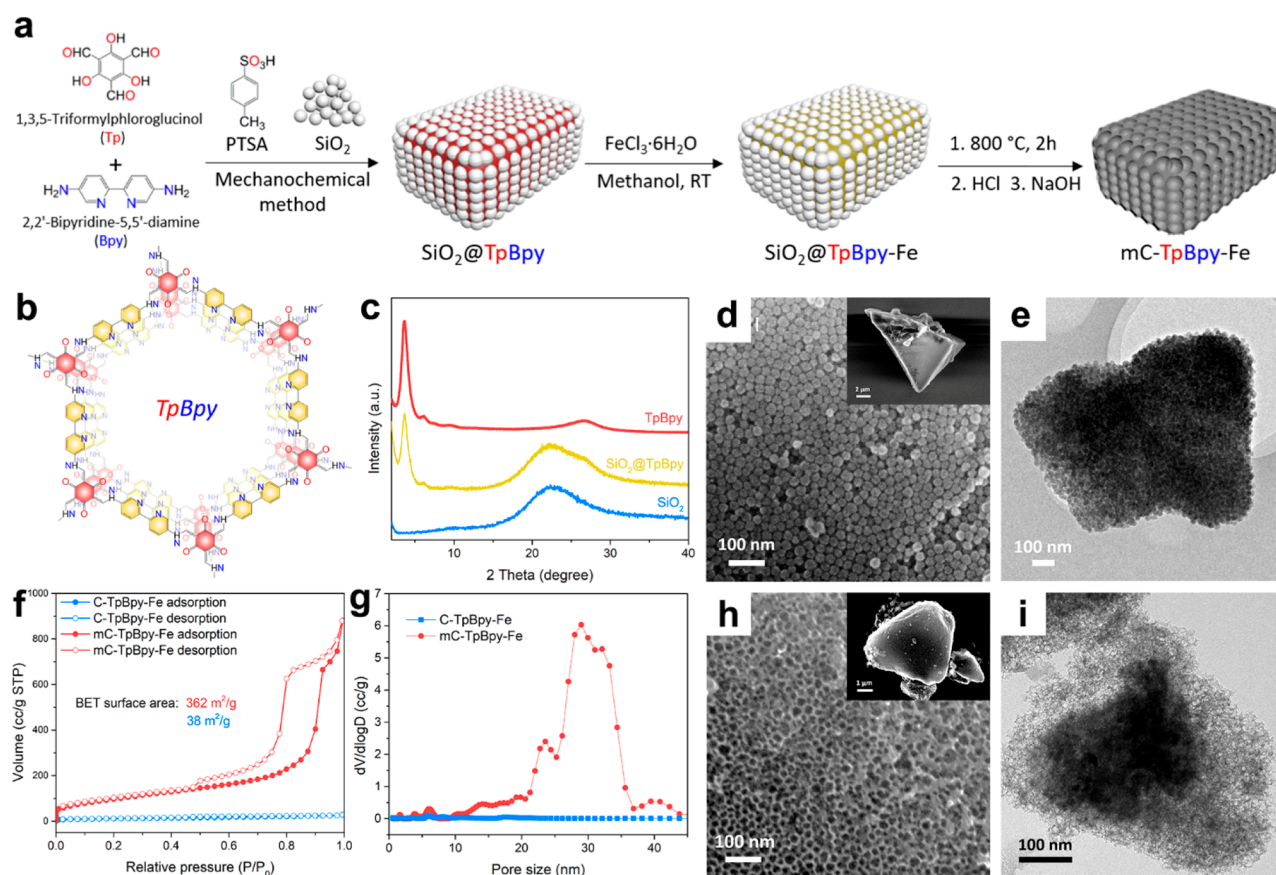
Article

Figure 1. Synthesis and characterization of COF and carbon structures. (a) Synthesis of mC-TpBpy-Fe via PTSA-assisted mechanochemical method, in the presence of silica nanoparticles. (b) Packing diagram of TpBpy showing the bipyridine coordination sites available in the COF backbone. (c) PXRD patterns of TpBpy, SiO$_2$@TpBpy, and SiO$_2$. (d) SEM and (e) TEM images of SiO$_2$@TpBpy. (f) N$_2$ adsorption−desorption isotherms of C-TpBpy-Fe and mC-TpBpy-Fe. (g) Pore size distribution of C-TpBpy-Fe and mC-TpBpy-Fe, calculated from the adsorption branch of isotherms by the QSDFT model. (h) SEM and (i) TEM images of mC-TpBpy-Fe.

into transition-metal and heteroatom-doped carbons with defined mesoporosity is so far not available.

Herein, a novel approach is described in which a silica-templated and iron-containing bipyridine-COF (TpBpy) is transformed into a mesoporous Fe−N$_x$ doped carbon (mC-TpBpy-Fe) via carbonization, as schematically illustrated in Figure 1a. In the first step, p-toluenesulfonic acid (PTSA) was used as a molecular organizer for the COF synthesis, and silica nanoparticles were used as a hard template to enable the formation of mesoporous structures.[11] Bipyridine moieties were deliberately chosen and incorporated within the COF backbone as they can strongly coordinate to metal ions, here iron (Fe) ions, which then could form Fe−N$_x$ active sites after a subsequent pyrolysis process (Figure 1b, Figure S1).[34,35]

EXPERIMENTAL SECTION

Materials. All chemicals were purchased from commercial sources and used without further treatment: phloroglucinol (Acros Organics, 99+%), hexamethylenetetramine (Sigma-Aldrich, ACS reagent, ≥99%), trifluoroacetic acid (Carl Roth, ≥99.9%), hydrochloric acid (Carl Roth, 37%), Celite Filter Cel (Sigma-Aldrich), benzidine (Simga Aldrich, ≥98%), 3,3′-dinitrobenzidine (TCI, ≥ 95%), 2,2′-bipyridine (Simga Aldrich, ≥99%), iron(III) chloride hexahydrate (Acro Organic, 97+%), p-toluenesulfonic acid monohydrate (Sigma-Aldrich, ACS reagent, ≥98.5%), silica powder (Sigma-Aldrich, Ludox AS-40), methanol (Carl Roth, ≥99%), dichloromethane (Carl Roth, ≥99.5%), and N,N-dimethylacetamide (Carl Roth, ≥99%). The triformylphloroglucinol (Tp) and 2,2′-bipyridine-5,5′-diamine (Bpy)

were synthesized according to previous reports with slight modifications (for details see the SI).

Synthesis of SiO$_2$@TpBpy. First, p-toluene sulfonic acid (PTSA; 475.5 mg, 2.5 mmol) and 2,2′-bipyridine-5,5′-diamine (Bpy; 83.8 mg, 0.45 mmol) were thoroughly ground in a mortar for 15 min. Then silica powder (SiO$_2$; 0.63 g) was added, and mixing was continued for another 15 min to form a homogeneous yellow powder. Then 1,3,5-triformylphloroglucinol (Tp; 63 mg, 0.3 mmol) was added and further mixed until the color changed from yellow to orange. Then 100 μL of water was added dropwise to the mixture, and grinding was continued for another 15 min. The addition of water yields a color change from orange to deep red. Finally, the mixture was transferred into a glass vial and heated for 16 h at 120 °C, producing a deep reddish powder. After cooling to room temperature, the powder was washed with hot water to remove PTSA. The obtained powder was extracted by Soxhlet with N,N-dimethylacetamide (DMA) overnight, followed by washing with DMA, water, and acetone sequentially for the removal of residual molecular contaminants and dried under reduced pressure until further use.

Synthesis of mC-TpBpy-Fe. Typically, SiO$_2$@TpBpy-Fe was heated from room temperature to 800 °C with a heating rate of 5 °C/min and then pyrolyzed at 800 °C for 2 h in Ar atmosphere to receive C-SiO$_2$@TpBpy-Fe. Subsequently, C-SiO$_2$@TpBpy-Fe was washed with 1 M HCl to remove residual metal salt, followed by immersing the sample into NaOH (2 M, ~300 mL) solution for 24 h at room temperature to remove the SiO$_2$ template. The black sample was collected by filtration, washed several times with water and ethanol, and then dried in a vacuum oven at 60 °C overnight. Before obtaining the final products, a secondary thermal treatment (800, 850, 900, and 950 °C; 2 h) was applied to further improve the conductivity and

structural stability of the catalyst to yield mC-TpBpy-Fe-800, mC-TpBpy-Fe-850, mC-TpBpy-Fe-900, and mC-TpBpy-Fe-950. If not otherwise noted the material mC-TpBpy-Fe discussed in the paper refers to mC-TpBpy-Fe-900. Further information for other samples can be found in the SI.

Electrochemical Measurement. All electrochemical measurements were carried out in a three-electrode cell using a Gamry Reference 600 Potentiostat at room temperature. A RDE with a glassy carbon dish (5.0 mm diameter) served as the working electrode. The graphite rod and Ag/AgCl (4.0 M KCl) were used as counter and reference electrodes, respectively. All measured potentials were converted to the reversible hydrogen electrode (RHE). The potential vs RHE was calibrated as $E_{RHE} = E_{Ag/AgCl} + 0.941$.

In a typical preparation of catalyst ink, 10 mg of each catalyst was blended with 1.0 mL of Nafion ethanol solution (0.5 wt %) in an ultrasonic bath for 30 min. Then 5 μL of catalyst ink (10 mg mL^{-1}) was pipetted onto the glassy carbon surface and dried in ambient environment to form a catalyst film with a mass loading to 0.25 mg cm^{-2}. The measured oxygen reduction reaction (ORR) polarization curves were carried out in an O$_2$-saturated 0.1 M KOH electrolyte with a sweep rate of 10 mV s^{-1} at 1600 rpm. For comparison, the commercial 20 wt % Pt on Vulcan carbon catalyst was measured under identical conditions. For the ORR at a RDE, the electron transfer number can be calculated with Koutecky–Levich equations (for details see SI). The kinetic current density was calculated from the mass-transport correction of RDE by

$$j_k = (j \times j_L)/(j_L - j)$$

The onset potential and half-wave-potential $E_{1/2}$ values of all catalysts were determined when the current density reached 10% and 50% of the limited current density of each catalyst, respectively.

Zn–air batteries were tested in homemade electrochemical cells, where catalysts were loaded on a carbon cloth with gas diffusion layer (catalysts loading 2 mg/cm^2) as the air cathode and zinc foil as the anode in 6.0 M KOH. Measurements were carried out on the as-constructed cell at room temperature with a Gamry Reference 600 Potentiostat.

Charaterization. PXRD patterns for the COFs and carbon samples were measured on a Bruker D8 Advance instrument with Cu Kα radiation (λ = 1.54 Å) at a generator voltage of 40 kV and a generator current of 40 mA with a scanning speed of 5°/min from 10° to 90° for carbon catalysts and with a step size of 0.02° and an exposure time of 2 s per step from 2° to 60° for COF samples. SEM measurements were conducted on ZEISS GeminiSEM500 NanoVP. TEM images were obtained from a Jeol-2100 and FEI Tecnai G2 20 S-TWIN electron microscope at an operating voltage of 200 kV, respectively. The samples for TEM analyses were prepared dispersing the electrocatalysts in ethanol, followed by dropping them onto a copper grid covered with carbon film. Nitrogen sorption measurements were carried out on a Quantachrome Quadrasorb SI instrument. All samples were degassed at 150 °C for 12 h before actual measurement. The surface area was calculated by using Brunauer–Emmett–Teller (BET) calculations, and the pore sized distribution plot was obtained from the adsorption branch of isotherms by the QSDFT model. XPS measurements were carried out using a Thermo Scientific K-Alpha$^+$ X-ray photoelectron spectrometer with Al Kα radiation.

X-ray absorption fine structure (XAFS) measurements were performed at P65 of PETRA III in DESY, Hamburg. XAFS spectra were recorded in transmission geometry with the conventional step-scan mode at the Fe K-edge. The double-crystal fixed exit monochromator equipped with Si(111) crystal as well as the ionization chamber were optimized for the Fe K-edge. The spectra were processed by using the Demeter software.

■ RESULTS AND DISCUSSION

In a typical synthesis, the silica-COF (SiO$_2$@TpBpy) composite was prepared using the Schiff base reaction between 1,3,5-triformylphloroglucinol (Tp) and 2,2′-bipyridine-5,5′-

diamine (Bpy), in the presence of silica nanoparticles with a diameter of ~24 nm (Figure S2; for details see the SI).[35] In a control experiment, pristine TpBpy was prepared following the same process but in the absence of silica nanoparticles. The Fourier transform infrared spectroscopy (FTIR) analyses of pristine TpBpy and SiO$_2$@TpBpy show the characteristic chemical functionalities, as reported in the literature for TpBpy COF (Figure S3).[34,36] The powder X-ray diffraction (PXRD) patterns of pristine TpBpy show an intense peak at 3.6° (2θ), corresponding to the reflections from the (100) plane of the COF, which is as well seen in SiO$_2$@TpBpy, confirming that the structure of TpBpy is well preserved even when templated with silica nanoparticles. TpBpy further shows a less intense diffraction peak at 27° indicating the interlayer stacking, while this peak in SiO$_2$@TpBpy is just seen as a shoulder of the broad peak attributable to amorphous silica (Figure 1c). Nitrogen sorption isotherms were measured to examine the specific surface area of the pristine TpBpy and SiO$_2$@TpBpy composite (Figure S4). The high surface area of the pristine TpBpy (1535 m^2/g) and SiO$_2$@TpBpy composite (877 m^2/g) can be attributed to the formation of ordered pore channels and long-range periodicity in the COF framework, which was also corroborated by PXRD analyses.

Scanning electron microscopy (SEM) analyses of SiO$_2$@TpBpy show particles with a size of ~10 μm and some sharp edges, which incorporate nearly densely packed silica nano-particles seen at higher magnifications. As the interstitial sites of the nanoparticles are not completely filled, formation of a thin coating of TpBpy COF on the surface of each individual nanoparticle can be assumed (Figures 1d and S5). Trans-mission electron microscopy (TEM) images of SiO$_2$@TpBpy also verified the formation densely packed silica nanoparticles (Figure 1e). In contrast, the pristine TpBpy showed the formation of bulk particles without any characteristic morphology (Figure S6). To gain more insight into the formation of SiO$_2$@TpBpy, the morphology of the COF particles was also studied after different times during the preparation process using SEM analyses, showing a dense incorporation of silica particles already within the monomers (Figure S7). To analyze the scope of this method for the preparation of SiO$_2$@COF composites, several other amine linkers were also tested and successfully transformed into the composites by mechanochemical treatment (Figures S8−S11).

Iron ions were introduced into SiO$_2$@TpBpy by soaking a defined amount of the composite in methanolic iron chloride (FeCl$_3$·6H$_2$O) solution and further stirring for 4 h to yield SiO$_2$@TpBpy-Fe. Fe ions were chosen here as they can catalyze the carbonization of organic compounds and have been described to form active Fe−N$_x$ sites efficient for various electrocatalytic reactions. Pyrolysis at 800 °C for 2 h in Ar atmosphere then yields a carbon−silica composite (C-SiO$_2$@TpBpy-Fe) which was treated first with HCl and then with NaOH to etch out residual metal salt and finally the silica template, followed by a secondary thermal treatment at 900 °C for 2 h to yield the final product named mC-TpBpy-Fe (Figure 1a). As confirmed from the SEM analyses, C-SiO$_2$@TpBpy-Fe preserved the initial morphology with tightly packed silica particles even after the pyrolysis process (Figure S12). When the silica template was etched out, the obtained carbonaceous materials (mC-TpBpy-Fe) showed a pronounced mesoporosity(Figure 1h). This is also confirmed by TEM images, again revealing the uniformly distributed mesoporous

structure (Figure 1i), which should be useful to promote the mass transfer during electrocatalytic reactions.[11]

Also the pristine COF sample prepared without silica nanoparticles (TpBpy-Fe) was pyrolyzed and as expected, a carbon material without any mesoporous structure was observed (C-TpBpy-Fe). Furthermore, to also determine the influence of the bipyridine moieties in the COF backbone on the final carbon materials, in a subsequent control experiment, TpBD COF (Tp, 1,3,5-triformylphloroglucinol; BD, benzidine), i.e., without coordinating sites, was used to synthesize mC-TpBD-Fe (Figure S10). Nitrogen sorption isotherms were measured to examine the specific surface area and pore volume of the obtained samples. As shown in Figure 1f, mC-TpBpy-Fe reveals a typical type IV isotherm, with an obvious hysteresis loop at higher relative pressures, indicating mesoporosity. In contrast, C-TpBpy-Fe just showed a typical type I isotherm, while the low overall gas uptake point to gas adsorption mainly on the outer surface and the absence of any characteristic porosity (Figure S13).[11,37] Indeed the calculated Brunauer−Emmett−Teller (BET) surface area of C-TpBpy-Fe is only 38 m^2/g. For mC-TpBpy-Fe, almost the entire surface area (362 m^2/g) can be attributed to mesopores (Figure S14). This is also reflected in the pore size distribution calculated by Quenched Solid State Functional Theory (QSDFT) confirming the formation of large mesopores for mC-TpBpy-Fe but a very low porosity for C-TpBpy-Fe (Figure 1g). The total pore volume of mC-TpBpy-Fe was calculated as 1.36 cm^3/g, which is expectedly much higher than for C-TpBpy-Fe (0.04 cm^3/g; Figure S14). On the other hand, mC-TpBD-Fe shows a similar surface area (257 m^2/g) and pore volume (0.98 cm^3/g) as well as morphology as mC-TpBpy-Fe (Figure S15 and Figure S16).

X-ray photoelectron spectroscopy (XPS) reveals that C, N, O, and Fe are present in C-TpBpy-Fe, mC-TpBD-Fe, and mC-TpBpy-Fe (Figure S17). The N and Fe contents in mC-TpBpy-Fe are 4.50 and 0.58 atomic %, respectively. The high-resolution Fe 2p spectrum with two relatively weak peaks centered at ∼711 eV (Fe $2p_{3/2}$) and ∼724 eV (Fe $2p_{1/2}$) illustrates the presence of Fe species in all the samples (Figure 2a and Figure S18). No metallic Fe was detected from XPS, which is consistent with the PXRD results, showing no peak associated with iron-based species (Figure S19). The high resolution N 1s spectra show a shift of the pyridinic N in mC-TpBpy-Fe to 398.5 eV compared with mC-TpBpy (398.0 eV) (Figure 2b), pointing to a coordination of Fe ions to the pyridinic N-heteroatoms within the carbon matrix, Fe−N_x.[11,38−40] On the other hand, the higher percentage of pyridinic N as well as Fe loading of mC-TpBpy-Fe compared with mC-TpBD-Fe promotes the important role of bipyridine moieties within the COF for the construction of highly dispersed and uniformly distributed Fe−N_x sites (Figure S17b).[34,40] To further elucidate the nature of the Fe species in mC-TpBpy-Fe, X-ray absorption fine structure (XAFS) measurements were performed. As shown in the X-ray absorption near-edge structure (XANES) spectra (Figure 2c), the absorption edge of mC-TpBpy-Fe is located between FeO and Fe_3O_4, indicating that the valence state of Fe is between Fe^{2+} and Fe^{3+}. This observation is consistent with the aforementioned results from XPS analysis as well as observations reported in the literature.[41−43] Figure 2d shows the extended X-ray absorption fine structure (EXAFS) spectra of mC-TpBpy-Fe, FeO, and Fe foil. The Fourier transform shows that the mC-TpBpy-Fe displays one main peak at 1.5 Å, which could be ascribed to the Fe−N/C first coordination
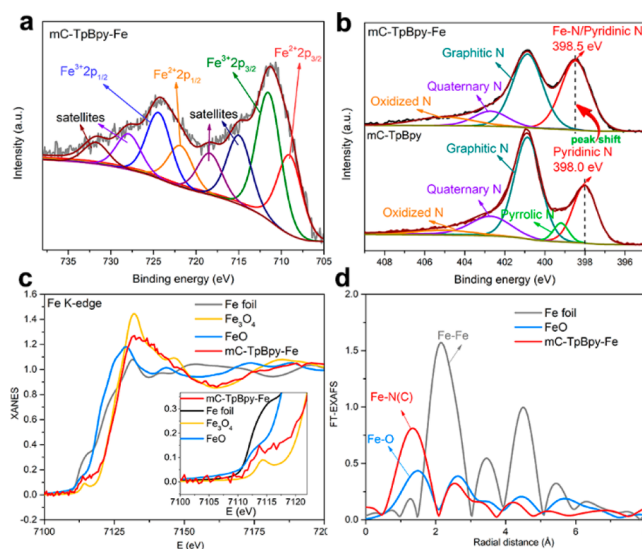
Figure 2. Characterization of mC-TpBpy-Fe. (a) High resolution Fe 2p XPS spectrum of mC-TpBpy-Fe and (b) high resolution N 1s XPS spectra of mC-TpBpy-Fe and mC-TpBpy. (c) XANES spectra at the Fe K-edge of mC-TpBpy-Fe, Fe_3O_4, FeO, and Fe foil. The inset shows the magnified image of the pre-edge XANES spectra. (d) Fourier transform (FT) at the Fe K-edge for mC-TpBpy-Fe, FeO, and Fe foil.

shell, and no appreciable Fe−Fe coordination peak or other high shell peaks are observed. Overall, considering the XPS analysis showing the shift for the pyridinic N peak, PXRD analyses showing the absence of peaks associated with crystalline iron species, and XAFS measurements showing the absence of Fe−Fe bonding, it can be concluded that the Fe atoms are dispersed atomically.

As a result, mesoporous, nitrogen-rich carbon materials with abundant Fe−N_x sites were observed by pyrolyzing a silica templated, Fe-containing COF. All these structural features make this material interesting for electrocatalytic applications. To further elucidate their influence on catalytic performance, mC-TpBpy-Fe was tested and compared to nonporous C-TpBpy-Fe or less nitrogen containing mC-TpBD-Fe as catalyst for ORR under basic conditions (0.1 M KOH). The cyclic voltammetry (CV) curve of mC-TpBpy-Fe displayed a much higher oxygen reduction peak than those of C-TpBpy-Fe and mC-TpBD-Fe, indicating its enhanced performance for ORR (Figure S20a). Linear sweep voltammetry (LSV) curves show a higher half-wave potential (0.845 V) for mC-TpBpy-Fe than for C-TpBpy-Fe (0.804 V) or mC-TpBD-Fe (0.808 V) and even a comparable value to that of commercially available Pt/C (0.852 V) (Figure 3a,b). mC-TpBpy-Fe also shows a higher onset potential of 0.920 V, compared to C-TpBpy-Fe (0.895 V) and mC-TpBD-Fe (0.892 V) (Table S2). Furthermore, the promising activity of mC-TpBpy-Fe is evidenced by the much higher kinetic current density (J_k) at 0.8 V (13.66 mA/cm²), compared to those of C-TpBpy-Fe (4.6 mA/cm²) and mC-TpBD-Fe (5.5 mA/cm²) (Figure 3b). The enhancement of ORR activity for mC-TpBpy-Fe can be attributed to the introduction of the mesoporous structures that efficiently promote the mass transfer and the accessibility of active sites to reactants during the electrocatalytic process. On the other hand, the Bpy moieties within the COF matrix are supposed to be beneficial to the formation of Fe−N active sites in mC-TpBpy-Fe to promote the ORR performance, which is confirmed by the inferior ORR activity of mC-TpBD-Fe. It
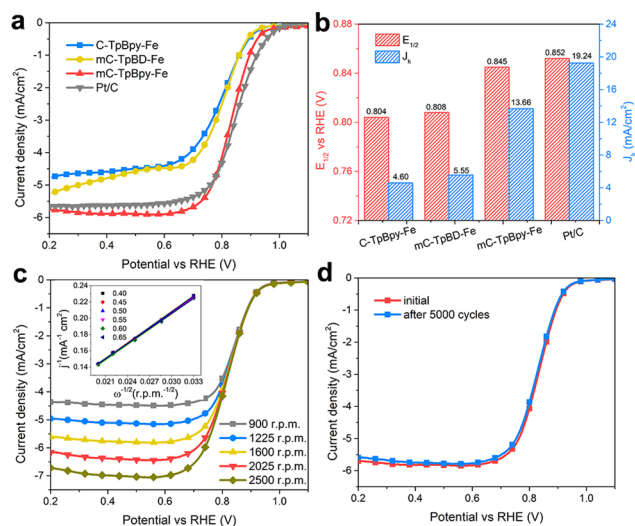
Figure 3. ORR performance of the obtained carbon catalysts. (a) LSV curves of C-TpBpy-Fe, mC-TpBD-Fe, mC-TpBpy-Fe, and Pt/C in oxygen-saturated 0.1 M KOH. (b) Half-wave potential and kinetic current (at 0.8 V) of the catalysts for ORR. (c) LSV curves of mC-TpBpy-Fe in oxygen-saturated 0.1 M KOH at various rotating speeds. Inset: K-L plots for mC-TpBpy-Fe at various potentials. (d) LSV of mC-TpBpy-Fe before and after 5000 cycles at a voltage range between 0.7 and 1.0 V.

can be assumed that also the thermal treatment of the materials has a significant influence on the catalytic performance, as important properties such as graphitization, conductivity, porosity, and the amount of heteroatoms are varied. Indeed, the LSV curves of mC-TpBpy-Fe prepared at different pyrolysis temperatures revealed that 900 °C (i.e., the one discussed in detail here) is the optimum temperature as the catalyst exhibits superior performance for ORR (Figure S20b). In addition, the ORR performances of mC-TpBpy-Fe under acidic media were also tested in 0.5 M H_2SO_4 (Figure S21).

The transferred number of electrons during ORR is measured by recording the LSV curves of mC-TpBpy-Fe at different rotating rates of the rotating disk electrode (RDE) (Figure 3c, inset).[7,44] Based on the Koutecký–Levich equation, the electron transfer number of mC-TpBpy-Fe is determined to be about 4.0, manifesting an ideal 4e$^-$ transfer ORR mechanism. Notably, the mC-TpBpy-Fe catalyst shows long-term durability, with almost negligible difference in the half-wave potential after 5000 cycles (Figure 3d). Moreover, no obvious changes in the morphology of the mC-TpBpy-Fe sample is obtained after 5000 cycles, further confirming its stability and durability (Figure S22). Unlike the conventional Pt/C catalyst, mC-TpBpy-Fe also shows tolerance to methanol during the ORR analyses, confirming its resistance against carbon monoxide (CO) poisoning (Figure S23). Finally, in comparison to literature data, mC-TpBpy-Fe possesses a competitive ORR performance to other the non-noble metal catalysts reported under alkaline conditions (Table S3). In addition, a plot of half-wave potential versus current density has been compiled to compare the ORR activities of mC-TpBpy-Fe with some recently reported FeN$_x$ doped mesoporous carbons derived from silica templating processes (Figure S24), showing the competitive performance of the mC-TpBpy-Fe.

To elucidate if the formation of a crystalline COF for the preparation of Fe−N-doped carbons is indeed necessary or

beneficial, two control experiments were conducted. First, bipyridine (Bpy) was thoroughly mixed with SiO$_2$ particles and FeCl$_3$·6H$_2$O, followed by pyrolysis to obtain a sample named mC-Bpy-Fe after removing the SiO$_2$ template. Furthermore, also a noncrystalline network from the same components (SiO$_2$@TpBpy-amorphous) was synthesized by exclusion of PTSA and H$_2$O from the original recipe. Pyrolysis and removal of the SiO$_2$ template then yield a second control sample named mC-TpBpy-Fe-amorphous (Figure S25, for details see the SI). mC-Bpy-Fe and mC-TpBpy-Fe-amorphous show a pronounced mesoporous structure, similar to that of mC-TpBpy-Fe (Figures S26 and S27). However, the ORR performance of mC-Bpy-Fe and mC-TpBpy-Fe-amorphous exhibits lower half-wave potentials and limited current densities compared with that of mC-TpBpy-Fe (Figure S28). It is supposed that the periodicity of the COF provides a more homogeneous distribution of functional groups, i.e., Bpy and Fe-Bpy moieties in the framework and, consequently, Fe−N$_x$ active sites in the carbon materials after pyrolysis. Indeed, the superior ORR performance of mC-TpBpy-Fe indicates that the formation of a crystalline COF precursor is beneficial for the preparation of highly active and porous Fe−N−C catalysts.

The performance of mC-TpBpy-Fe for ORR makes it an interesting cathode material, e.g., in Zn−air batteries, devices which have attracted attention due to their high specific energy density and the low cost for next-generation green and sustainable energy technologies (Figure 4a and Figure S29). The open-circuit potential (OCP) of a two-electrode primary Zn−air battery using mC-TpBpy-Fe as electrocatalyst is as
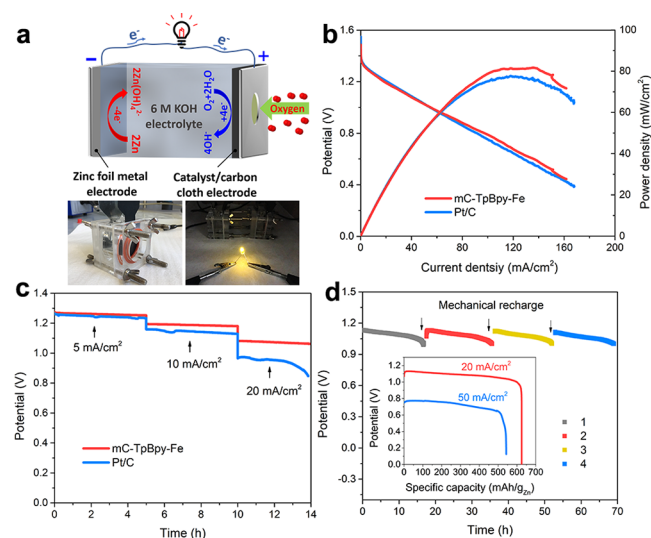

Figure 4. Performance of mC-TpBpy-Fe in a Zn−air battery. (a) Schematic diagram of a Zn−air battery and photographs of a lab-made Zn−air battery with a zinc foil as anode, mC-TpBpy-Fe loaded on carbon cloth as cathode (left), and a LED connected to two batteries (right). Comparison of (b) polarization and power density curves of primary Zn−air batteries using mC-TpBpy-Fe and Pt/C as ORR catalysts and (c) discharge curves of the primary Zn−air batteries using mC-TpBpy-Fe and Pt/C as ORR catalysts at various current densities (5, 10, and 20 mA/cm^2). (d) Long-time durability of a primary Zn−air battery using mC-TpBpy-Fe at a current density of 20 mA/cm^2. The battery is mechanically rechargeable; i.e., the Zn foil and electrolyte were replaced at the time indicated by arrows. Inset: Specific capacities of the Zn−air batteries using mC-TpBpy-Fe normalized to the mass of the consumed Zn at various current densities (20 and 50 mA/cm^2).

Chemistry of Materials   Article

high as 1.5 V, suggesting a good catalytic performance of mC-TpBpy-Fe. Two of such batteries connected in series can light up a 2.0 V light-emitting diode (LED) easily. Figure 4b compares the polarization and power density curves for Zn—air batteries using mC-TpBpy-Fe and Pt/C air cathodes. The mC-TpBpy-Fe shows a peak power density of ~81 mW/cm^2, comparable to that of the conventional Pt/C catalyst (77 mW/cm^2). Discharge curves of the batteries under different current densities (5, 10, and 20 mA/cm^2) were also tested for both mC-TpBpy-Fe and Pt/C equipped devices (Figure 4c). The mC-TpBpy-Fe battery possesses a better discharge stability than the Pt/C battery, especially at a high current density of 20 mA/cm^2. Although Zn is gradually consumed during the discharging process, the battery can be mechanically recovered by replacing the Zn foil and KOH electrolyte, featuring no obvious potential decrease after 4 cycles (~70 h) (Figure 4d). When normalized to the mass of consumed Zn, the specific capacity of mC-TpBpy-Fe was found to be as high as ~625 mAh/g$_{Zn}$ at a current density of 20 mA/cm^2 and ~543 mAh/g$_{Zn}$ at 50 mA/cm^2 (Figure 4d, inset). These results support the high ORR catalytic activity and excellent stability of the mC-TpBpy-Fe, promoting its promising potential for practical application in the Zn—air battery.

CONCLUSIONS

In summary, we have developed a facile strategy to convert COFs into mesoporous carbons by a PTSA-assisted mechanochemical method for COF growth in the presence of silica nanoparticles. Bipyridine moieties within the COF are assisting metal ion coordination, yielding abundant Fe- and N-doping within the resulting carbon material. The mesoporous structure and large pore volume efficiently promote the diffusion of O$_2$ and electrolyte to the homogeneously dispersed Fe—N$_x$ active sites, eventually yielding an excellent ORR performance, making these materials a very promising candidate for an efficient oxygen electrode in Zn—air batteries. It is further shown that the PTSA-assisted silica-templated synthetic route can be applied to yield various SiO$_2$@COF composites as precursors for tailor-made carbon materials for energy conversion and storage.

ASSOCIATED CONTENT

Ⓢ Supporting Information

The Supporting Information is available free of charge on the ACS Publications website at DOI: 10.1021/acs.chemmater.9b00204.

Experimental details and additional data (PDF)

AUTHOR INFORMATION

Corresponding Author

*(A.T.) E-mail: arne.thomas@tu-berlin.de.

ORCID Ⓞ

Pradip Pachfule: 0000-0002-0804-541X

Shuang Li: 0000-0001-7414-630X

Arne Thomas: 0000-0002-2130-4930

Notes

The authors declare no competing financial interest.

ACKNOWLEDGMENTS

REFERENCES

(1) Li, W.; Liu, J.; Zhao, D. Y. Mesoporous materials for energy conversion and storage devices. *Nat. Rev. Mater.* **2016**, *1*, 16023.

(2) Benzigar, M. R.; Talapaneni, S. N.; Joseph, S.; Ramadass, K.; Singh, G.; Scaranto, J.; Ravon, U.; Al-Bahily, K.; Vinu, A. Recent advances in functionalized micro and mesoporous carbon materials: synthesis and applications. *Chem. Soc. Rev.* **2018**, *47*, 2680−2721.

(3) Zhang, P. F.; Zhang, J. S.; Dai, S. Mesoporous Carbon Materials with Functional Compositions. *Chem. - Eur. J.* **2017**, *23*, 1986−1998.

(4) Zhang, J. T.; Xia, Z. H.; Dai, L. M. Carbon-based electrocatalysts for advanced energy conversion and storage. *Sci. Adv.* **2015**, *1*, No. e1500564.

(5) Paraknowitsch, J. P.; Thomas, A. Doping carbons beyond nitrogen: an overview of advanced heteroatom doped carbons with boron, sulphur and phosphorus for energy applications. *Energy Environ. Sci.* **2013**, *6*, 2839−2855.

(6) Wang, J.; Huang, Z.; Liu, W.; Chang, C.; Tang, H.; Li, Z.; Chen, W.; Jia, C.; Yao, T.; Wei, S.; Wu, Y.; Li, Y. Design of N-Coordinated Dual-Metal Sites: A Stable and Active Pt-Free Catalyst for Acidic Oxygen Reduction Reaction. *J. Am. Chem. Soc.* **2017**, *139*, 17281−17284.

(7) Yin, P. Q.; Yao, T.; Wu, Y.; Zheng, L. R.; Lin, Y.; Liu, W.; Ju, H. X.; Zhu, J. F.; Hong, X.; Deng, Z. X.; Zhou, G.; Wei, S. Q.; Li, Y. D. Single Cobalt Atoms with Precise N-Coordination as Superior Oxygen Reduction Reaction Catalysts. *Angew. Chem., Int. Ed.* **2016**, *55*, 10800−10805.

(8) Zhang, J. T.; Zhao, Z. H.; Xia, Z. H.; Dai, L. M. A metal-free bifunctional electrocatalyst for oxygen reduction and oxygen evolution reactions. *Nat. Nanotechnol.* **2015**, *10*, 444−452.

(9) Ranjbar Sahraie, N.; Paraknowitsch, J. P.; Gobel, C.; Thomas, A.; Strasser, P. Noble-Metal-Free Electrocatalysts with Enhanced ORR Performance by Task-Specific Functionalization of Carbon using Ionic Liquid Precursor Systems. *J. Am. Chem. Soc.* **2014**, *136*, 14486−14497.

(10) Wu, G.; More, K. L.; Johnston, C. M.; Zelenay, P. High-performance electrocatalysts for oxygen reduction derived from polyaniline, iron, and cobalt. *Science* **2011**, *332*, 443−447.

(11) Li, S.; Cheng, C.; Zhao, X. J.; Schmidt, J.; Thomas, A. Active Salt/Silica-Templated 2D Mesoporous FeCo-N$_x$-Carbon as Bifunctional Oxygen Electrodes for Zinc-Air Batteries. *Angew. Chem., Int. Ed.* **2018**, *57*, 1856−1862.

(12) Meng, F. L.; Wang, Z. L.; Zhong, H. X.; Wang, J.; Yan, J. M.; Zhang, X. B. Reactive Multifunctional Template-Induced Preparation of Fe-N-Doped Mesoporous Carbon Microspheres Towards Highly Efficient Electrocatalysts for Oxygen Reduction. *Adv. Mater.* **2016**, *28*, 7948−7955.

(13) Palaniselvam, T.; Kashyap, V.; Bhange, S. N.; Baek, J. B.; Kurungot, S. Nanoporous Graphene Enriched with Fe/Co-N Active Sites as a Promising Oxygen Reduction Electrocatalyst for Anion Exchange Membrane Fuel Cells. *Adv. Funct. Mater.* **2016**, *26*, 2150−2162.

(14) Liang, H.-W.; Wei, W.; Wu, Z.-S.; Feng, X. L.; Müllen, K. Mesoporous Metal-Nitrogen-Doped Carbon Electrocatalysts for Highly Efficient Oxygen Reduction Reaction. *J. Am. Chem. Soc.* **2013**, *135*, 16002−16005.

(15) Lee, K. J.; Lee, J. H.; Jeoung, S.; Moon, H. R. Transformation of Metal-Organic Frameworks/Coordination Polymers into Functional Nanostructured Materials: Experimental Approaches Based on Mechanistic Insights. *Acc. Chem. Res.* **2017**, *50*, 2684−2692.

8.3 Silica-Templated Covalent Organic Framework-derived Fe-N-doped Mesoporous Carbon as Oxygen Reduction Electrocatalyst   111

Chemistry of Materials   Article

(16) Lin, C. Y.; Zhang, D. T.; Zhao, Z. H.; Xia, Z. H. Covalent Organic Framework Electrocatalysts for Clean Energy Conversion. *Adv. Mater.* **2018**, *30*, 1703646.

(17) Liao, Y. Z.; Li, J. H.; Thomas, A. General Route to High Surface Area Covalent Organic Frameworks and Their Metal Oxide Composites as Magnetically Recoverable Adsorbents and for Energy Storage. *ACS Macro Lett.* **2017**, *6*, 1444−1450.

(18) Li, S. W.; Dong, Y.; Zhou, J. W.; Liu, Y.; Wang, J. M.; Gao, X.; Han, Y. Z.; Qi, P. F.; Wang, B. Carbon dioxide in the cage: manganese metal-organic frameworks for high performance CO_2 electrodes in Li-CO_2 batteries. *Energy Environ. Sci.* **2018**, *11*, 1318.

(19) Dawson, R.; Cooper, A. I.; Adams, D. Nanoporous organic polymer networks. *Prog. Polym. Sci.* **2012**, *37*, 530−563.

(20) Pachfule, P.; Shinde, D.; Majumder, M.; Xu, Q. Fabrication of carbon nanorods and graphene nanoribbons from a metal-organic framework. *Nat. Chem.* **2016**, *8*, 718−724.

(21) Hao, L.; Ning, J.; Luo, B.; Wang, B.; Zhang, Y. B.; Tang, Z. H.; Yang, J. H.; Thomas, A.; Zhi, L. J. Structural Evolution of 2D Microporous Covalent Triazine-Based Framework toward the Study of High-Performance Supercapacitors. *J. Am. Chem. Soc.* **2015**, *137*, 219−225.

(22) Zhao, X. J.; Pachfule, P.; Li, S.; Simke, J. R. J.; Schmidt, J.; Thomas, A. Bifunctional Electrocatalysts for Overall Water Splitting from an Iron/Nickel-Based Bimetallic Metal-Organic Framework/Dicyandiamide Composite. *Angew. Chem.* **2018**, *130*, 9059−9064.

(23) Joseph, S.; Kempaiah, D. M.; Benzigar, M.; Baskar, A. V.; Talapaneni, S. N.; Jhung, S. H.; Park, D. H.; Vinu, A. Metal Organic Framework Derived Mesoporous Carbon Nitrides with a High Specific Surface Area and Chromium Oxide Nanoparticles for CO_2 and Hydrogen Adsorption. *J. Mater. Chem. A* **2017**, *5*, 21542−21549.

(24) Ren, Q.; Wang, H.; Lu, X. F.; Tong, Y. X.; Li, G. R. Recent Progress on MOF-Derived Heteroatom-Doped Carbon-Based Electrocatalysts for Oxygen Reduction Reaction. *Adv. Sci.* **2018**, *5*, 1700515.

(25) Yang, L.; Zeng, X.; Wang, W.; Cao, D. Recent Progress in MOF-Derived, Heteroatom-Doped Porous Carbons as Highly Efficient Electrocatalysts for Oxygen Reduction Reaction in Fuel Cells. *Adv. Funct. Mater.* **2018**, *28*, 1704537.

(26) Xu, Q.; Tang, Y.; Zhang, X.; Oshima, Y.; Chen, Q.; Jiang, D. Template Conversion of Covalent Organic Frameworks into 2D Conducting Nanocarbons for Catalyzing Oxygen Reduction Reaction. *Adv. Mater.* **2018**, *30*, 1706330.

(27) Xu, Q.; Tang, Y. P.; Zhai, L. P.; Chen, Q. H.; Jiang, D. L. Pyrolysis of covalent organic frameworks: a general strategy for template converting conventional skeletons into conducting microporous carbons for high-performance energy storage. *Chem. Commun.* **2017**, *53*, 11690−11693.

(28) Romero, J.; Rodriguez-San-Miguel, D.; Ribera, A.; Mas-Balleste, R.; Otero, T. F.; Manet, I.; Licio, F.; Abellan, G.; Zamora, F.; Coronado, E. Metal-functionalized covalent organic frameworks as precursors of supercapacitive porous N-doped graphene. *J. Mater. Chem. A* **2017**, *5*, 4343−4351.

(29) Li, L. Y.; Li, L.; Cui, C. Y.; Fan, H. J.; Wang, R. H. Heteroatom-doped Carbon Spheres from Hierarchical Hollow Covalent Organic Framework Precursors for Metal-Free Catalysis. *ChemSusChem* **2017**, *10*, 4921−4926.

(30) Huang, Y. B.; Pachfule, P.; Sun, J. K.; Xu, Q. From covalent-organic frameworks to hierarchically porous B-doped carbons: a molten-salt approach. *J. Mater. Chem. A* **2016**, *4*, 4273−4279.

(31) Chen, L. Y.; Zhang, L.; Chen, Z. J.; Liu, H. J.; Luque, R.; Li, Y. W. A covalent organic framework-based route to the in situ encapsulation of metal nanoparticles in N-rich hollow carbon spheres. *Chem. Sci.* **2016**, *7*, 6015−6020.

(32) Kim, G.; Yang, J.; Nakashima, N.; Shiraki, T. Highly Microporous Nitrogen doped Carbon Synthesized from Azine-linked Covalent Organic Framework and its Supercapacitor Function. *Chem. - Eur. J.* **2017**, *23*, 17504−17510.

(33) Ding, S. Y.; Wang, W. Covalent organic frameworks (COFs): from design to applications. *Chem. Soc. Rev.* **2013**, *42*, 548−568.

(34) Aiyappa, H. B.; Thote, J.; Shinde, D. B.; Banerjee, R.; Kurungot, S. Cobalt-Modified Covalent Organic Framework as a Robust Water Oxidation Electrocatalyst. *Chem. Mater.* **2016**, *28*, 4375−4379.

(35) Karak, S.; Kandambeth, S.; Biswal, B. P.; Sasmal, H. S.; Kumar, S.; Pachfule, P.; Banerjee, R. Constructing Ultraporous Covalent Organic Frameworks in Seconds via an Organic Terracotta Process. *J. Am. Chem. Soc.* **2017**, *139*, 1856−1862.

(36) Kandambeth, S.; Mallick, A.; Lukose, B.; Mane, M. V.; Heine, T.; Banerjee, R. Construction of Crystalline 2D Covalent Organic Frameworks with Remarkable Chemical (Acid/Base) Stability via a Combined Reversible and Irreversible Route. *J. Am. Chem. Soc.* **2012**, *134*, 19524−19527.

(37) Zhao, X. J.; Li, S.; Cheng, H. F.; Schmidt, J.; Thomas, A. Ionic Liquid-Assisted Synthesis of Mesoporous Carbons with Surface-Enriched Nitrogen for the Hydrogen Evolution Reaction. *ACS Appl. Mater. Interfaces* **2018**, *10*, 3912−3920.

(38) Li, Q.; Chen, W.; Xiao, H.; Gong, Y.; Li, Z.; Zheng, L.; Zheng, X.; Yan, W.; Cheong, W. C.; Shen, R.; Fu, N.; Gu, L.; Zhuang, Z.; Chen, C.; Wang, D.; Peng, Q.; Li, J.; Li, Y. Fe Isolated Single Atoms on S, N Codoped Carbon by Copolymer Pyrolysis Strategy for Highly Efficient Oxygen Reduction Reaction. *Adv. Mater.* **2018**, *30*, 1800588.

(39) Cheng, C.; Li, S.; Xia, Y.; Ma, L.; Nie, C.; Roth, C.; Thomas, A.; Haag, R. Atomic Fe-Nx Coupled Open-Mesoporous Carbon Nanofibers for Efficient and Bioadaptable Oxygen Electrode in Mg−Air Batteries. *Adv. Mater.* **2018**, *30*, 1802669.

(40) Tu, T. N.; Nguyen, M. V.; Nguyen, H. L.; Yuliarto, B.; Cordova, K. E.; Demir, S. Designing bipyridine-functionalized zirconium metal-organic frameworks as a platform for clean energy and other emerging applications. *Coord. Chem. Rev.* **2018**, *364*, 33−50.

(41) Chen, Y. J.; Ji, S. F.; Wang, Y. G.; Dong, J.; Chen, W. X.; Li, Z.; Shen, R. G.; Zheng, L. R.; Zhuang, Z. B.; Wang, D. S.; Li, Y. D. Isolated Single Iron Atoms Anchored on N-Doped Porous Carbon as an Efficient Electrocatalyst for the Oxygen Reduction Reaction. *Angew. Chem., Int. Ed.* **2017**, *56*, 6937−6941.

(42) Zhang, M. L.; Wang, Y. G.; Chen, W. X.; Dong, J. C.; Zheng, L. R.; Luo, J.; Wan, J. W.; Tian, S. B.; Cheong, W. C.; Wang, D. S.; Li, Y. D. Metal (Hydr)oxides@Polymer Core-Shell Strategy to Metal Single-Atom Materials. *J. Am. Chem. Soc.* **2017**, *139*, 10976−10979.

(43) Yin, P. Q.; Yao, T.; Wu, Y. E.; Zheng, L. R.; Lin, Y.; Liu, W.; Ju, H. X.; Zhu, J. F.; Hong, X.; Deng, Z. X.; Zhou, G.; Wei, S. Q.; Li, Y. D. Single Cobalt Atoms with Precise N-Coordination as Superior Oxygen Reduction Reaction Catalysts. *Angew. Chem., Int. Ed.* **2016**, *55*, 10800−10805.

(44) Wei, J.; Liang, Y.; Hu, Y. X.; Kong, B. A.; Simon, G. P.; Zhang, J.; Jiang, S. P.; Wang, H. T. A Versatile Iron-Tannin-Framework Ink Coating Strategy to Fabricate Biomass-Derived Iron Carbide/Fe-N-Carbon Catalysts for Efficient Oxygen Reduction. *Angew. Chem., Int. Ed.* **2016**, *55*, 1355−1359.

Supporting Information

Silica-Templated Covalent Organic Framework-derived Fe-N-doped Mesoporous Carbon as Oxygen Reduction Electrocatalyst

Xiaojia Zhao,[†] Pradip Pachfule,[†] Shuang Li,[†] Thomas Langenhahn,[†] Mengyang Ye,[†] Guiying Tian,[‡] Johannes Schmidt,[†] Arne Thomas,[†]*

[†] Functional Materials, Department of Chemistry, Technische Universität Berlin, Hardenbergstr. 40, 10623 Berlin, Germany

[‡] Institute for Applied Materials (IAM-ESS), Karlsruhe Institute of Technology (KIT), Hermann-von-Helmholtz-Platz 1, 76344 Germany

Corresponding Author

*arne.thomas@tu-berlin.de

Section 1. Experiment section

1.1 Monomer Synthesis

The monomers were synthesized according to previous reports with slight modifications. Typical synthetic procedures are described below.

1.1.1 Synthesis of triformylphloroglucinol (Tp)[1]
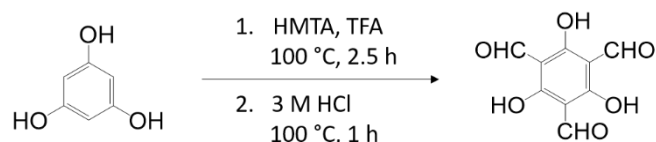
Phloroglucinol (6.0 g, 49 mmol), hexamethylenetetramine (HMTA, 15.1 g, 108 mmol) and trifluoroacetic acid (TFA, 90 mL) were refluxed at 100 °C under N_2 for 2.5 h. After that, approximately 150 mL of 3 M HCl was added slowly and the mixture was heated at 100 °C for 1 h. After cooling to room temperature, the solution was filtered through Celite, extracted with 350 mL dichloromethane and the solution was evaporated under reduced pressure to afford 1.6 g of an off-white powder. ^{1}H NMR indicated near 99% purity; a pure sample was obtained by sublimation.

1.1.2 Synthesis of 2,2'-Bipyridine-5,5'-diamine (Bpy)[2]

The compound 2,2'-bipyridine-5,5'-diamine (Bpy) was synthesized according to reported methods and the structural integrity confirmed by IR, ^{1}H-NMR, and ^{13}C-NMR.
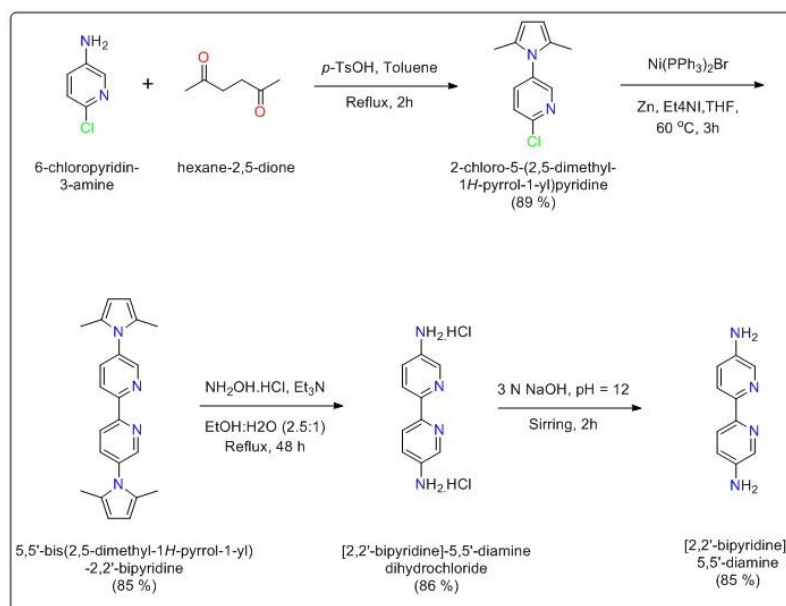
Scheme 1. Scheme of the synthesis of 2,2'-bipyridine-5,5'-diamine.

1.2 Synthesis of TpBpy-COF

1.2.1 Synthesis of pristine TpBpy

The pristine TpBpy was synthesized following the same procedure as described for
SiO_2@TpBpy by exclusion of SiO_2 powder.

1.2.2 Synthesis of SiO_2@TpPa, SiO_2@TpBD and SiO_2@TpBD(NO$_2$)

Other SiO_2@COFs were synthesized following the same procedure as described for
SiO_2@TpBpy but using the respective amine-linkers (p-Phenylenediamine (Pa) for
SiO_2@TpPa, Benzidine (BD) for SiO_2@TpBD and 3,3'-Dinitrobenzidine (BD(NO$_2$)) for
SiO_2@TpBD(NO$_2$)).

1.2.3 Synthesis of SiO_2@TpBpy-Fe and SiO_2@TpBD-Fe

50 mg of the as synthesized SiO_2@TpBpy was treated with $FeCl_3 \cdot 6H_2O$ (20 mg) dissolved in
20 ml methanol. The solution was stirred for 4 h at room temperature, followed by washing
with methanol. The obtained material dried in a vacuum oven overnight at 60 °C to get the
SiO_2@TpBpy-Fe.

The SiO_2@TpBD-Fe was prepared by the same process, just using SiO_2@TpBD instead of
SiO_2@TpBpy.

1.2.4 Synthesis of SiO_2@TpBpy-amorphous

The SiO_2@TpBpy-amorphous was synthesized following the same procedure as described for
SiO_2@TpBpy by exclusion of PTSA and H_2O.

1.2.5 Synthesis of SiO_2@Bpy-Fe

500 mg of 2,2'-bipyridine (Bpy) was treated with $FeCl_3 \cdot 6H_2O$ (150 mg) and SiO_2 powder
(630 mg) dissolved in 50 ml methanol. The solution was stirred for 4 h at room temperature,
followed by removing the methanol using the rotary evaporator. The obtained material dried
in a vacuum oven overnight at 60 °C to get the SiO_2@Bpy-Fe.

1.2.6 Synthesis of TpBpy-Fe

TpBpy-Fe was synthesized following the same procedure as SiO_2@TpBpy-Fe, just using the
obtained TpBpy instead of SiO_2@TpBpy.

1.3 Synthesis of COF-derived carbon catalysts

1.3.1 Synthesis of C-TpBpy-Fe

The C-TpBpy-Fe derived from TpBpy-Fe, was synthesized following the similar procedure to mC-TpBpy-Fe, without using 2 M NaOH to remove the silica. The secondary thermal treatment was operated under 900 °C for 2 h.

1.3.2 Synthesis of mC-TpBD-Fe

The mC-TpBD-Fe derived from SiO_2@TpBD-Fe, was synthesized following the similar procedure to mC-TpBpy-Fe. The secondary thermal treatment was operated under 900 °C for 2 h.

1.3.3 Synthesis of mC-TpBpy

The mC-TpBpy derived from SiO_2@TpBpy without Fe^{3+} impregnation, was synthesized following the similar procedure to mC-TpBpy-Fe. The secondary thermal treatment was operated under 900 °C for 2 h.

1.3.4 Synthesis of mC-TpBpy-Fe-amorphous

The mC-TpBpy-Fe-amorphous was synthesized following the similar procedure to mC-TpBpy-Fe by using the precursor of SiO_2@TpBpy-amorphous.

1.3.5 Synthesis of mC-Bpy-Fe

The mC-Bpy-Fe derived from SiO_2@Bpy-Fe, was synthesized following the similar procedure to mC-TpBpy-Fe. The secondary thermal treatment was operated under 900 °C for 2 h.

Section 2. Electrochemical measurements

For the ORR at a RDE, the electron transfer number can be calculated with Koutecky-Levich equations:

$$\frac{1}{j} = \frac{1}{j_L} + \frac{1}{j_k} = \frac{1}{B\omega^{1/2}} + \frac{1}{j_k}$$

$$B = 0.2nFC_0(D_0)^{2/3}v^{-1/6}$$

Where j is the measured current density; j_L is the diffusion-limiting current density; j_k is the kinetic current density; ω is the angular velocity of the disk ($= 2\pi N$, N is the linear rotation speed); n is the overall electron transfer number during ORR; F is the Faraday constant (96485 C/mol); C_0 is the bulk concentration of O_2 (1.2×10^{-6} mol/cm^3); D_0 is the diffusion coefficient of O_2 in 0.1 M KOH electrolyte(1.9×10^{-5} cm^2/s); v is the kinematics viscosity for electrolyte (0.01 cm^2/s).
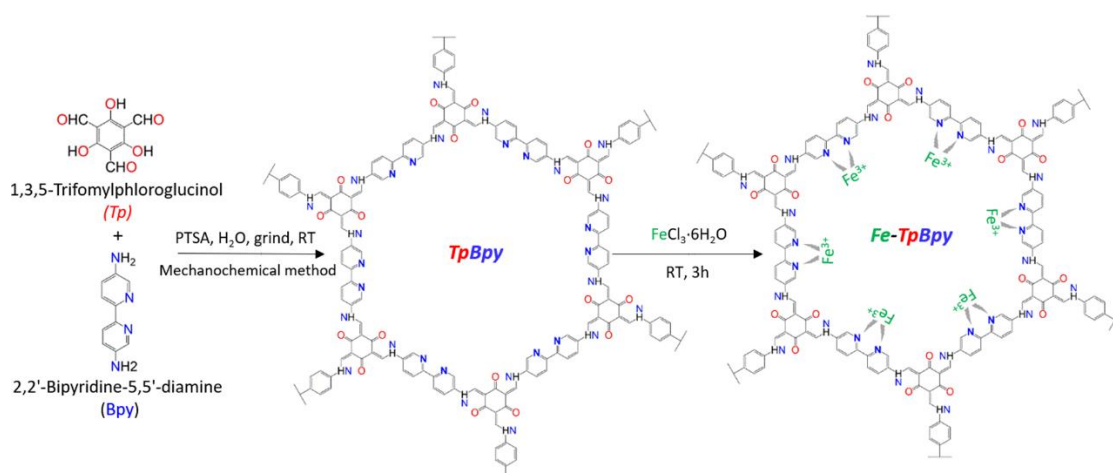
Figure S1. Structure and synthetic procedure for TpBpy *via* mechanochemical method and TpBpy-Fe via Fe(III) impregnation
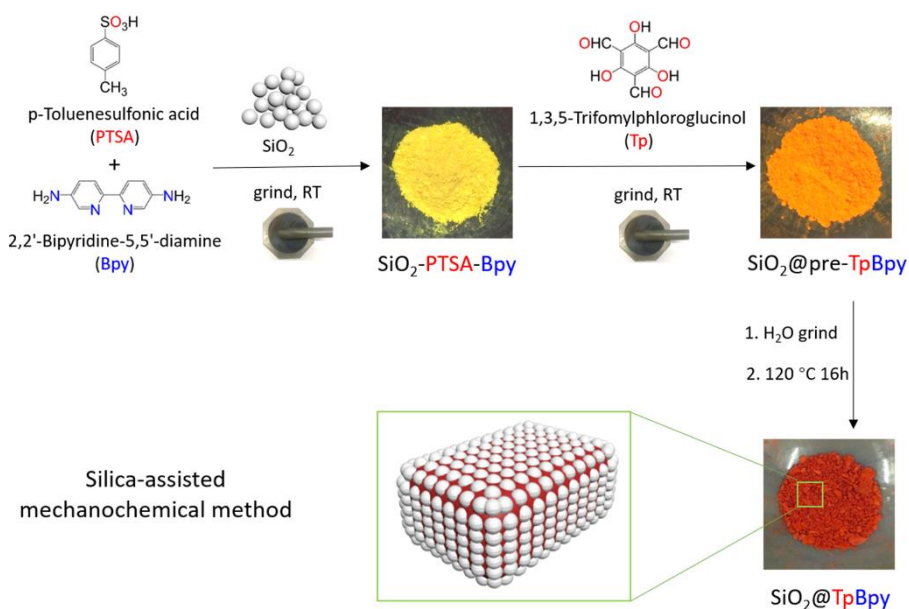
Figure S2. Synthesis of SiO$_2$@TpBpy via silica-assisted mechanochemical method.
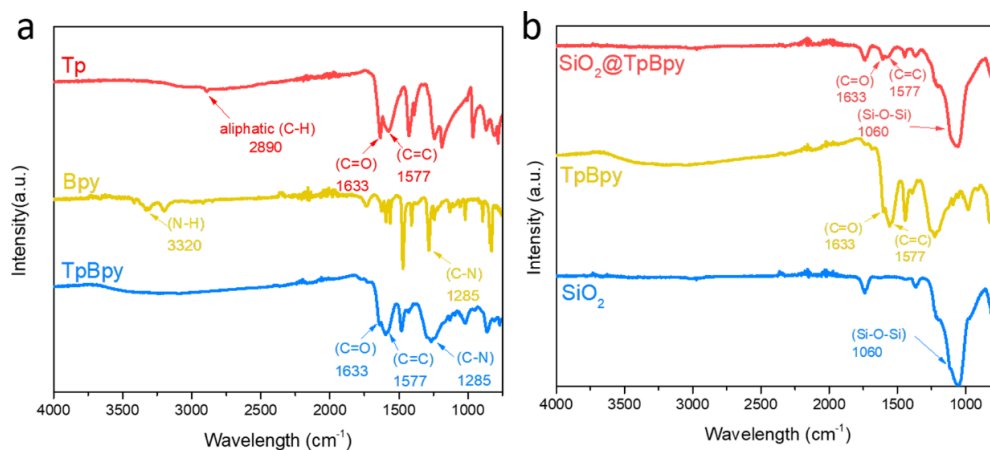
Figure S3. FT-IR spectra of SiO$_2$, Tp, Bpy, TpBpy and SiO$_2$@TpBpy.
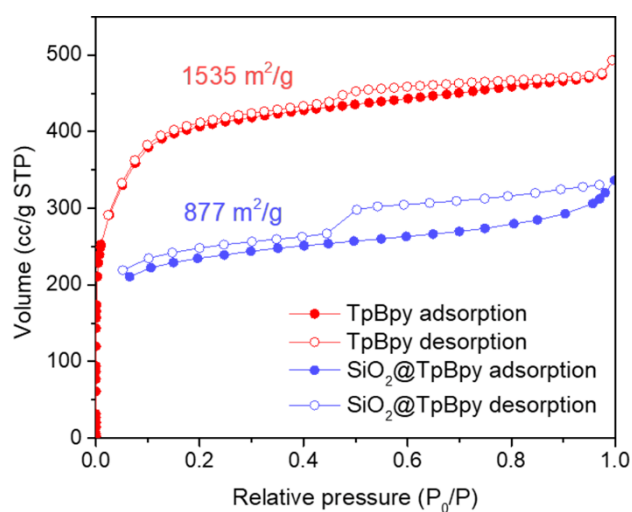
Figure S4. N$_2$ adsorption-desorption isotherms of the pristine TpBpy and SiO$_2$@TpBpy.
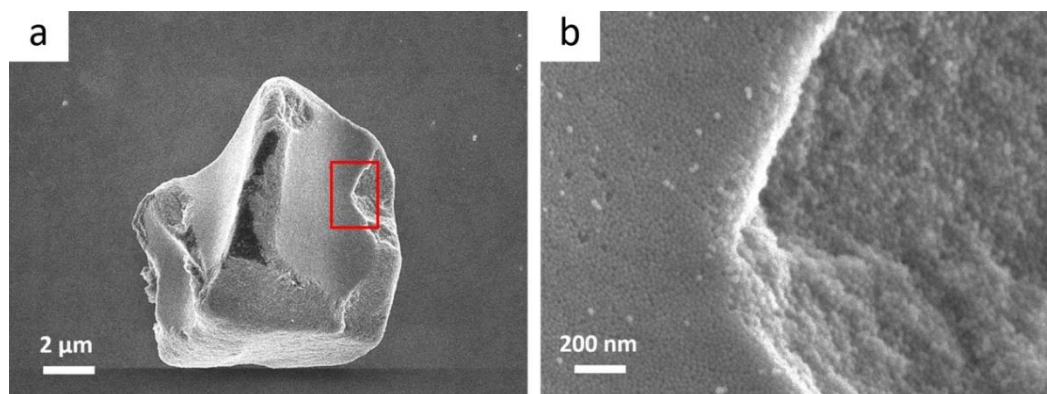
Figure S5. SEM images of $SiO_2@$ TpBpy.
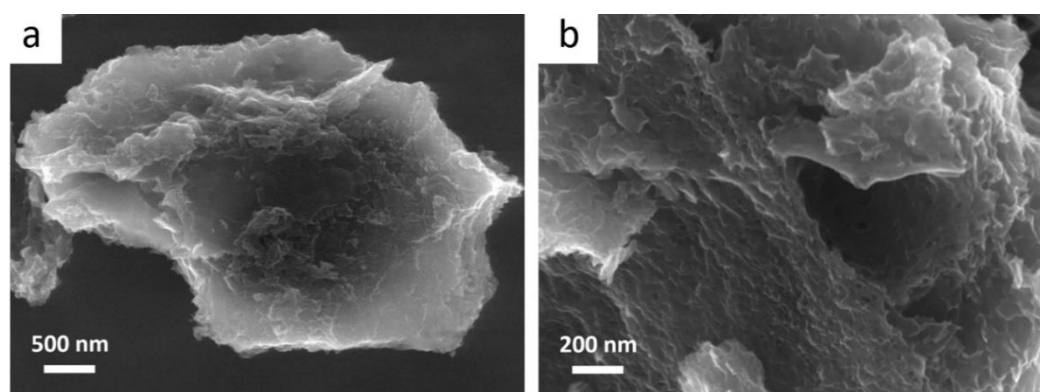
Figure S6. SEM images of pristine TpBpy without silica
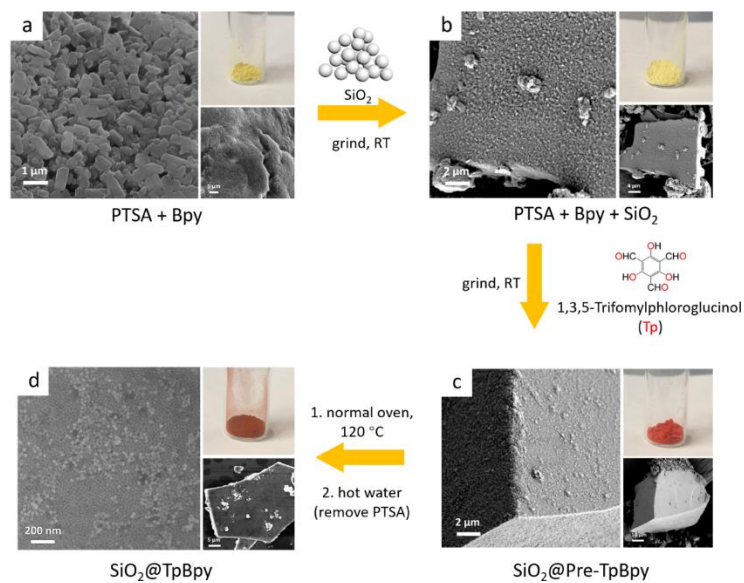
Figure S7. SEM images of the intermediate steps involved during the synthesis of
SiO$_2$@TpBpy at different time spans.
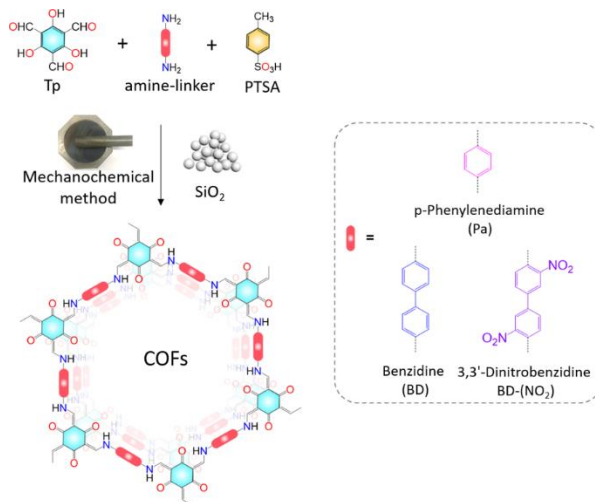
Figure S8. General synthesis of SiO$_2$@COFs from Tp and corresponding amines (Pa, BD and
BD-NO$_2$) by *p*-toluenesulfonic acid (PTSA) mediated Schiff base reaction via silica-assisted
mechanochemical method.

Figure S9. a) Synthesis of SiO$_2$@TpPa via silica-assisted mechanochemical method. b) Packing diagram of TpPa. c) PXRD pattern of SiO$_2$@TpPa, TpPa and SiO$_2$. d) SEM image of SiO$_2$@TpPa.

Figure S10. a) Synthesis of SiO$_2$@TpBD via silica-assisted mechanochemical method. b) Packing diagram of TpBD. c) PXRD pattern of SiO$_2$@TpBD, TpBD and SiO$_2$. d) SEM image of SiO$_2$@TpBD.
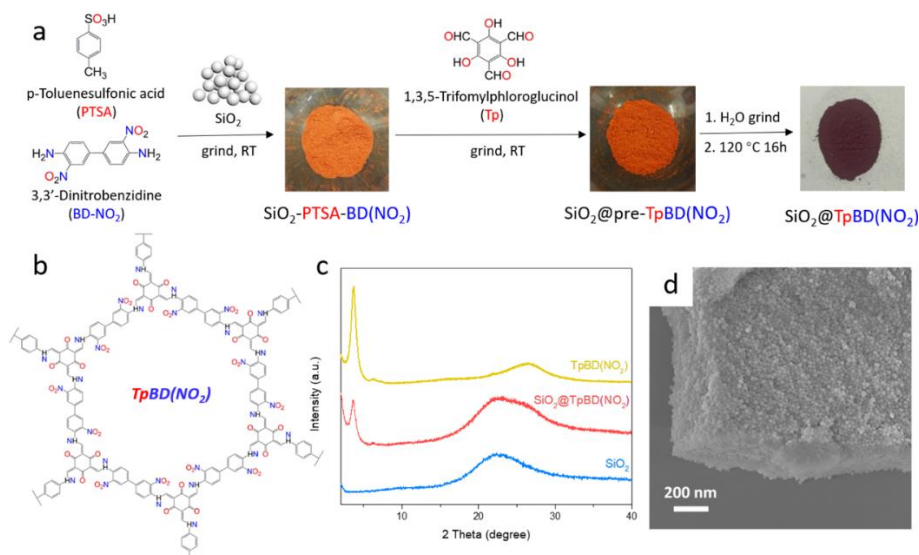
Figure S11. a) Synthesis of SiO$_2$@TpBD(NO$_2$) via silica-assisted mechanochemical method.
b) Packing diagram of TpBD(NO$_2$). c) PXRD pattern of SiO$_2$@TpBD(NO$_2$), TpBD(NO$_2$) and
SiO$_2$. d) SEM image of SiO$_2$@TpBD(NO$_2$).
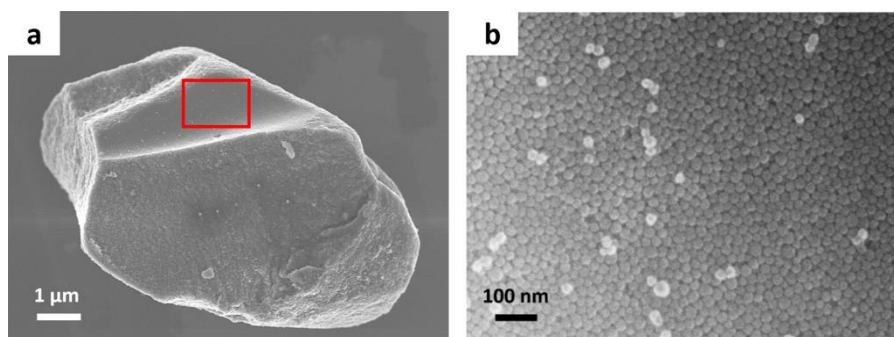
Figure S12. SEM images of C-SiO$_2$@TpBpy-Fe.
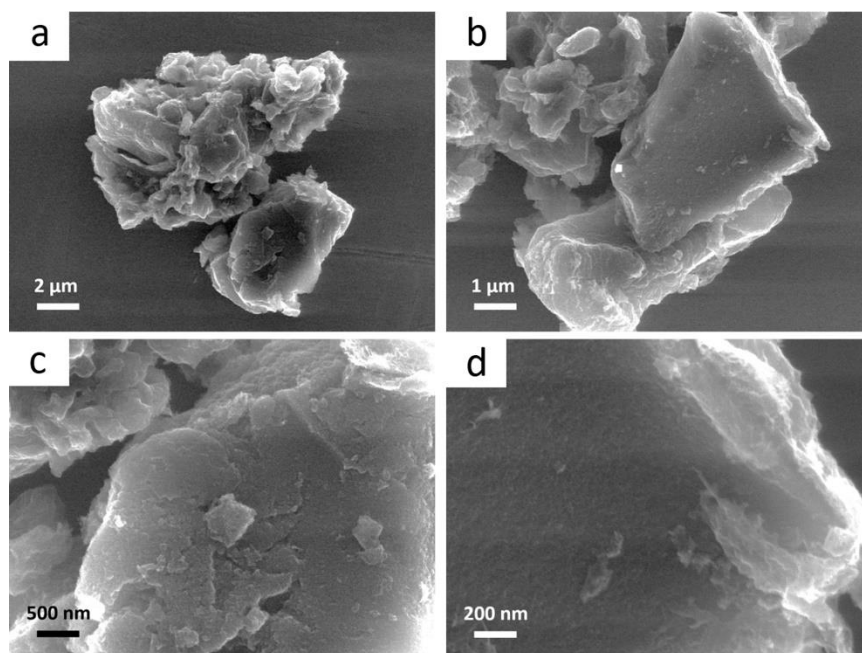
Figure S13. SEM images of C-TpBpy-Fe.
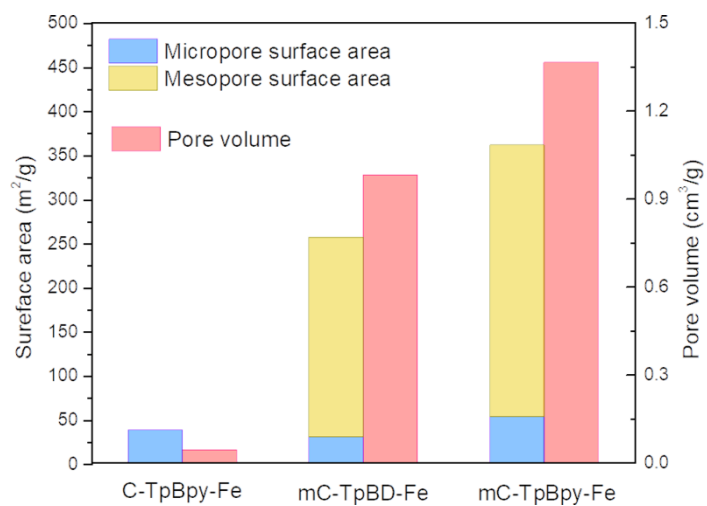
Figure S14. Specific surface area and pore volume of C-TpBpy-Fe, mC-TpBD-Fe and mC-TpBpy-Fe.
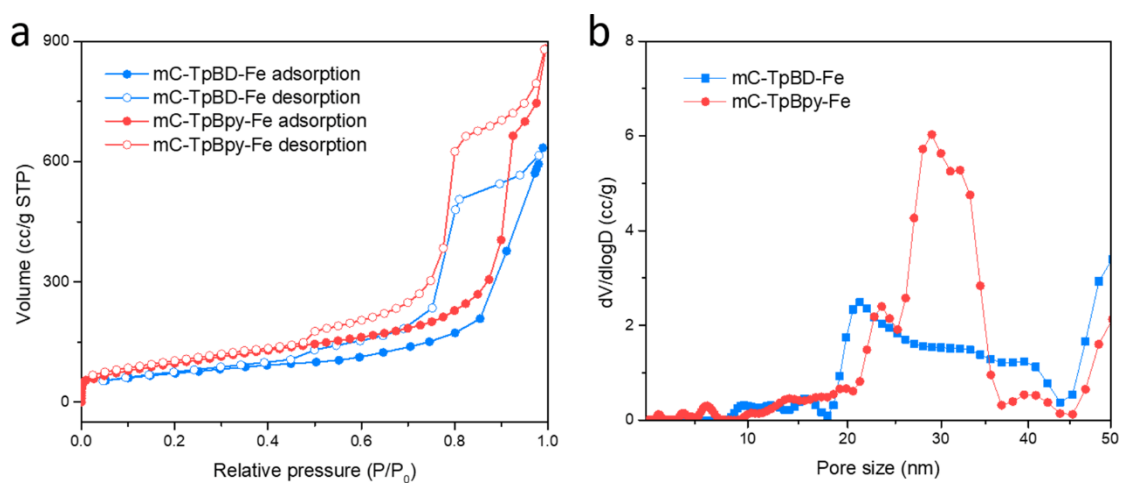
Figure S15. a) N_2 adsorption-desorption isotherms of the mC-TpBD-Fe and mC-TpBpy-Fe. b) Pore size distribution of the mC-TpBD-Fe and mC-TpBpy-Fe.
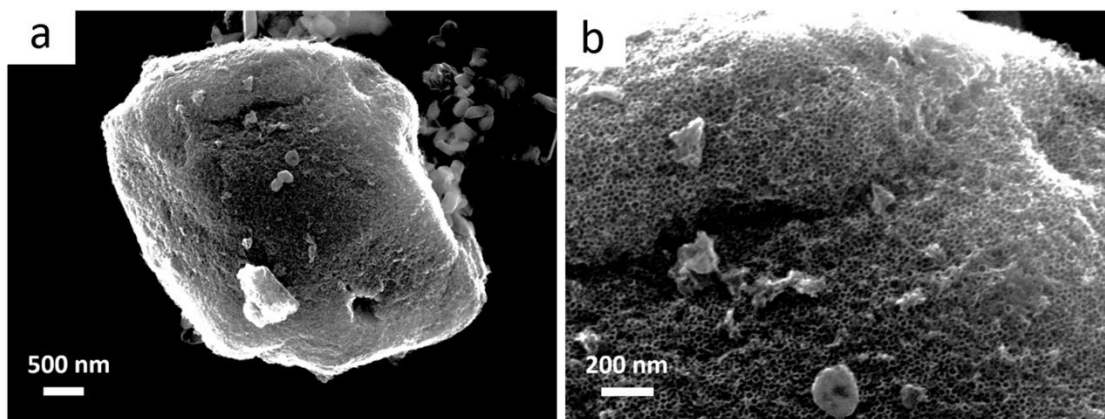
Figure S16. SEM images of mC-TpBD-Fe.
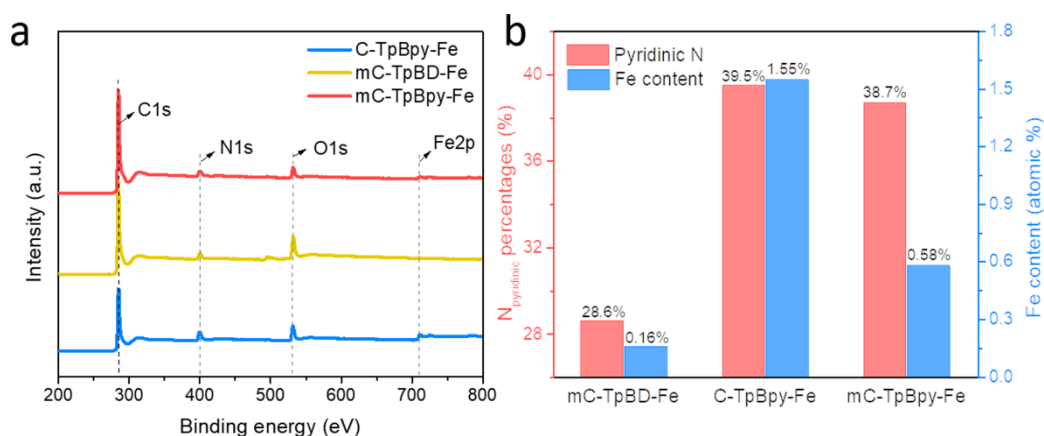
Figure S17. a) Survey scan of the C-TpBpy-Fe, mC-TpBD-Fe and mC-TpBpy-Fe showing the presence of C, N, O and Fe in carbon matrix. b) Pyridinic nitrogen and iron contents of the C-TpBpy-Fe, mC-TpBD-Fe and mC-TpBpy-Fe, calculated from XPS analyses.
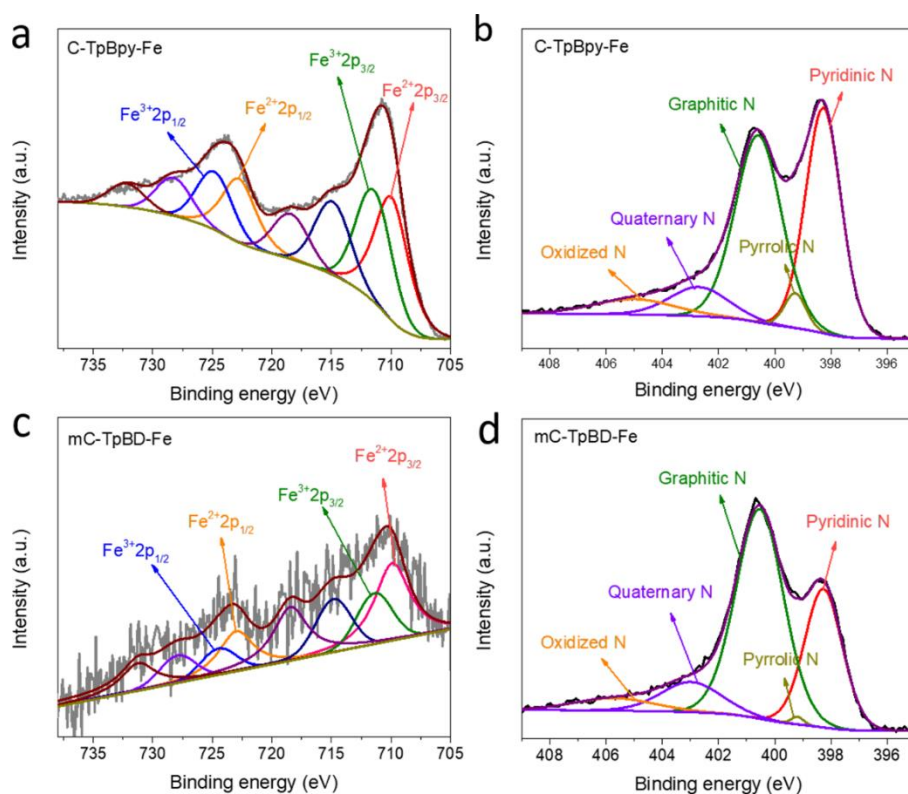
Figure S18. High resolution Fe2p and N1s of a, b) C-TpBpy-Fe and c, d) mC-TpBD-Fe.
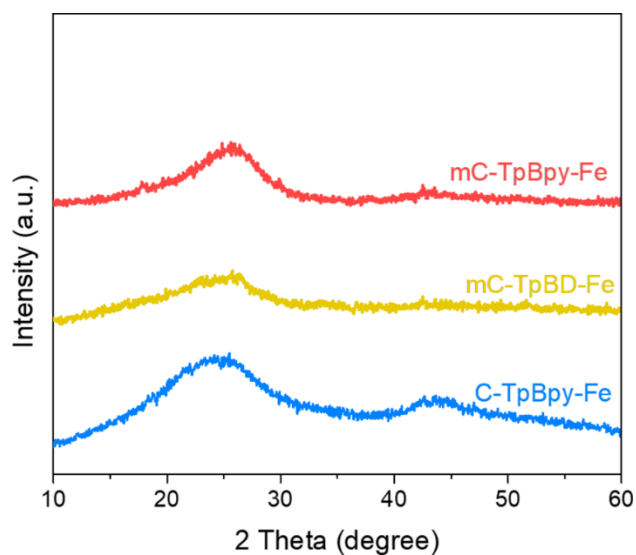
Figure S19. PXRD patterns of C-TpBpy-Fe, mC-TpBD-Fe and mC-TpBpy-Fe.
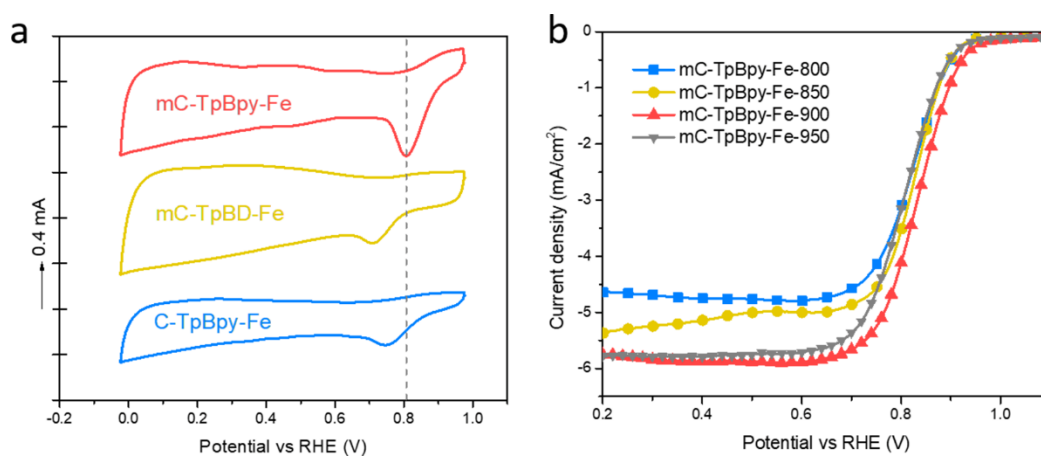
Figure S20. a) CV curves of C-TpBpy-Fe, mC-TpBD-Fe and mC-TpBpy-Fe in oxygen-saturated 0.1 M KOH. b) LSV curves of mC-TpBpy-Fe at different pyrolysis temperature.
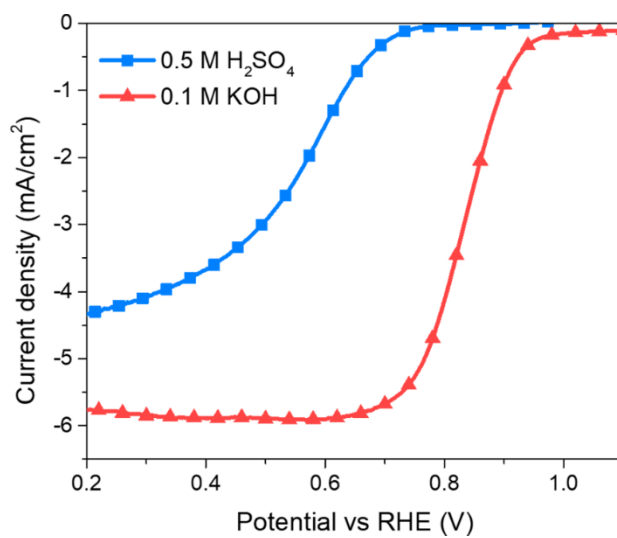
Figure S21. LSV curves of mC-TpBpy-Fe in 0.1 M KOH and 0.5 M H_2SO_4.
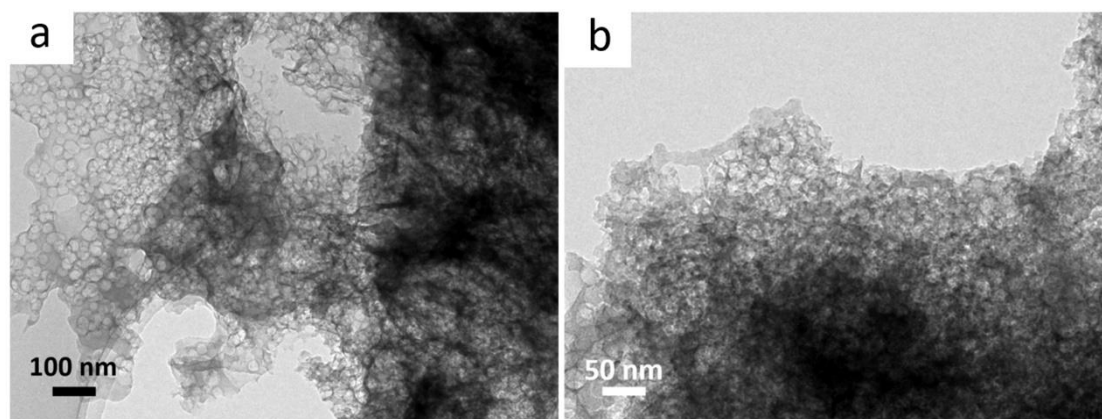
Figure S22. SEM images of mC-TpBpy-Fe after 5000 cycles at a voltage range between 0.7
to 1.0 V.
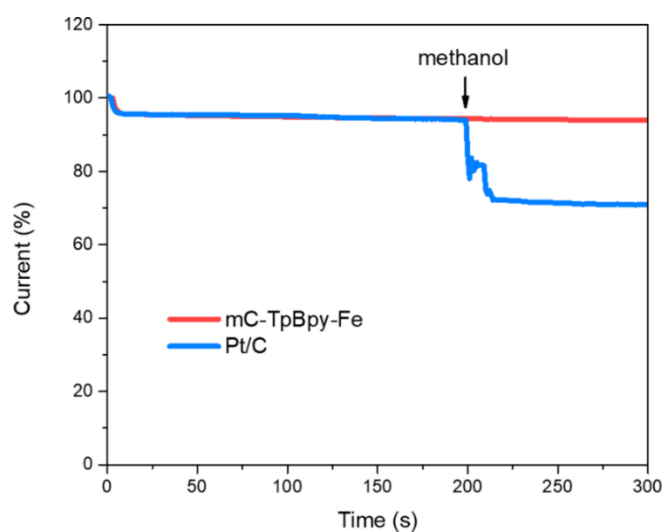
Figure S23. Chronoamperometric response of mC-TpBpy-Fe and Pt/C as ORR catalysts on addition of 9 mL methanol after about 200 s.
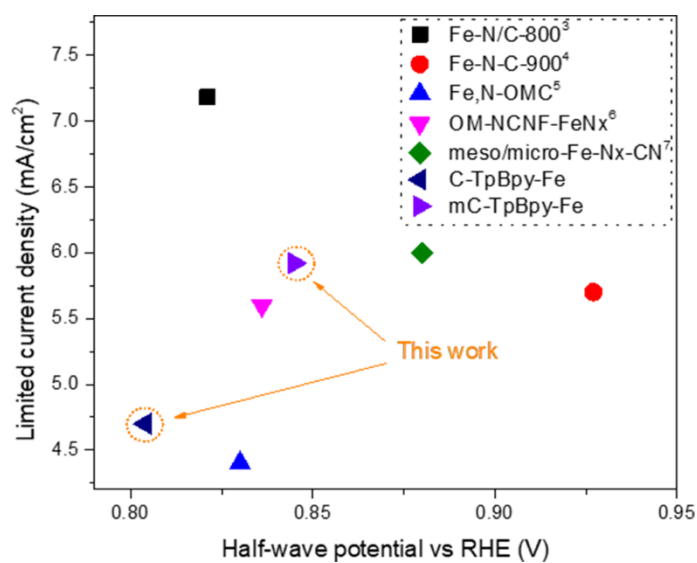
Figure S24. Comparison of half-wave potential versus current density between mC-TpBpy-Fe and some recently reported FeN_x doped mesoporous carbons derived by silica templated processes; these OER performances are adapted from references.[3-7]
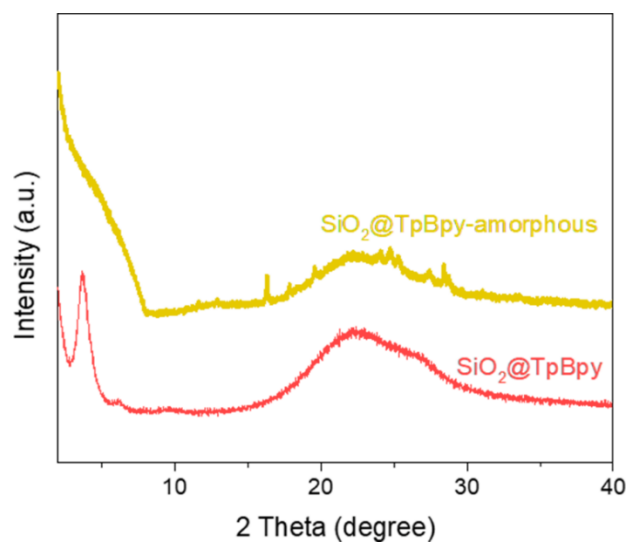
Figure S25. PXRD patterns of SiO$_2$@TpBpy and SiO$_2$@TpBpy-amorphous.
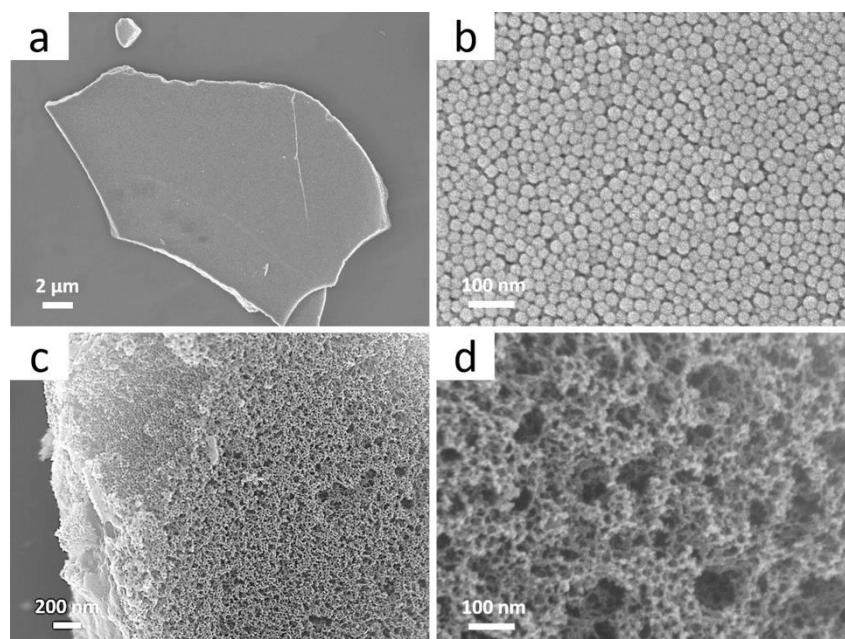
Figure S26. SEM images of a, b) C-SiO$_2$@Bpy-Fe; c, d) mC-Bpy-Fe
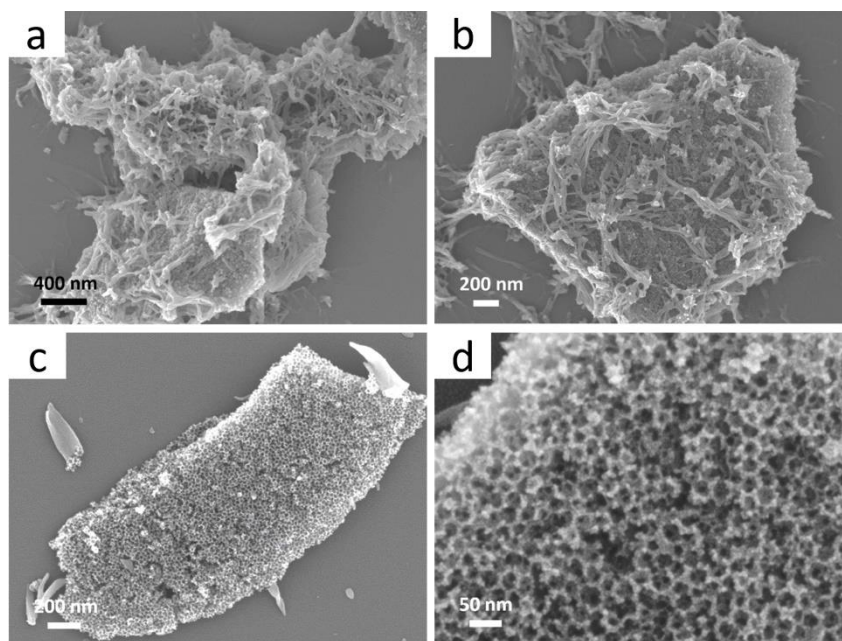
Figure S27. SEM images of a, b) C-SiO$_2$@TpBpy-Fe-amorphous; c, d) mC-TpBpy-Fe-
amorphous.
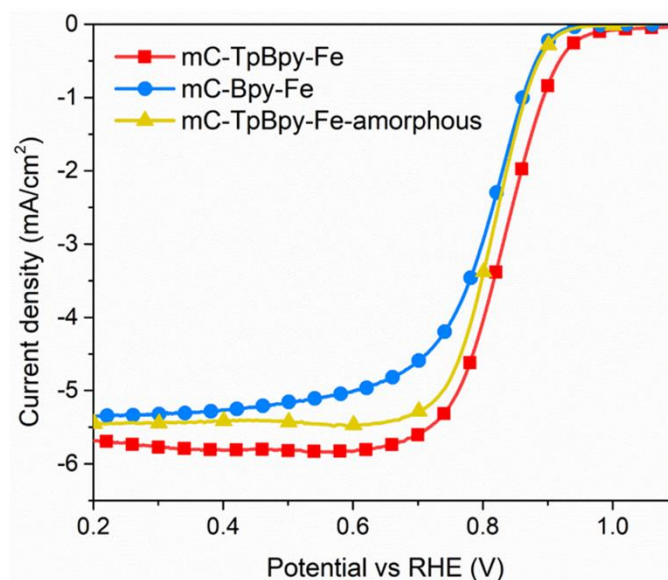
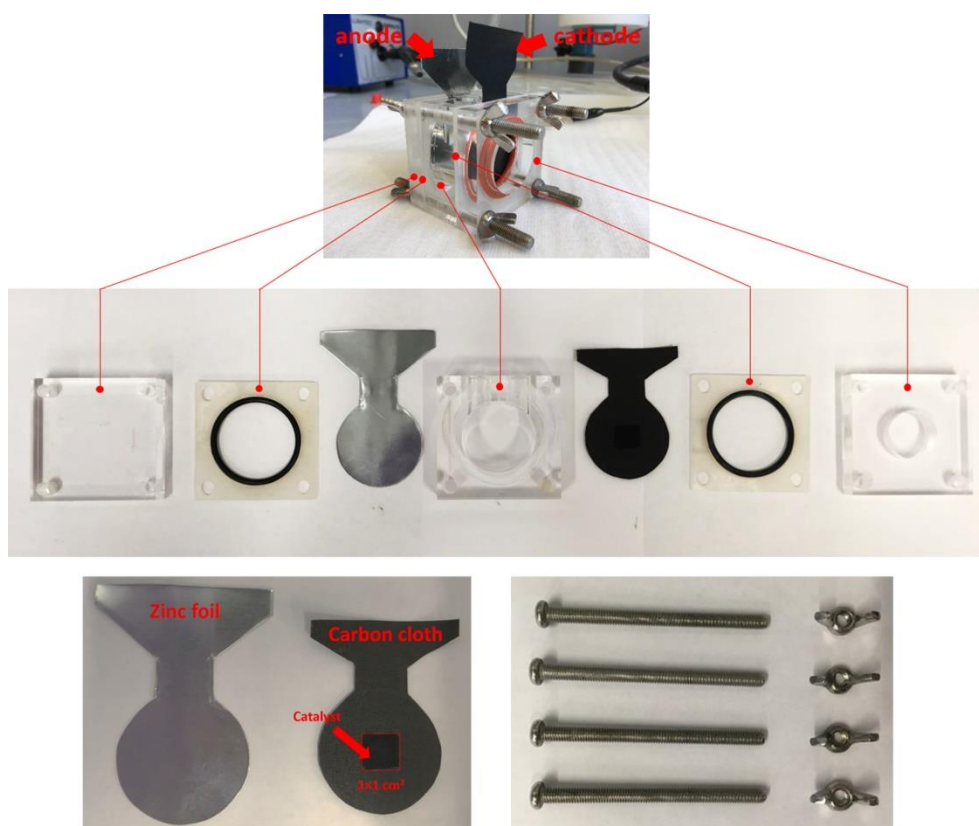**Figure S28.** LSV curves of mC-TpBpy-Fe, mC-Bpy-Fe and mC-TpBpy-Fe-amorphous in 0.1
M KOH.

Figure S29. Photographs of the homemade Zn-air battery with a zinc foil as anode and catalyst loaded (1.0×1.0 cm^2) on carbon cloth with gas diffusion layer as cathode.

Table S1. Structural properties and element content of the obtained COF-derived carbon catalysts.

	[a]Total surface area (m²/g)	[b]Total pore volume (cm³/g)	Fe content (atomic %)	N content (atomic %)					
				Total N content	Pyridinic N	Pyrrolic N	Graphitic N	Quaternary N	Oxidized N
C-TpBpy-Fe	38.8	0.044	1.55	9.28	3.67	0.34	3.93	0.77	0.57
mC-TpBD-Fe	257	0.981	0.16	4.78	1.37	0.02	2.66	0.47	0.26
mC-TpBpy-Fe	362	1.364	0.58	4.5	1.74	-	1.89	0.44	0.43

[a]BET specific surface areas calculated in P/P_0 from 0.003 to 0.05. [b]Total pore volumes calculated based on the volume adsorbed at P/P_0 of ~ 0.995.

Table S2. ORR performance of the as-synthesized COF-derived carbon catalysts

	[a]Onset potential (V vs RHE)	[b]$E_{1/2}$ (V vs RHE)	$J_{limited}$ (mA/cm²)	$J_{at\ 0.8V}$ (mA/cm²)	J_k (mA/cm²)
C-TpBpy-Fe	0.895	0.804	4.41	2.25	4.60
mC-TpBD-Fe	0.892	0.808	4.58	2.51	5.55
mC-TpBpy-Fe	0.920	0.845	5.92	4.13	13.66
Pt/C	0.951	0.852	5.57	4.32	19.24

[a]The onset potential values of all catalysts were based on the current density of 10% of the limited current density; [b]Half-wave-potentials $E_{1/2}$ were determined at the point where the current density reached 50% of the limited current density of each catalyst

Table S3. Summary of recently reported ORR performances of different porous carbon catalysts under alkaline conditions (0.1 M KOH).

Catalysts	Catalyst loading (mg/cm^2)	E$_{1/2}$ (V vs RHE)	E$_{1/2}$ of reported Pt/C (V vs RHE)	Reference
mC-TpBpy-Fe	**0.25**	**0.845**	**0.852**	**This work**
FeSAs/PTF-600	0.05	0.87	0.81	*ACS Energy Lett., **2018**, 3, 883-889*
FeBNC-800	0.6	0.838	0.851	*ACS Energy Lett. **2018**, 3, 252-260*
N/S hierarchically porous carbon	0.14	0.85	0.85	*Energy. Environ. Sci., **2017**, 10, 742-749*
Rh/C-800	0.8	0.806	0.879	*Nanoscale, **2017**, 9, 1834-1839*
S, N-Fe/N/C-CNT	0.6	0.85	0.82	*Angew. Chem. Int. Ed., **2017**, 56, 610-614*
N/S hierarchically porous carbon from silica templating	0.14	0.85	0.85	*Energy. Environ. Sci., **2017**, 10, 742-749*
Fe/SNC	0.5	0.86	0.83	*Angew. Chem. Int. Ed., **2017**, 56, 13800-13804*
Fe-ISAs/CN	0.408	0.9	0.845	*Angew. Chem. Int. Ed., **2017**, 56, 6937-6941*
NFe/CNs-700-800-N2	0.10	0.855	0.85	*Adv. Mater., **2017**, 29, 1700707*
Defective activatd-carbon with Mn-Co nanoparticles	0.16	0.803	0.80	*Adv. Mater., **2016**, 28, 8771-8778*
NCNTFs	0.2	0.87	0.85	*Nat. Energy **2016**, 1, 15006*
CNT/PC	0.8	0.88	-	*J. Am. Chem. Soc., **2016**, 138, 15046-15056*
Fe-N-C/Fe/Fe$_3$C	0.7	0.899	-	*J. Am. Chem. Soc. **2016**, 138, 3570−3578*
Co SAs/N-C(900)	0.408	0.881	0.811	*Angew. Chem. Int. Ed. **2016**, 55, 10800-10805*
Fe-N/C electrocatalysts	0.8	0.88	0.87	*J. Am. Chem. Soc., **2016**, 138, 15046-15056*
Fe-N-C catalyst	0.8	0.85	0.84	*Nat. Commun., **2015**, 6, 8618*
Fe-N-C-3HT-2AT	0.8	0.85	0.84	*Nat. Commun. **2015**, 6, 8618*

(Fe,Mn)-N-C-3HT-2AT		0.9		
N, P-doped carbon foam	0.15	0.85	0.85	*Nat. Nanotechnol., **2015**, 10, 444*
Fe$_3$N encapsulated in graphitic layers	0.4	0.860	0.840	*Adv. Mater*., **2015**, 27, 2521-2527
N/S-doped carbon nanotube core-sheath nanostructure	0.6	0.82	0.85	*Angew. Chem. Int. Ed.,* **2014**, 53, 4102-4106
Fe-N/C-800	0.1	0.809	0.818	*J. Am. Chem. Soc.,* **2014**, 136, 11027-11033

References

[1] Chong, J. H.; Sauer, M.; Patrick, B. O.; MacLachlan, M. J. Highly Stable Keto-enamine Salicylideneanilines. *Org. Lett.,* **2003**, 5, 3823-3826.

[2] Albrecht, M.; Janser, I.; Lützen, A.; Hapke, M.; Fröhlich, R.; Weis, P. 5, 5′-Diamino-2, 2′-bipyridine: A Versatile Building Block for the Synthesis of Bipyridine/Catechol Ligands That Form Homo- and Heteronuclear Helicates. *Chem. Eur. J.* **2005,** 11, 5742-5748.

[3] Liu, Y.; Li, S.; Li, X.; Mao, L.; Liu, F. Fe-N Co-doped Porous Carbon Derived from Ionic Liquids as an Efficient Electrocatalyst for the Oxygen Reduction Reaction. *Ind. Eng. Chem. Res*. **2018**, 57, 15638-15646

[4] Zhu, C.; Shi, Q.; Xu, B. Z.; Fu, S.; Wan, G.; Yang, C.; Yao, S.; Song, J.; Zhou, H.; Du, D.; Beckman, S. P. Hierarchically Porous M-N-C (M= Co and Fe) Single-Atom Electrocatalysts with Robust MN$_x$ Active Moieties Enable Enhanced ORR Performance. *Adv. Energy Mater*. **2018,** 8, 1801956.

[5] Liu, X.; Zou, S.; Chen, S. Ordered Mesoporous Carbons Codoped with Nitrogen and Iron as Effective Catalysts for Oxygen Reduction Reaction. *Nanoscale*. **2016,** 8, 9249-9255.

[6] Cheng, C.; Li, S.; Xia, Y.; Ma, L.; Nie, C.; Roth, C.; Thomas, A.; Haag, R. Atomic Fe-N$_x$ Coupled Open-Mesoporous Carbon Nanofibers for Efficient and Bioadaptable Oxygen Electrode in Mg-Air Batteries. *Adv. Mater*. **2018,** 30, 1802669.

[7] Li, S.; Cheng, C.; Zhao, X.; Schmidt, J.; Thomas, A. Active Salt/Silica-Templated 2D Mesoporous FeCo-N$_x$-Carbon as Bifunctional Oxygen Electrodes for Zinc-Air Batteries. *Angew. Chem. Int. Ed.* **2018,** 57, 1856-1862.

8.4 Macro/Microporous Covalent Organic Frameworks for Efficient Electrocatalysis

Published version

X. J. Zhao, P. Pachfule, S. Li, T. Langenhahn, M. Y. Ye, C. Schlesiger, S. Praetz, J. Schmidt, A. Thomas, Macro/Microporous Covalent Organic Frameworks for Efficient Electrocatalysis, *J. Am, Chem, Soc.* **2019**, 141, 6623-6630.
https://pubs.acs.org/doi/abs/10.1021/jacs.9b01226

JACS

JOURNAL OF THE AMERICAN CHEMICAL SOCIETY

Article

pubs.acs.org/JACS

Macro/Microporous Covalent Organic Frameworks for Efficient Electrocatalysis

Xiaojia Zhao,[†] Pradip Pachfule,[†] Shuang Li,[†] Thomas Langenhahn,[†] Mengyang Ye,[†] Christopher Schlesiger,[‡] Sebastian Praetz,[‡] Johannes Schmidt,[†] and Arne Thomas*,[†]

[†]Department of Chemistry, Division of Functional Materials, Technische Universität Berlin, Hardenbergstraße 40, 10623 Berlin, Germany

[‡]Institute of Optics and Atomic Physics, Technische Universität Berlin, Hardenbergstraße 36, 10623 Berlin, Germany

S *Supporting Information*

ABSTRACT: Covalent organic frameworks (COFs) are of interest for many applications originating from their mechanically robust architectures, low density, and high accessible surface area. Depending on their linkers and binding patterns, COFs mainly exhibit microporosity, even though COFs with small mesopores have been reported using extended linkers. For some applications, especially when fast mass transport is desired, hierarchical pore structures are an ideal solution, e.g., with small micropores providing large surface areas and larger macropores providing unhindered transport to and from the materials surface. Herein, we have developed a facile strategy for the fabrication of crystalline COFs with inherent microporosity and template-induced, homogeneously distributed, yet tunable, macroporous structures. This method has been successfully applied to obtain various β-ketoenamine-based COFs with interconnected macro−microporous structures. The as-synthesized macroporous COFs preserve high crystallinity with high specific surface area. When bipyridine moieties are introduced into the COF backbone, metals such as Co^{2+} can be coordinated within the hierarchical pore structure (macro-TpBpy-Co). The resulting macro-TpBpy-Co exhibits a high oxygen evolution reaction (OER) activity, which is much improved compared to the purely microporous COF with a competitive overpotential of 380 mV at 10 mA/cm². This can be attributed to the improved mass diffusion properties in the hierarchically porous COF structures, together with the easily accessible active Co^{2+}-bipyridine sites.

INTRODUCTION

Extended crystalline microporous materials have been intensively studied within recent years not only because of their fascinating structural features but also because they have a range of possible applications from chemical process industries to advanced uses in optics, electronics, catalysis, and drug delivery.[1−11] However, the sole presence of micropores in many crystalline porous materials often imposes diffusion limitations, which is especially problematic for catalytic processes requiring essential mass transfer, as in this case just a low utilization of active sites can be achieved.[6] The construction of hierarchical porous structures, for example the introduction of meso- or macropores in crystalline microporous materials is considered to be an effective way to minimize these adverse effects, and a few progressive examples including mesoporous crystalline zeolites[4,6,12] and macroporous MOFs[13,14] have been achieved. It was shown that the introduction of hierarchical porosity is advantageous by substantially improving mass transfer and accessibility of the high surface areas.

Covalent organic frameworks (COFs), as an emerging class of crystalline porous materials with well-defined and predictable structures, exhibit low density and high accessible surface areas.[3,11,15−21] Just after the first successful report of porous and crystalline COFs (COF-1 and COF-5) by Yaghi and co-workers in 2005, several new COFs have been studied for application in gas separation, heterogeneous catalysis, optoelectronics, and energy storage.[3,19,22,23] However, due to the synthesis conditions, most reported COFs are synthesized and isolated as microcrystalline powders, exhibiting porosities restricted to the microporous or small mesopore regime, which largely limits their applications for diffusion-limited processes. Even though synthetic strategies to generate secondary porosities within COFs have been explored, including hollow spherical COFs with mesoporous wall and imine COFs with hollow microtubular morphology,[24−26] the obtained hierarchical porous COFs usually exhibited disconnected and uncontrolled porous architectures. The principle limitation toward the synthesis of hierarchical COF structures is the instability of templates in the COF synthesis reaction medium, as most of the COFs have been synthesized solvothermally
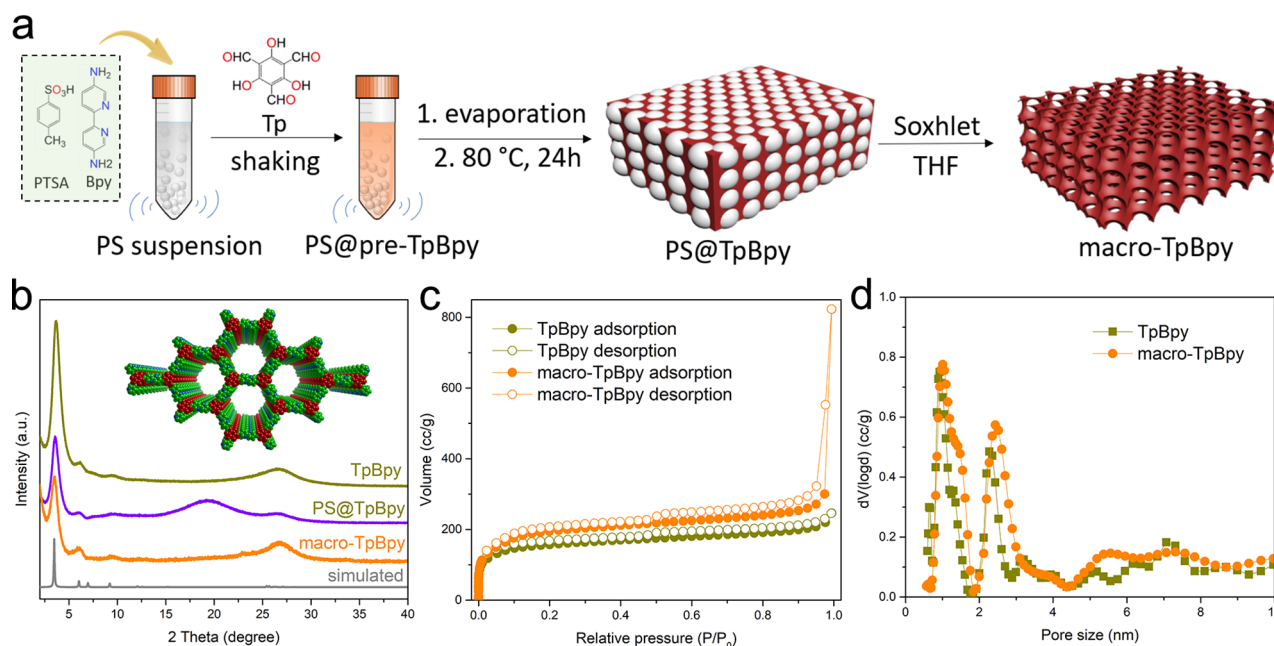
Figure 1. Synthesis and characterization of macro−microporous COF. (a) Schematic representation of macro-TpBpy fabrication in the presence of PSs. (b) PXRD pattern of TpBpy, PS@TpBpy, and macro-TpBpy showing the preservation of crystallinity in macro-TpBpy with and after removing the PSs. Inset: Space-filling packing diagram of TpBpy COF. (c) N_2 adsorption−desorption isotherms of the TpBpy and macro-TpBpy. (d) Pore size distribution of the TpBpy and macro-TpBpy, calculated from the adsorption branch of isotherms by the QSDFT model.

under acidic or basic conditions. In these regards, the synthesis of meso- or macroporous COF with controllable porosity structures is very challenging, yet highly desirable, particularly for a diffusion-limited process such as the oxygen evolution reaction (OER), where a macroporous structure can efficiently enhance the formation and transport of O_2 gas bubbles, thereby promoting the reaction.[27−30]

Herein, we report a practical and efficient approach for the preparation of crystalline and hierarchical COF structures, that is, with macropores in addition to their inherent microporosity (macro-TpBpy), via a template-assisted method. Polystyrene spheres (PSs) have been utilized as a hard template to enable the formation of interconnected macropores within COF structures. In particular, the size of macropores can be tuned through the size modulation of PSs, and the composition can be altered by changing the COF precursors. The obtained macroporous COFs preserve a high crystallinity with high specific surface area, hierarchical pore structures, and chemically stable frameworks, hence resulting in fast mass transport and more accessible active sites. Fast mass and ion transport in hierarchical COF structures have been confirmed by utilizing cobalt-coordinated bipyridine-based COFs as an OER catalyst. The as-synthesized Co-coordinated macro-microporous COFs (macro-TpBpy-Co) exhibit excellent performance as OER catalysts, especially compared to the Co-coordinated purely microporous COF but also to most of the reported cobalt-doped polymer-based electrocatalysts, proving the advantage of hierarchically COF structures for catalytic application.

◼ RESULTS AND DISCUSSION

Macroporous TpBpy (macro-TpBpy) was synthesized by reacting the organic linkers 1,3,5-triformylphloroglucinol (Tp) and 2,2′-bipyridine-5,5′-diamine (Bpy) in the presence of PSs via Schiff base reaction, as schematically illustrated in Figure 1a. The monodispersed colloidal PSs used as a hard template have been synthesized according to a literature

reported procedure,[13] and p-toluenesulfonic acid (PTSA) was used as a catalyst for the COF formation.[16,31] In the first step, the colloidal PSs (∼10 wt % in water, 5 mL) were mixed with the Bpy linker (83.8 mg, 0.45 mmol) and PTSA (475.5 mg, 2.5 mmol) which formed an organic salt. Then the resulting salt and Tp (63 mg, 0.3 mmol) were thoroughly shaken for 10 min, and the dispersion was poured into a Petri dish to evaporate excess water at room temperature overnight. Further drying at 80 °C for 24 h yielded an orange-colored PS@TpBpy composite (Figure S1). Subsequently, Soxhlet extraction of PS@TpBpy was conducted using tetrahydrofuran (THF) as solvent to remove the PS template as well as unreacted monomers, to obtain a COF with a macroporous structure (macro-TpBpy). In a control experiment, pristine TpBpy was prepared following the same process, but in the absence of PSs (TpBpy).

To test the crystallinity of the macroporous COFs, powder X-ray diffraction (PXRD) measurements were conducted for macro-TpBpy, PS@TpBpy, and pristine TpBpy. As shown in Figure 1b, macro-TpBpy displays an intense peak at 3.6° (2θ) corresponding to the reflection from the (100) plane, very similar to the pristine TpBpy, confirming the retention of the crystalline structure of TpBpy even after removing the PS template.[32] The presence of broad peaks at 26° (2θ) was assigned to the (001) plane that corresponds to the π−π stacking of the COF layers. In addition to these prominent peaks, PS@TpBpy shows a broad peak at 19° (2θ) attributed to the amorphous PS, while the disappearance of this peak in macro-TpBpy indicates the complete removal of the PS template after the Soxhlet treatment. Nitrogen sorption isotherms were collected to examine the specific surface area and microporosity of pristine TpBpy and macro-TpBpy. As shown in Figure 1c, the isotherm of pristine TpBpy exhibits a typical type I isotherm with a steep increase at low relative pressures, indicating the microporosity of the COF, which was further corroborated using the corresponding pore size

distribution (Figure 1d). In the case of macro-TpBpy, the isotherm also shows a type I isotherm but with an additional significant increase in nitrogen uptake at high relative pressure, indicating that an additional macroporosity has been successfully introduced by the PS template. The calculated pore volume further confirms the presence of macroporosity in hierarchical macro-TpBpy, as the total pore volume of macro-TpBpy (1.273 cm^3/g) is much higher compared to pristine TpBpy (0.381 cm^3/g) (Table S2). On the other hand, the calculated Brunauer−Emmett−Teller (BET) surface areas of macro-TpBpy (723 m^2/g) are higher than that of pristine TpBpy (588 m^2/g), showing that the formation of macropores can efficiently promote the accessibility of micropores.

The morphological features of the as-synthesized PS-COF composite and macroporous COF were characterized by scanning electron microscopy (SEM) analyses. Figure 2a
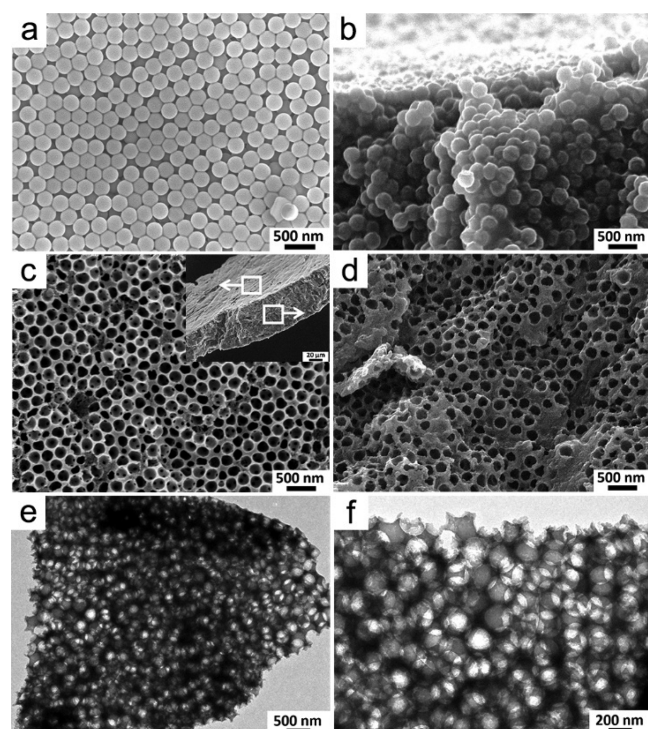
Figure 2. SEM images of (a) monodisperse colloidal PSs, (b) PS@TpBpy, and (c, d) macro-TpBpy. (e, f) TEM images of macro-TpBpy.

shows the successful preparation of PSs with a uniform size and an average diameter of ∼270 nm. The monodisperse colloidal PSs form a stable dispersion in aqueous solution without any aggregation or sedimentation and thus can be easily used for the fabrication of homogeneous PS−COF composites (Figure S2). As shown in Figure 2b, the PS@TpBpy composites display a pile of densely packed PS nanoparticles with a coating of TpBpy COF on the surface, as confirmed from high-magnification images, indicating the formation of homogeneous PS−COF composites (Figure S3). After removing the PS template using Soxhlet extraction with THF, the obtained macro-TpBpy displays a replica of the PS spheres yielding an interconnected uniform macroporous structures (Figure 2c). In order to confirm the uniformity of the macroporous structure within the materials, cross-section SEM analyses were performed, and a pronounced inner macroporous structures was observed, similar to the porous

structure seen at the outer surface of macro-TpBpy particles (Figure 2d). The corresponding statistical diameter of the macropores was calculated to illustrate the macropore size distribution (Figure S4). Furthermore, transmission electron microscopy (TEM) proved the interconnected porous structures (Figure 2e, f), which should be advantageous for mass transfer, e.g., during heterogeneous catalysis. In contrary, the pristine TpBpy synthesized without PS template features bulk particles without any characteristic morphologies (Figure S5).

As it can be expected that the nature of the template affects the pore structure and morphology of the COF replica, we studied the influence of particle size and template amount on the porosity as well as the crystallinity of the resulting structures. PS suspensions with different solid content (5 wt % and 15 wt % in water) were applied to prepare the corresponding macro-TpBpy (denoted as macro-TpBpy-5 wt % and macro-TpBpy-15 wt %). Both samples show comparable PXRD patterns as seen before, demonstrating the retention of the robust COF framework structure (Figure S6). However, macro-TpBpy-5 wt % exhibits an inhomogeneous macroporous structure with larger nontemplated areas due to the low amount of PSs used (Figure S7), while the morphology of macro-TpBpy-15 wt % is comparable to macro-TpBpy-10 wt % (Figure S8). Subsequently, a series of macro-TpBpy with macropore sizes ranging from ∼160 nm to ∼360 nm were prepared by applying different sized PS templates (Figure 3a−c). The corresponding macro-TpBpy replicas show the expected macroporous sizes of ∼160, 320, and 360 nm, respectively (Figure 3d−f), all with retained crystallinity (Figure S9), confirming that this approach can be applied for various PS templates. Furthermore, to identify the general applicability of the proposed strategy, several other amine linkers (benzidine (BD); 2,6-dimethoxybenzidine (BD-Me$_2$); p-azoaniline (Azo); and 4,4″-diamino-p-terphenyl (TD)) were used to fabricate the corresponding macro-COFs (Figure 3g and Figures S10−13). The PXRD patterns of these macro-COFs show intense reflection peaks corresponding to the (100) plane at the 2θ value of 3.6° (macro-TpBD), 3.6° (macro-TpBD-Me$_2$), 3.1° (macro-TpAzo), and 2.9° (macro-TpTD), respectively (Figure 3h). N$_2$ sorption analyses of these macroporous COFs exhibit the typical type I isotherm with the additional increase in nitrogen uptake at high relative pressure, consistent with the one observed for macro-TpBpy (Figure S14). In addition, SEM images show the pronounced macroporous structures for each of these macro-COFs, confirming the versatility of this approach to other amine linkers (Figures S10−13).

Co-based catalytic systems are widely investigated as promising electrocatalysts for OER.[33−41] In this approach, the bipyridine amine linker was therefore deliberately chosen as it can strongly coordinate to metal ions, mimicking metal−bipyridine molecular systems. Herein, as a proof of concept, cobalt ions were used to form macro-TpBpy-Co by soaking a defined amount of macro-TpBpy in cobalt acetate (Co(OAc)$_2$·4H$_2$O) solutions in methanol and further stirring for 4 h at room temperature (Figure 4a).[32,42] As reference, TpBpy-Co was prepared by following the same protocol but using pristine TpBpy. The PXRD patterns of macro-TpBpy-Co and TpBpy-Co show that the crystallinity of the COF frameworks is retained after cobalt coordination (Figure S15a). N$_2$ sorption analyses of macro-TpBpy-Co and TpBpy-Co show a decreased BET surface area of 387 and 314 m^2/g, respectively, probably
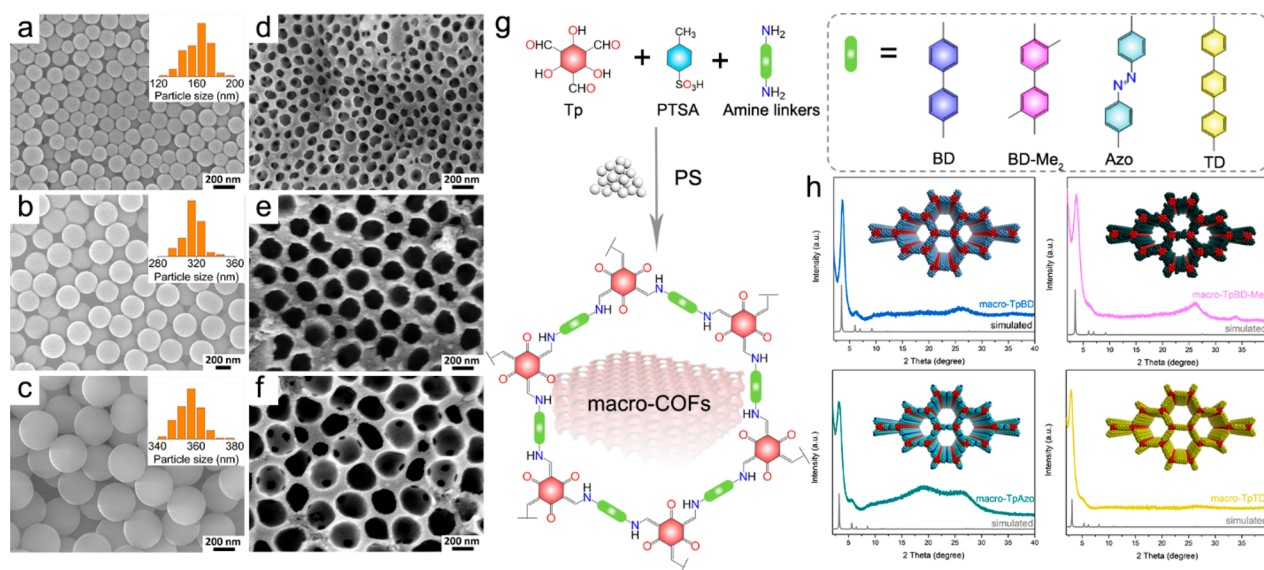
Figure 3. SEM images of PSs and macro-TpBpy with macropore sizes of (a, d) ~160 nm, (b, e) ~320 nm, and (c, f) ~360 nm. (g) General synthesis of macro-COFs from different amines (BD, BD-Me$_2$, Azo, and TD) in the presence of PSs. (h) The corresponding PXRD patterns of macro-TpBD, macro-TpBD-Me$_2$, macro-TpAzo, and macro-TpTD and their respective simulated structures. Inset: Space-filling packing models of respective COFs.
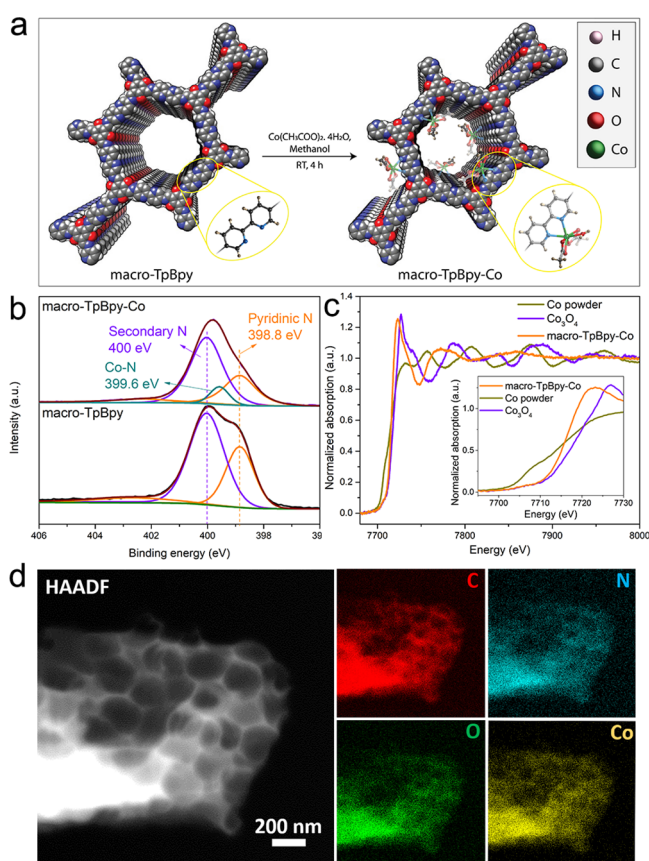

Figure 4. Synthesis and characterization of macro-TpBpy-Co. (a) Schematic representation of the synthesis of macro-TpBpy-Co. (b) High-resolution N 1s spectra of macro-TpBpy and macro-TpBpy-Co. (c) Normalized Co K-edge XAS spectra for macro-TpBpy-Co referenced by Co$_3$O$_4$ and Co powder. The inset shows the magnified image of the pre-edge XAS spectra. (d) HAADF-STEM images and the corresponding element mapping of C, N, O, and Co.

due to the increased mass by adding the cobalt salt (Figure S15b). In addition, SEM images reveal the preservation of the uniformly distributed macroporous structures (Figure S15c,d), which are supposed to be important to promote the accessibility of active sites and mass transfer during the OER electrocatalytic process. Subsequently, X-ray photoelectron spectroscopy (XPS) was conducted to confirm the presence of Co species at macro-TpBpy-Co and TpBpy-Co, yielding an amount of 2.84 and 3.01 atomic %, respectively (Figure S16a and Table S2). The high-resolution Co 2p spectra exhibit two main peaks centered at 781 and 797 eV, which were assigned to the Co 2p$_{3/2}$ and Co 2p$_{1/2}$ core levels, respectively, and the feature of the satellite at 786 eV specifies the presence of Co^{2+} (Figure S16b).[43] The high-resolution N 1s spectra of macro-TpBpy-Co show an extra peak corresponding to the Co−N bond appearing at 399.6 eV compared with macro-TpBpy, pointing to a coordination of Co ions to the pyridine N within the COF backbone (Figure 4b).[44] Similar spectra confirm the existence of a Co−N bond in the TpBpy-Co sample as well (Figure S16c). To further elucidate the nature of the Co species in macro-TpBpy-Co, X-ray absorption spectroscopy (XAS) was performed. As shown in the normalized Co K-edge spectra (Figure 4c), the rising-edge position of macro-TpBpy-Co is located between the Co powder and Co$_3$O$_4$ standard, indicating that the oxidation state of Co within macro-TpBpy-Co is +2 and +3. The Fourier transformed extended X-ray absorption fine structure (EXAFS) data reveal a variation of the neighboring environment for Co^{2+}, where macro-TpBpy-Co displays one main peak at 1.5 Å, which is clearly distinct from Co$_3$O$_4$ standard, Co powder, and Co(acac)$_2$, confirming the existence of the Co−N first coordination shell (Figure S17). Moreover, high-angle annular dark-field scanning transmission electron microscopy (HAADF-STEM) imaging was conducted to reveal the morphology and element distribution in the macro-TpBpy-Co. The HAADF-STEM images and corresponding elemental mapping for C, N, O, and Co prove the uniform distribution of N and Co species within the macro-TpBpy-Co matrix (Figure 4d).

In order to analyze the role of hierarchical porosity in heterogeneous catalysis, the OER activity of macro-TpBpy-Co in an alkaline aqueous electrolyte (0.1 M KOH) using a typical three-electrode system was evaluated. The catalysts were casted onto a rotating disk electrode (RDE), rotating at a rate of 1600 rpm to counteract bubble accumulation at the electrode surface. For comparison, the electrocatalytic activities of macro-TpBpy, TpBpy-Co, and commercial RuO_2 with the same mass loading of 0.25 mg/cm^2 (geometrical area) were studied. As shown in Figure 5a, macro-TpBpy-Co requires an
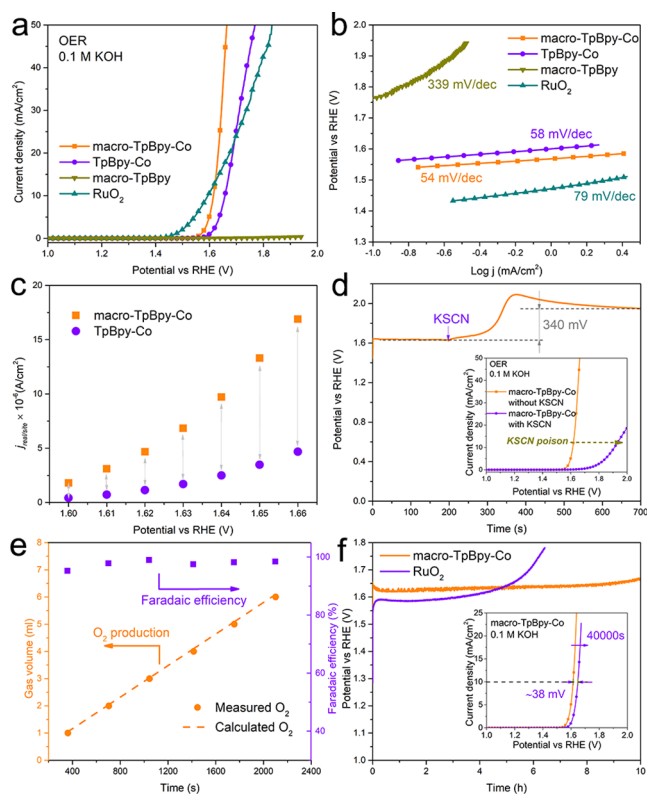
Figure 5. OER performance of macro-COF-Co. (a) OER polarization curves and (b) corresponding Tafel plots for macro-TpBpy, macro-TpBpy-Co, TpBpy-Co, and a commercial RuO_2 catalyst. (c) Scatter plot of $j_{real/site}$ for macro-TpBpy-Co and TpBpy-Co, versus applied potential. (d) Chronopotentiometry response of macro-TpBpy-Co as OER catalysts on addition of 10 mM KSCN in 0.1 M KOH after about 200 s. Inset: OER polarization plots of macro-TpBpy-Co with and without 10 mM KSCN in 0.1 M KOH, indicating that SCN$^-$ ions strongly poison the macro-TpBpy-Co catalyst. (e) Faradaic efficiency of macro-TpBpy-Co for oxygen production. (f) Chronopotentiometry test of macro-TpBpy-Co and RuO_2 catalysts at a constant current density of 10 mA cm^{-2}. Inset: OER polarization plots of macro-TpBpy-Co before and after 40 000 s.

overpotential of 380 mV versus the reversible hydrogen electrode (RHE) to achieve an anodic current density of 10 mA/cm^2, much lower than that of macro-TpBpy, TpBpy-Co, and some other reported Co cation-based catalysts (Figure S18 and Table S4). In particular, the macro-TpBpy-Co catalyst shows an overpotential of only 430 mV at current density of 50 mA/cm^2, which is 170 mV lower than the benchmark RuO_2 catalyst (overpotential of 600 mV at 50 mA/cm^2). In the corresponding Tafel slope, both macro-TpBpy-Co and TpBpy-Co exhibit a lower linear slope of 54 mV/dec and 58 mV/dec, respectively, than that of macro-TpBpy (339 mV/dec) and

RuO_2 (79 mV/dec), indicating favorable reaction kinetics in the OER process (Figure 5b). The superior OER performance of macro-TpBpy-Co with respect to TpBpy-Co can be attributed to the homogeneous and interconnected macroporous structures, which was further confirmed by the normalization process from current density (j) to the activity per active sites ($j_{real/site}$) (for details see SI, Section 1). As shown in Figure 5c, a scatter plot containing $j_{real/site}$ versus applied potential was established in which a much higher $j_{real/site}$ for macro-TpBpy-Co indicates an enhanced catalytic activity per active sites compared to TpBpy-Co. In particular, under a higher potential with larger amount of oxygen production, the prominent enhancement of $j_{real/site}$ for macro-TpBpy-Co gives strong evidence for the advantage of an additional macroporous structure that efficiently promotes the mass transfer and the accessibility of active sites to reactants during the electrocatalytic process. The OER performance of macro-TpBpy-Co with different macropore size has also been conducted under identical conditions, yielding almost similar OER activities (Figure S19a), showing that all tested pore sizes in the macropore regime are enabling sufficient mass transport. On the other hand, the negligible electrocatalytic activity of macro-TpBpy shows the important role of Co ions in COFs which coordinate with bipyridine linkers to form the OER active sites as well as improve the conductivity of the catalytic system (Figure S19b).[33]

To verify that Co ions are representing the active sites in the catalysts, the influence of thiocyanate ions (SCN$^-$), which strongly bind to metal sites, on the OER activity of macro-TpBpy-Co was investigated.[45,46] On introducing SCN$^-$ into the electrolyte (10 mM), the overpotential of macro-TpBpy-Co increased substantially at a current density of 10 mA/cm^2, indicating the crucial role of Co ions during the OER catalytic process (Figure 5d).[47] The cyclic voltammetry (CV) of macro-TpBpy-Co and TpBpy-Co shows the presence of redox peaks at 1.0−1.1 V (vs RHE) which can be attributed to the quasi-reversible Co(II)/Co(III) couple (Figure S20).[33,48] The electrochemical surface area (ECSA) of the COFs was estimated by measuring the capacitance of the double layer (C_{dl}) at the solid−liquid interface using CV. TpBpy and macro-TpBpy both show moderate electrochemical surface areas, with a small increase in ECSA for the COF with additional macropores, macro-TpBpy (Figure S21).

In addition, other metal ions such as iron (Fe^{2+}), nickel (Ni^{2+}), copper (Cu^{2+}), zinc (Zn^{2+}), and manganese (Mn^{2+}) were tested instead of cobalt ions by conducting the OER performance test. However, first XPS analyses were performed to elucidate the nature and environment of the different metals in the macroporous COFs. The high-resolution N 1s spectra show an additional peak which can be attributed to metal−N bonds, thus confirming the coordination of metal ions to the pyridine moieties within the COF backbone (Figure S22). Furthermore, the high-resolution spectra of each metal show their different oxidation states without any detected metallic (0) species (Figure S23), which is consistent with the PXRD results, showing no peaks for metal particles (Figure S24). The C_{dl} of these catalysts were also calculated based on capacitance, showing the equivalent electrochemical active sites for each material (Figure S25). Subsequently, the OER performance and EIS of these catalysts were conducted under the same conditions as for macro-TpBpy-Co (Figure S26). However, all the macro-COFs with other metal species than Co exhibit a lower OER activity.

The turnover frequency (TOF), indicating the intrinsic catalytic activity of a catalyst at an atomic level, has been calculated to build a plot of TOF values against the applied overpotential (Figure S27). It can be observed that macro-TpBpy-Co shows the highest TOF value compared to TpBpy-Co and RuO$_2$. Moreover, the Faradaic efficiency of macro-TpBpy-Co was determined by comparing the experimentally produced gas volume with the theoretically calculated one (Figure 5e, for details see SI). The good agreement of the experimentally generated and theoretically calculated amount of O$_2$ reveals a Faradaic efficiency of ~98% for OER in 0.1 M KOH, confirming the high activity of macro-TpBpy-Co.

Electrochemical stability is an important factor for catalysts in electrocatalytic processes, especially for polymer-based catalysts. To value the stability of macro-TpBpy-Co after OER studies, a chronopotentiometry test was carried out at a current density of 10 mA/cm^2 in 0.1 M KOH. As shown in Figure 5f, the catalyst shows almost negligible difference in the required overpotential after 10 h of testing. The OER polarization of macro-TpBpy-Co only exhibits a slight negative shift (38 mV shift of the overpotential at 10 mA/cm^2) after 40 000 s, indicating its excellent stability in electrochemical OER under alkaline conditions. The electrochemical surface area (ECSA) of macro-TpBpy-Co before and after electrocatalytic catalysis was also estimated by measuring the capacitance (Figure S21). The calculated C_{dl} of macro-TpBpy-Co-40000s is 1.93×10^{-5} F cm^{-2} after long-term electrocatalysis, very similar to the one observed for macro-TpBpy-Co (1.83×10^{-5} F cm^{-2}). Subsequently, the structural features and chemical compositions of macro-TpBpy-Co after OER stability tests were investigated using SEM and XPS analyses. As shown in Figure 6a and 6b, the morphology and

TpBpy-Co are observed, except for the disappearance of the satellite peak (786 eV) at Co 2p in macro-TpBpy-Co-40000s, which shows that both oxidation states, Co(II) and Co(III), are present after OER. In addition, the high-resolution O 1s spectra show a change of the peak at 533.1 eV after OER that can be assigned to a cobalt oxyhydroxide formed after the long-term catalytic process under alkaline conditions (Figure S28). Finally, OER analyses under high current density of 50 mA/cm^2 were conducted, showing a satisfying chemical stability even after a long-term reaction (Figure S29).

CONCLUSION

In summary, we have developed a pathway to fabricate hierarchical and crystalline COFs with interconnected and uniform macroporous structures by employing a facile PS-mediated templating method. The obtained macroporous COFs preserve their crystallinity and high specific surface areas. Confirmation of enhanced mass transport in hierarchical COF structures was given by testing Co-coordinated bipyridine-based COFs as OER catalysts. The macro-TpBpy-Co exhibits excellent performance as OER catalysts, with much improved activity compared to the only microporous TpBpy-Co and also compares favorably to other reported cobalt-doped polymer-based electrocatalysts. The enhanced performance of macro-TpBpy-Co can be attributed to the improved mass diffusion properties in the hierarchically porous structure, together with more accessible active sites. The here presented PS templating method was successfully extended to obtain various macro-microporous imine-based COFs by modulating the corresponding amine linkers, showing its potential as a convenient route for the preparation of macro-microporous COFs with different functional groups for various applications.

ASSOCIATED CONTENT

Ⓢ Supporting Information

The Supporting Information is available free of charge on the ACS Publications website at DOI: 10.1021/jacs.9b01226.

Supplementary experimental methods, and characterization of the materials and products (PDF)

AUTHOR INFORMATION

Corresponding Author
*arne.thomas@tu-berlin.de

ORCID Ⓘ
Pradip Pachfule: 0000-0002-0804-541X
Shuang Li: 0000-0001-7414-630X
Arne Thomas: 0000-0002-2130-4930

Notes
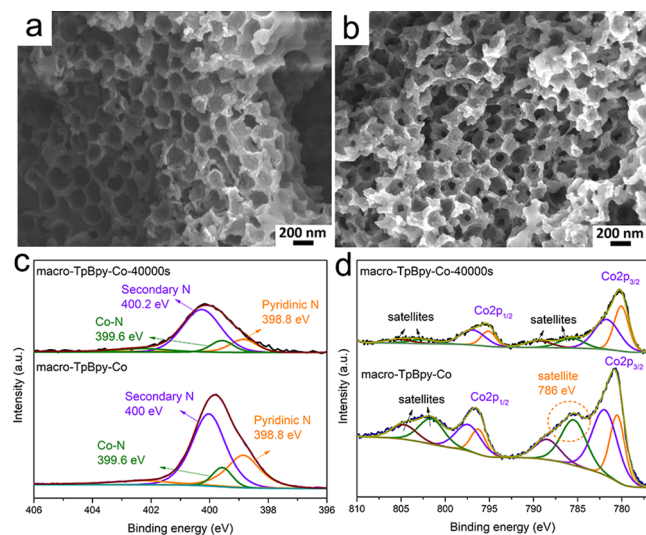The authors declare no competing financial interest.

Figure 6. Structural features of macro-TpBpy-Co after electrocatalytic analyses. SEM images (a) before and (b) after and high-resolution (c) N 1s and (d) Co 2p spectra of macro-TpBpy-Co before and after 40 000 s of OER testing.

macroporous structures for macro-TpBpy-Co before and after OER analysis are preserved. XPS analyses of macro-TpBpy-Co-40 000s were conducted to analyze the chemical and structural changes after long-term reaction under alkaline conditions. As shown in Figure 6c and 6d, no distinct changes for the binding energy at N 1s and Co 2p levels compared to that of macro-

■ REFERENCES

(1) Zhou, H. C.; Long, J. R.; Yaghi, O. M. Introduction to Metal-Organic Frameworks. *Chem. Rev.* **2012**, *112*, 673−674.

(2) Furukawa, H.; Cordova, K. E.; O'Keeffe, M.; Yaghi, O. M. The Chemistry and Applications of Metal-Organic Frameworks. *Science* **2013**, *341*, 974.

(3) Côté, A. P.; Benin, A. I.; Ockwig, N. W.; O'Keeffe, M.; Matzger, A. J.; Yaghi, O. M. Porous, Crystalline, Covalent Organic Frameworks. *Science* **2005**, *310*, 1166−1170.

(4) Serrano, D. P.; Escola, J. M.; Pizarro, P. Synthesis Strategies in the Search for Hierarchical Zeolites. *Chem. Soc. Rev.* **2013**, *42*, 4004−4035.

(5) Roeser, J.; Prill, D.; Bojdys, M.; Fayon, P.; Trewin, A.; Fitch, A.; Schmidt, M.; Thomas, A. Anionic Silicate Organic Frameworks Constructed from Hexacoordinate Silicon Centres. *Nat. Chem.* **2017**, *9*, 977−982.

(6) Pérez-Ramírez, J.; Christensen, C. H.; Egeblad, K.; Christensen, C. H.; Groen, J. C. Hierarchical Zeolites: Enhanced Utilisation of Microporous Crystals in Catalysis by Advances in Materials Design. *Chem. Soc. Rev.* **2008**, *37*, 2530−2542.

(7) Krishna, R. Diffusion in Porous Crystalline Materials. *Chem. Soc. Rev.* **2012**, *41*, 3099−3118.

(8) Gallego, E. M.; Portilla, M. T.; Paris, C.; Leon-Escamilla, A.; Boronat, M.; Moliner, M.; Corma, A. Ab initio" Synthesis of Zeolites for Preestablished Catalytic Reactions. *Science* **2017**, *355*, 1051−1054.

(9) Moliner, M.; Martínez, C.; Corma, A. Multipore Zeolites: Synthesis and Catalytic Applications. *Angew. Chem., Int. Ed.* **2015**, *54*, 3560−3579.

(10) Kuhn, P.; Antonietti, M.; Thomas, A. Porous, Covalent Triazine-Based Organic Frameworks Prepared by Ionothermal Synthesis. *Angew. Chem., Int. Ed.* **2008**, *47*, 3450−3453.

(11) Fang, Q. R.; Wang, J. H.; Gu, S.; Kaspar, R. B.; Zhuang, Z. B.; Zheng, J.; Guo, H. X.; Qiu, S. L.; Yan, Y. S. 3D Porous Crystalline Polyimide Covalent Organic Frameworks for Drug Delivery. *J. Am. Chem. Soc.* **2015**, *137*, 8352−8355.

(12) White, R.; Fischer, A.; Goebel, C.; Thomas, A. A Sustainable Template for Mesoporous Zeolite Synthesis. *J. Am. Chem. Soc.* **2014**, *136*, 2715−2718.

(13) Shen, K.; Zhang, L.; Chen, X. D.; Liu, L. M.; Zhang, D. L.; Han, Y.; Chen, J. Y.; Long, J. L.; Luque, R.; Li, Y. W.; Chen, B. L. Ordered macro-microporous metalorganic framework single crystals. *Science* **2018**, *359*, 206−210.

(14) Wu, Y. N.; Li, F. T.; Zhu, W.; Cui, J. C.; Tao, C. A.; Lin, C.; Hannam, P. M.; Li, G. T. Metal-Organic Frameworks with a Three-Dimensional Ordered Macroporous Structure: Dynamic Photonic Materials. *Angew. Chem., Int. Ed.* **2011**, *50*, 12518−12522.

(15) Yahiaoui, O.; Fitch, A. N.; Hoffman, F.; Fröba, M.; Thomas, A.; Roeser, J. 3D Anionic Silicate Covalent Organic Framework with srs Topology. *J. Am. Chem. Soc.* **2018**, *140*, 5330−5333.

(16) Kandambeth, S.; Biswal, B. P.; Chaudhari, H. D.; Rout, K. C.; Kunjattu, H. S.; Mitra, S.; Karak, S.; Das, A.; Mukherjee, R.; Kharul, U. K.; Banerjee, R. Selective Molecular Sieving in Self-Standing Porous Covalent-Organic-Framework Membranes. *Adv. Mater.* **2017**, *29*, 1603945.

(17) Diercks, C. S.; Yaghi, O. M. The Atom, the Molecule, and the Covalent Organic Framework. *Science* **2017**, *355*, 1585.

(18) Pachfule, P.; Acharjya, A.; Roeser, J.; Langenhahn, T.; Schwarze, M.; Schomacker, R.; Thomas, A.; Schmidt, J. Diacetylene Functionalized Covalent Organic Framework (COF) for Photo-catalytic Hydrogen Generation. *J. Am. Chem. Soc.* **2018**, *140*, 1423−1427.

(19) Segura, J. L.; Mancheno, M. J.; Zamora, F. Covalent Organic Frameworks Based on Schiff-base Chemistry: Synthesis, Properties and Potential Applications. *Chem. Soc. Rev.* **2016**, *45*, 5635−5671.

(20) Feng, X.; Ding, X. S.; Jiang, D. L. Covalent Organic Frameworks. *Chem. Soc. Rev.* **2012**, *41*, 6010−6022.

(21) Halder, A.; Karak, S.; Addicoat, M.; Bera, S.; Chakraborty, A.; Kunjattu, S. H.; Pachfule, P.; Heine, T.; Banerjee, R. Ultra-Stable Imine-based Covalent Organic Frameworks for Sulfuric acid

Recovery: An Effect of Interlayer Hydrogen Bonding. *Angew. Chem., Int. Ed.* **2018**, *57*, 5797−5802.

(22) Lin, S.; Diercks, C. S.; Zhang, Y. B.; Kornienko, N.; Nichols, E. M.; Zhao, Y. B.; Paris, A. R.; Kim, D.; Yang, P. D.; Yaghi, O. M. Covalent Organic Frameworks Comprising Cobalt Porphyrins for Catalytic CO_2 Reduction in Water. *Science* **2015**, *349*, 1208−1213.

(23) Colson, J. W.; Woll, A. R.; Mukherjee, A.; Levendorf, M. P.; Spitler, E. L.; Shields, V. B.; Spencer, M. G.; Park, J.; Dichtel, W. R. Oriented 2D Covalent Organic Framework Thin Films on Single-Layer Graphene. *Science* **2011**, *332*, 228−231.

(24) Kandambeth, S.; Venkatesh, V.; Shinde, D. B.; Kumari, S.; Halder, A.; Verma, S.; Banerjee, R. Self-templated Chemically Stable Hollow Spherical Covalent Organic Framework. *Nat. Commun.* **2015**, *6*, 6786.

(25) Pachfule, P.; Kandmabeth, S.; Mallick, A.; Banerjee, R. Hollow Tubular Porous Covalent Organic Framework (COF) Nanostructures. *Chem. Commun.* **2015**, *51*, 11717−11720.

(26) Gole, B.; Stepanenko, V.; Rager, S.; Grune, M.; Medina, D. D.; Bein, T.; Wurthner, F.; Beuele, F. Microtubular Self-Assembly of Covalent Organic Frameworks. *Angew. Chem., Int. Ed.* **2018**, *57*, 846−850.

(27) Liang, J.; Zheng, Y.; Chen, J.; Liu, J.; Hulicova-Jurcakova, D.; Jaroniec, M.; Qiao, S. Z. Facile Oxygen Reduction on a Three-Dimensionally Ordered Macroporous Graphitic C_3N_4/Carbon Composite Electrocatalyst. *Angew. Chem., Int. Ed.* **2012**, *51*, 3892−3896.

(28) McCrory, C. C. L.; Jung, S. H.; Peters, J. C.; Jaramillo, T. F. Benchmarking Heterogeneous Electrocatalysts for the Oxygen Evolution Reaction. *J. Am. Chem. Soc.* **2013**, *135*, 16977−16987.

(29) Hu, W.; Wang, Y. Q.; Hu, X. H.; Zhou, Y. Q.; Chen, S. L. Three-Dimensional Ordered Macroporous IrO_2 as Electrocatalyst for Oxygen Evolution Reaction in Acidic Medium. *J. Mater. Chem.* **2012**, *22*, 6010−6016.

(30) Zhao, X. J.; Pachfule, P.; Li, S.; Simke, J. R. J.; Schmidt, J.; Thomas, A. Bifunctional Electrocatalysts for Overall Water Splitting from an Iron/Nickel-Based Bimetallic Metal-Organic Frame-work/Dicyandiamide composite. *Angew. Chem.* **2018**, *130*, 9059−9064.

(31) Karak, S.; Kumar, S.; Pachfule, P.; Banerjee, R. Porosity Prediction through Hydrogen Bonding in Covalent Organic Frameworks. *J. Am. Chem. Soc.* **2018**, *140*, 5138−5145.

(32) Aiyappa, H. B.; Thote, J.; Shinde, D. B.; Banerjee, R.; Kurungot, S. Cobalt-Modified Covalent Organic Framework as a Robust Water Oxidation Electrocatalyst. *Chem. Mater.* **2016**, *28*, 4375−4379.

(33) Wang, J.; Ge, X.; Liu, Z.; Thia, L.; Yan, Y.; Xiao, W.; Wang, X. Heterogeneous Electrocatalyst with Molecular Cobalt Ions Serv-ing as the Center of Active Sites. *J. Am. Chem. Soc.* **2017**, *139*, 1878−1884.

(34) Song, F.; Hu, X. L. Ultrathin Cobalt-Manganese Layered Double Hydroxide Is an Efficient Oxygen Evolution Catalyst. *J. Am. Chem. Soc.* **2014**, *136*, 16481−16484.

(35) McAlpin, J. G.; Surendranath, Y.; Dinca, M.; Stich, T. A.; Stoian, S. A.; Casey, W. H.; Nocera, D. G.; Britt, R. D. EPR Evidence for Co (IV) Species Produced During Water Oxidation at Neutral pH. *J. Am. Chem. Soc.* **2010**, *132*, 6882−6883.

(36) Zhao, L.; Dong, B.; Li, S. Z.; Zhou, L. J.; Lai, L. F.; Wang, Z. W.; Zhao, S. L.; Han, M.; Gao, K.; Lu, M.; Xie, X. J.; Chen, B.; Liu, Z. D.; Wang, X. J.; Zhao, H.; Li, H.; Liu, J. Q.; Zhang, H.; Huang, X.; Huang, W. Interdiffusion Reaction-Assisted Hybridization of Two-Dimensional Metal-Organic Frameworks and $Ti_3C_2T_x$ Nanosheets for Electrocatalytic Oxygen Evolution. *ACS Nano* **2017**, *11*, 5800−5807.

(37) Huang, J.; Li, Y.; Huang, R. K.; He, C. T.; Gong, L.; Hu, Q.; Wang, L. S.; Xu, Y. T.; Tian, X. Y.; Liu, S. Y.; Ye, Z. M.; Wang, F. X.; Zhou, D. D.; Zhang, W. X.; Zhang, J. P. Electrochemical Exfoliation of Pillared-Layer Metal-Organic Framework to Boost the Oxygen Evolution Reaction. *Angew. Chem., Int. Ed.* **2018**, *57*, 4632−4636.

(38) Wang, H.; Yin, F. X.; Chen, B. H.; He, X. B.; Lv, P. L.; Ye, C. Y.; Liu, D. J. ZIF-67 Incorporated with Carbon Derived from Pomelo Peels: A Highly Efficient Bifunctional Catalyst for Oxygen Reduction/Evolution Reactions. *Appl. Catal., B* **2017**, *205*, 55−67.

Journal of the American Chemical Society   Article

(39) Lu, X. F.; Liao, P. Q.; Wang, J. W.; Wu, J. X.; Chen, X. W.; He, C. T.; Zhang, J. P.; Li, G. R.; Chen, X. M. An Alkaline-Stable, Metal Hydroxide Mimicking Metal-Organic Framework for Efficient Electrocatalytic Oxygen Evolution. *J. Am. Chem. Soc.* **2016**, *138*, 8336−8339.

(40) Mullangi, D.; Dhavale, V.; Shalini, S.; Nandi, S.; Collins, S.; Woo, T.; Kurungot, S.; Vaidhyanathan, R. Low-Overpotential Electrocatalytic Water Splitting with Noble-Metal-Free Nanoparticles Supported in a sp(3) N-Rich Flexible COF. *Adv. Energy Mater.* **2016**, *6*, 1600110.

(41) He, X. B.; Yin, F. X.; Li, G. R. A Co/Metal-Organic-Framework Bifunctional Electrocatalyst: The Effect of the Surface Cobalt Oxidation State on Oxygen Evolution/Reduction Reactions in an Alkaline Electrolyte. *Int. J. Hydrogen Energy* **2015**, *40*, 9713−9722.

(42) Tu, T. N.; Nguyen, M.; Nguyen, H.; Yuliarto, B.; Cordova, K.; Demir, S. Designing Bipyridine-Functionalized Zirconium Metal−Organic Frameworks as a Platform for Clean Energy and Other Emerging Applications. *Coord. Chem. Rev.* **2018**, *364*, 33−50.

(43) Biesinger, M. C.; Payne, B. P.; Grosvenor, A. P.; Lau, L. W. M.; Gerson, A. R.; Smart, R. S. Resolving Surface Chemical States in XPS Analysis of First Row Transition Metals, Oxides and Hydroxides: Cr, Mn, Fe, Co and Ni. *Appl. Surf. Sci.* **2011**, *257*, 2717−2730.

(44) Cheng, C.; Li, S.; Xia, Y.; Ma, L.; Nie, C. X.; Roth, C.; Thomas, A.; Haag, R. Atomic Fe-N$_x$ Coupled Open-Mesoporous Carbon Nanofibers for Efficient and Bioadaptable Oxygen Electrode in Mg-Air Batteries. *Adv. Mater.* **2018**, *30*, 1802669.

(45) Dou, S.; Dong, C. L.; Hu, Z.; Huang, Y. C.; Chen, J. L.; Tao, L.; Yan, D. F.; Chen, D. W.; Shen, S. H.; Chou, S. L.; Wang, S. Y. Atomic-Scale CoO$_x$ Species in Metal-Organic Frameworks for Oxygen Evolution Reaction. *Adv. Funct. Mater.* **2017**, *27*, 1702546.

(46) Liu, Y.; Li, F.; Yang, H. D.; Li, J.; Ma, P.; Zhu, Y.; Ma, J. T. Two-Step Synthesis of Cobalt Iron Alloy Nanoparticles Embedded in Nitrogen-Doped Carbon Nanosheets/Carbon Nanotubes for the Oxygen Evolution Reaction. *ChemSusChem* **2018**, *11*, 2358−2366.

(47) Liang, H. W.; Bruller, S.; Dong, R. H.; Zhang, J.; Feng, X. L.; Mullen, K. Molecular Metal-N-x Centres in Porous Carbon for Electrocatalytic Hydrogen Evolution. *Nat. Commun.* **2015**, *6*, 7992.

(48) Araujo, C. M.; Doherty, M. D.; Konezny, S. J.; Luca, O. R.; Usyatinsky, A.; Grade, H.; Lobkovsky, E.; Soloveichik, G. L.; Grabtree, R. H.; Batista, V. S. Tuning Redox Potentials of Bis(imino)pyridine Cobalt Complexes: An Experimental and Theoretical Study involving Solvent and Ligand Effects. *Dalton Trans.* **2012**, *41*, 3562−3573.

Supporting Information

Macro/Microporous Covalent Organic Frameworks for Efficient Electrocatalysis

Xiaojia Zhao,[†] Pradip Pachfule,[†] Shuang Li,[†] Thomas Langenhahn,[†] Mengyang Ye,[†] Christopher Schlesiger,[‡] Sebastian Praetz,[‡] Johannes Schmidt,[†] Arne Thomas*[†]

[†]Department of Chemistry, Division of Functional Materials, Technical University Berlin, Hardenbergstraße 40, 10623 Berlin, Germany
[‡]*Institute of Optics and Atomic Physics, Technische Universität Berlin, Hardenbergstraße 36, 10623 Berlin, Germany*

Section 1. Materials and Methods

1.1. Material

All chemicals were purchased from commercial sources and used without further treatment: phloroglucinol (Acros Organics, 99+%), hexamethylenetetramine (Sigma Aldrich, ACS reagent, ≥ 99%), trifluoroacetic acid (Carl Roth, ≥ 99.9%), hydrochloric acid (Carl Roth, 37%), Celite® Filter Cel (Sigma Aldrich), Benzidine (Simga Aldrich, ≥ 98%), 3,3′-Dimethylbenzidin (Alfa Aesar, 98%), 4,4′′-Diamino-p-terphenyl (TCL, >95%), 4,4′-Diaminoazobenzol (abcr, 95%), 5,5-Diamino-2,2-bipyridine (Biosynth), styrene (Sigma Aldrich, >99%), Polyvinylpyrrolidone (Sigma Aldrich, PVP, M_w~29,000), Potassium persulfate (Sigma Aldrich, >99%), Potassium thiocyanate (Alfa Aesar, 98.5%), Cobalt(II) acetate tetrahydrate (Alfa Aesar), Iron(II) acetate (Sigma Aldrich), Nickel(II) acetate tetrahydrate (Sigma Aldrich), Zinc acetate dihydrate (Merck), Manganese(II) acetate tetrahydrate (Sigma Aldrich), Copper(II) acetate (Sigma Aldrich), Ruthenium(IV) oxide (RuO_2, Alfa Aesar, anhydrous, 99.9%), p-Toluenesulfonic acid monohydrate (Sigma Aldrich, ACS reagent, ≥ 98.5%), methanol (Carl Roth, ≥ 99%), Tetrahydrofuran (Acros Organics, 99+%), dichloromethane (Carl Roth, ≥99.5%)

1.2. Electrochemical measurements

1.2.1. Electrocatalytic OER

All electrochemical measurements were carried out in a three-electrode cell using a Gamry Reference 600 Potentiostat at room temperature. A RDE with a glassy carbon dish (5.0 mm diameter) severed as the working electrode. A graphite rod and Ag/AgCl (4.0 M KCl) were used as counter and reference electrodes, respectively. All measured potentials were converted to the reversible hydrogen electrode (RHE). The potential vs RHE was calibrated as $E_{RHE} = E_{Ag/AgCl} + 0.941$.

In a typical preparation of the catalyst ink, 10 mg of each catalyst was blended with 1.0 mL Nafion ethanol solution and stirred until a homogeneous solution formed. Then 5 µl of catalyst ink (10 mg/mL) was pipetted onto the glassy carbon surface and dried in ambient environment to form a catalyst film with a mass loading to 0.25 mg/cm^2. The measured oxygen evolution reaction (OER) polarization curves were carried out in a N_2-saturated 0.1 M KOH electrolyte with a sweep rate of 10 mV/s at 1600 r.p.m. For comparison, the commercial Ruthenium oxide (RuO_2) catalyst was measured under identical conditions.

The electrochemical surface area (ECSA) of the catalysts were estimated by measuring the capacitance of the double layer (C_{dl}) at the solid-liquid interface with cyclic voltammetry (CV). A series of scan rates ranging from 30 to 150 mV/s were applied to build a plot of the charging current density differences against the scan rate at a fixed potential 0.55 V *vs* RHE. The slope of the obtained linear is twice of the double-layer capacitance C_{dl}, which is used to estimate ECSA. Electrochemical impedance spectroscopy (EIS) was carried out in an N_2-saturated 0.1 M KOH electrolyte from 10 kHz to 0.01 Hz with a 5 mV AC potential at 1600 r.p.m. The stability tests for the macro-TpBpy-Co were conducted using chronopotentiometry at a current density of 10 mA/cm^2 and 50 mA/cm^2.

1.2.2. Normalization of current density (j)

The normalization process from current density (j) to the activity per active sites ($j_{real/site}$) was operated by following:

j_{real} (A/cm^2) = j (A/cm^2 geo) × (1/catalyst mass loading (mg(cat)/cm^2 geo) × (1/ Real active area (cm^2 real / mg(cat)))

Real active surface area (cm^2 real / mg(cat)) = BET (cm^2 real /mg(cat)) × total Co at%

1.2.3. Faradaic efficiency

The Faradaic efficiency was calculated by comparing the experimentally produced gas volume with the theoretically calculated one:

$$\eta_{Faraday} = V_{experimental}/V_{theoretical}$$

The experiment volume of O_2 can be obtained from experimental data. The theoretical volume can be calculated using the formula:

$$V_{theoretical} = I·t·V_m / n·F$$

where I is the current measured in the experiment, t is the measured time, V_m is the molar volume of O_2 in 1/mol, n is the number of electrons required for one molecule O_2 and F is the Faraday's constant and it is equal to 96485 C/mol.

1.2.4. Turnover frequency (TOF)

The turnover frequency (TOF) was evaluated by the following standard equation: [s1, s2]

$$TOF= (J×A)/(4×F×n)$$

Where j (A/cm^2) is the current density at a given overpotential, A is the geometric surface area of the electrode, F = 96500 C/mol stands for the Faraday constant, n (mol) is mole number of cobalt loaded on the GC electrode which was determined by the XPS analysis. All metal cations in COF were assumed to be catalytically active, so the calculated value represents the lower limits of TOF.

1.3. Characterization

PXRD patterns were measured on a Bruker D8 Advance instrument with Cu Kα radiation (λ=1.54 Å) at a generator voltage of 40 kV and a generator current of 40 mA with a scanning speed of 5 °/min from 2° to 60°. Nitrogen sorption measurements were carried out on a Quantachrome Quadrasorb SI instrument. All samples were degassed at 150 °C for 12 h before actual measurement. The surface area was calculated by using Brunauer-Emmett-Teller (BET) calculations and the pore sized distribution plot was obtained from the adsorption branch of isotherms by the QSDFT model (N_2 at 77 K on carbon). XPS spectra were performed on a Thermo Scientific K-Alpha[+] X-ray Photoelectron Spectrometer with Al Kα radiation. SEM measurement were conducted on ZEISS GeminiSEM500 NanoVP. TEM images were obtained from FEI Tecnai G^2 20 S-TWIN electron microscope at an operating voltage of 200 kV. STEM measurement was performed with an additional upgrade using a DISS5 scan generator, attached with a BF/ADF/HAADF STEM detector. The samples for TEM analyses were prepared dispersing the electrocatalysts in ethanol, followed by dropping it onto a copper grid covered with carbon film.

X-ray absorption measurements were carried out with a novel self-developed wavelength dispersive spectrometer in von Hamos geometry. The spectrometer is equipped with a microfocus X-ray tube, a

curved Highly Annealed Pyrolytic Graphite mosaic crystal and a ccd camera with a pixel size of 13.5 µm × 13.5 µm. The tube was operated with a high voltage of 14 kV and a current of 187 µA. The samples were prepared as powders on scotch tape and constantly moved during the measurements to minimize effects of local thickness inhomogeneity. The beam size on the samples is around 3mm × 3mm. The gathered spectral range is covering the Co K absorption edge at 7708 eV. The EXAFS evaluation was performed by using the Demeter software [s3]

Section 2. Experiment section

2.1. Synthesis of triformylphloroglucinol (Tp)[s4]
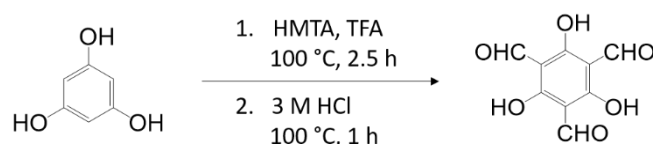
Phloroglucinol (6.0 g, 49 mmol), hexamethylenetetramine (HMTA, 15.1 g, 108 mmol) and trifluoroacetic acid (TFA, 90 mL) were refluxed at 100 °C under N_2 for 2.5 h. After that, 150 mL of 3 M HCl was added slowly and the mixture was heated at 100 °C for 1 h. After cooling to room temperature, the solution was filtered through Celite, extracted with 350 mL dichloromethane and the solution was evaporated under reduced pressure to afford 1.6 g of an off-white powder. ^{1}H NMR indicated near 99% purity; a pure sample was obtained by sublimation.

2.2. Synthesis of PS suspension

Monodisperse colloidal polystyrene spheres (PS) were synthesized according to reported work[5]. Different sizes of PS spheres (~160, 270, 320 and 360 nm) can be achieved by changing the synthetic conditions (Table S1). Briefly, in a typical procedure, 39 mL of styrene was washed with 12 mL NaOH aqueous solution (10 wt %) and subsequently deionized water to remove the stabilizer. Then a defined amount of Poly(vinylpyrrolidone) (PVP, M_w~29000) was added to a triple-neck, 500 mL round-bottom flask containing 300 mL water. The mixture was bubbled with nitrogen for 15 min and followed by refluxing at a specified temperature for 30 min under magnetic stirring. Then, a calculated amount of $K_2S_2O_8$ with 50 mL water was added into the flask to initiate the polymerization of styrene. After keep stirring (<500 r.p.m.) for 24 h at this temperature, a turbid dispersion was observed formed from monodisperse colloidal PS spheres with a solid content ~5wt%. For further use, the colloidal PS was poured into a petri dish at 80 °C to get the colloidal PS with different solid contents (~10wt% and ~15wt%).

2.3. Synthesis of macro-TpBpy and macro-TpBpy-Co

To a clean 15 mL vial, 5 mL of colloidal PS with a solid content of ~10wt%, *p*-Toluenesulfonic acid (PTSA, 500 mg, 2.5 mmol) and *2,2′*-bipyridine-*5,5′*-diamine (Bpy) powder (83.8 mg, 0.45 mmol) were added and mixed thoroughly in a vortex shaker for 10 min. Then, 63 mg of 1,3,5-Triformylphloroglucinol (Tp, 0.3 mmol) was added and further shaken for several minutes until an obvious color change is observed (milky white to orange-yellow). The solution was poured into an open petri dish to evaporate the water, followed by transferring into an oven at 80 °C for 24 h. Then, the sample (PS@TpBpy) was thoroughly washed with hot water to remove PTSA and subsequently Soxhlet extraction was conducted to remove the PS template with tetrahydrofuran (THF) to obtain the macro-TpBpy. Colloidal PS with a solid content of 5wt% and 15wt% were used to prepare the corresponding macroporous COFs, named macro-TpBpy-5% and macro-TpBpy-15%, respectively. If not otherwise noted the material macro-TpBpy discussed in the paper refers to the macro-TpBpy-10wt%. Other well-ground aromatic diamine powder [83 mg, benzidine (BD) for macro-TpBD; 95 mg, *2,6*-dimethoxybenzidine (BD-Me$_2$) for macro-TpBD-Me$_2$; 117 mg, *4,4″*-diamino-*p*-terphenyl (TD) for macro-TpTD; 86 mg, *p*-azoaniline (Azo) for macro-TpAzo] were used for the corresponding macro-COFs formation using the same procedure.

macro-TpBpy-Co was synthesized by soaking a defined amount of macro-TpBpy in methanolic cobalt acetate (Co(OAc)$_2$·4H$_2$O) solution and further stirring for 4 h. In brief, 30 mg of macro-TpBpy was added into 20 mL dry methanol with 20 mg Co(OAc)$_2$·4H$_2$O. The solution was stirred at room temperature for 4 h and then the solid was filtered and washed with a large amount of dry methanol. The macro-TpBpy-Co was finally obtained after drying overnight in a vacuum oven at 60 °C. Other transition mental salts [Fe(OAc)$_2$ for macro-TpBpy-Fe; Ni(OAc)$_2$·4H$_2$O for macro-TpBpy-Ni; Cu(OAc)$_2$ for macro-TpBpy-Cu; Zn(OAc)$_2$·2H$_2$O for macro-TpBpy-Zn; Mn(OAc)$_2$·4H$_2$O for macro-TpBpy-Mn;] were used for the corresponding macro-COF-M preparation with the similar procedure.
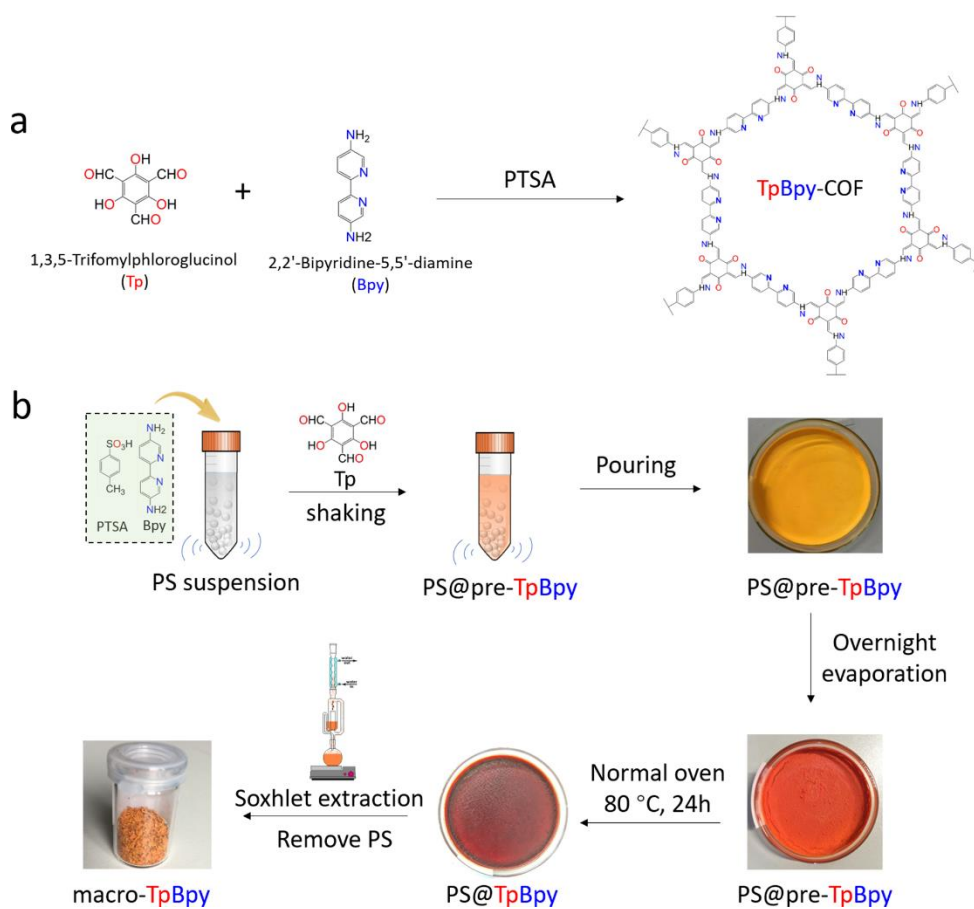
Figure S1. Structure and synthetic procedure for macro-TpBpy *via* PS-templating method.
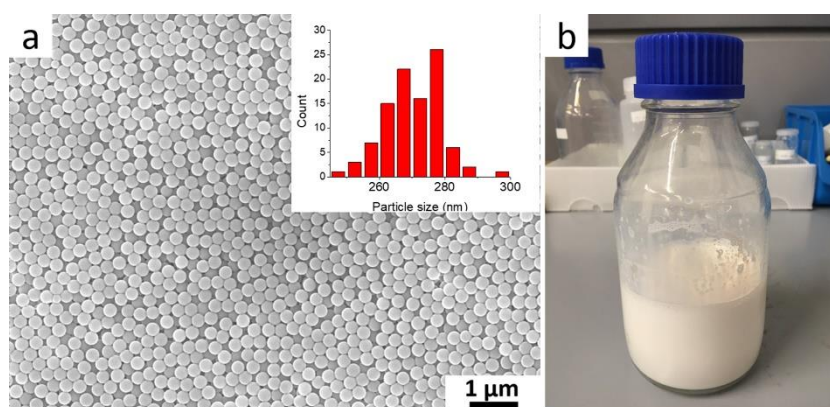
Figure S2. a) The monodisperse colloidal PSs with an average diameter of ~270 nm. Inset: statistic diameter of polystyrene nanoparticles (Calculated using an average of 100 particles at different locations). b) The PS aqueous dispersion (solid content: ~10wt%).
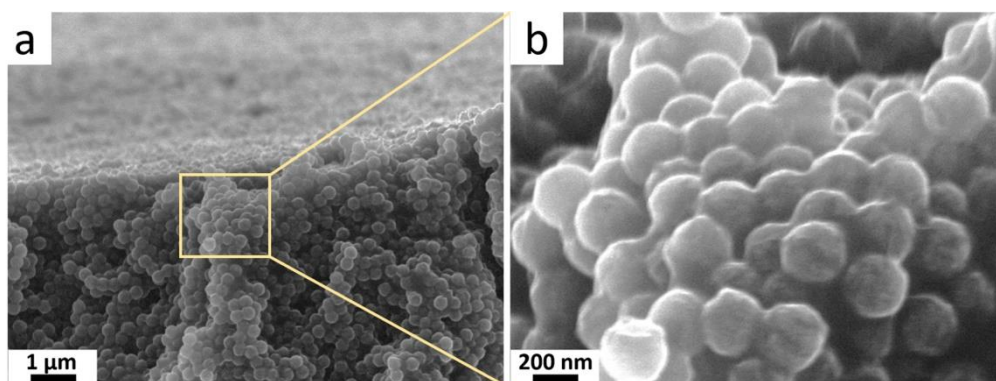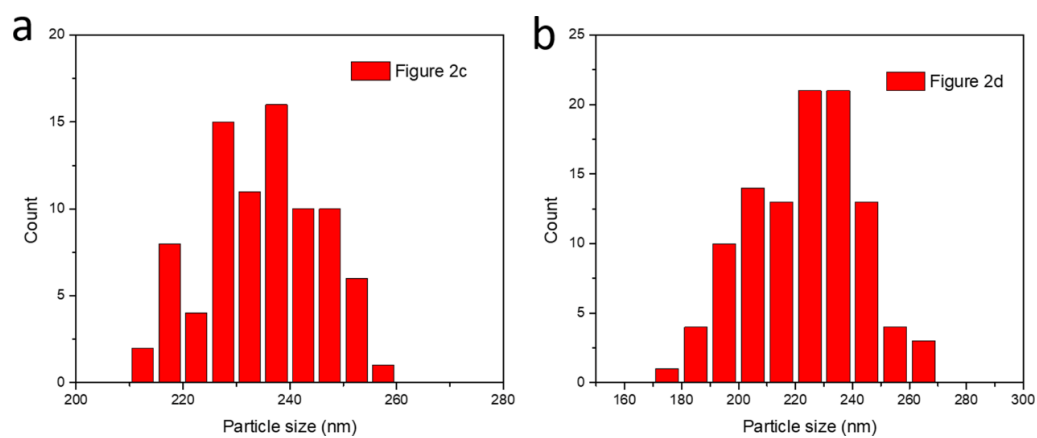
Figure S3. SEM images of PS@TpBpy.

Figure S4. Diameter of macropores in macro-TpBpy (derived by measuring the diameter of 100 pores at different locations.)
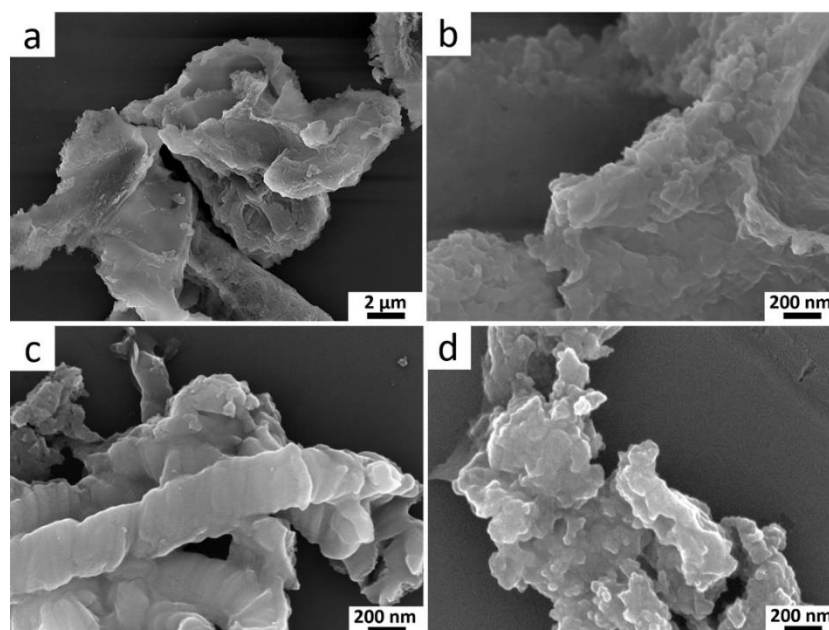
Figure S5. SEM images of pristine TpBpy.
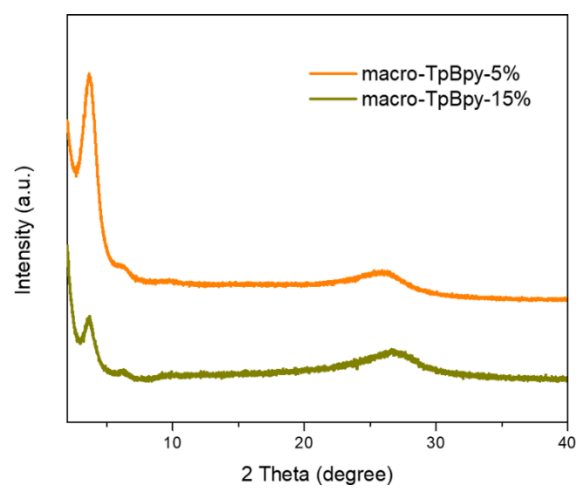
Figure S6. PXRD patterns of macro-TpBpy-5wt% and macro-TpBpy-15wt%.
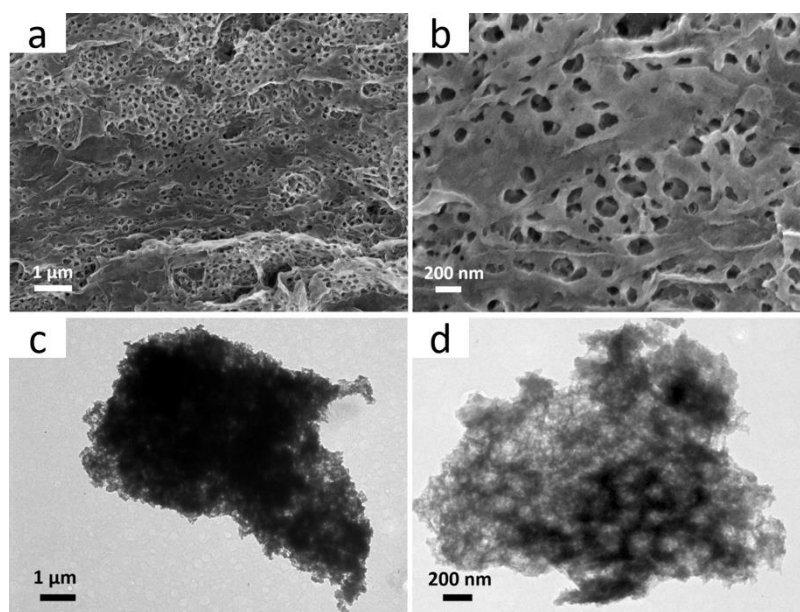
Figure S7. a, b) SEM images and c, d) TEM images of macro-TpBpy-5wt%.
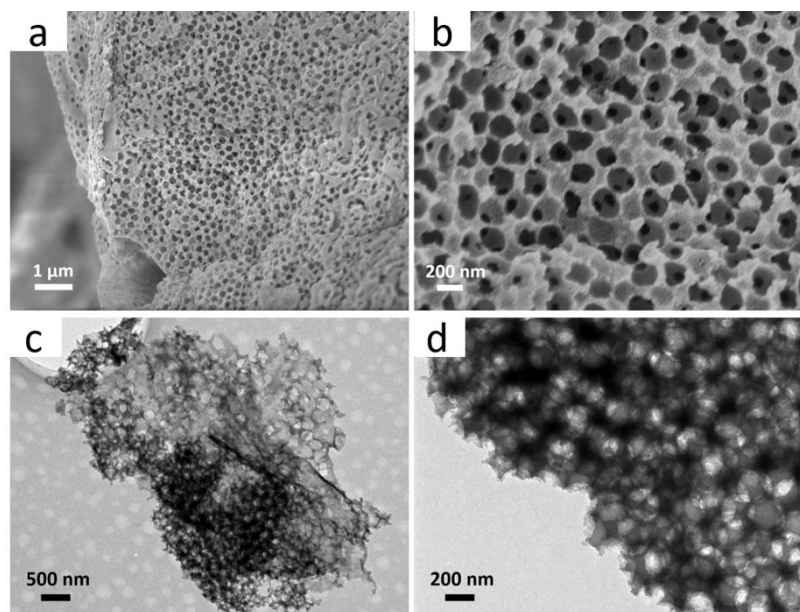
Figure S8. a, b) SEM images and c, d) TEM images of macro-TpBpy-15wt%.
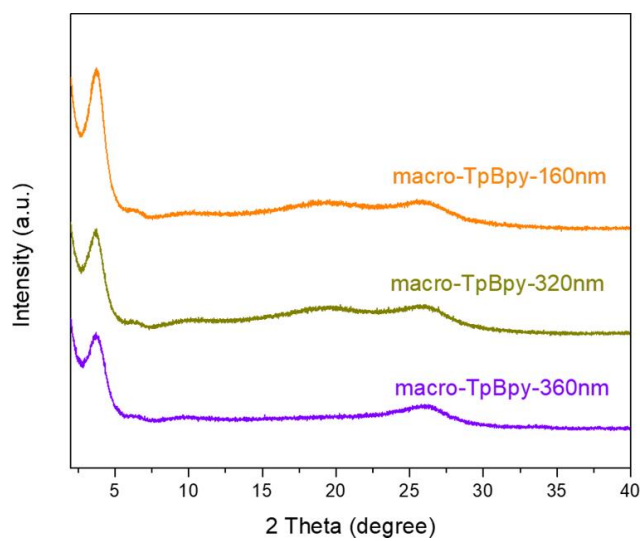
Figure S9. PXRD patterns of macro-TpBpy with different diameter of macropores.
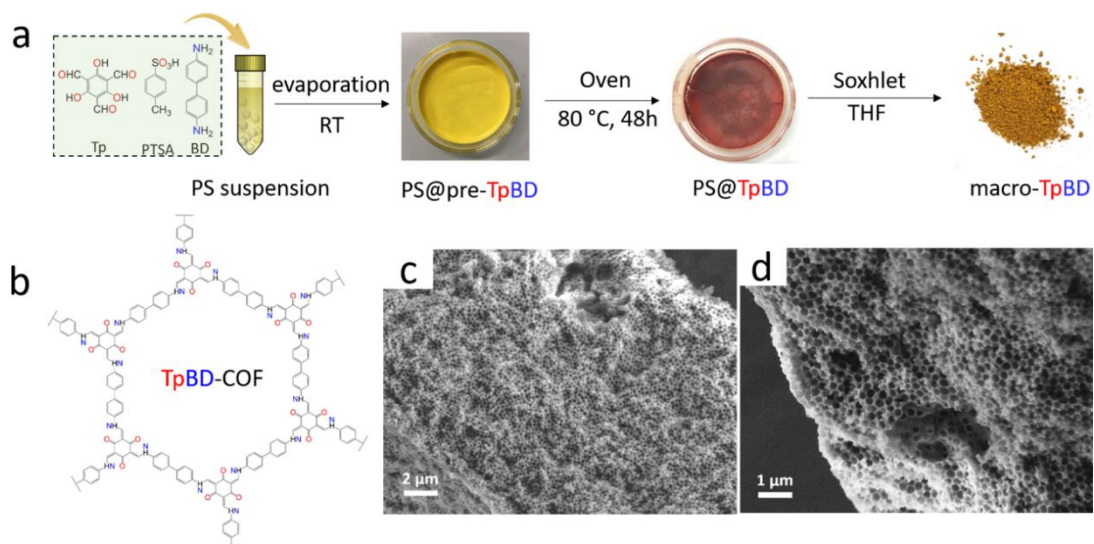
Figure S10. a) Synthesis of macro-TpBD *via* the PS-templating method. b) Chemical structure of TpBD. c, d) SEM images of macro-TpBD.
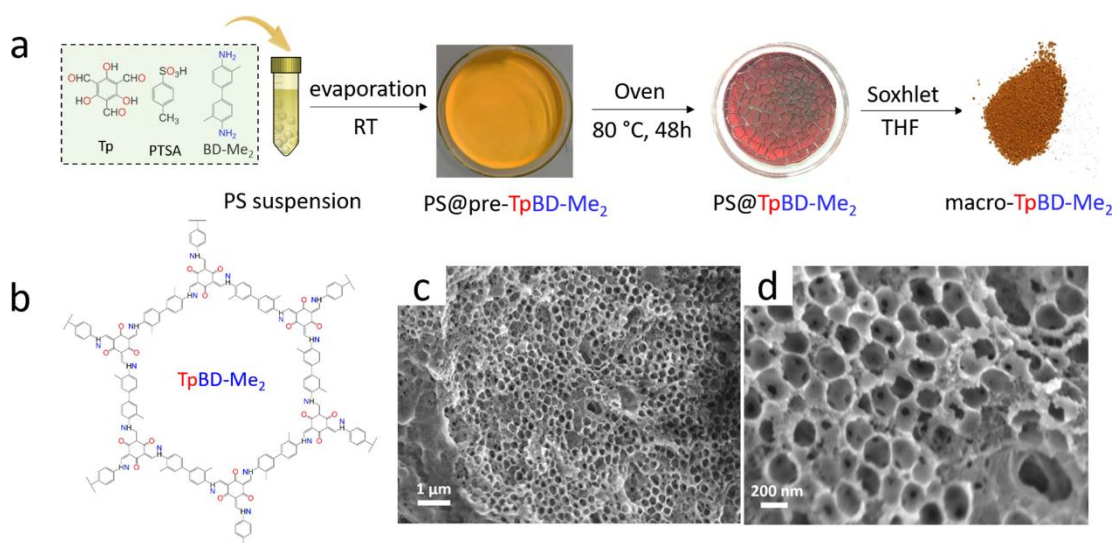
Figure S11. a) Synthesis of macro-TpBD-Me$_2$ *via* PS-templated method. b) Chemical structure of TpBD-Me$_2$. c, d) SEM images of macro-TpBD-Me$_2$.
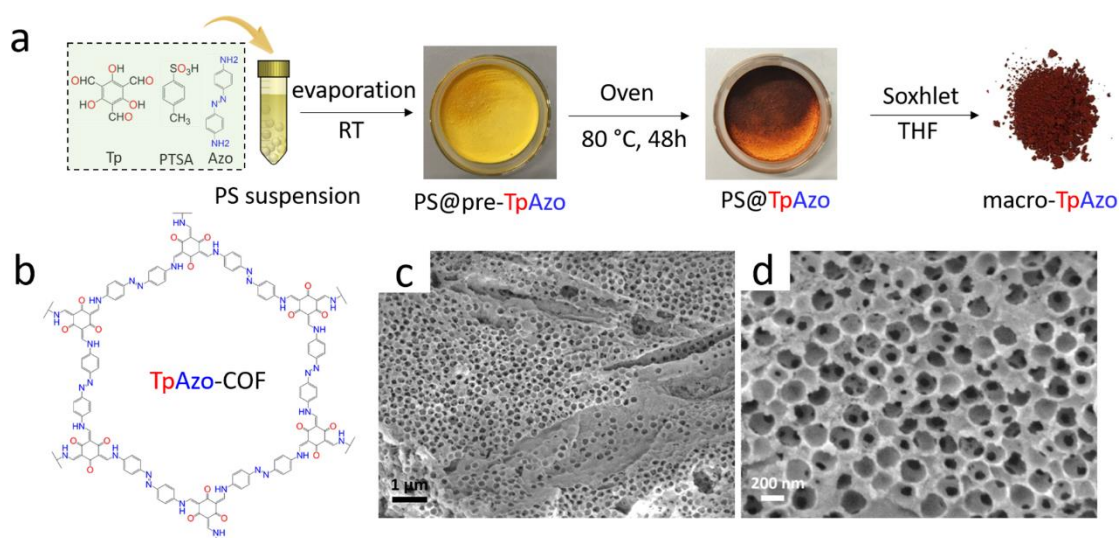
Figure S12. a) Synthesis of macro-TpAzo *via* PS-templated method. b) Chemical structure of TpAzo. c, d) SEM images of macro-TpAzo.
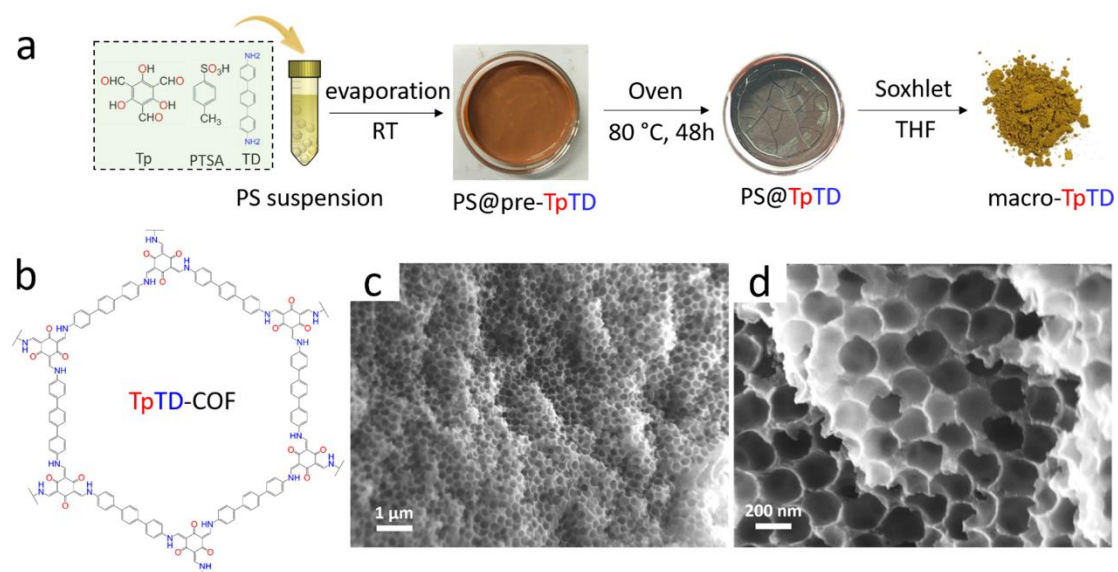
Figure S13. a) Synthesis of macro-TpTD *via* PS-templated method. b) Chemical structure of TpTD. c, d) SEM images of macro-TpTD.
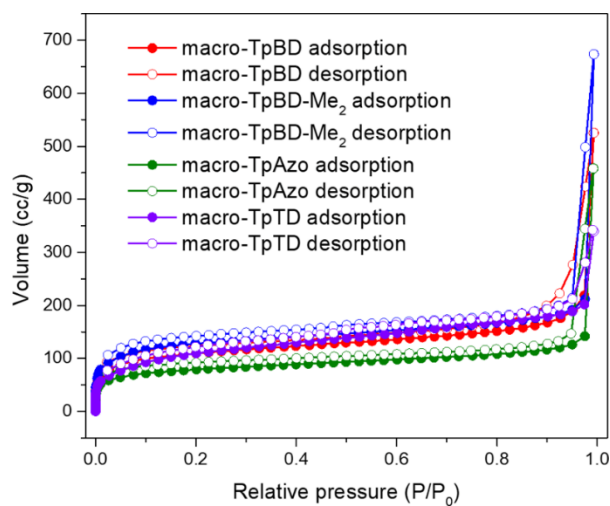
Figure S14. N_2 adsorption-desorption isotherms of the macro-TpBD, macro-TpBD-Me$_2$, macro-TpAzo and macro-TpTD.
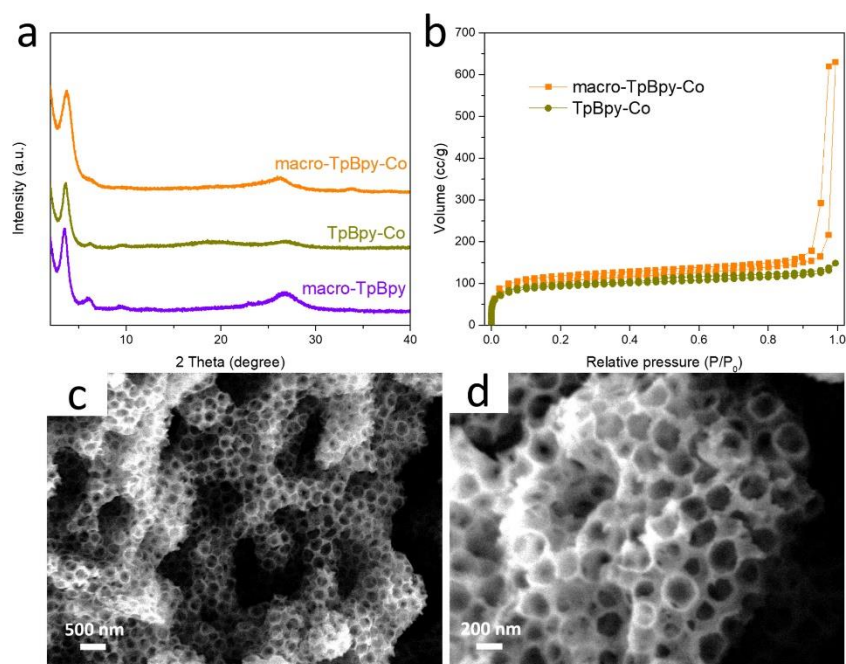
Figure S15. a) PXRD patterns, b) N_2 adsorption-desorption isotherms of macro-TpBpy-Co and TpBpy-Co. c, d) SEM images of macro-TpBpy-Co.
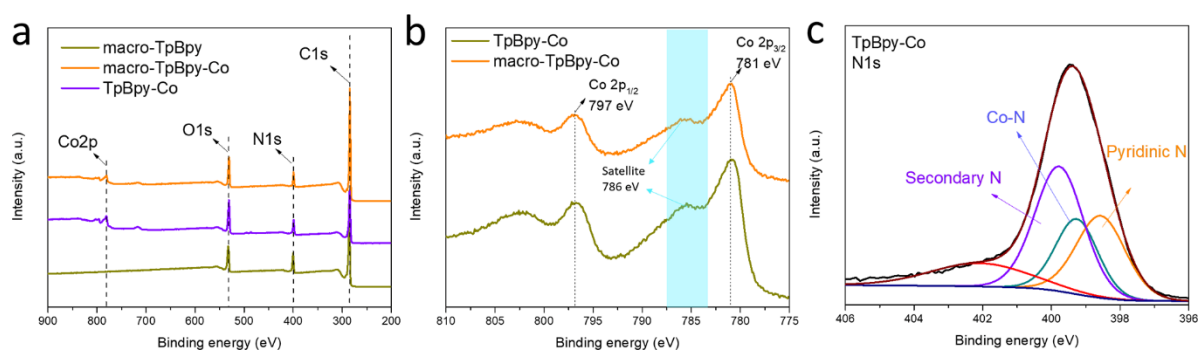

Figure S16. a) XPS survey scan of macro-TpBpy, TpBpy-Co and macro-TpBpy-Co. b) High resolution Co 2p spectra of TpBpy-Co and macro-TpBpy-Co. c) High resolution N1s spectra of TpBpy-Co.
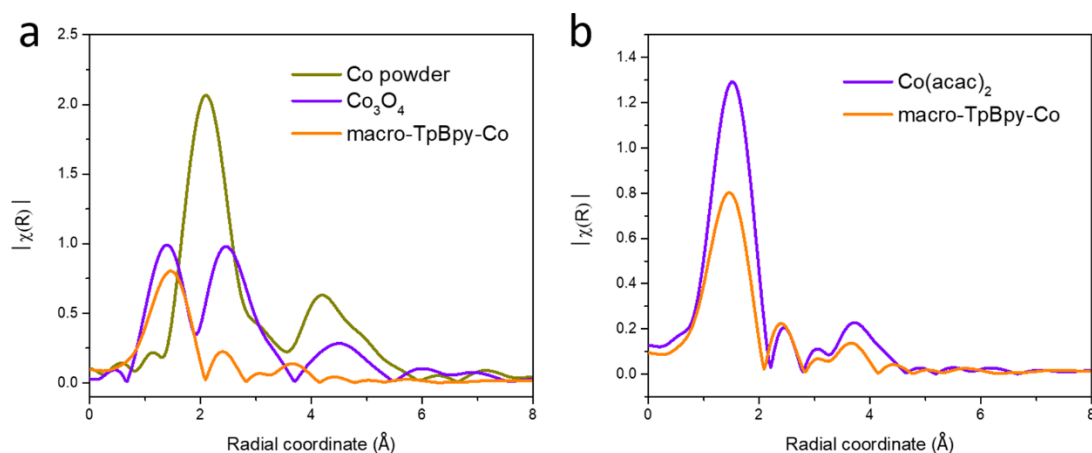
Figure S17. Corresponding Fourier-transformed EXAFS spectra collected at Co K-edge.
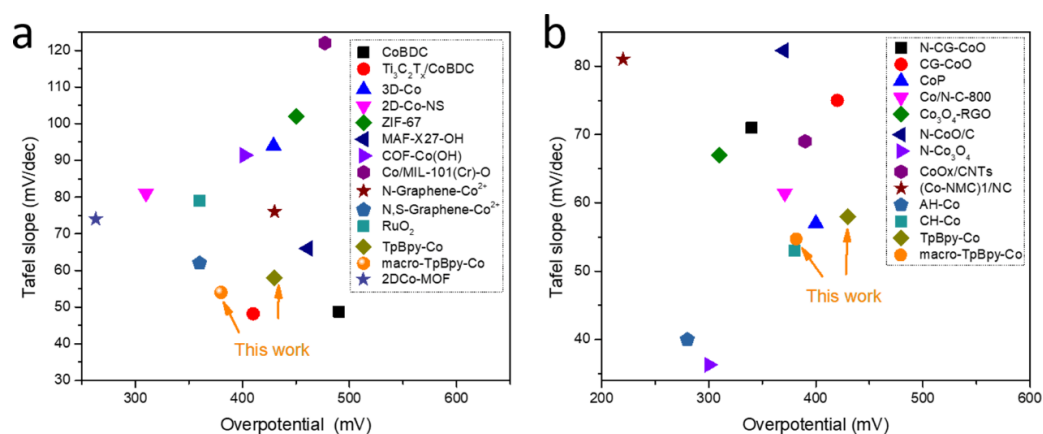

Figure S18. Comparison of Tafel slopes versus overpotential at 10 mA/cm^2 between macro-TpBpy-Co, TpBpy-Co and some recently reported a) Co-doped polymer-based OER catalysts; these OER performances are adapted from references.[33,36,37,38,39,40,41,s6] b) Co-based electrocatalysts; these OER performances are adapted form references.[s7-s14]
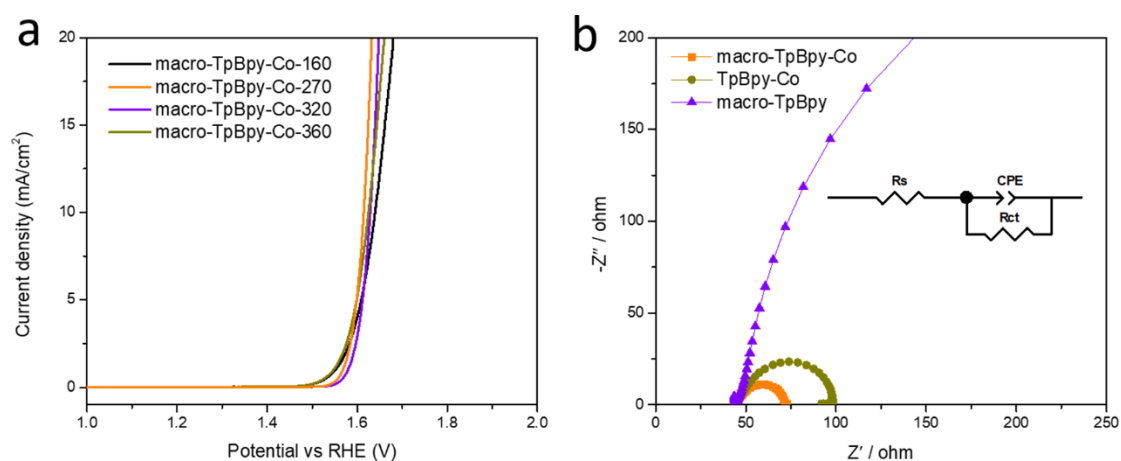
Figure S19. a) OER polarization curves for macro-TpBpy-Co with different macropore size. b) EIS spectra of the catalysts recorded at a constant potential of 1.61 V (vs. RHE); Inset shows the equivalent circuit used to fit the experimental data (Rs: electrolyte resistance, CPE: double layer capacity, Rct: charge transfer resistance).

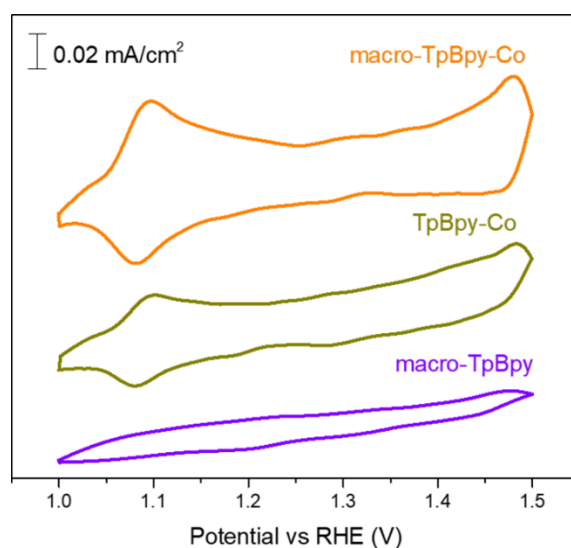**Figure S20.** CVs of macro-TpBpy, TpBpy-Co and macro-TpBpy-Co at 1.0-1.5 V (*vs* RHE) in 0.1 M KOH.
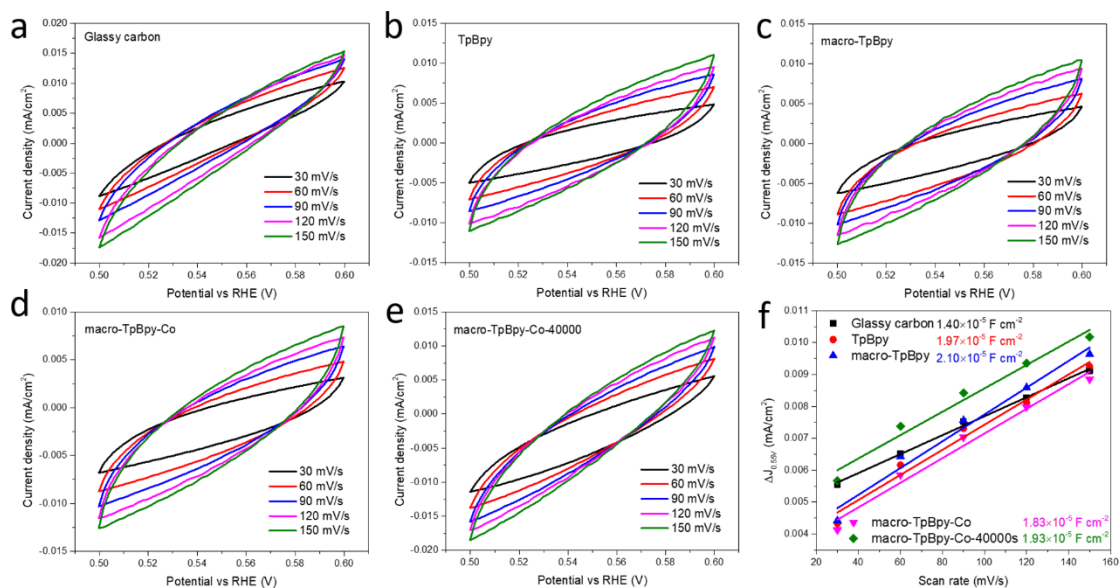
Figure S21. Cyclic voltammetry scans for as-prepared catalysts with different rates from 30 to 150 mV/s to calculate the electrochemical double-layer capacitances.
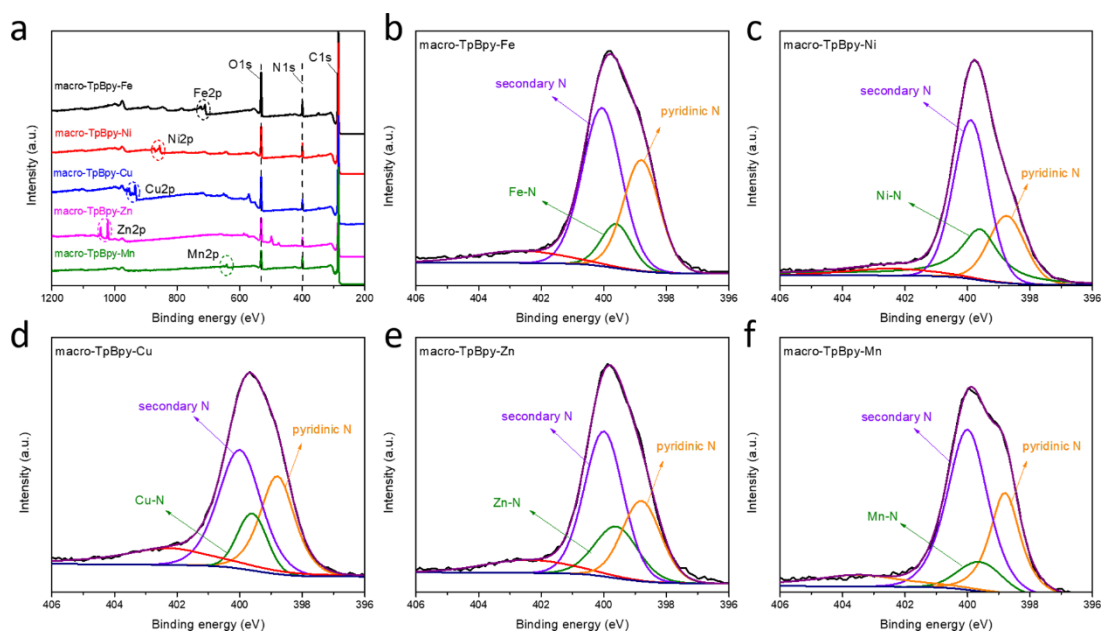

Figure S22. a) XPS survey scan, b-f) Corresponding high resolution N1s of macro-TpBpy complexing with various metal ions.
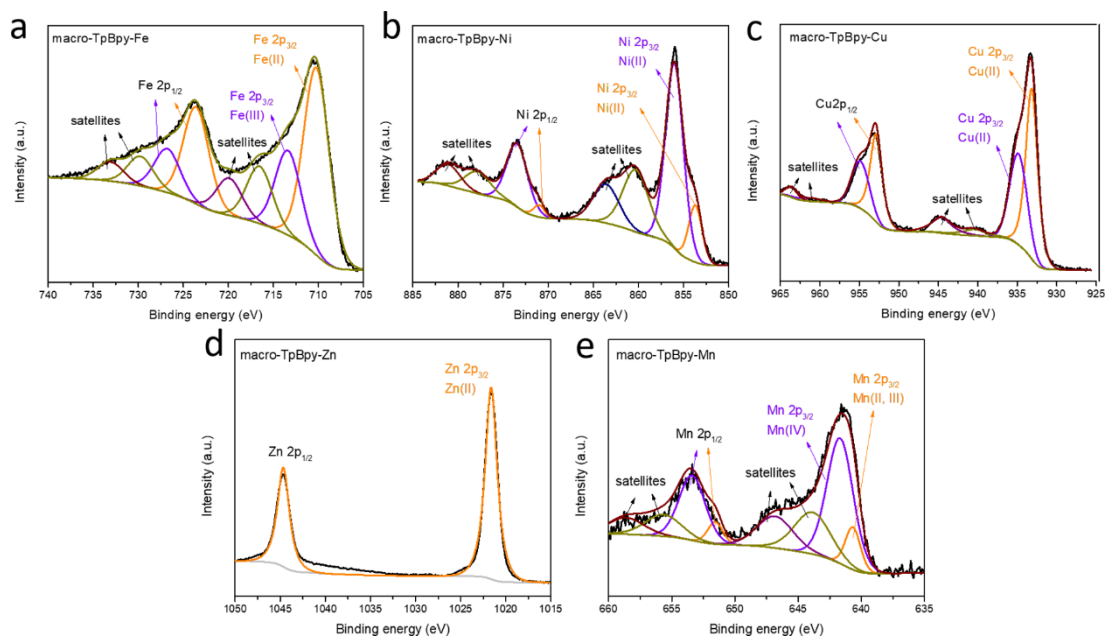
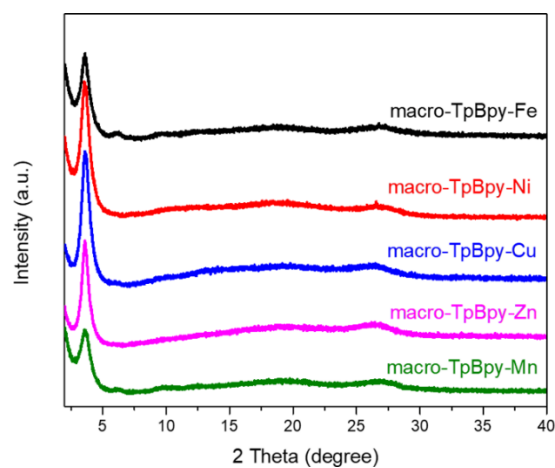**Figure S23.** High resolution metal spectra of macro-TpBpy with various metal ions.

Figure S24. PXRD patterns of macro-TpBpy with various metal ions.
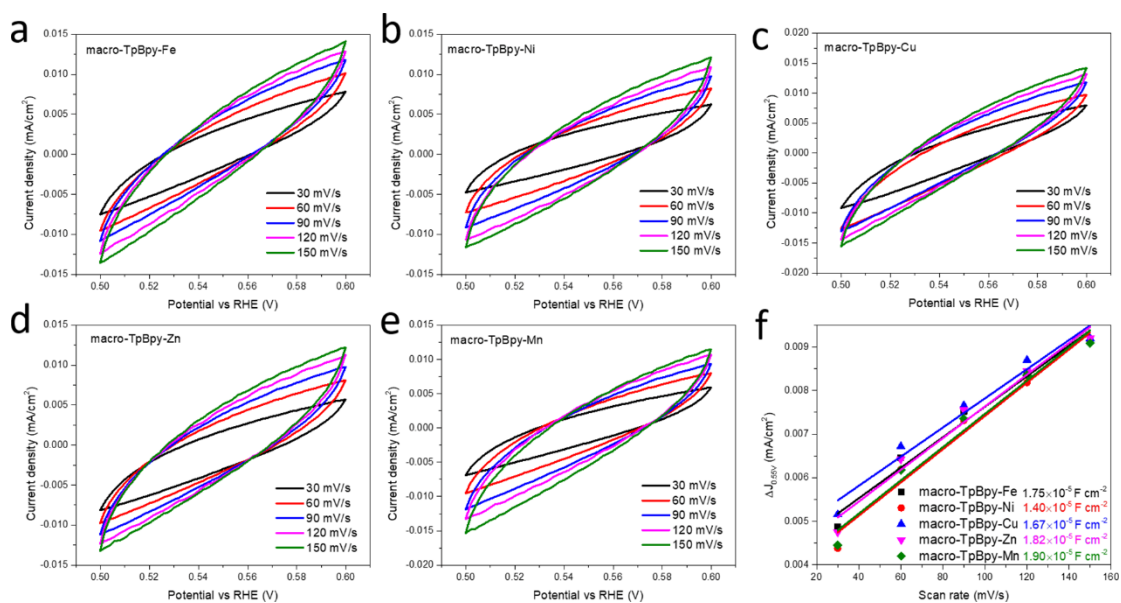
Figure S25. Cyclic voltammetry scans for macro-TpBpy with various metal ions, with different rates from 30 to 150 mV/s to calculate the electrochemical double-layer capacitances.

Figure S26. a) OER polarization curves, b) Corresponding EIS spectra for macro-TpBpy with various metal ions; Inset shows the equivalent circuit used to fit the experimental data (Rs: electrolyte resistance, CPE: double layer capacity, Rct: charge transfer resistance).
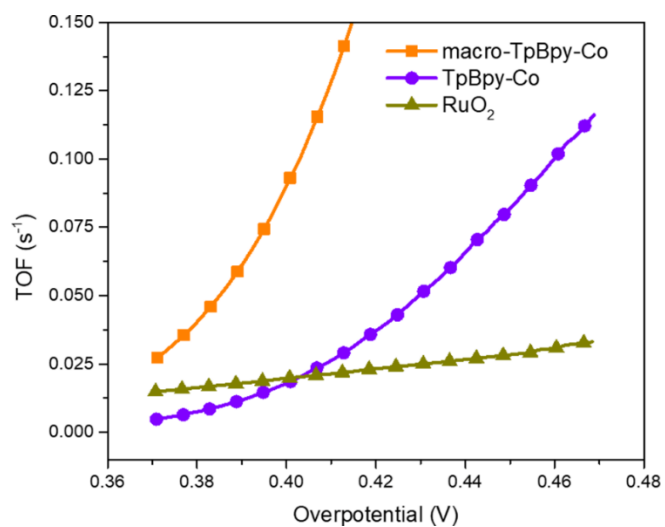
Figure S27. TOF plots of macro-TpBpy-Co, TpBpy-Co and RuO_2.
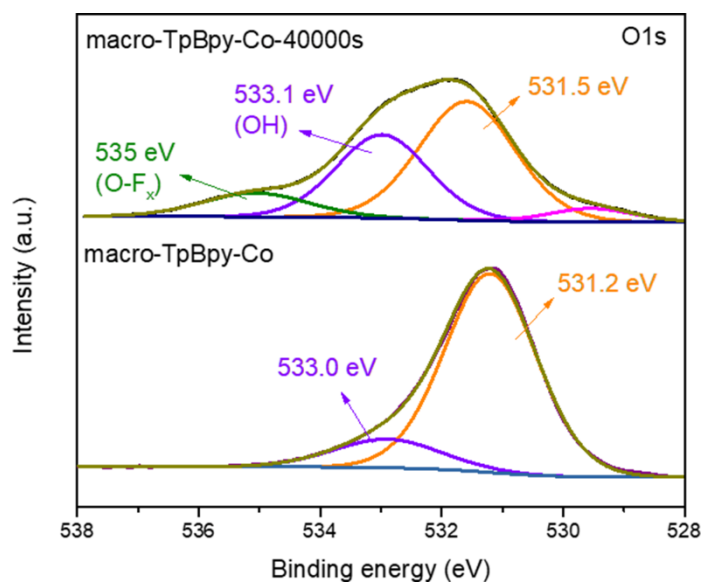
Figure S28. High resolution O1s spectra of macro-TpBpy-Co and macro-TpBpy-Co-40000s.

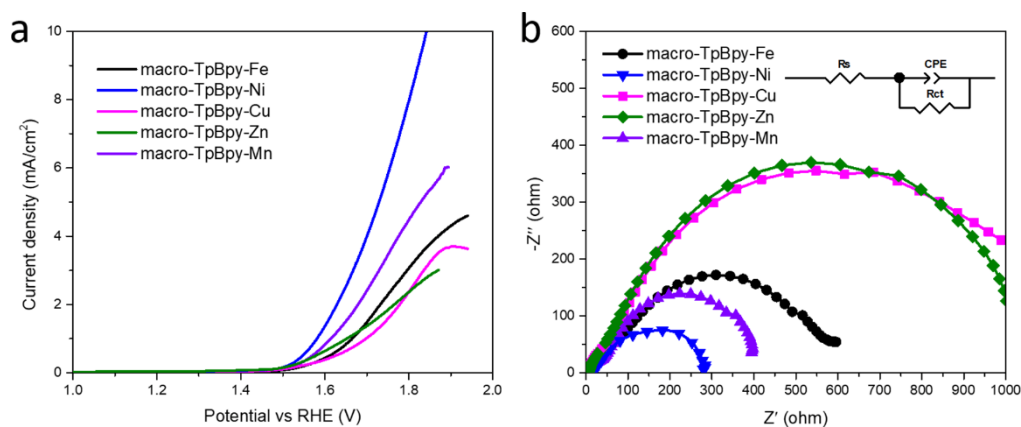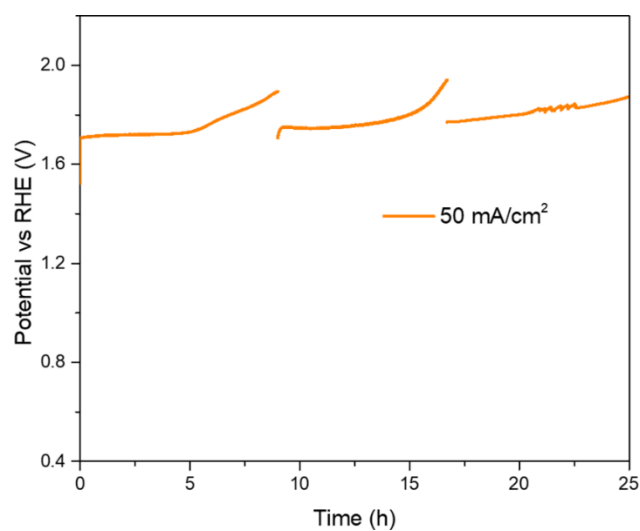**Figure S29.** Chronopotentiometry test of macro-TpBpy-Co at a current density of 50 mA/cm^2 in 0.1 M KOH. (Note that under high current density, a large amount of gas (H$_2$) production is observed on the counter electrode, which can displace the electrolyte from the fritted glass tube of the counter electrode and thus decrease the contact between counter electrode and electrolyte, resulting in a fast increase of the potential after a certain time. The chronopotentiometric measurement was therefore carried out refreshing the electrolyte in the fritted glass tube for the counter electrode every 10 hours.)

Table S1. The polymerization parameters for the synthesis of polystyrene spheres with different sizes.

Styrene / mL	PVP / g	$K_2S_2O_8$ / g	Temperature/ °C	Size / nm
39	1.5	0.5	95	160
39	1.5	0.5	75	270
39	1.5	0.5	60	320
39	1.5	0.1	75	360

Table S2. Structural properties and element content of the obtained COF-based catalysts.

	[a]Total surface area (m^2/g)	[b]Total pore volume (cm^3/g)	XPS N content (atomic %)	XPS Co content (atomic %)
TpBpy	588	0.381	10.54	-
macro-TpBpy	723	1.273	10.17	-
TpBpy-Co	314	0.316	10.96	3.01
macro-TpBpy-Co	387	0.974	9.76	2.84

[a]BET specific surface areas calculated in P/P_0 from 0.003 to 0.05. [b]Total pore volumes calculated based on the volume adsorbed at P/P_0 of ~ 0.995.

Table S3. OER performance of the as-synthesized COF-based catalysts

	Overpotential at 10 mA/cm^2 (mV)	Tafel slope (mV/dec)	Overpotential at 50 mA/cm^2 (mV)	$J_{real/active}$ (A/cm^2) at 1.61 V
macro-TpBpy	-	339	-	-
TpBpy-Co	430	58	530	0.72×10^{-6}
macro-TpBpy-Co	380	54	430	3.10×10^{-6}
RuO_2	360	79	600	-

Table S4. Summary of recently reported OER performances of other reported Co-based electrocatalysts under alkaline conditions.

Sample	η_{10} (mV)	Tafel slope(mV/dec)	Electrolyte	Substrate	Loading mass (mg/cm^2)	Reference
macro-TpBpy-Co	**380**	**54**	**0.1 M KOH**	**GC**	**0.25**	**This work**
TpBpy-Co	**430**	**58**				
CoNiS	274	45	0.1 M KOH	GC	0.25	*Adv. Mater.* **2019**, 31, 1805658
3D-Co	429	94	0.1 M KOH	GC	0.2	*Angew. Chem. Int. Ed.,* **2018,** 57, 4632-4636
2D-Co-NS	310	81				
Fe:2D-Co-NS	282	59				
N-CoO/C	370	82.3	0.1M KOH	GC		*Adv. Funct. Mater.* **2018,** 28, 1800886
N-Co$_3$O$_4$	300	36.3				
C-MOF-C2-900	350	79	0.1 M KOH	GC	0.2	*Adv. Mater.* **2018,** 30, 1705431
AH-Co	280	40	1 M KOH	GC	0.1	*Small* **2018**, 14, 1703514
CH-Co	380	53				
CoBDC	490	48.8	0.1 M KOH	GC	0.21	*ACS Nano,* **2017,** 11, 5800-5807
Ti$_3$C$_2$T$_x$/CoBDC	410	48.2		GC	0.21	
MCF-49	283	43	0.1 M KOH	GC	0.2	*J. Am. Chem. Soc.,* **2017**, 139, 1778-1781
ZIF-67	450	102	0.1 M KOH	GC	0.24	*Appl. Catal. B-Environ.,* **2017,** 205, 55-67
ZIF-67/NPC-2	410	117				
FeCo-ONS	308	37	0.1 M KOH	GC	0.39	*Adv. Mater.* **2017,** 29, 1606793
Co$_3$FeS$_{1.5}$(OH)$_6$	358	79	0.1 M KOH	GC	0.25	*Adv. Mater.* **2017,** 29, 1702327
MAF-X27-OH	461	66	0.1 M KOH	GC	0.18	*J. Am. Chem. Soc.,* **2016,** 138, 8336-8339
2D-Co-MOF	263	74	1 M KOH	GC	-	*J. Mater. Chem. A* **2018**, 6, 22070-22076
FeTPyP-Co	351 (1mA/cm^2)	-	0.1 M NaOH	GC	0.2	*J. Am. Chem. Soc.,* **2016,** 138, 3623-3626
Co-WOC-1	390 (1mA/cm^2)	128	0.1 M KOH	GC	0.2	*Angew. Chem, Int. Ed.,* **2016,** 55, 2425-2430
ZIF-67	443 (4mA/cm^2)	-	0.1 M KOH	FTO	-	*New J. Chem.,* **2016,** 40, 3032-3035
Ni/Fe-BTC	270	43	0.1 M KOH	Ni foam	0.5	*ACS Appl. Mater. Interfaces,* **2016,** 8, 16736-16743

COF-Ni(OH)$_2$	487	89.3	0.1 M KOH	GC	0.28	*Adv. Energy. Mater,* **2016,** 6, 1600110
COF-Co(OH)$_2$	402	91.4				
CoP hollow polyhedron	400	57	1M KOH	GC	-	*ACS Appl. Mater. Interfaces* **2016,** 8, 2158-2165
Plasma-engraved Co$_3$O$_4$	300	68	0.1 M KOH	GC	-	*Angew. Chem. Int. Ed.* **2016,** 55, 5277
PCPTF	330$_{30}$	65	1 M KOH	Glass slide		*Adv. Mater.* **2015,** 27, 3175-3180
CoO$_x$(4.3)/CNTs	390	69	0.1M KOH	GC		*ACS Catal.* **2016,** 6, 4347
CoOx@N	232	-	1M KOH	GC	0.42	*J. Am. Chem. Soc.* **2015,** 137, 2688-2694
(Co-NMC)$_1$/NC	220	81	0.1M KOH	GC		*Small* **2016,** 12, 3703-3711
IrO$_2$	350	55	0.1 M KOH	GC	-	*Adv. Energy Mater.* **2015,** 5, 1401660
Co/MIL-101(Cr)-O	477	122	0.1 M KOH	GC	-	*J. Hydrogen Energy,* **2015,** 40, 9713-9722
BCFSn-721	420	69	0.1 M KOH	GC		*Adv. Sci.,* **2015,** 1500187
Co-ZIF-9	510 (1mA/cm^2)	93	0.1 M KOH	FTO	0.2	*Nanoscale,* **2014,** 6, 9930-9934
Co/N-C-800	371	61.4	0.1M KOH	GC		*Nanoscale* **2014,** 6, 15080-15089
Co$_3$O$_4$C-NA	290	70	0.1 M KOH	GC	-	*J. Am. Chem. Soc.* **2014,** 136, 13925-13931
N-CG-CoO	340	71	1M KOH	GC		*Energy Environ. Sci.* **2014,** 7, 609-616
CG-CoO	420	75				
Co$_3$O$_4$-RGC	310	67	0.1M KOH	GC	0.17	*Nat. Mater.* **2011,** 10, 780-786

References

[s1] Xu, J. Y.; Li, J. J.; Xiong, D. H.; Zhang, B. S.; Liu, Y. F.; Wu, K. H.; Amorim, I.; Li, W.; Liu, L. F. Trends in activity for the oxygen evolution reaction on transition metal (M= Fe, Co, Ni) phosphide pre-catalysts. *Chem. Sci.* **2018,** 9, 3470-3476.

[s2] Zhao, S. L.; Wang, Y.; Dong, J. C.; He, C. T.; Yin, H. J.; An, P. F.; Zhao, K.; Zhang, X. F.; Cao, C.; Zhang, L. J.; Lv, J. W.; Wang, J. X.; Zhang, J. Q.; Khattak, A. M.; Khan, N. A.; Wie, Z. X.; Zhang, J.; Liu, S. Q.; Zhao, H. J.; Tang, Z. Y. Ultrathin metal-organic framework nanosheets for electrocatalytic oxygen evolution. *Nat. Energy* **2016,** 184, 16184.

[s3] Ravel, B.; Newville, MA. ATHENA, ARTEMIS, HEPHAESTUS: data analysis for X-ray absorption spectroscopy using IFEFFIT. *J. Synchrotron Radiat.* **2005,** 12, 537-541.

[s4] Chong, J. H.; Sauer, M.; Patrick, B. O.; MacLachlan, M. J. Highly Stable Keto-Enamine Salicylideneanilines. *Org. Lett.,* **2003**, 5, 3823-3826.

[s5] Shen, K.; Zhang, L.; Chen, X. D.; Liu, L. M.; Zhang, D. L.; Han, Y.; Chen, J. Y.; Long, J. L.; Luque, R.; Li, Y. W.; Chen, B. L. Ordered macro-microporous metal-organic framework single crystals. *Science* **2018,** 359, 206-210.

[s6] Xu, Y.; Li, B.; Zheng, S.; Wu, P.; Zhan, J.; Xue, H.; Xu, Q.; Pang, H. Ultrathin Two-Dimensional Cobalt–Organic Framework Nanosheets for High-Performance Electrocatalytic Oxygen Evolution. *J. Mater. Chem. A.* **2018,** 6, 22070-22076.

[s7] Mao, S.; Wen, Z.; Huang, T.; Hou, Y.; Chen, J. High-Performance Bifunctional Electrocatalysts of 3D Crumpled Graphene-Cobalt Oxide Nanohybrids for Oxygen Reduction and Evolution Reactions. *Energy Environ. Sci.* **2014,** 7, 609-616.

[s8] Liu, M. J.; Li, J. H. Cobalt Phosphide Hollow Polyhedron as Efficient Bifunctional Electrocatalysts for the Evolution Reaction of Hydrogen and Oxygen. *ACS Appl. Mater. interfaces* **2016,** 8, 2158-2165.

[s9] Su, Y.; Zhu, Y.; Jiang, H.; Shen, J.; Yang, X.; Zou, W.; Chen, J.; Li, C. Cobalt Nanoparticles Embedded in N-Doped Carbon as an Efficient Bifunctional Electrocatalyst for Oxygen Reduction and Evolution Reactions. *Nanoscale* **2014**, 6, 15080-15089.

[s10] Liang, Y. Y.; Li, Y. G.; Wang, H. L.; Zhou, J. G.; Wang, J.; Regier, T.; Dai, H. J. Co3O4 Nanocrystals on Graphene as a Synergistic Catalyst for Oxygen Reduction Reaction. *Nat. Mater.* **2011**, 10, 780-786.

[s11] Li, X.; Wei, J.; Li, Q.; Zheng, S.; Xu, Y.; Du, P.; Chen, C.; Zhao, J.; Xue, H.; Xu, Q.; Pang, H. Nitrogen-Doped Cobalt Oxide Nanostructures Derived from Cobalt-Alanine Complexes for High-Performance Oxygen Evolution Reactions. *Adv. Funct. Mater.* **2018,** 28, 1800886.

[s12] Seo, B.; Sa, Y. J.; Woo, J.; Kwon, K.; Park, J.; Shin, T. J.; Jeong, H. Y.; Joo, S. H. Size-Dependent Activity Trends Combined with In Situ X-ray Absorption Spectroscopy Reveal Insights into Cobalt Oxide/Carbon Nanotube-Catalyzed Bifunctional Oxygen Electrocatalysis. *ACS Catal.* **2016**, 6, 4347-4355.

[s13] Bayatsarmadi, B.; Zheng, Y.; Tang, Y.; Jaroniec, M.; Qiao, S. Z. Significant Enhancement of Water Splitting Activity of N-Carbon Electrocatalyst by Trace Level Co Doping. *Small*. **2016,** 12, 3703-3711.

[s14] Liu, J.; Nai, J.; You, T.; An, P.; Zhang, J.; Ma, G.; Niu, X.; Liang, C.; Yang, S.; Guo, L. The Flexibility of an Amorphous Cobalt Hydroxide Nanomaterial Promotes the Electrocatalysis of Oxygen Evolution Reaction. *Small.* **2018,** 14, 1703514.